Universitat Politècnica de València

Instituto de Tecnología Química

Carbene reactions catalyzed by silver-supported or metal-free microporous solids

Doctoral Thesis, PhD in Sustainable Chemistry

Presented by: Yongkun Zheng

Supervised by: Dr. Antonio Leyva Pérez

Dr. Marta Mon Conejero

Valencia, June 2024

Antonio Leyva Pérez, Scientific Researcher at Instituto de Tecnología Química, the Valencia Polythecnic University- Spanish Research Council,
Marta Mon Conejero, Post doct researcher at Instituto de Tecnología Química, the Valencia Polythecnic University- Spanish Research Council,

CERTIFY: That the thesis entitled "**Carbene reactions catalyzed by silver-supported or metal-free microporous solids**". Mr. Yongkun Zheng has been carried out under our supervision by at Instituto de Tecnología Química.

Dr. Antonio Leyva Pérez

Dr. Marta Mon Conejero

Acknowledges

In January 2021, the global COVID-19 pandemic emerged, resulting in a total worldwide death toll of 14.9 million. Parents firmly objected to the idea of studying abroad, but now, as I'm on the verge of graduating with my PhD after four years, I am filled with happiness.

First of all, I should thank my government for giving me the opportunity to study abroad and providing me with living support. In addition, I have to thank ITQ for providing me with an excellent scientific research platform. My deepest gratitude goes to my supervisor Antonio. He has professional knowledge and an excellent team. He treats students seriously and is dedicated to his work, and I appreciate his continuous encouragement. I also want to express my thanks to Marta for her assistance in revising my doctoral thesis and other support. Not to forget Serigo and Frank, who extended a helping hand when I first arrived in 2021, and with whom I have maintained a strong friendship. I am also thankful to Cristina, Paloma, Susi, Silvia, Francesco, Judit, Amarawati, Belen, Jordi, Miguel, and many others for their kindness and support.

Finally, I love here, Valencia, the city where I have lived for four years.

Abstract

Carbenes represent a class of highly potent reagents used in the field of organic synthesis, showcasing an ability to effectively engage during insertion processes within a diverse array of typically inert chemical bonds, thereby facilitating the creation of two fresh bonds in a direct and efficient manner. For that, catalysts are needed. The exploration conducted here involved the fabrication of various forms of silver catalysts, including single atoms, dimers or clusters, on microporous solids like zeolites or metal-organic frameworks (MOFs), achieved through uncomplicated methods such as ion exchange and calcination or reduction procedures, as shown in *Chapters 4* and *5*. These innovative catalysts demonstrated exceptional catalytic performance in facilitating the Buchner reaction involving carbenes, yielding high product quantities while maintaining favorable selectivity. The zeolites and MOFs functioned as macroscopic ligands that served to stabilize the silver active sites, thereby enabling the utilization of cost-effective and recyclable catalysts for *in-situ* carbene generation from diazoacetate, subsequently promoting the selective insertion into C-C, C-H, O-H, and O-O bonds. Furthermore, in *Chapter 6*, we have gone one step further, generating and stabilizing carbenes in metal-free commercially available dealuminized HY zeolites.

In this thesis, two distinct solid-supported carbenes were characterized, encompassing a silver carbene-mediated variant that was successfully identified through *in-situ* Raman spectroscopy and *in-situ* ^{13}C CP/MAS NMR analyses, alongside a zeolite-stabilized carbene that was effectively elucidated via *in-situ* Fourier Transform Infrared Spectroscopy and ^{13}C CP/MAS NMR techniques.

Resumen

Los carbenos representan una clase de reactivos altamente potentes utilizados en el campo de la síntesis orgánica, que muestran la capacidad de participar eficazmente durante los procesos de inserción en una amplia variedad de enlaces químicos, típicamente inertes, facilitando así la creación de dos nuevos enlaces de manera directa y eficiente. Para ello, son necesario catalizadores. La investigación realizada aquí implicó la fabricación de diversas formas de catalizadores de plata, incluidos átomos individuales, dímeros o clústeres, en sólidos microporosos como zeolitas o polímeros de coordinación porosos, también llamados MOFs (del inglés, *Metal-Organic Frameworks*), logrados a través de métodos sencillos como el intercambio iónico y procedimientos de calcinación o reducción, como se muestra en los *Capítulos 4* y *5*. Estos catalizadores innovadores demostraron un rendimiento catalítico excepcional para la reacción de Buchner que involucra carbenos, obteniendo buenos rendimientos del producto mientras mantenían una selectividad favorable. Las zeolitas y los MOFs funcionaron como ligandos macroscópicos que sirvieron para estabilizar los sitios activos de plata, lo que permitió la utilización de catalizadores baratos y reciclables para la generación *in-situ* de carbenos a partir de diazoacetato, promoviendo posteriormente la inserción selectiva en enlaces C-C, C-H, O-H y O-O. Además, en el *Capítulo 6*, dimos un paso más allá, generando y estabilizando carbenos en zeolitas HY dealuminizadas, comercialmente disponibles y libres de metal.

En esta tesis, se caracterizaron dos carbenos sólidos distintos, que incluyen una variante mediada por carbeno de plata que fue identificada con éxito mediante espectroscopía de Raman *in-situ* y

análisis de RMN ^{13}C CP/MAS *in-situ*, junto con un carbeno estabilizado en zeolita que fue efectivamente elucidado a través de espectroscopía de infrarrojo con transformada de Fourier *in-situ* y técnicas de RMN ^{13}C CP/MAS.

Resum

Els carbens representen una classe de reactius altament potents utilitzats en el camp de la síntesi orgànica, que mostren la capacitat de participar d'una manera eficaç durant els processos d'inserció en una àmplia varietat d'enllaços químics, típicament inerts, facilitant així la creació de dos nous enllaços de manera directa i eficient. La investigació realitzada ací va implicar la fabricació de diverses formes de catalitzadors de plata, inclosos àtoms individuals, dímers o clústers, en sòlids microporosos com a zeolites o polímers de coordinació porosos, també anomenats MOFs (de l'anglés, *Metal-Organic Frameworks*), aconseguits a través de mètodes senzills com l'intercanvi iònic i procediments de calcinació o reducció, com es mostra en els *Capítols 4* i *5*. Estos catalitzadors innovadors van demostrar un rendiment catalític excepcional per a la reacció de Buchner que inclou carbens, obtenint bons rendiments del producte mentres mantenien una selectivitat favorable. Les zeolites i els MOFs van funcionar com lligands macroscòpics que van servir per a estabilitzar els llocs actius de plata, la qual cosa va permetre la utilització de catalitzadors rendibles i reciclables per a la generació *in-situ* de carbens a partir de diazoacetat, promovent posteriorment la inserció selectiva en enllaços C-C, C-H, O-H i O-O. A més, en el *Capítol 6*, vam fer un pas més enllà, generant i estabilitzant carbens en zeolites HY dealuminitzades, comercialment disponibles i lliures de metall.

En esta tesi, es van caracteritzar dos carbens sòlids diferents, que inclouen una variant mitjançant carben de plata que va ser identificada amb èxit mitjançant espectroscopía de Raman in-situ i anàlisi de RMN ^{13}C CP/MES in-situ, juntament amb un carben

estabilitzat en zeolita que va ser efectivament elucidat per mitjà de espectroscopía d'infraroig amb transformada de Fourier *in-situ* i tècniques de RMN ^{13}C CP/MAS.

Abbreviations

AC HAADF-STEM Aberration Corrected High-angle Annular Dark-field

Scanning Transmission Electron Microscopy

AES Absorption Emission Spectroscopy

AFM Atomic Force Microscopy

BE Binding Energy

BET Brunauer−Emmett−Teller

BF Bright-field

DFT Density-functional Theory

DR Diffuse-Reflectance

DRIFTS Diffuse Reflection Infrared Fourier Transformed Spectroscopy

EDA Ethyl Diazoacetate

EDX Energy Dispersive X-ray

ESI Electrospray Ionization

EXAFS Extended X-ray Absorption Fine Structure

FAU Faujasite-Type Zeolites

FT-IR Fourier Transformed Infrared Microscopy

FESEM Field Emission Scanning Electron Microscopy

GC Gas Chromatography

GC-MS Gas Chromatography-Mass Spectrometry

HRTEM High Resolution Transmission Electron Microscopy

ICP Inductively Coupled Plasma

iDPC Integrated Differential Phase Contrast

IR Infrared

KIE Kinetic Isotopic Effect

MAS Magic Angle Spinning

MAS ss-NMR Magic Angle Spinning-Solid State Nuclear Magnetic Resonance

MC Metal Cluster

MOF Metal-organic Framework

NCs Nanoclusters

NHC N-heterocyclic carbenes

NMR Nuclear Magnetic Resonance

NPs Nanoparticles

SA Single Atom

SAC Single Atoms Catalyst

SBU Secondary Building Unity

SCXRD Single Crystal X-ray Diffraction

SDAs structure-directing agents

SEM Scanning Electron Microscopy

STEM Scanning Transmission Electron Microscopy

TEM Transmission Electron Microscopy

TGA Thermogravimetric Analyses

TPD Temperature-programmed desorption

UV-Vis Ultraviolet-Visible spectroscopy

UWT Wavelet Transforms

XANES X-ray Absorption Near Edge Structure

XAS X-ray Absorption Spectroscopy

XPS X-Ray Photoelectron Spectroscopy

XRD X-Ray Diffraction

Contents

Chapter 1. General introduction

1.1 *Carbenes*

1.1.1 *Structure of carbenes*

Carbene initially regarded as chemical curiosities, have an important role in organic and organometallic chemistry. In 1885, the Buchner ring expansion reaction, in which a carbene formed from diazoacetic ester, was reported by E. Bucher and T. Curtis. [1] The chemistry of carbenes began with the work of many scientists such as Staudinger, [2] Tschugajeff, [3] Breslow, [4] Doering, [5] and Fischer, [6] Wanzlick, [7] Skell, [8] Arduengo, [9] and Nguyen. [10] Over the past five decades, carbenes have assumed the role of transient intermediates, participating in numerous reactions of significant synthetic importance.

A carbene is a neutral compound containing a divalent carbon with six valence electrons, [11] out of which two are unshared valence electrons. Carbenes exhibit two distinct structures, referred to as the singlet state and the triplet state in spectroscopy (see in **Figure 1.1**). Whether a carbene is in the singlet or triplet state depends on its electronic structure.

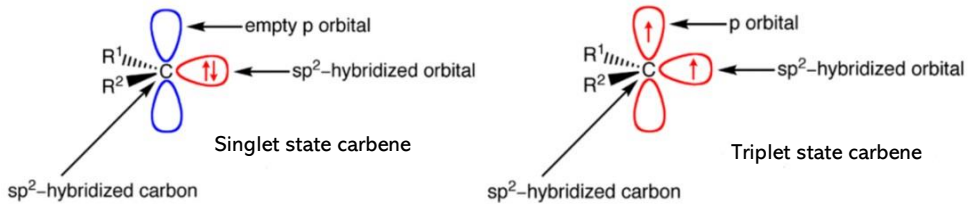

Figure 1.1 Electronic configurations and geometry of singlet and triplet carbenes at ground state.

Carbenes usually contain sp^2 hybridized carbon atoms according to the valance bond theory. Two of the three sp^2-hybrid orbitals bond with their carbene substituents by covalent bonds and two vacant orbitals remain, consisting in the sp^2-hybrid orbital

and the p orbital. The two non-bonding electrons of carbenes must be placed in these vacant orbitals. In singlet carbenes (see in **Figure 1.1**), the two non-bonding electrons occupy the lower-energy sp^2 hybrid orbitals and have opposite spins, while the p-orbital (P) remains unoccupied and is perpendicular to the three sp^2 hybrid orbitals. This arrangement allows us to predict that the singlet carbene can exhibit characteristics of both a carbocation (with the empty p-orbital) and a carboanion (with the paired electrons in the sp^2 hybrid orbitals), that is, it possesses both electrophilic and nucleophilic character. Therefore, these carbenes are generally involved in cyclopropanation reaction [12, 13, 14] and cheletropic addition, [15] and usually have a bond angle of approximately 103° (see **Figure 1.2**).

On the other hand, triplet carbenes are those in which the two non-bonding electrons occupy different orbitals, with parallel spin orientation (see in **Figure 1.1**). In this case, there are two possibilities, they may be either linear or bent, that is, sp or sp^2 hybridized, respectively. The linear geometry implies an sp-hybridized carbene center with two nonbonding degenerate orbitals (p_x and p_y). Bending the molecule breaks this degeneracy and the carbon atom adopts a sp^2-type hybridization: the p_y orbital remains almost unchanged (called p_π), while the orbital that starts as pure p_x orbital is stabilized since it acquires some s character (called σ). [16] **Figure 1.2** indicates that triplet carbenes are typically bent because this conformation lowers the energy of the occupied orbitals. Since the two electrons in triplet carbenes occupy separate p-orbitals, they exhibit biradical behavior and have a bond angle of approximately 136°. Additionally, triplet carbenes exhibit less stereospecificity in their reactions, unlike singlet carbenes, [17-19] because the triplet carbene have two single electrons, and they can be detected by EPR. [20-24]

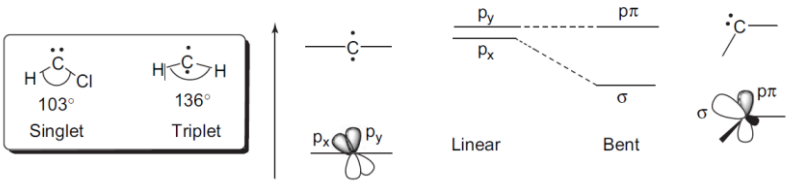

Figure 1.2 Relationship between carbene bond angle and the nature of the frontier orbitals. [25] Reference: In *Advances in Organometallic Chemistry*, Pérez, P. J. Ed.; Vol. 66; Academic Press, 2016.

A singlet carbene might seem to have lower energy because of the unshared electron pair resides in a sp^2 hybrid orbital. However, when we consider the electron repulsion energy required to pair two electrons in a single orbital (see **Figure 1.3**), the situation changes. The energy of triplet carbenes is generally 33 kJ/mol lower than that of singlet carbenes (following Hund's maximum multiplicity rule). Consequently, in the ground state, triplets carbene are more stable, [16] while in the excited state, singlets carbene are more stable.

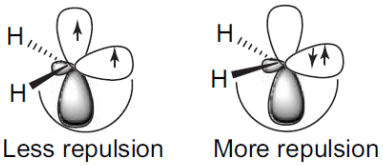

Figure 1.3 Electronic repulsion in triplet and singlet states.

Additionally, there are some methods to stabilize carbenes. Firstly, by introducing bulky substituents at the α-position of the carbene center, we can enhance the kinetic stability of singlet carbenes. [25] These bulky groups hinder the reactivity of the carbene, making it less prone to rapid reactions. The α-position refers to the carbon atom directly attached to the carbene center.

On the other hand, in terms of thermodynamic stabilization, it involves interactions between the carbon orbitals (σ and p_π) and appropriate substituents since the nature of these affects the electronic properties of the carbene.

If the substituents attached to the carbene carbon are electron withdrawing groups, the carbene prefers the singlet structure. These groups stabilize the σ orbital through inductive effects. Examples of such substituents include ester (e.g., COOEt) or halogens (e.g., Br), which pull electron density away from the carbene center. On the contrary, if the substitutes attached to the carbon of the carbene are electron-donating groups through the σ bond, the carbene prefers the triplet structure. In addition, the electron-donating groups, that is, those that have non-bonding pairs of electrons (nitrogen, oxygen, sulfur, halogen, etc.), easily donate their electrons to the vacant p orbital of the carbene, stabilizing the singlet state through resonance effects. Some examples follow:

1) σ-Electron-withdrawing substituent groups, stabilize the σ orbital through inductive effects. Examples of such substituents include halogens (e.g., Br), which pull electron density away from the carbene center.

2) π -Electron-withdrawing substituent groups stabilize the σ orbital through resonance effects. Resonance effects involve delocalization of electron density. For instance, cyano groups (CN) can stabilize singlet carbenes by resonance donation of electron density from the filled p-orbital of the carbenic carbon into the π orbital network of the CN triple bond.

3) π -Electron-donating groups: These groups raise the energy of the vacant pπ orbital. Examples include alkoxy (OR), thioalkyl (SR), and amino (NR_2) groups. [16, 26] Substituents capable of donating electron pairs can stabilize the singlet state by delocalizing the pair into an empty p-orbital. If the energy of the singlet state is sufficiently reduced, it may indeed become the ground state. Unfortunately, there are no viable strategies for stabilizing triplets. [25]

1.1.2 *Generation of carbenes*

Carbenes are fascinating reactive intermediates in organic chemistry and can be generated through various methods. Exposure to heat, light, or transition metal catalysts leads to the decomposition of diazoalkanes, resulting in the formation of carbenes. Additionally, the Bamford-Stevens reaction provides an alternative route for generating carbenes, yielding either carbenes in aprotic solvents or carbenium ions in protic solvents. Another method involves the induced elimination of halogens from gem-dihalides or HX from a CHX_3 moiety using organolithium reagents or other strong bases. While it remains uncertain whether completely free carbenes are formed in these reactions, metallocarbenes (or carbenoids) still give the expected products. [25] Below, the most common methods for preparing carbenes, which are depicted in **Figure 1.4**, are described in detail.

1) Decomposition of diazo compounds by thermolysis, photolysis or transition metal catalysts. Diazo compounds are widely used as carbene precursors. Their exposure to heat, light or metal catalysts, such as rhodium or copper, results in the loss of nitrogen gas and the formation of the corresponding carbene. This is the reason we will employed in thesis herein. The stability of this type of compounds depends significantly on the substituents, simple diazoalkanes (e.g., diazomethane) tend to be unstable.

2) Induced elimination of halogen from gem-dihalides or HX from a CHX_3 moiety. Gem-dihalides, compounds with halogens directly bonded to the same carbon, can undergo elimination reactions. Organolithium reagents (strong bases) are employed to induce the elimination of halogens (HX) from gem-dihalides. The resulting species may include carbenes, although it remains uncertain whether completely free carbenes are formed. In some cases, evidence suggests that metal-carbene complexes may be present instead of isolated free carbenes. Despite this complexity, these metallocarbenes (or carbenoids) still yield the expected products.

3) Sulfonyl hydrazone under basic conditions (Bamford Stevens Reaction). Tosylhydrazones serve as carbene precursors and are widely used. These compounds are readily prepared by reacting aldehydes or ketones with 4-toluenesulfonyl hydrazide. These tosylhydrazones are stable and serve as starting materials for further transformations. When treated with a strong base, tosylhydrazones undergo elimination of toluenesulfinate. This process generates transient diazo compounds. The diazo compound formed is not normally isolated. Upon heating, the diazo compound decomposes to yield the corresponding carbene.

4) Photolysis of diazirines. Diazirines are three-membered heterocycles containing two nitrogen atoms. Carbenes can also be synthesized from diazirines upon exposure to heat or light.

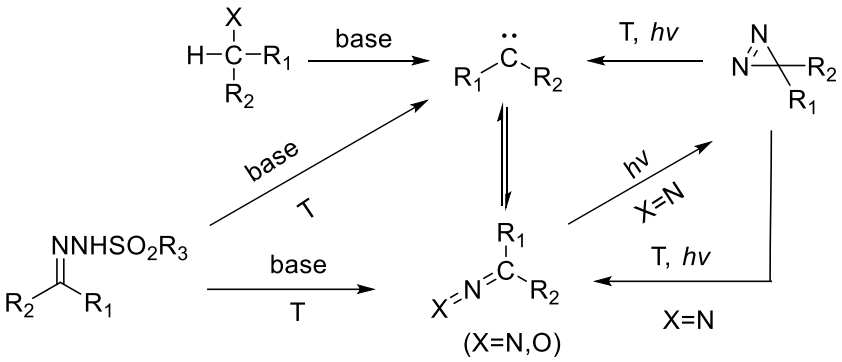

Figure 1.4 Some preparation methods of carbenes.

1.1.3 *The transition metal carbene complexes*

Carbenes are generally unstable, but they can form stable transition metal carbene complexes by bonding with metals. [27-32] The transition metal carbene complexes can be thought of as a class of divalent carbon intermediates coordinated with metals. In these complexes, the highly reactive and short-lived free carbenes are stabilized by bonding with metals, where two unpaired electrons form a stable metal-carbon bond through interaction with the metal's empty d-orbitals. The two common types of metal carbenes are the "Fischer-type" and the "Schrock-type" carbenes (see **Figure 1.5**). [20, 26, 33-35]

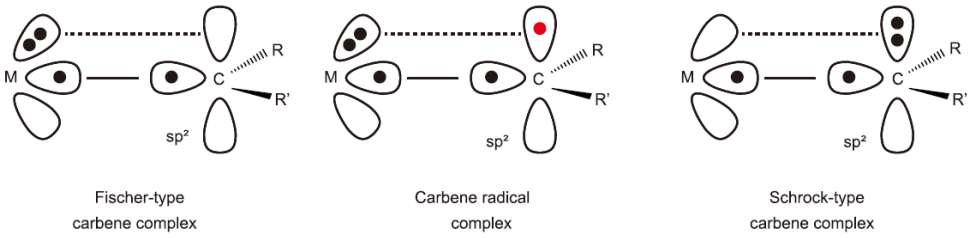

Figure 1.5 The "Fischer-type" and the "Schrock-type" carbenes.

The "Fischer-type" carbenes involve transition metals from groups VI to VIII. [36] The metal centers are normally in a low oxidation state and are typically stabilized by a series of electron-withdrawing ligands, such as carbon monoxide (CO). [37-40] In these complexes, the carbene carbon atom is sp^2-hybridized and possesses an empty p-orbital. Although the carbene carbon is electron-deficient, it is compensated by the interaction with a lone pair of electrons on adjacent atoms. In Fischer-type carbenes, the carbene carbon is positively charged (cationic) and readily engages in electrophilic reactions with electron-rich substrates. A representative example is the metal hexacarbonyls complex, where the carbene carbon bears heteroatom substituents (e.g., R = OMe or NMe_2) to enhance its cationic character and facilitate metal-to-ligand π-back donation.

On the other hand, the "Schrock-type" metal carbenes are exemplified by compounds like bis(cyclopentadienyl) metal complexes. These typically feature early transition metals (such as Ti, Zr, and Ta) as the central metal, without CO ligands. Unlike the "Fischer-type," the "Schrock-type" carbenes lack the electron-withdrawing CO ligands and exhibit distinct reactivity. In Schrock-type carbenes, the carbene carbon is negatively charged and can be thought of as an analog of the Wittig reagent. These carbenes readily undergo addition reactions with electrophilic reagents.

There is another type of metal-carbene complex (carbene radicals), distinct from the two previously mentioned structures. This particular complex can be seen as a borderline between the other two. [41-45]

1.1.4 *Metal carbenes from diazo compounds*

Currently, the most common method for generating metal carbenes involves the transition metal-catalyzed decomposition of diazo compounds, as briefly described in the previous section. Under the influence of transition metal catalysts, diazo compounds lose a molecule of N_2, resulting in the formation of metal-coordinated carbenes, also known as carbenoids. Diazo compounds are generally unstable, which is why moderately stable α-diazoketones are often used as precursors for carbenes in research, as shown in **Figure 1.6**.

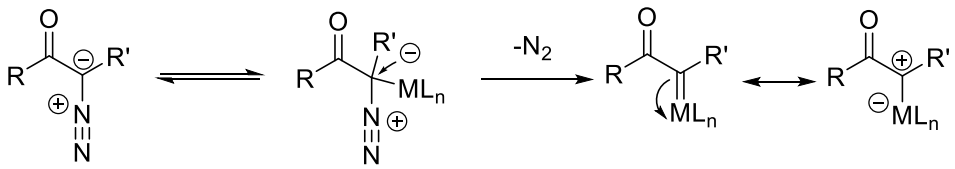

Figure 1.6 The formation mechanism of metal carbene or carbenoids from α-diazoketones.

Common transition metals employed for diazo compound decomposition include copper and rhodium complexes, although other transition metals such as zinc, iridium, iron, gold, tungsten, and tantalum complexes are also used.

The transition metal complexes essentially act as Lewis acids, [46] a overlooked consequence of converting a diazocarbonyl compound to its metal carbene is the alteration in polarity of the carbenic carbon. This change occurs alongside the conversion process. Specifically, the carbon position adjacent to the electron-withdrawing carbonyl group becomes electrophilic due to its interaction with the ligated metal, [47] and their catalytic activity depends on the unsaturation of the metal center coordination, driving them to serve as electrophilic centers for reactions with diazo compounds.

In 1952, P. Yates proposed the mechanism of formation of electrophilic metallic carbenes based on the research he carried out on the decomposition of diazoketones with copper catalysts. [48] In this mechanism, a transition metal complex **1**, possessing an available coordination site, acts as an electrophilic reagent attacking diazo compound **2**, leading to the formation of intermediate **3**. Subsequently, intermediate **3** releases nitrogen gas while simultaneously generating metal carbene **4**. Finally, electrophilic metal carbene **4** reacts with a nucleophilic substrate **5**, resulting in the formation of product **6.** Simultaneously, the regenerated catalyst **1** enters the next round of the catalytic cycle, as shown in **Figure 1.7**.

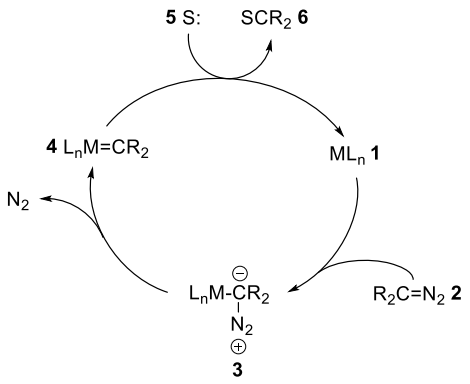

Figure 1.7 Illustrates the mechanism proposed by Yates for generating electrophilic metal carbenes.

Diazoazetates are another type of diazo compounds used, which were the first diazocarbonyl compounds synthesized, given their easy production from glycine [49] These compounds have found extensive use in transition metal-catalyzed reactions. Efforts to enhance the stability and selectivity of diazo compounds in catalytic processes led to the prominence of diazo ketoesters and diesters. [50]

In recent times, aryldiazoacetates, vinyldiazoacetates, and enoldiazoacetates have emerged, exhibiting enhanced selectivity and reactivity across a broader range of catalytic chemical transformations. [51] The dipolar character of metal carbenes derived from vinyl- and enoldiazoacetates grants them versatility in diverse chemical reactions. [52] These metal carbenes are classified as either “donor” or “acceptor”, signifying their respective electron-donating or electron-withdrawing capabilities based on the groups attached to the carbenic carbon.

The catalytic activity of transition metal complexes in diazo compound decomposition is jointly determined by the electrophilicity of the transition metal and the stability of the diazo compound. Substituents on the diazo carbon significantly impact the compound’s stability. The substituents will be categorized into three subdivisions: carbenoids containing a single acceptor group, those with two acceptor groups, and those possessing both an acceptor and a donor group. The terms “donor”

and "acceptor" refer, respectively, to electron donation or withdrawal through resonance effects. An acceptor group tends to render the carbenoid more electrophilic and reactive, while a donor group enhances its stability and chemoselectivity. [53]

Figure 1.8 shows carbenoid precursors with an acceptor substituent, which contain a single electron-withdrawing substituent. [53, 54] This type of carbenoids have found extensive application in intramolecular C-H activation reactions. In these reactions, their high reactivity can be controlled by entropic factors. [53-55] Alkyl diazoacetates are the most used acceptor-substituted R-diazocarbonyls in metallocarbenoid chemistry.

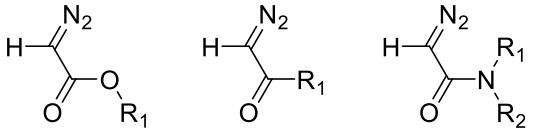

Figure 1.8 Common precursors to acceptor-substituted carbenoids.

Acceptor/acceptor-substituted carbenoids present two electron-withdrawing substituents, encompassing derivatives originating from diazoacetoacetates, diazomalonates, diazodiketones, diazoacetoacetamides, and methoxycarbonyl-diazoacetamides, as shown in **Figure 1.9**. [56] The presence of a second electron-withdrawing group significantly stabilizes the diazo compound, necessitating the use of highly active catalysts for its decomposition. [57]

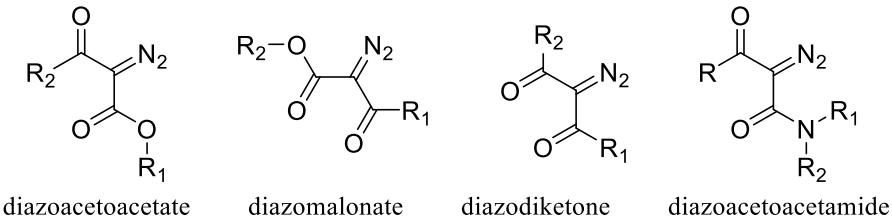

Figure 1.9 Common precursors to acceptor/acceptor-substituted -substituted carbenoids.

The donor/acceptor-substituted carbenoids, a relatively recent addition to the field of metal-carbenoid chemistry, involve the presence of a donor substituent, such as vinyl or aryl groups **(see Figure 1.10**). The donor substituent plays a crucial role in stabilizing the carbenoid through resonance. These intriguing intermediates exhibit a remarkable ability to undergo highly chemoselective intermolecular C-H activation. [58-61]

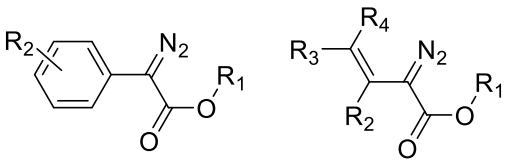

aryldiazoacetate vinyldiazoacetate

Figure 1.10 Common precursors to donor/acceptor-substituted -substituted carbenoids.

Therefore, the activity of transition metal complexes in catalyzing the decomposition of diazo compounds is determined by the electrophilicity of the transition metal and the stability of the diazo compound. Generally, compounds with an α-carbon substituent exhibit greater stability, and those with two substituents are relatively more stable than those with only one substituent. It is worth mentioning that aromatic α-diazoketones tend to be more stable than aliphatic ones, and the stability order of different diazo compounds is as follows: α-diazo amides > α-diazo esters > α-diazo ketones. [53, 62]

1.1.5 *Reactions of carbene from diazo compounds*

Metal carbenes have been employed for a diversity of chemical transformations, such as cycloaddition reaction, [39, 53, 63] insertion reaction, rearrangement reaction, ylide formation, etc, [53, 64, 65] as shown in **Figure 1.11**. These transformations have received enormous attention and are the subjects of numerous studies.

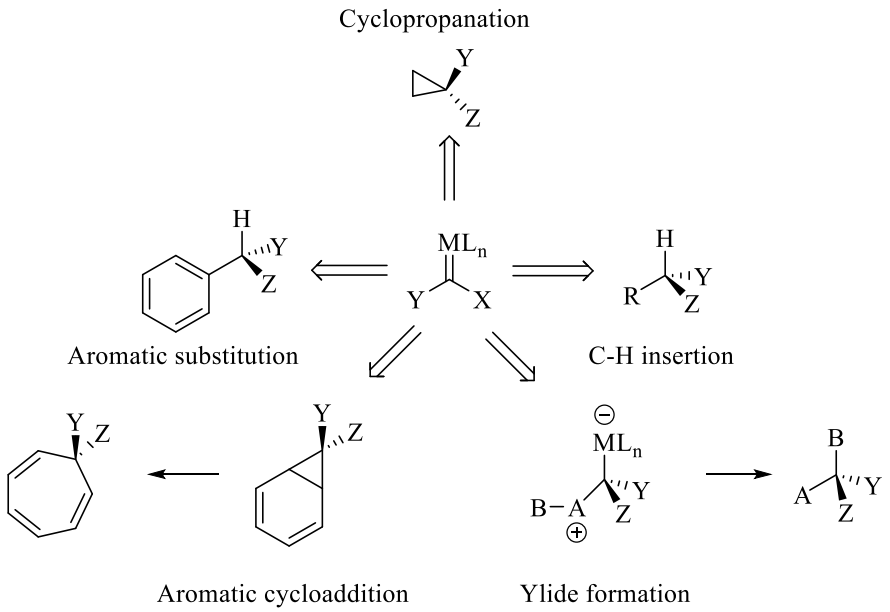

Figure 1.11 Representative traditional transformations of metal carbenes. [47]

1.1.5.1 *Catalytic C-H insertions by metal carbenes*

As catalysts and diazo compounds underwent refinements, C-H insertion reaction processes[55, 62, 66-69] (often referred to as "C-H functionalization") was earliest observed as an unusual reaction only a half century ago, and carbenes with a carbon−hydrogen bonds have attracted considerable interest because of its potential in forming new carbon-carbon bonds, however, few of these reactions have shown potential for synthetically meaningful transformations. [62] Abundant and cost-effective

feedstocks from the petrochemical and natural gas industries have made alkanes an appealing choice as potential raw materials for synthesis. However, selectively functionalizing the carbon-hydrogen bonds of alkanes to create value-added products is a challenging task. In recent years, innovative methods have emerged, relying on catalysis by transition metals or Lewis acids, reigniting interest in alkane chemistry. [66-70] C-H functionalization of alkanes via diazo compounds transformation to other useful chemicals is a good way to utilize these alkanes. [68, 71-73] Here, we mainly take into account of process of functionalizing the carbon-hydrogen bonds of saturated hydrocarbons (C_nH_{2n+2} or cyclic C_nH_{2n}) through carbene incorporation from diazo compounds.

Figure 1.12 shows that the dissociation energy of the C-H bond with heteroatoms, aryl, or olefin, is smaller than the dissociation energy of the saturated alkane. Considering the low nucleophilicity of the specific C-H bonds targeted, the effectiveness of carbene transfer relies on achieving elevated electrophilicity in the metallocarbene intermediate, which in turn arises from the catalyst precursor and the diazo reagent. To enhance reactivity toward the weak electrophile, the carbenic carbon must be depleted of electron density. [68]

The ligands on the metal complex have an impact on the stereoselectivity and regioselectivity of the reaction. [74] Furthermore, the substituents on the diazo reagent play a crucial role, as already explained above. These substituents can be electron-withdrawing, electron-donating, or neutral. While it might seem that employing two electron-withdrawing groups would enhance reactivity, this approach is not always optimal. Other side reactions can occur, and highly reactive metallocarbene may lead to the formation of undesired products. Achieving a delicate balance between the ancillary ligand, the metal center, and the diazo substituent is essential for optimizing the overall reaction outcome.

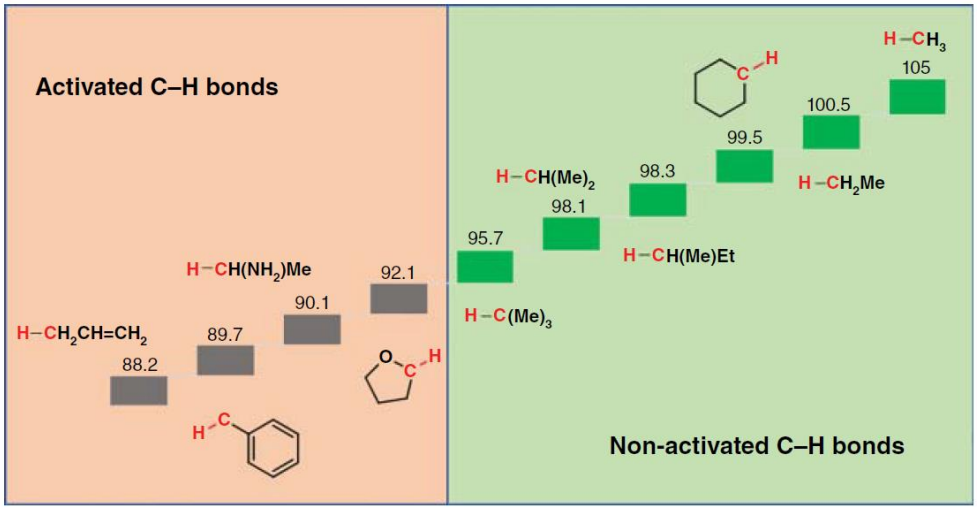

Figure 1.12 Bond dissociation energies of representative carbon-hydrogen bonds. Values in kcal mol^{-1}. Reference: Álvarez, M.; Caballero, A.; Pérez, P. J. Alkane Functionalization by Metal-Catalyzed Carbene Insertion from Diazo Reagents. In *Transition Metal-Catalyzed Carbene Transformations*, **2022**.

1.1.5.2 *Catalytic alkene cyclopropanation by metal carbene*

The catalytic cyclopropanation of alkenes using metal-carbene intermediates is a highly effective method for creating stereoselective cyclopropane derivatives, finding applications in both fundamental research and practical contexts, such as the synthesis of natural products, [75, 76] organic synthesis, [77] asymmetric catalysis[78] and medicinal chemistry. [79] Among the various methods for constructing these all-carbon cyclic molecules, metal-catalyzed asymmetric cyclopropanation of alkenes using diazo reagents stands out as a versatile and stereoselective approach. This process allows chemists to selectively form cyclopropane derivatives, contributing to the rich toolbox of synthetic chemistry.

However, the yield of such reactions is often diminished by side reactions, including cross-coupling or self-coupling of the metal carbene intermediate with the

diazo reagent or with itself. Additionally, even when using a low diazo concentration to prevent coupling, the self-coupling reaction tends to dominate over the main cyclization/insertion processes. [80, 81] As a result, these reactions continue to pose challenges, and the substrate scope is typically limited to terminal, activated, or aliphatic internal alkenes. [82-84] Therefore, it is crucial to develop efficient methods for synthesizing cyclopropane products from internal alkenes, especially those with significant steric hindrance. Some metals that have been shown to be suitable for this type of reaction are Au, Ag, Cu, Pd, Ru, Rh and Co. [85-91]

1.2 *Zeolites*

1.2.1 *Zeolite structure and classification*

The term zeolite was coined by Axel F. Cronstedt, a Swedish mineralogist, in 1756, [92] subsequent to his observation of froth forming on the surface of a mineral sample when subjected to heat. In the light of this, Cronstedt named the mineral "zeolite" by drawing on the Greek words zein, meaning "to boil," and lithos, meaning "stone." Subsequently, it was determined that this phenomenon was due to the liberation of hydration water present in the mineral's pores upon heating. The mineral discovered by Cronstedt is now recognized as a combination of stellerite and stilbite. [93, 94]

Zeolites are crystalline microporous solids composed of corner-sharing tetrahedral TO_4 units (T = Si, Al, P, etc.) that form one-dimensional to three-dimensional channels with an aperture size of typically < 2 nm. Tetrahedra are basic shapes that make up larger units called secondary building units (SBUs) in zeolites, with each SBU having up to 16 atoms. SBUs must appear in at least two different shapes to count, and common ones are shown in a **Figure 1.13(left)**. Zeolites are 3D structures made by stacking SBUs into cages or channels, with examples in another **Figure 1.13(right)**. [95] Zeolites may be classified according to the size of the channels, defined by the number of T-atoms conforming the channel window or ring, into six T-atoms (six-member ring - 6MR), small (8R), medium (10R), large (12R), and extra-large (14R or larger), which can be arranged in various shapes and either be connected or not to other tunnels. For examples, high-silica zeolite ECNU-13 has a new three-dimensional pore system consisting of 10-membered ring medium pores and one set of 8-membered ring small pores. [96]

The Structure Commission of the International Zeolite Association (IZA) provides an up-to-date inventory of all materials classified as zeolite-type. In 2001, a

comprehensive guideline for the nomenclature of structural and compositional features of ordered microporous and mesoporous materials, in accordance with the IUPAC recommendations, was issued. Currently, the IZA recognizes 225 different zeolitic structures based on how the TO_4 tetrahedra are organized.

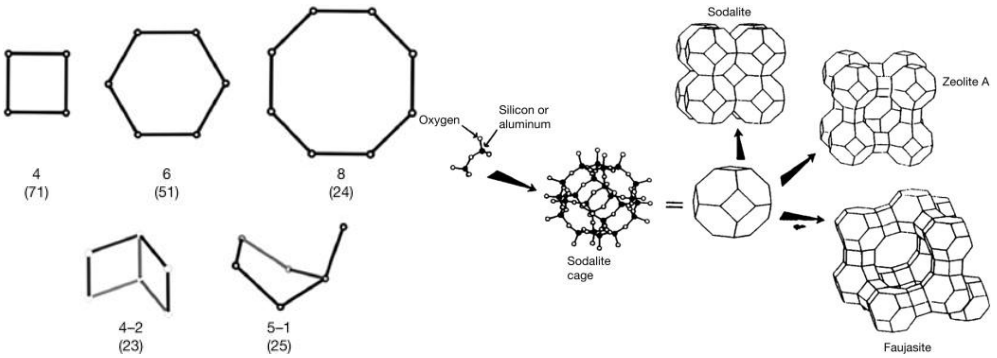

Figure 1.13 Secondary building units and their symbols (**left**, the number in parenthesis represents frequency of occurrence). Schematic of zeolite frameworks. Construction of a sodalite cage and of three different framework topologies containing this building unit **(right)**. [95] Reference: Martínez, C.; Corma, A. 5.05 - Zeolites. In *Comprehensive Inorganic Chemistry II (Second Edition)*, Reedijk, J., Poeppelmeier, K. Eds.; Elsevier, **2013;** 103-131.

Zeolites are classified based on their framework type, Si/Al ratio, and extra-framework cations. [97] From a strict perspective of structure, the connected framework of zeolite is comprised of aluminate $[AlO_4]^-$ and silicate $[SiO_4]$ tetrahedra that share corners. While pure silicate frameworks (SiO_2) are electrically neutral, the substitution of Si^{4+} with Al^{3+} in framework positions creates a negative charge. This negative charge must be balanced by cations in extra-framework positions, which are situated within the structure's cages and/or pores. These cations can be either organic or inorganic, and the original cations in the as-synthesized sample can be replaced by more suitable ones. This substitution process enhances the zeolite's cation-exchange capacity and imparts other specific properties that will be discussed later on. Additionally, the micropores may contain neutral guest molecules, such as water, which can hydrate the aforementioned cations in some cases. [95]

In particular, FAU-type zeolites are widely used in industry and are the ones that have been used in this thesis. This type of zeolites exhibits large specific surface area and strong acid sites, including Brønsted and Lewis acid sites, contributing to their catalytic properties. [98] Zeolite X and Y both have Faujasite frameworks. The FAU framework is comprised of sodalite building blocks that are interconnected through double 6 rings (6R), resulting in the formation of a supercage with a 12MR (MR: member ring) window (see **Figure 1.14**). The sole distinction between zeolite X and Y lies in their Si/Al ratio, which ranges from 1 to 1.5 for zeolite X and exceeds 1.5 for zeolite Y. In zeolite Y, sites I and I' are also found to have a high occupancy rate in the Na-form. However, the presence of cations other than Na^+ can lead to the occupation of alternative sites. For instance, K^+ and Cs^+ may also occupy site III', and Cs^+ is too large to fit into site I, therefore it is additionally found in site II'. Conversely, zeolite X contains a greater number of cations in each repeating unit of the structure, resulting in a higher occupancy rate for sites III and III' compared to zeolite Y. Faujasite zeolites also demonstrate high thermal and hydrothermal stability, making it suitable for use in harsh reaction conditions. [99]

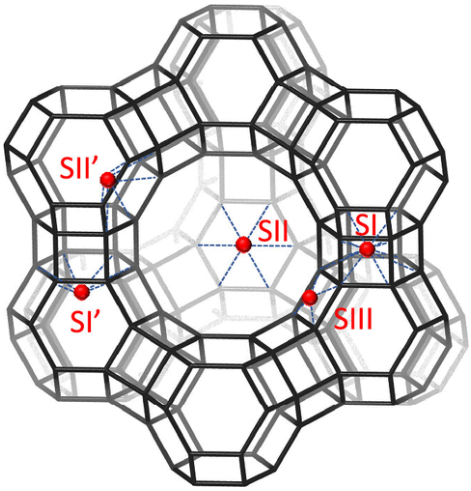

Figure 1.14 Sites in which countercations can be located in Faujasite frameworks. [77]

1.2.2 *Properties of zeolites*

Zeolites are characterized by their unique and versatile properties, which make them applicable in a wide range of industries, from agriculture to environmental decontamination.

1) One of the primary properties of zeolites is their crystalline structure, which consists of a system of interconnected chambers and channels, allowing for high adsorption capacity due to their porosity. This structure is composed of a hydrated aluminosilicate framework, containing channels and cages occupied by exchangeable active metal ions and water molecules, which contribute to their remarkable cation exchange capacity. [100]

2) The ability of zeolites to undergo ion exchange is pivotal, as it enables the removal of toxic cations from solutions, making them invaluable in water purification and environmental remediation efforts. Furthermore, their molecular sieving properties, which allow for the selective adsorption of molecules, are essential in applications such as gas separation and catalysis. [101]

3) Another significant property of zeolites is their role as catalysts, facilitated by the presence of acid sites within their structure. These acid sites are created through the isomorphous substitution of Si, Al, and P atoms in the zeolite framework, which can generate Bronsted and Lewis acid sites of varying strengths, crucial for numerous catalytic reactions. Zeolites also exhibit high thermal stability, along with hydrophilic and hydrophobic properties, depending on their structure, which is beneficial in various catalytic and adsorption processes.

In summary, the main properties of zeolites include their unique crystalline structure, high adsorption capacity, cation exchange capability, molecular sieving properties, thermal stability, hydrophilicity and hydrophobicity, catalytic activity

through acid sites, and reversible hydration-dehydration ability, making them highly valuable across multiple domains.

1.2.3 *Synthesis of zeolites*

Zeolite synthesis can be achieved using various methods and materials. The hydrothermal route is the prevailing approach utilized in the synthesis of zeolite. [102] Byrappa et al. [103] adopt the term "hydrothermal" to denote any chemical process that takes place in a closed system, employing aqueous solvents, at temperatures and pressures higher than ambient conditions. This process facilitates the dissolution and recrystallization of materials that are relatively insoluble. The reaction mentioned above is occasionally referred to as solvothermal synthesis in cases when the solvent used is nonaqueous, as opposed to hydrothermal synthesis, where water is always the solvent. [104] These two methods of synthesis pertain to comparable chemical processes. However, hydrothermal synthesis of zeolite has some drawbacks, including being energy-intensive due to the high temperatures and pressures required for the process, and may lead to non-uniform particle sizes and morphologies, which can affect the performance of the zeolites. [105]

Over the past ten years, various novel synthetic methods have been created to produce zeolites possessing distinct structures and properties. These methods included pre-designed organic structure-directing agents (SDAs), [106-110] heteroatom substitution, topotactic transformations, and charge density mismatch. [111]

Especially, structure directing agents have helped design new zeolites with unique channels and shapes. Structure directing agents (SDAs) play a crucial role in the synthesis of crystalline materials. Various SDAs, such as organic compounds and ammonium salts, have been utilized to control the morphology and properties of these materials. The choice of SDAs influences the surface area, pore volume, shape, and electrochemical performance of the resulting materials, impacting their energy storage and capacitive abilities. [112-115] Atomistic simulation techniques have been employed to

study the effects of different SDAs, including isomorphic heteroatom substitutions, anions, and organic compounds, on the synthesis of zeolites, highlighting the interplay and individual contributions of these agents to the process. [116-118]

The heteroatom substitution, [119] it refers to replacing some atoms in the zeolite with other types of atoms (like aluminum, silicon, or others). Zeolites are made of TO_4 units, with T being elements like silicon, aluminum, or phosphorus. Other elements can replace T to give zeolites new properties like catalysis or luminescence. Adding different elements (heteroatoms) helps create new types of zeolites with unique features like large pores or low density, which are different from traditional zeolites.

The topotactic transformation involves the assembly, disassembly, organization, and reassembly of precursor materials to form the desired zeolite structure. [120-124] Therefore, it involves solid-state structural transformations through various treatments. This method can be used to prepare zeolite structures with specific layers, cages, and pores.

Overall, new zeolite structures are being predicted using advanced computer methods, which help choose the right building blocks and conditions for making them. Understanding how zeolites form is key, and the creativity of scientists will continue to push zeolite research forward.

1.2.4 *Application of zeolites*

Advances in synthetic methodologies and characterization techniques have led to the fabrication of new zeolitic materials with emerging applications in diverse areas. Zeolites have a wide range of applications such as catalysis, adsorption and ion exchange, even on an industrial scale. In addition, they can be used as medicinal products for various therapeutic treatments, such as active agents, carriers, and oral formulations. [125]

Zeolites are extremely useful as catalysts for several important reactions involving organic molecules. [126-128] Indeed, they are the most used catalyzed around worldwide for the cracking petroleum. They have been studied for their framework structures, catalytically active sites, and intermolecular interactions, providing insights into their catalytic behavior. Attempts are continually being made to design new types of zeolites suitable for specific applications. As is the case of the synthesis of zeolite nanosheets, that is zeolites with two-dimensional structures, which have emerged as a hot topic in the past decades, as it provides more accessible active sites contributing to shortened diffusion pathways and allowing bulky molecules to undergo catalytic reactions. [127]

Zeolite-based catalysts have shown remarkable catalytic performance in biomass valorization, such as the conversion of biomass into high-value biochemicals and biofuels. [129, 130] They have also played a significant role in C_1 chemistry, which involves the catalytic transformation of C_1 molecules such as methane, carbon dioxide, carbon monoxide or methanol. [131] The conversion of CO_2 into hydrocarbons, especially gasoline, olefins and aromatic products, is an example of this chemistry. Reaction for which microporous materials have shown excellent results, which is a promising way to deal with climate change issues and energy crises while meeting environmental requirements (see **Figure 1.15**). [132]

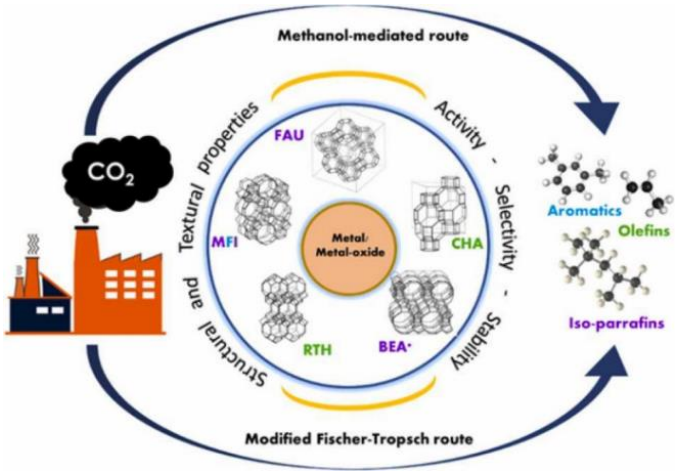

Figure 1.15 CO_2 conversion to hydrocarbon over zeolite-based catalysts. Reference: Azhari, N. J.; Nurdini, N.; Mardiana, S.; Ilmi, T.; Fajar, A. T. N.; Makertihartha, I. G. B. N.; Subagjo; Kadja, G. T. M. Zeolite-based catalyst for direct conversion of CO_2 to C_{2+} hydrocarbon: A review. *Journal of CO_2 Utilization* **2022**, *59*, 101969.

Given the high porosity of the zeolites, they have also emerged as ideal supports for metallic species, demonstrating excellent catalytic activity, stability, and shape-selectivity. [128, 133, 134] Recent, progress in using these zeolite-supported metal particles for different types of reactions, like making and breaking dihydrogen, changing chemicals, and cleaning harmful gases, has been shown. However, there are still some challenges. One of them is to ensure that the metal particles are evenly distributed and remain the proper size during the reaction. Another challenge is that these catalysts can sometimes decompose or lose activity when they are reused under harsh reaction conditions.

In addition, zeolites are also used as adsorbents, [93, 135, 136] and ion exchangers in various industries such as oil refining, fuels, petrochemical, coal chemical, and daily chemical industries. [97] Their potential in electronic devices has also been explored, as they have been demonstrated to be ultrawide-direct-band-gap semiconductors. This opens up new possibilities for zeolites in applications such as sensing, optics, and electronics. [137]

1.2.5 *Carbenes in zeolites*

Carbenes play a crucial role in both homogeneous and heterogeneous catalysis. Understanding their function is essential for regulating and controlling reaction pathways. However, the high reactivity and limited stability of carbenes pose challenges for in-depth experimental investigations into their chemistry. Over the years, numerous scientists have strived to isolate carbene molecules or synthesize stable variants. Bertrand [138] and Arduengo, [9] for instance, achieved this by intrinsically stabilizing carbene structures using the substituent groups, phosphonyl and amino groups, respectively. Other scientists have explored a supramolecular approach to encapsulate carbenes within a host. [139, 140] By introducing carbene precursors (such as diazirine and diazo) into hosts like cyclodextrins (see **Figure 1.16 (a)**), [133] hemicarcerands (see **Figure 1.16 (b)**), [141] and zeolites (see in **Figure 1.16 (c)**), [142] they were able to generate various carbenes through photolysis. However, cyclodextrins and hemicarcerands have certain structural limitations. Cyclodextrins provide insufficient protection, and hemicarcerands are overly restrictive when it comes to carbene behavior. [139]

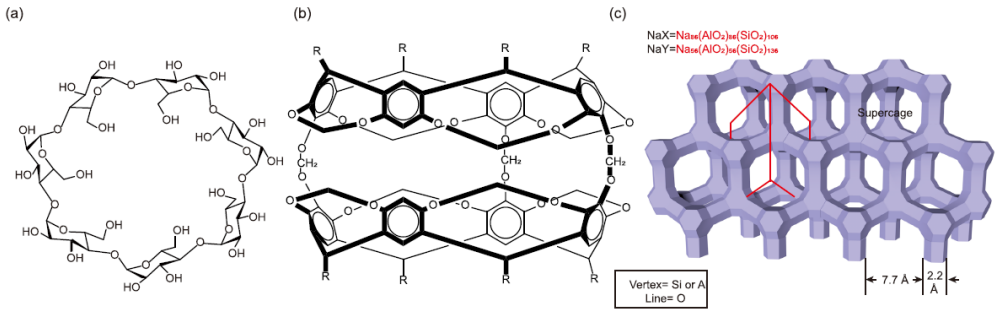

Figure 1.16 (a) The basketball-hoop-shaped heptamer β-cyclodextrin (axial view). (b) General hemicarcerand (HC) structure (e.g., R =$CH_2CH_2(C_6H_5)$). (c) The structure of faujasite-type (FAU) zeolites X and Y with the diamond-like unit cell is outlined in red. [143]

Zeolites, when compared to cyclodextrins and hemicarcerands, are in the middle and offer certain advantages. However, they also come with specific challenges. The primary concern is achieving optimal confinement for stabilizing the desired carbene molecules. This challenge arises due to the diverse topologies of zeolite frameworks, each possessing unique cavity and pore sizes. When it comes to aluminosilicate zeolites, the choice of counterions plays a crucial role in balancing the framework charge. Sodium (Na^+), lithium (Li^+), cesium (Cs^+), calcium (Ca^{2+}), and barium (Ba^{2+}) are examples of larger cations. They help adjust the available space within the zeolite pores and contribute to reducing the acidity of the zeolite framework. [144, 145]

In the mid-1990s, Brinker[142] and Kupfer[146] introduced the first examples of zeolite-carbene complexes. They employed diazirines, which break down into nitrogen and corresponding carbenes through photolysis or thermolysis. In their initial study, they utilized adamantine-2-spiro-3-diazirine as a carbene precursor and hosted it within several alkali/alkaline earth cation-exchanged X-type/Y-type Faujasite zeolites.

In 2004 and 2006, Moya-Barrios and Cozens continued research in this field. They presented the first spectroscopic evidence for the formation of halo-phenylcarbenes (where halo represents Cl and Br) within alkaline cation-exchanged Y zeolites[144, 147] (as depicted in **Figure 1.17**). These carbenes were generated through photolysis of host-guest complexes within a vacuum cell, and their properties were analyzed using nanosecond diffuse reflectance spectroscopy. The observed absorption bands closely resembled those of the corresponding halophenyl-carbenes. Notably, the Lewis acidity/basicity of the cations played a crucial role in stabilizing these carbenes. They delved deeper into the decay pathway of carbenes in cation-exchanged Y zeolites (with cations like Li, Na, K, Rb, and Cs) through additional studies using diffuse reflectance spectroscopy during photolysis. Based on their detailed investigations, they proposed two distinct mechanisms for capturing carbenes within the zeolite matrix. These mechanisms depend on the philicity of the carbene molecule and the nature of charge-balancing cations within the zeolite pores-whether

nucleophilic [Si−O−Al]− species (from the zeolite framework) or electrophilic cations can effectively capture and react with the carbenes, as illustrated in **Figure 1.18**.

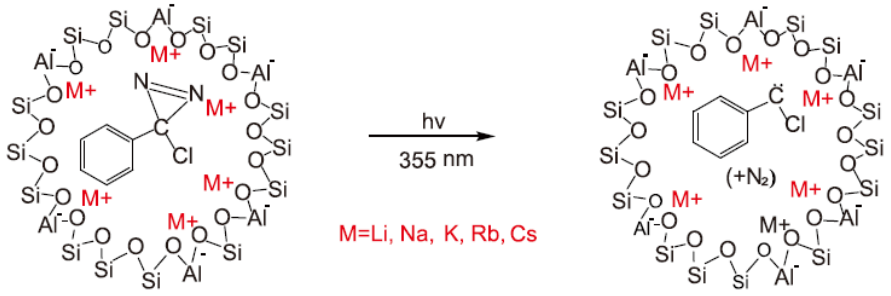

Figure 1.17 Chloro(phenyl)carbene formation within the cavities of cation-exchanged Y zeolites upon the photolysis of 3 chromo-3-phenyldiazirines.

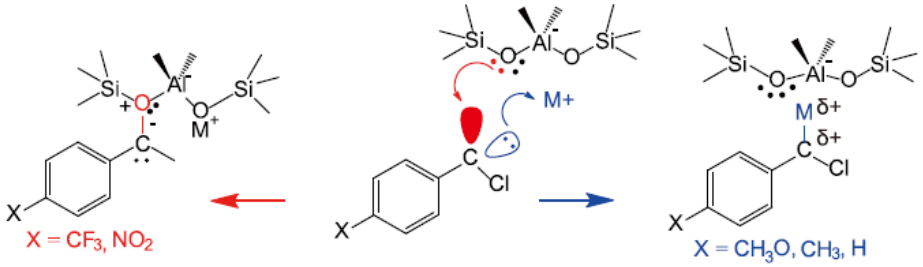

Figure 1.18 Reactions occur upon generating chloro(aryl)carbenes: depending on the electron donating/withdrawing properties of the aryl substituents and the zeolite charge balancing cations, whether the nucleophilic [Si−O−Al]− (framework of zeolite) or electrophilic cations, M^+ can form an adduct with chloro(aryl)carbenes.

In 2005, Tomioka and colleagues reported their efforts to generate and characterize a triplet carbene within the framework of VPI-5. [148] VPI-5 is an aluminophosphate material with a VFI topology, featuring 18-membered rings and a one-dimensional structure. However, the diffuse reflectance absorption spectra revealed that the neutral framework of VPI-5, which lacks Brønsted acid sites, provided better stabilization for bis(2,4,6-trichlorophenyl)diazomethane (the precursor to the carbene). Subsequent analysis of the guest-loaded VPI-5 sample,

following photolysis at 77 K using emission spectroscopy, revealed the presence of bis(2,4,6-trichlorophenyl) methyl radicals.

While no recent studies specifically employing the zeolite-based supramolecular approach to stabilize fleeting carbenes have been conducted, intrinsically stable *N*-heterocyclic carbenes (NHC) find widespread use as surface ligands in heterogeneous catalysis. [149, 150] These NHCs are anchored to supported surfaces and particles, which can range from elemental metal allotrope species to bulk crystals. For example, Pd for application in the Suzuki cross-coupling reaction, [151] Au and Rh(NHC)NN-pincer complexes on MCM-41 silica support, [152, 153] Au cluster [154, 155] and gold nanoparticles, [156, 157] supported heterogeneous Ru/K-Al_2O_3 catalysts, [158] or zeolite. [159]

1.3 *Silver catalysts*

1.3.1 *Properties of silver*

Silver, the chemical element with the symbol Ag and atomic number 47, is known for its soft, white, lustrous characteristics as a transition metal. It displays remarkable electrical conductivity, thermal conductivity and reflectivity, surpassing other metals in these properties. Silver is a precious metal that it is utilized in the production of many bullion coins. Apart from its traditional uses in currency and as an investment vehicle (coins and bullion), silver finds application in various modern industries. These include solar panels, [160-164] water purification systems, [165-168] jewelry, decorative items, tableware and utensils, electrical components and conductors, [169] specialized mirrors, coatings for windows, catalytic agents in chemical processes, [170-172] colorants in stained glass production, and additives in certain confectionery items. Compounds of silver play a role in photographic and X-ray film development. [173] Furthermore, diluted solutions of silver nitrate and other compounds are employed as disinfectants and microbicides, integrated into bandages, wound dressings, catheters, and medical tools.

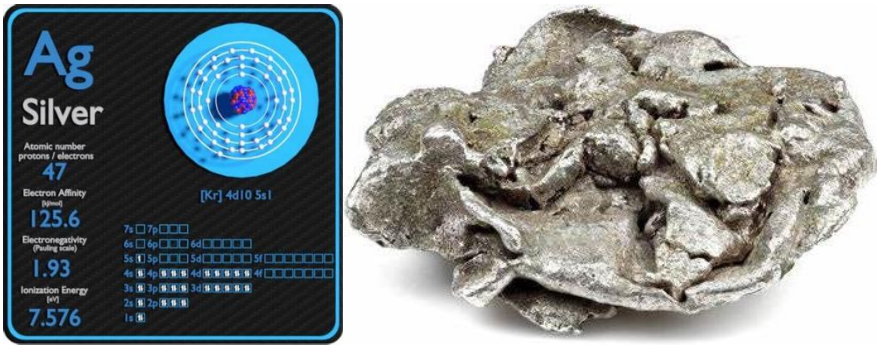

Figure 1.19 Schematic representation of the electron configuration of silver and appearance of silver metal.

Silver shares similar physical and chemical properties with copper and gold, like having a unique electron arrangement (silver, $[Kr]4d^{10}5s^{1}$) that contributes to its special properties. It is a soft metal that is less malleable than gold, with a crystal structure that makes it less hard and more ductile.

For the chemical properties, silver is considered a relatively unreactive metal due to the inefficiency of its filled 4d shell in shielding the electrostatic forces from the nucleus to the outermost 5s electron. This positioning places silver towards the lower end of the electrochemical series with an $E^{0}(Ag^{+}/Ag)$ value of +0.799 V. In the group 11 elements, silver exhibits the lowest first ionization energy, indicating the instability of the 5s orbital.

1.3.2 *Silver nanoparticle catalysts*

Metal species with different size (single atoms, nanoclusters, and nanoparticles) show different catalytic behavior for various heterogeneous catalytic reactions. It has been shown in the literature that many factors, including the particle size, shape, chemical composition, metal-support interaction, and metal-reactant/solvent interaction, can have significant influences on the catalytic properties of metal catalysts. Previously, with the resolution of the available characterization techniques, it was not possible to visualize metal particles below 1 nm. However, it could already be inferred that the electronic properties of metal particles should change significantly when they going below 1 nm (see **Figure 1.20**). [174]

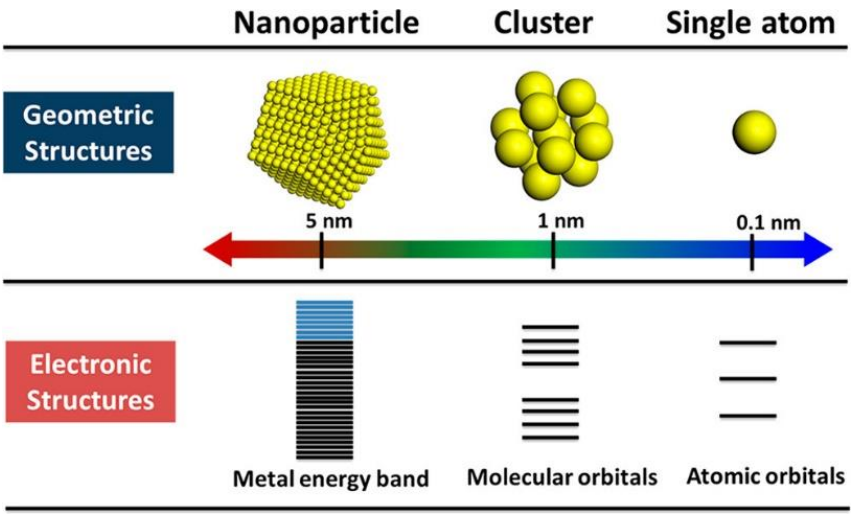

Figure 1.20 Geometric and electronic structures of single atom, clusters, and nanoparticles. [174]

Metallic nanoparticles have attracted the attention from researchers globally due to their intriguing optical, electrical, magnetic and catalytic characteristics. These nanoparticles offer a surface modification chemistry, enabling the attachment of diverse molecules like ligands, targeting agents, biomolecules, drugs and antibodies. Owing to their varied properties and facile modification chemistry, these nanoparticles find extensive utilization across various fields such as biomedical, solar, catalysis, among others. [175]

Silver nanoparticles (Ag NPs) have found significant applications in biomedical [176, 177] and pharmaceutical research. [178] They are widely used in antimicrobial therapy, [179] drug delivery, [180] diagnosis, therapeutics, and tissue regeneration. [181] Ag NPs are versatile materials that can be used in various applications, including personalized healthcare, food industry, and everyday life products. [182] On the other way, silver nanoparticles have been extensively studied for their catalytic properties. Compared to other catalysts, such as manganese oxides, cobalt oxides, or rare-earth composite oxides, the supported nanometer metallic silver catalyst has higher catalytic activity and lower cost. [183] Additionally, silver nanoparticles have been shown to exhibit high

catalytic activity for the oxidation or reduction of hydrocarbons, in contrast, gold traditionally being considered catalytically inactive. [184] The ability to tailor the size, shape, and surface of silver nanoparticles can lead to improved or new catalytic properties. [185] Silver metallic nanoparticles are used as heterogeneous photocatalysts for light-driven catalytic processes. [186]

Silver nanoparticles can be synthesized using various methods such as physical, chemical, and biological synthesis methods. Hundreds of research articles reporting different synthesis methods for Ag-NP are published every year. [187]

1.3.3 *Silver cluster catalysts*

Subnanometer metal clusters are metal particles with a size smaller than 1 nanometer. These clusters have unique physical and chemical properties, such as quantum size effects, strong photoluminescence, and high catalytic activity. [188] In catalysis, subnanometer metal clusters have shown outstanding capabilities as electro/photo catalysts due to their ultra-small size, abundant active sites, large specific surface area, and unique electronic structure. [189-191] These clusters offer atom-by-atom tunability of their performance and allow for an atom-efficient use of metal loading, making them economically attractive for catalytic processes. [192] The Ag subnanometer metal clusters (SNMCs) utilized various fields such as photovoltaic cells, biological sensors, biomedical devices, and gas sensors. DNA-stabilized silver nanoclusters (AgN-DNAs) are promising biosensors and fluorophores due to their small sizes and bright fluorescence. [193] AgNCs also exhibit antibacterial performance and excellent biocompatibility with various tissue cells, making them adaptable for applications such as biosensing, bioimaging, and antibacterial agents. [194] Ag nanoclusters were used to improve the sensitivity and response rate of SnO_2-based gas sensors to CO and H_2, while depressing the sensor response to ozone, [195] and the application of silver clusters in reducing pathogenic and conditionally pathogenic microorganisms in waste sludge has been shown. [196]

In the catalysis field, silver nanoclusters have been used as a support for chiral ligands in heterogeneous phase asymmetric catalysis, showing high catalytic efficiency and the ability to be easily recovered and reused without loss of efficiency. [197] Nanocluster catalysts, including silver nanoclusters, have non-uniform active sites due to surface heterogeneity or structural diversity, which require a comprehensive understanding of all surface sites for rational improvement. [198, 199] Atomically precise nanoclusters provide a platform for investigating the active sites and reaction mechanisms of electrocatalysis at the atomic or molecular scale. [200] However, the scarcity of examples involving Ag zeolites can be attributed to the propensity of silver to aggregate within the zeolite structure, [145] because the utilization of different starting reagents and heating conditions can result in polymorphism, showcasing distinct metal core arrangements in the resulting products. Additionally, the nature of the anion in the starting salt influences the type of metal clusters observed. [201, 202]

Chapter 2. Objectives

The general aim of this *Thesis* is focused on carbene-mediated reaction using heterogeneous catalysts, including Ag-supported zeolite and MOF materials, for C-H insertion reaction and cyclopropanation reaction of aromatic or aliphatic hydrocarbons. To achieve these objectives this *Thesis* was developed as follows:

1. Preparation of solid zeolite catalysts and MOF.
2. Study of the synthesis of the Ag clusters and single atoms within zeolites.
3. Search of the best reaction conditions for carbenes derived from diazo compounds.
4. Characterization of the zeolite and MOF catalysts used in the reactions.
5. Study of the mechanism of formation of the carbenoids in the zeolites surface and of the reaction itself, comparing the catalysts with more common catalytic systems.

This *Thesis* constitutes a segment of the prior and ongoing endeavors of our research group. Undoubtedly, we have previously synthesized the silver clusters and single atom silver, thereby enhancing the reactivity of the Buchner reactions. A conventional approach to stabilize these entities involves their support onto various solid matrices possessing appropriate functionalities. Conversely, employing these diminutive entities in the absence of ligands, represents one of the most effective strategies to maximize the availability of metal atoms for the reaction substrate. The utilization of these highly activated species holds significant importance in the domain of catalysis for organic reactions, such as C-H insertion or C-C formation.

Chapter 3. Methods and characterization techniques

3.1 *Materials*

Unless otherwise specified, all chemicals used were of reagent grade quality. They were purchased from commercial sources and used without any further purification. In the case of synthesized precursors or reagents, their experimental synthesis and characterization will be specified.

3.2 *Reactions*

Glassware was washed with acetone and then dried in an oven at 60 ºC before use. Reactions were typically performed in 2.0 ml vials equipped with a magnetic stirrer and closed with a steel cap having a rubber septum part to sample out, and placed in steel heaters.

3.3 *Characterization techniques*

3.3.1 *Gas chromatography (GC)*

Gas chromatography (GC) is an analytical technique used to separate and analyze components in a mixture based on their polarity. GC is widely used in various fields such as quality control, forensic science, petrochemistry, food chemistry, and environmental analytics. [203, 204] In the field of gas chromatography, a capillary column is utilized for the examination of gaseous samples, which are propelled through the column by a carrier gas such as nitrogen or helium. Prior to entering the column, the sample undergoes a process in which all species are converted into the gaseous state through the injector. For the quantification of compounds in this *thesis*, the GC Bruker

430-GC equipped with an HP-5MS column (30 m × 0.25 mm × 0.25 μm) was employed, where the stationary phase consists of 5% phenylmethylsilicon. The internal standard method was implemented, and the response factor was determined by means of calibration curves.

3.3.2 *Gas chromatography-mass spectrometry (GC-MS)*

Gas Chromatography-Mass Spectrometry (GC-MS) involves the separation of components in a sample using gas chromatography based on their polarity, followed by detection and identification of these components using mass spectrometry. It is particularly useful for analyzing volatile organic compounds and is often coupled with other techniques like sample preparation, derivatization, and multivariate statistical analysis for comprehensive data analysis. [205] This technique of chromatography coupled with mass spectrometry can identify compounds in a mixture by fragmenting them into smaller ions or radicals. The mass spectrometer is responsible for the fragmentation and mass analysis of the molecule fragments, and then it is possible to determine the species present in our solution by comparing them with results libraries. In this *thesis*, a GC-MS Agilent 6890N was used with a column HP-5MS (30 m × 0.25 mm × 0.25 μm) with the stationary phase made up of 5% phenylmethylsilicon and the detector 5973N.

3.3.3 *Nuclear magnetic resonance (NMR)*

Nuclear Magnetic Resonance (NMR) is a spectroscopy technique that uses high magnetic fields and radiofrequency pulses to investigate specific isotope populations in a target sample. It has applications in chemistry, physics, and medicine, and is known for its versatility and power. [206] NMR can be used to study the composition of complex solutions and identify the molecular structure of purified molecules. [207] The most common nuclei analyzed by NMR are ^{1}H, ^{13}C, and ^{15}N. In the present study, room temperature ^{1}H, ^{13}C, and DEPT NMR spectra were acquired on a 400 MHz

spectrometer (Bruker Ascend 400), utilizing the appropriate solvent, and incorporating TMS as an internal standard. The organic products obtained were extensively characterized using GC-MS, ^{1}H-NMR, ^{13}C-NMR, DEPT, and IR techniques. The characterization provided in the literature was employed for comparison purposes.

3.3.4 *In-situ magic angle spinning-solid state nuclear magnetic resonance spectroscopy (MAS ss-NMR)*

Magic angle spinning-solid state nuclear magnetic resonance (MAS-ssNMR) spectroscopy utilizes the principles of nuclear magnetic resonance (NMR) to probe the interactions between nuclear spins in solid systems. It involves the mechanical rotation of the sample at high speeds (100 kHz and above) to obtain high-resolution and sensitive NMR spectra of solids. [208] In addition, *in-situ* high-temperature, high-pressure MAS-ssNMR methods have been developed to observe chemical interactions under different conditions, making it a versatile tool for studying diverse fields such as carbon sequestration, catalysis, material science, geochemistry, and biology. [209] The combination of high magnetic field strength and fast MAS rates has also improved the spectral resolution and sensitivity of MAS-ssNMR, particularly for the analysis of surface species relevant to catalysis. [210]

Here, in my *thesis*, silver carbene on zeolite detected by MAS ss-NMR, a glass insert containing 200 mg of zeolite was subjected to degassing at 200 °C under vacuum for a duration of 18 hours. Subsequently, ethyl diazoacetate (EDA) was introduced into the system using a nitrogen stream while still under vacuum, and the glass insert was sealed and immersed in liquid nitrogen. Room temperature ^{13}C solid-state NMR spectra were acquired using a Bruker AVIII HD 400 WB spectrometer. The glass insert was placed in 7 mm rotors and spun at a rate of 5 kHz using a Bruker BL7 probe. ^{13}C CP/MAS NMR spectra were recorded with proton decoupling,

employing a ^{1}H 90° pulse length of 5 μs and a recycle delay of 3 s. In this particular experiment, solid ^{13}C NMR analysis was conducted using a Varian instrument operating at 400 MHz.

3.3.5 *Inductively coupled plasma atomic emission spectroscopy (ICP-AES)*

Inductively coupled plasma atomic emission spectroscopy (ICP-AES) is a technique used to determine the energy states of atoms or molecules by measuring the amount of light absorbed or emitted during their transition states. It involves transforming a liquid sample into an aerosol form, which is then introduced into a plasma zone where it is vaporized, atomized, and excited at high temperatures. The excited atoms and ions release radiation at specific wavelengths, which is detected and converted into electronic signals for analysis. ICP-AES is commonly used for the estimation of metals in various samples and is particularly effective for identifying first-row transition metals. [211] In this *thesis*, the metal content of the catalysts solids was determined by instrument Varian 715-ES after disaggregation of the solid in hydrofluoric acid or aqua regia and later dilution.

3.3.6 *Diffuse-reflectance ultraviolet visible spectroscopy (DR UV-Vis)*

Diffuse-reflectance (DR) UV-Vis spectroscopy is a powerful analytical method for studying heterogeneous catalysts. It allows for the investigation of catalysts in both the liquid-phase and solid-state, as well as their interfaces, at elevated temperatures and pressures. [212] It is particularly useful for studying the working principles of various types of catalysts, including heterogeneous, homogeneous, electrocatalysts, and photocatalysts. [213] DR-UV-Vis spectroscopy is often combined with other analytical

methods, such as X-ray absorption spectroscopy, vibrational spectroscopy, and magnetic resonance methods, to provide complementary information. In this *thesis*, reflectance spectra in the region comprised between 190 and 1100 nm were recorded at room temperature on a spectrophotometer equipped with an integrating sphere.

3.3.7 *Emission spectroscopy (fluorescence UV-vis)*

Fluorescent of metal nanoparticles and nanoclusters have shown great potential as catalysts in various applications. They have size-dependent properties and can be used as fluorophores for imaging and sensing purposes. [214] Furthermore, metal nanoclusters have been found to exhibit unique excited-state properties and can participate in photocatalytic reduction processes, making them potential candidates for biological probes, sensors, and catalysts in energy conversion devices. [215] In my *thesis*, the fluorescence spectra were utilized to ascertain the size of silver clusters, and results were obtained using an LP S-220B instrument (Photon Technology International) coupled with a 75 W Xe lamp.

3.3.8 *Infrared spectroscopy (IR)*

Infrared spectroscopy is a technique used to identify functional groups and determine the structure of unknown compounds. [216] The technique involves the measurement of the absorption of infrared radiation by molecules in a sample. The absorbed radiation corresponds to the frequencies of bond vibrations in the molecule, providing information about its composition. [217] Infrared spectroscopy utilizes the infrared region of the electromagnetic spectrum, with organic chemists primarily interested in the middle IR region ranging from 4,000 to 400 cm^{-1}. [218] In this *thesis* attenuated total reflection infrared spectroscopy be used in a JASCO FT/IR-4700, was employed to record the IR spectra from 400 to 4000 cm^{-1} of the different solid catalysts. Absorption spectra were recorded on a spectrophotometer under diffuse reflectance mode.

3.3.9 *Diffuse reflection infrared Fourier transformed spectroscopy of adsorbed CO (DRIFTS-CO)*

Diffuse reflectance infrared Fourier transform spectroscopy (DRIFTS) is used to study the adsorption of CO with metal surfaces. The technique provides information on both surface and gas phase species, allowing for the correlation between the oxidation state of metal catalysts and their catalytic activity to be investigated. [219] In addition, infrared spectroscopy has been shown to be a valuable *in-situ* laboratory probe for the growth of metal nanoparticles (NPs) on a substrate. [220] In my *thesis*, DRIFTS using CO as a probe molecule was used to evaluate electronic properties of Ag-HY. The experiments have been carried out in a homemade IR cell able to work in the high and low (77 K) temperature range. Prior to CO adsorption experiments, the sample was activated at 473 K under vacuum (10-6 mbar) for 2 h. CO adsorption experiments were performed at 77 K in the 0.2-20 mbar range. Spectra were recorded once complete coverage of CO at the specified CO partial pressure was achieved.

3.3.10 *Raman spectroscopy*

Raman spectroscopy is an optical spectroscopic tool used for studying catalyst structure and surface chemistry in heterogeneous catalysis. It has gained importance in catalysis research due to advancements in instrumentations and combination with other techniques, allowing for *in-situ* and operando studies with high temporal and spatial resolutions. [221] It has also been applied in the field of electrochemical CO_2 reduction reaction (CO_2RR), allowing for the tracking of structure evolution of catalyst surfaces and identification of reaction intermediates during CO_2RR over selected Cu catalysts. [222] In the context of this study, the presence of silver carbene was detected using in-situ Raman spectra. The Raman spectra experiments were conducted at room temperature with a 514 nm laser excitation on a Renishaw Raman

Spectrometer ("in via") equipped with a CCD detector. The laser power applied to the sample was 25 mW, and a total of 20 acquisitions were performed for each spectrum. The experiments were carried out using a commercially available Linkam FTIR600 catalytic cell. For the *in-situ* study, the sample was activated in a flow of N_2 at 200 ºC for 1.5 hours. After activation, the sample was cooled down, and ethyl diazoacetate (EDA) was adsorbed by flushing N_2 at room temperature through a saturator containing EDA. Spectra were acquired over time until a total of 1 hour.

3.3.11 *X-ray photoelectron spectroscopy (XPS)*

X-ray photoelectron spectroscopy (XPS) is a characterization tool used to identify and quantify surface functionalities in materials. [223] XPS has various applications in catalysts, including exploring the chemical nature of important elements in energy storage and conversion materials, detecting the presence of doping and defects in transition metal oxides, and identifying mechanistic pathways of pollutant degradation by photocatalysts. [224] In this study, the XPS measurements were conducted on zeolite samples that were adhered onto a molybdenum plate using scotch tape film, without the need for sieving, followed by air drying. The measurements were performed using a SPECS spectrometer equipped with a Phoibos 150 MCD-9 analyzer, employing a non-monochromatic Mg KR (1253.6 eV) X-ray source operating at 50 W. To establish an internal reference for the peak positions in the XPS spectra, the C1s peak was set at 284.5 eV. The X-ray diffraction spectra of the various catalysts were recorded using a CubiX PRO (PAN Analytical) spectrometer, employing a Cu K(α) radiation source with a wavelength of 1.5406 Å.

3.3.12 *X-ray absorption spectroscopy (XAS)*

X-ray absorption spectroscopy (XAS) is a technique used to characterize catalysts by analyzing the interaction of X-rays with different chemical elements. [225] It has become an important analytical method for studying catalytic reactions, particularly in the field of transient X-ray absorption spectroscopy (TR-XAS) which focuses on structural changes in molecular systems under photoactivation. [226] XAS can also be used to investigate the structure of hybrid photocatalysts, such as metal-ligand complexes deposited on surfaces, for applications in solar CO_2 reduction. [227] In my *thesis*, experiments on X-ray absorption spectroscopy were conducted at the ALBA synchrotron (Cerdanyolla del Vallès, Spain) at the Ag K-edge. The white beam was monochromatized using a Si (311) double crystal that was cooled by liquid nitrogen. Harmonic rejection was achieved by employing Rh-coated silicon mirrors. The spectra were collected in transmission mode, and reference patterns (e.g. silver and silver oxide) were simultaneously measured between I1 and I2, which were then used for spectra alignment.

3.3.13 *X-ray diffraction (XRD)*

Single-crystal X-ray diffraction is a method used to determine the absolute configuration of molecules by analyzing the scattering of X-rays from individual atoms in a crystal structure. [228] X-ray diffraction is also used for the characterization of crystalline substances, including polycrystalline aggregates and minerals such as MOFs, by analyzing their diffraction patterns. [229]

In addition to single-crystal X-ray diffraction, another technique known as Powder X-Ray Diffraction (PXRD) is used for various purposes such as phase identification, quantitative analysis, determination of crystal structure imperfections, and extraction of three-dimensional microstructural properties. Specifically, in the study of zeolite and MOF catalysts, PXRD plays a crucial role in the identification

and characterization of extra-framework species, such as cations and adsorbed gas molecules. By providing valuable information on the crystallinity, structure, and reactivity of zeolite and MOF crystals, PXRD enables researchers to establish structure-activity relationships, contributing to a deeper understanding of these catalysts.

To perform Single-Crystal X-Ray Diffraction, synchrotron radiation at the I19 beamline of the Diamond Light Source is utilized, with a wavelength (λ) value of 0.6889 Å. Alternatively, the Bruker-Nonius X8APEXII CCD area detector diffractometer employing graphite monochromated Mo Kα radiation (λ = 0.71073 Å) can also be used for this purpose.

For Powder X-Ray Diffraction, the powder diffractometer Empyrean PANalytical is employed, utilizing Cu Kα radiation with a wavelength (λ) value of 1,54056 Å.

3.3.14 *Brunauer-Emmett-Teller surface area analysis (BET)*

Brunauer-Emmett-Teller (BET) surface area analysis is a method used to estimate the surface area of porous materials. It is commonly applied to characterize the specific surface area of zeolite and MOF-based catalysts. [230] The BET analysis is a widely used technique for surface area determination, and its application to zeolite and MOF catalysts has been explored using various approaches. In this study, N_2 adsorption-desorption isotherms were conducted at 77 K on sieved zeolites after subjecting them to a vacuum for 16 h with the use of a Micromeritics ASAP2020 instrument.

3.3.15 *Thermogravimetry analysis (TG)*

Thermogravimetry is a technique used to evaluate the thermal stability and degradation of catalysts. It involves measuring the weight change of a sample as it is

heated or cooled. It can also be used to evaluate the thermal and catalytic degradation of petroleum residues, with mesoporous materials showing efficiency in catalytic degradation. [231] In this *thesis*, the elimination of NO_3^- and other volatile substances, including water and CO_2, is achieved through thermal decomposition reactions. Consequently, these conversions result in the generation of catalytically active Ag species. As a consequence, the identification of an appropriate calcination temperature is of paramount importance for the effective preparation of zeolite catalysts. The thermogravimetric analyses were conducted on pelletized samples with a size range of 0.5-0.8 mm, under a dry N2 atmosphere, utilizing a thermobalance operating at a heating rate of 10 ºC min^{-1}, within a temperature range of 25 to 450 °C.

3.3.16 *Transmission electron microscopy (TEM)*

Transmission Electron Microscopy (TEM) is a powerful technique used for the characterization of nanostructures. It provides information on morphology, crystal structure, and chemical composition through imaging, diffraction, and spectroscopic analysis. [232] High-resolution transmission electron microscopy (HRTEM) allows for the observation of nanomaterials at the atomic scale, providing detailed information about their structure and properties. Other techniques that can be performed using HRTEM include high-angle annular-dark-field scanning transmission electron microscopy (HAADF-STEM), which images atom clusters with atomic resolution chemical information, electron holography of magnetic materials. In this *thesis*, samples for electron microscopy studies were prepared by dropping the solid sample suspension in dichloromethane onto carbon-coated copper grids. For Ag-containing zeolite powder samples were embedded in epoxy resin, sliced, and deposited on carbon copper grids for TEM observation. HR HAADF-STEM and STEM-iDPC studies were performed on a monochromated FEI Titan3 Themis 60-300 microscope. 2048 × 2048 HAADF-iDPC image pairs were recorded simultaneously using specific convergence angles and collection angles. A fast image-recording protocol was used to limit damage by the electron beam. iDPC imaging allows for atomically resolved

images and is used to analyze zeolite structures. A specific methodology for digital analysis of the images was used, including denoising and clustering techniques. HR HAADF-STEM image simulation was carried out using TEMSIM software and complex structural models were used as inputs.

3.3.17 *Field emission scanning electron microscopy (FESEM)*

A Field Emission Scanning Electron Microscope (FESEM) is a type of electron microscope that is used for high-resolution imaging of surface structures. It can provide detailed information about the topography and organization of samples at a nanometer scale. FESEM uses a focused beam of primary electrons that interact with the sample, resulting in the emission of secondary or backscattered electrons. These electrons are then collected and used to generate an image of the sample's surface. [233, 234] FESEM, being a type of SEM, also uses an electron beam to scan the surface of a specimen, but it utilizes a field emission electron gun as the electron source, which allows for selective scanning technology and the ability to irradiate arbitrary regions in the SEM image at arbitrary intensity. [235]

3.3.18 *Temperature-programmed desorption (TPD) analysis*

Temperature-programmed desorption (TPD) analysis is a technique used to determine the thermodynamic and kinetic parameters of a reaction by measuring the desorption of molecules from a surface as a function of temperature. TPD is commonly used in surface science experiments to study the properties of catalysts and adsorbate. It involves heating the sample at a controlled rate and measuring the desorbed molecules using various detection methods. TPD can provide information about the binding energy, activation energy, and surface coverage of adsorbates on solid surfaces. It can also be used to study the effect of metal cluster size on desorption profiles. TPD analysis is a valuable tool for understanding the fundamental properties

of catalysts and adsorbates, [236, 237] and it has applications in fields such as catalysis, [238, 239] nanotechnology, and surface chemistry. [238]

3.4 *Experimental procedures*

3.4.1 *General reaction procedure*

Corresponding to *Chapter 4*: The corresponding solid catalyst and the substrate were introduced in a glass vial equipped with a magnetic stirrer, ethyl diazoacetate **1** (EDA, 0.1 mmol) was added, and the vial was sealed by a steel cap with a rubber septum. Then, the vial was placed in a magnetically stirred pre-heated oil bath at 60 ºC overnight. After the reaction is complete, filtration is carried out to separate the solid catalyst. The reaction mixture was analyzed by GC and GC-MS.

Corresponding to *Chapter 5*: MOF **23** (9.5 mg, 10 mol% Ag) was weighed in a 2 mL vial with a magnetic stirrer, and the aromatic substrate (0.8 mL) was added. Then, the vial was placed in a pre-heated oil batch at 60 ºC and ethyl diazoacetate **1** (0.1 mmol) was added, either at once or by syringe pump (solution in dichloromethane). The mixture was allowed to react for 0.5-2 h. After the reaction is complete, filtration is carried out to separate the solid catalyst. The reaction mixture was analyzed by GC and GC-MS.

Corresponding to *Chapter 6*:

The corresponding dealuminated HY solid catalyst (30mg) and the aromatic, alcohols substrate (0.8 mL) was introduced in a glass vial equipped with a magnetic stirrer, ethyl diazoacetate (EDA 1, 0.1 mmol) was added, and the vial was sealed. Then, the vial was placed in a magnetically stirred pre–heated oil bath at 60 ºC. After the reaction is complete, filtration is carried out to separate the solid catalyst. The reaction mixture was analyzed by GC and GC–MS.

The corresponding dealuminated HY zeolites (30 mg) and hexane (0.5 mL) were introduced in a glass vial equipped with a magnetic stirrer, ethyl diazoacetate (EDA **1**, 0.1 mmol, 12 ul) and styrene (0.1mmol, 10 ul) was added, and the vial was sealed. Then, the vial was placed in a magnetically stirred pre-heated oil bath at 50 ºC overnight 20 h. After the reaction is complete, filtration is carried out to separate the solid catalyst. The reaction mixture was analyzed by GC and GC-MS.

3.4.2 *Hot filtration test*

Following the general reaction procedure, two parallel reactions were carried out and one of them was rapidly filtrated at the reaction temperature (60 ºC) after reaction time (~30% conversion). Then, the kinetic profiles for both the solid-containing reaction and the filtrates were assessed and compared.

3.4.3 *Reuses*

Following the general reaction procedure, the solid catalyst was separated by centrifugation at 8000 r.p.m. during 5 min, washed with dichloromethane (1 mL) for three times, separated again and dried. Fresh reactants were placed for a new reaction.

3.4.4 *Scope tests*

Corresponding to *Chapter 5*:

MOF 23 (9.5 mg, 10 mol% Ag) was weighed in a 2 mL vial with a magnetic stirrer, and the aromatic substrate (0.7 mL) was added. Then, the vial was placed in a pre-heated oil batch at 60 ºC and ethyl diazoacetate 1 (0.1 mmol) was added, either at once or by syringe pump (solution in dichloromethane). The mixture was allowed to react for 0.5-2 h. After the reaction is complete, filtration is carried out to separate the solid catalyst. The reaction mixture was analyzed by GC and GC-MS.

Corresponding to *Chapter 6*:

The corresponding dealuminated HY solid catalyst (30mg) and the alkanes alkenes, aromatics, alcohols, silanes, amines substrate (0.7 mL) was introduced in a glass vial equipped with a magnetic stirrer, ethyl diazoacetate (EDA 1, 0.1 mmol) was added, and the vial was sealed. Then, the vial was placed in a magnetically stirred pre–heated oil bath under nitrogen atmosphere at 60 ºC. After the reaction is complete, filtration is carried out to separate the solid catalyst. The reaction mixture was analyzed by GC and GC–MS.

The corresponding dealuminated HY solid catalyst (30mg) and the alkenes, substrate (0.1 mmol) were introduced in a glass vial equipped with hexane solvent (0.7mL) and a magnetic stirrer, ethyl diazoacetate (EDA 1, 0.1 mmol) was added, and the vial was sealed. Then, the vial was placed in a magnetically stirred pre–heated oil bath under nitrogen atmosphere at 60 ºC. After the reaction is complete, filtration is carried out to separate the solid catalyst. The reaction mixture was analyzed by GC and GC–MS.

3.5 *Characterization of isolated compounds*

3.5.1 *Characterization of the products.*

Corresponding to *Chapter* 4:

^{1}H, ^{13}C, DEPT135 NMR and GC-MS copies:

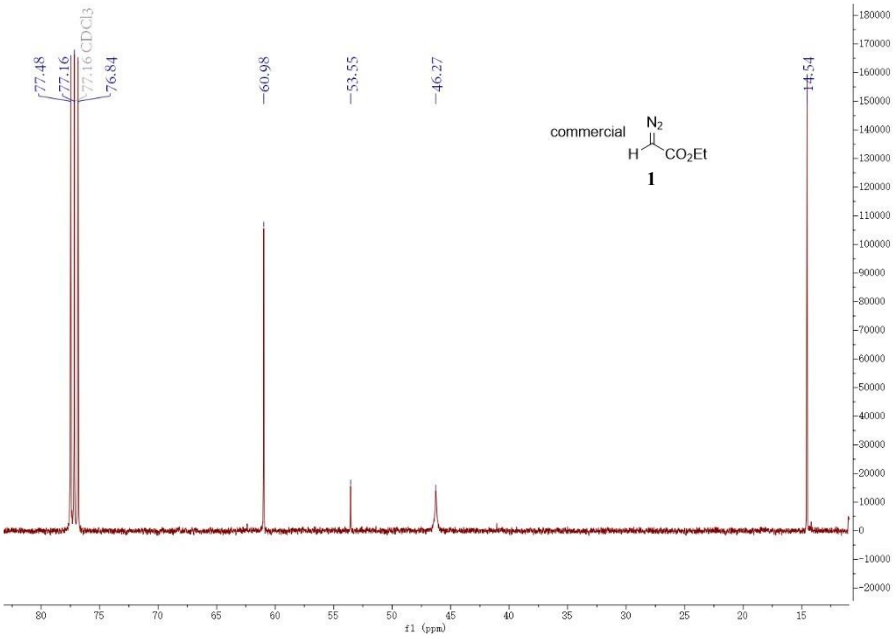

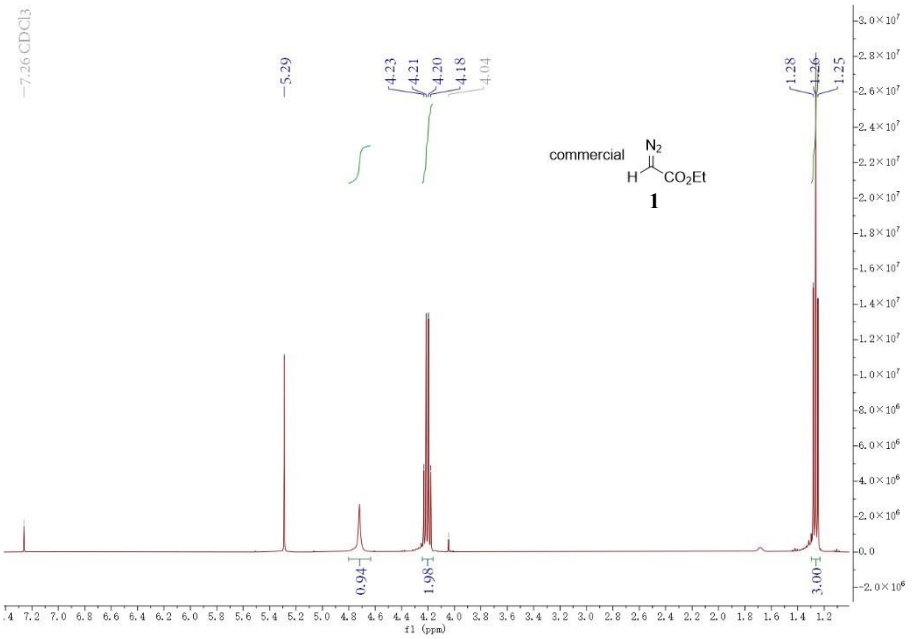
7.26 CDCl3
5.29
4.23
4.21
4.20
4.18
4.04
1.28
1.26
1.25
commercial
N2
H
CO2Et
1
0.94
1.98
3.00
f1 (ppm)

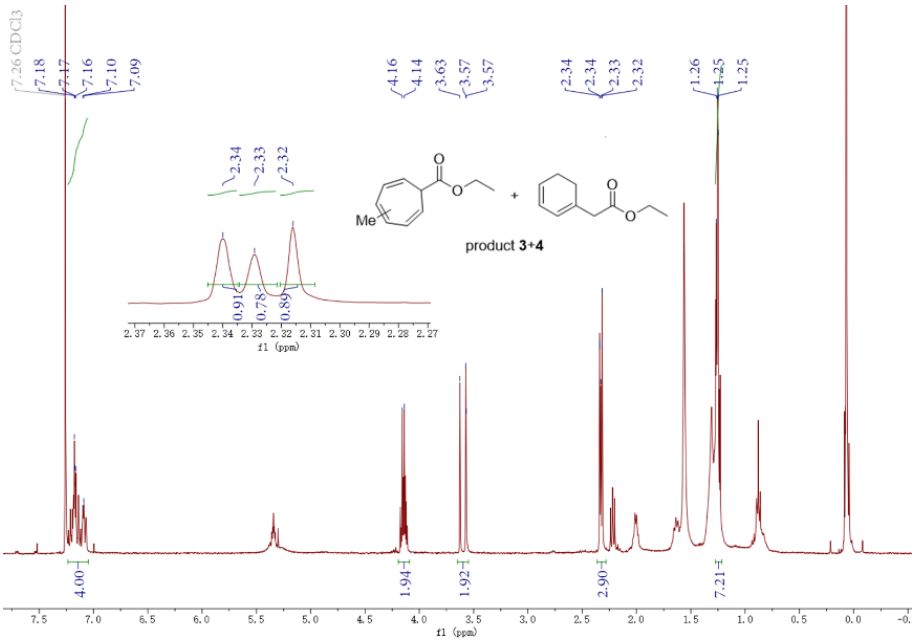
7.26 CDCl3
7.18
7.17
7.16
7.10
7.09
4.16
4.14
3.63
3.57
3.57
2.34
2.34
2.33
2.32
1.26
1.25
1.25
2.34
2.33
2.32
Me
product 3+4
0.91
0.78
0.89
4.00
1.94
1.92
2.90
7.21
f1 (ppm)

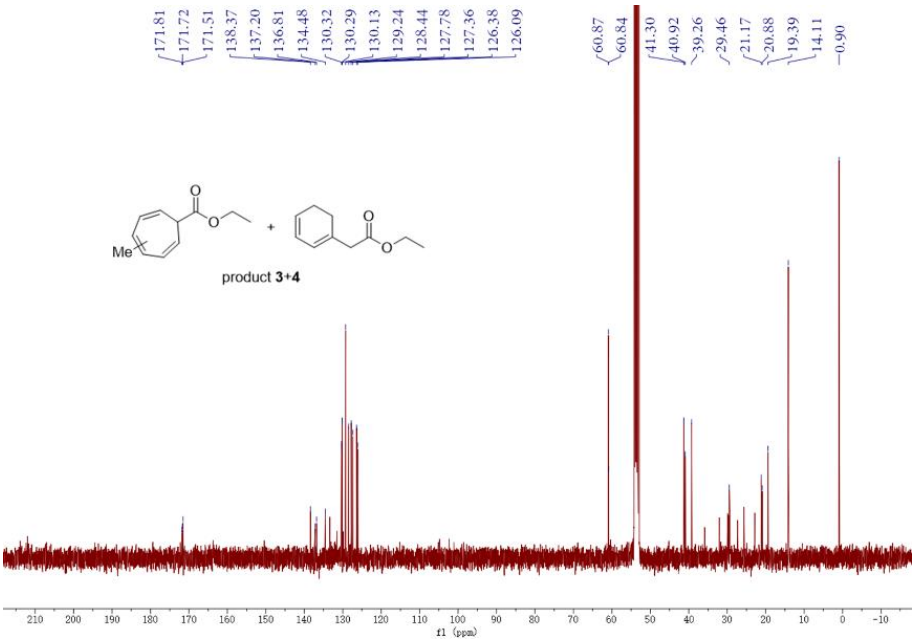
171.81
171.72
171.51
138.37
137.20
136.81
134.48
130.32
130.29
130.13
129.24
128.44
127.78
127.36
126.38
126.09
60.87
60.84
41.30
40.92
39.26
29.46
21.17
20.88
19.39
14.11
0.90
Me
product 3+4
f1 (ppm)

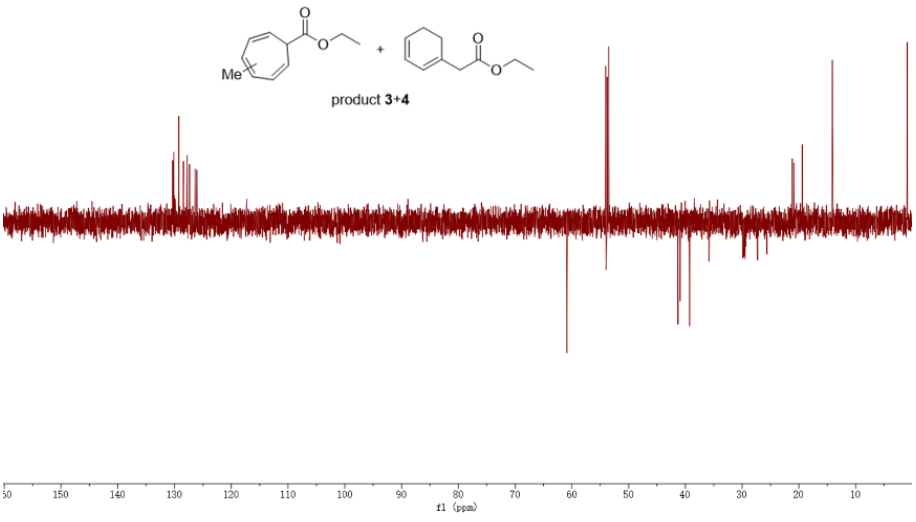
Me
product 3+4
f1 (ppm)

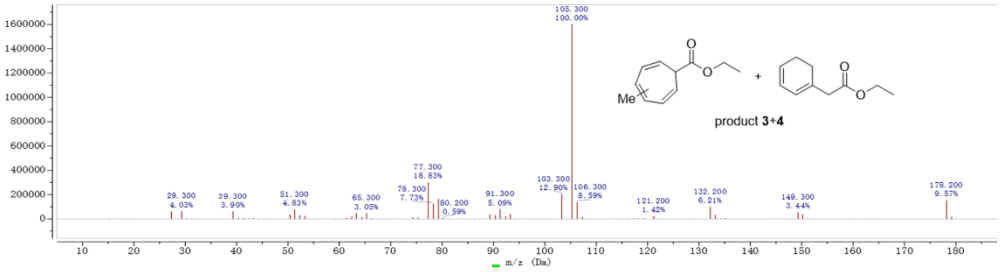
105.300
100.00%
77.300
18.83%
103.300
12.90%
106.300
8.59%
29.300
4.03%
39.300
3.90%
51.300
4.83%
65.300
3.05%
78.300
7.73%
80.200
0.59%
91.300
5.09%
121.200
1.42%
132.200
6.21%
149.300
3.44%
178.200
9.57%
Me
product 3+4
m/z (Da)

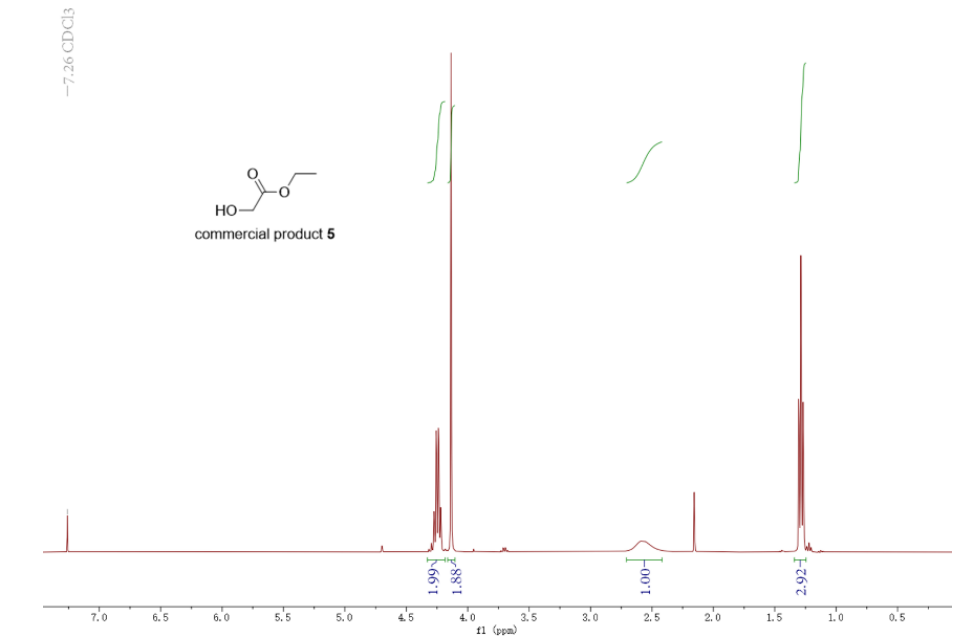
~7.26 CDCl3
HO
O
O
commercial product 5
1.99
1.88
1.00
2.92
7.0
6.5
6.0
5.5
5.0
4.5
4.0
3.5
3.0
2.5
2.0
1.5
1.0
0.5
f1 (ppm)

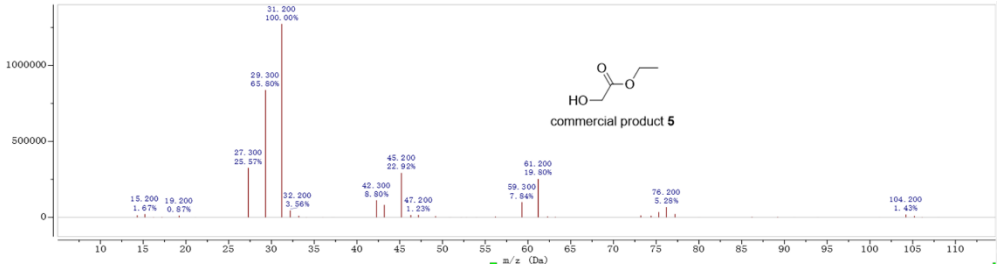
31.200
100.00%
29.300
65.80%
27.300
25.57%
15.200
1.67%
19.200
0.67%
32.200
3.56%
42.300
8.80%
45.200
22.92%
47.200
1.23%
59.300
7.84%
61.200
19.80%
76.200
5.28%
104.200
1.43%
1000000
500000
0
HO
O
O
commercial product 5
10
15
20
25
30
35
40
45
50
55
60
65
70
75
80
85
90
95
100
105
110
m/z (Da)

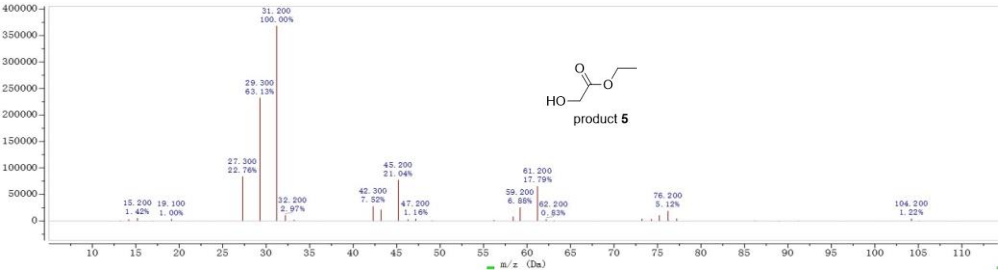
31.200
100.00%
29.300
63.13%
27.300
22.76%
15.200
1.42%
19.100
1.00%
32.200
2.97%
42.300
7.52%
45.200
21.04%
47.200
1.16%
59.200
6.88%
61.200
17.79%
62.200
0.83%
76.200
5.12%
104.200
1.22%
400000
350000
300000
250000
200000
150000
100000
50000
0
HO
O
O
product 5
10
15
20
25
30
35
40
45
50
55
60
65
70
75
80
85
90
95
100
105
110
m/z (Da)

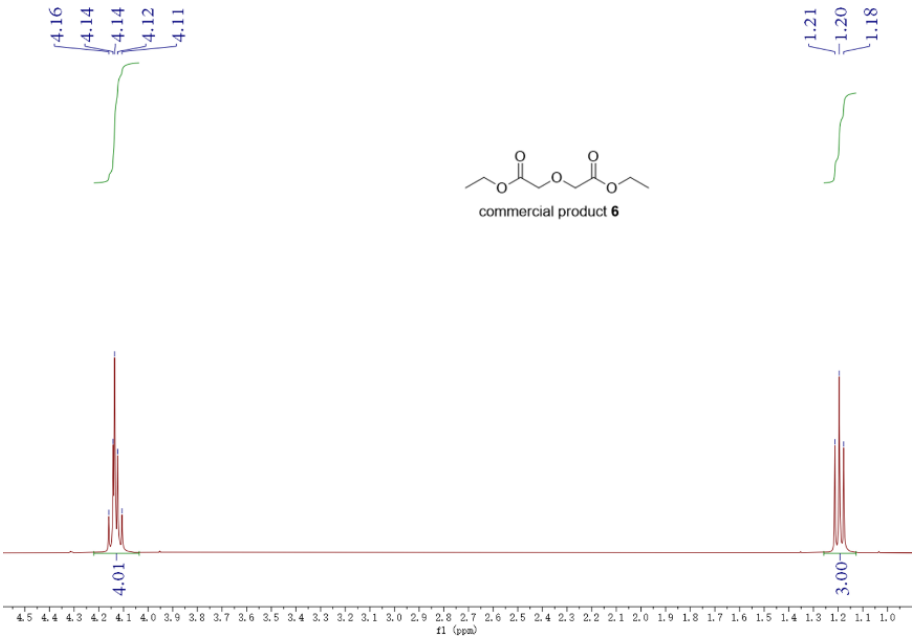
4.16
4.14
4.14
4.12
4.11
1.21
1.20
1.18
commercial product **6**
4.01
3.00
f1 (ppm)

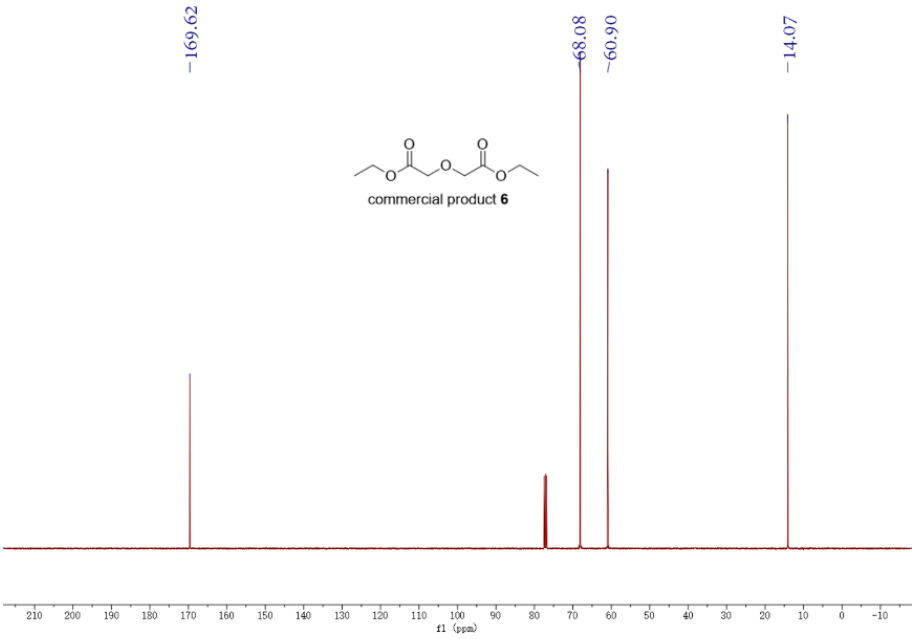
169.62
68.08
60.90
14.07
commercial product **6**
f1 (ppm)

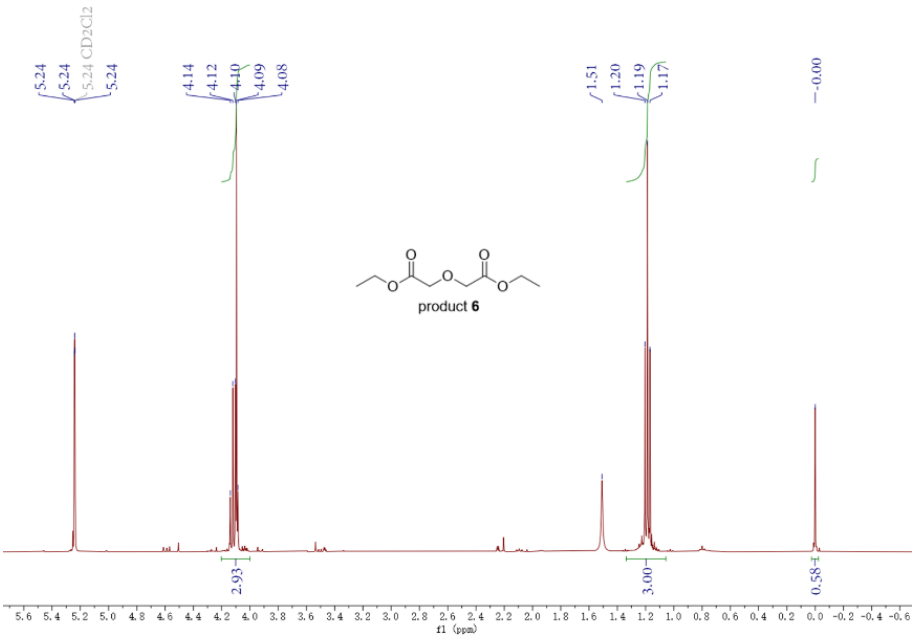
5.24
5.24
5.24 CD2Cl2
5.24
4.14
4.12
4.11
4.09
4.08
1.51
1.20
1.19
1.17
-0.00
product 6
2.93
3.00
0.58
f1 (ppm)

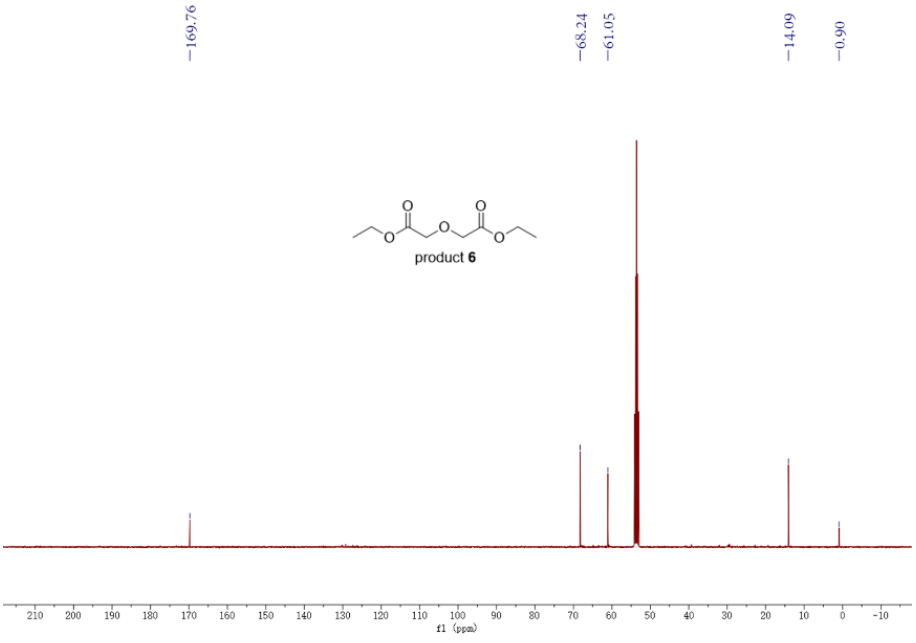
169.76
68.24
61.05
14.09
0.90
product 6
f1 (ppm)

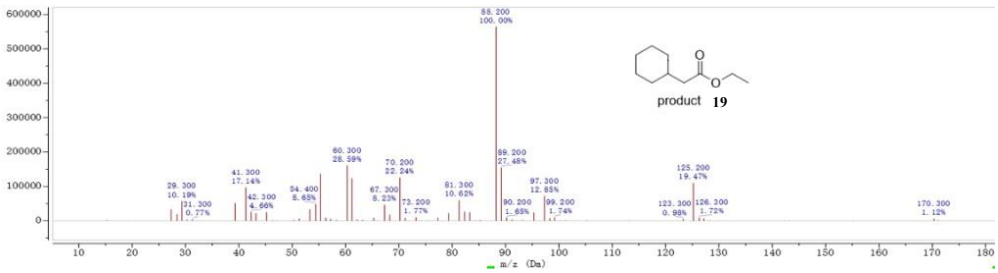
88.200
100.00%
product 19
89.200
27.48%
60.300
28.59%
70.200
22.24%
41.300
17.14%
97.300
12.85%
125.200
19.47%
29.300
10.19%
54.400
8.65%
67.300
8.23%
81.300
10.62%
31.300
0.77%
42.300
4.66%
73.200
1.77%
90.200
1.65%
99.200
1.74%
123.300
0.98%
126.300
1.72%
170.300
1.12%
m/z (Da)

Corresponding to *Chapter 5*: GC-MS copies:

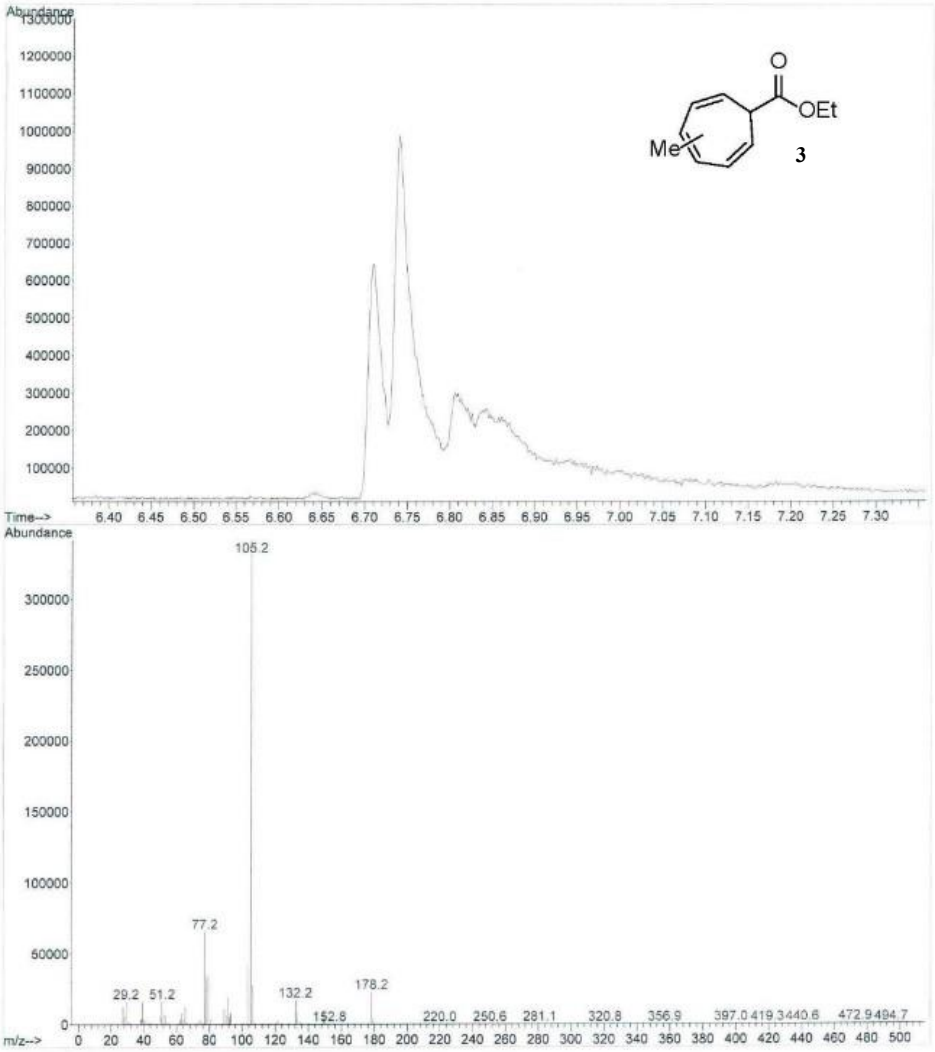

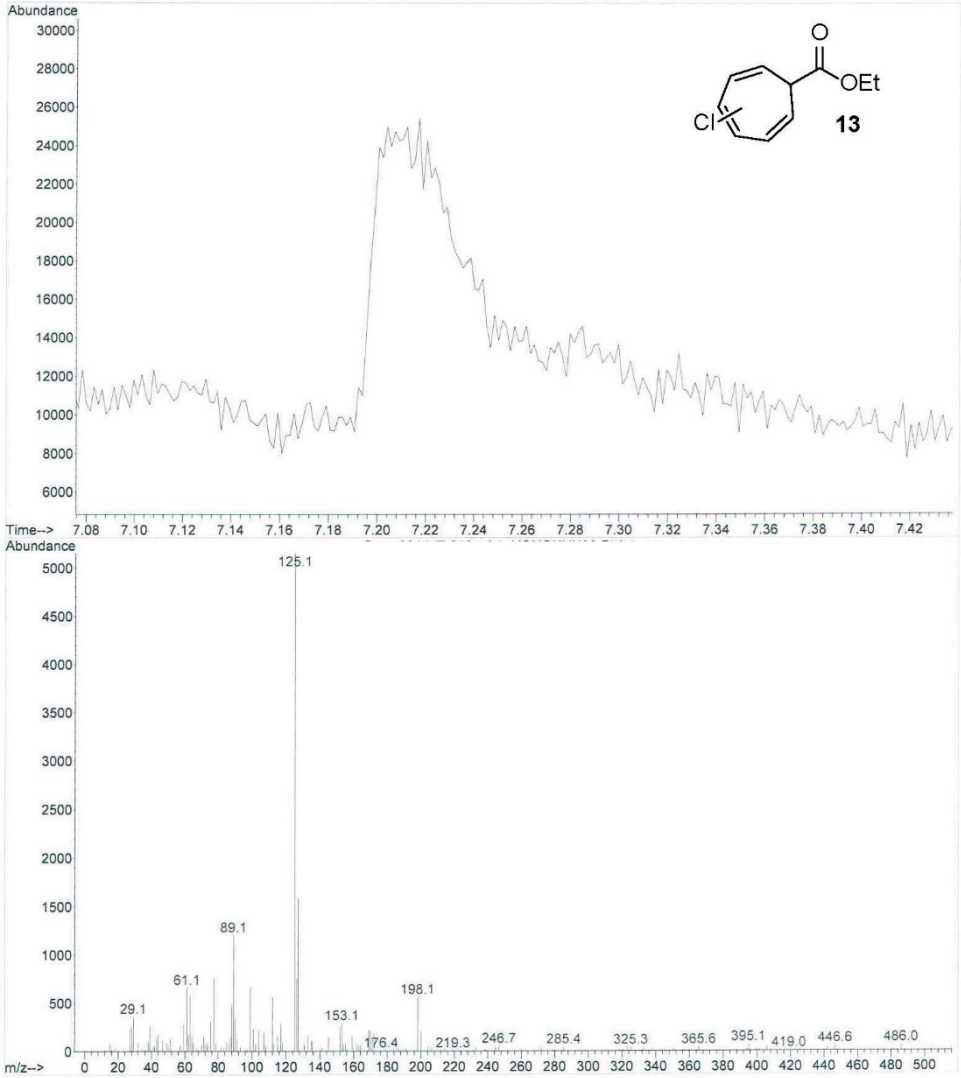
Abundance
30000
28000
26000
24000
22000
20000
18000
16000
14000
12000
10000
8000
6000
Time-->
7.08 7.10 7.12 7.14 7.16 7.18 7.20 7.22 7.24 7.26 7.28 7.30 7.32 7.34 7.36 7.38 7.40 7.42
O
OEt
Cl
13
Abundance
5000
4500
4000
3500
3000
2500
2000
1500
1000
500
0
m/z-->
125.1
89.1
61.1
29.1
153.1
198.1
176.4
219.3
246.7
285.4
325.3
365.6
395.1
419.0
446.6
486.0
0 20 40 60 80 100 120 140 160 180 200 220 240 260 280 300 320 340 360 380 400 420 440 460 480 500

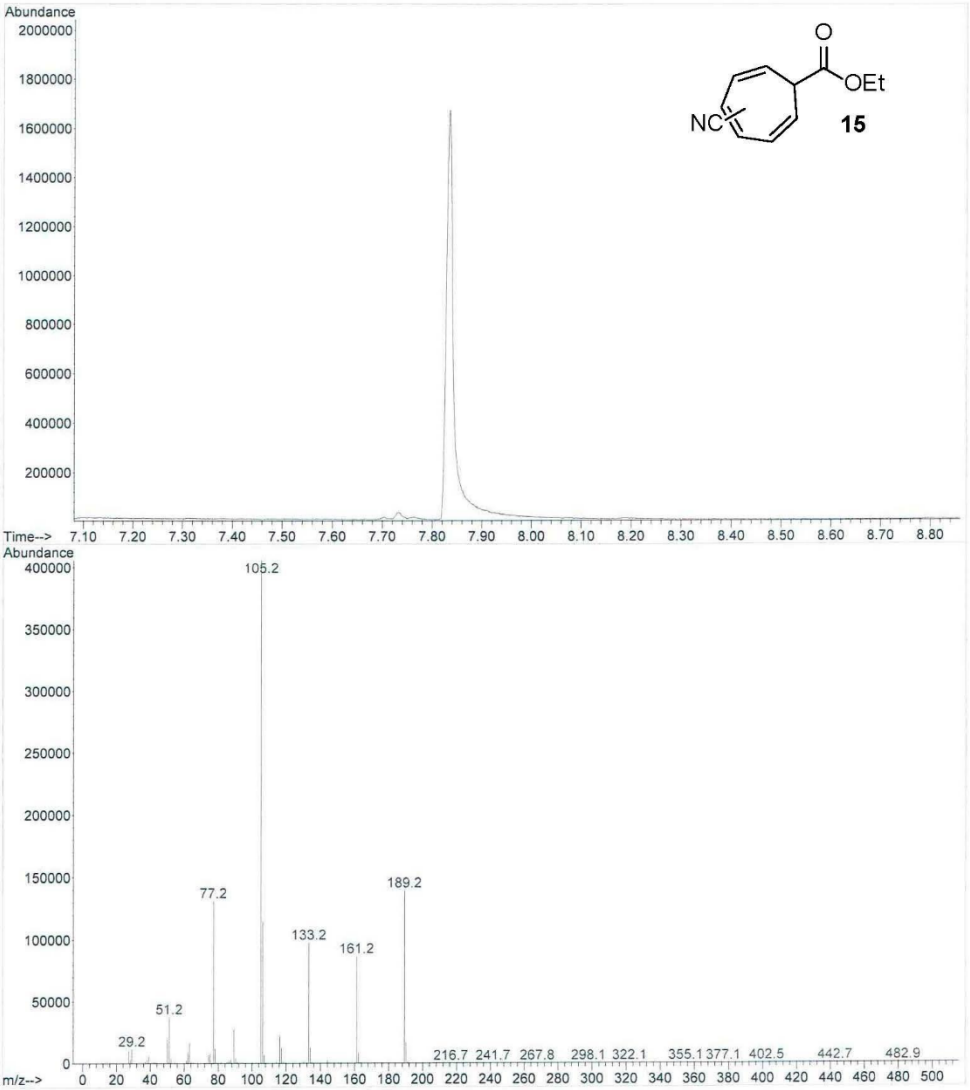
Abundance
2000000
1800000
1600000
1400000
1200000
1000000
800000
600000
400000
200000
Time-->
7.10 7.20 7.30 7.40 7.50 7.60 7.70 7.80 7.90 8.00 8.10 8.20 8.30 8.40 8.50 8.60 8.70 8.80
O
OEt
NC
15
Abundance
400000
350000
300000
250000
200000
150000
100000
50000
0
m/z-->
105.2
77.2
189.2
133.2
161.2
51.2
29.2
216.7 241.7 267.8 298.1 322.1 355.1 377.1 402.5 442.7 482.9
0 20 40 60 80 100 120 140 160 180 200 220 240 260 280 300 320 340 360 380 400 420 440 460 480 500

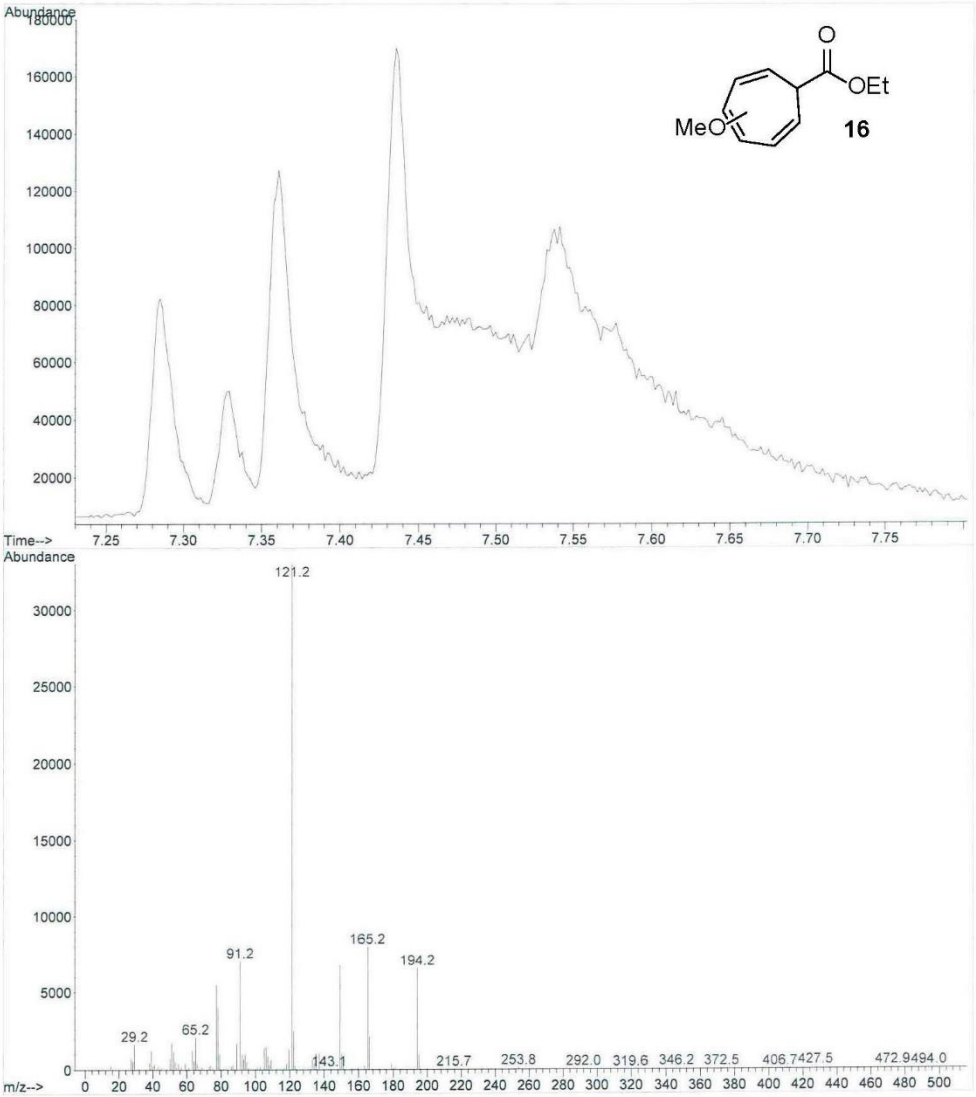
Abundance
180000
160000
140000
120000
100000
80000
60000
40000
20000
Time-->
7.25
7.30
7.35
7.40
7.45
7.50
7.55
7.60
7.65
7.70
7.75
O
OEt
MeO
16
Abundance
30000
25000
20000
15000
10000
5000
0
121.2
165.2
91.2
194.2
29.2
65.2
143.1
215.7
253.8
292.0
319.6
346.2
372.5
406.7
427.5
472.9
494.0
m/z-->
0 20 40 60 80 100 120 140 160 180 200 220 240 260 280 300 320 340 360 380 400 420 440 460 480 500

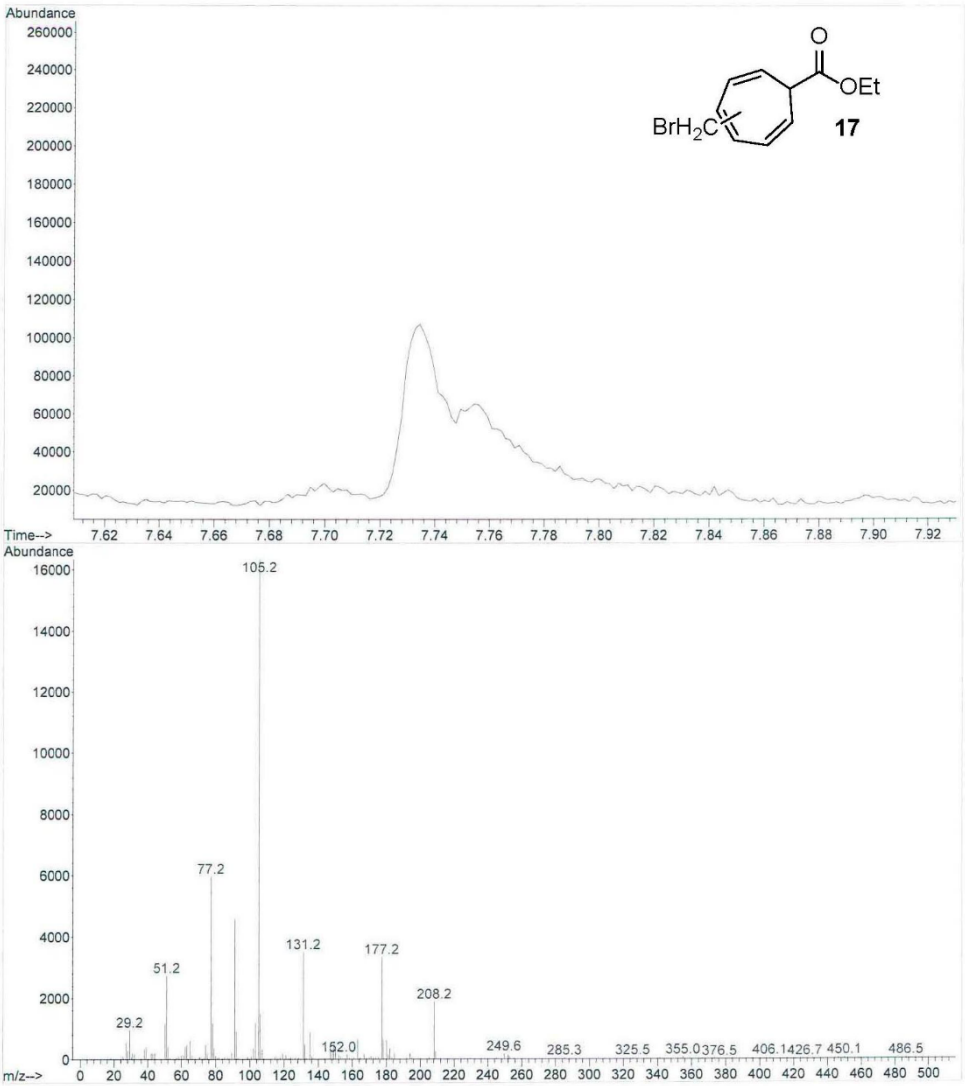
Abundance
260000
240000
220000
200000
180000
160000
140000
120000
100000
80000
60000
40000
20000
Time-->
7.62 7.64 7.66 7.68 7.70 7.72 7.74 7.76 7.78 7.80 7.82 7.84 7.86 7.88 7.90 7.92
O
OEt
BrH2C
17
Abundance
16000
14000
12000
10000
8000
6000
4000
2000
0
m/z-->
0 20 40 60 80 100 120 140 160 180 200 220 240 260 280 300 320 340 360 380 400 420 440 460 480 500
105.2
77.2
131.2
177.2
51.2
208.2
29.2
152.0
249.6
285.3
325.5
355.0
376.5
406.1
426.7
450.1
486.5

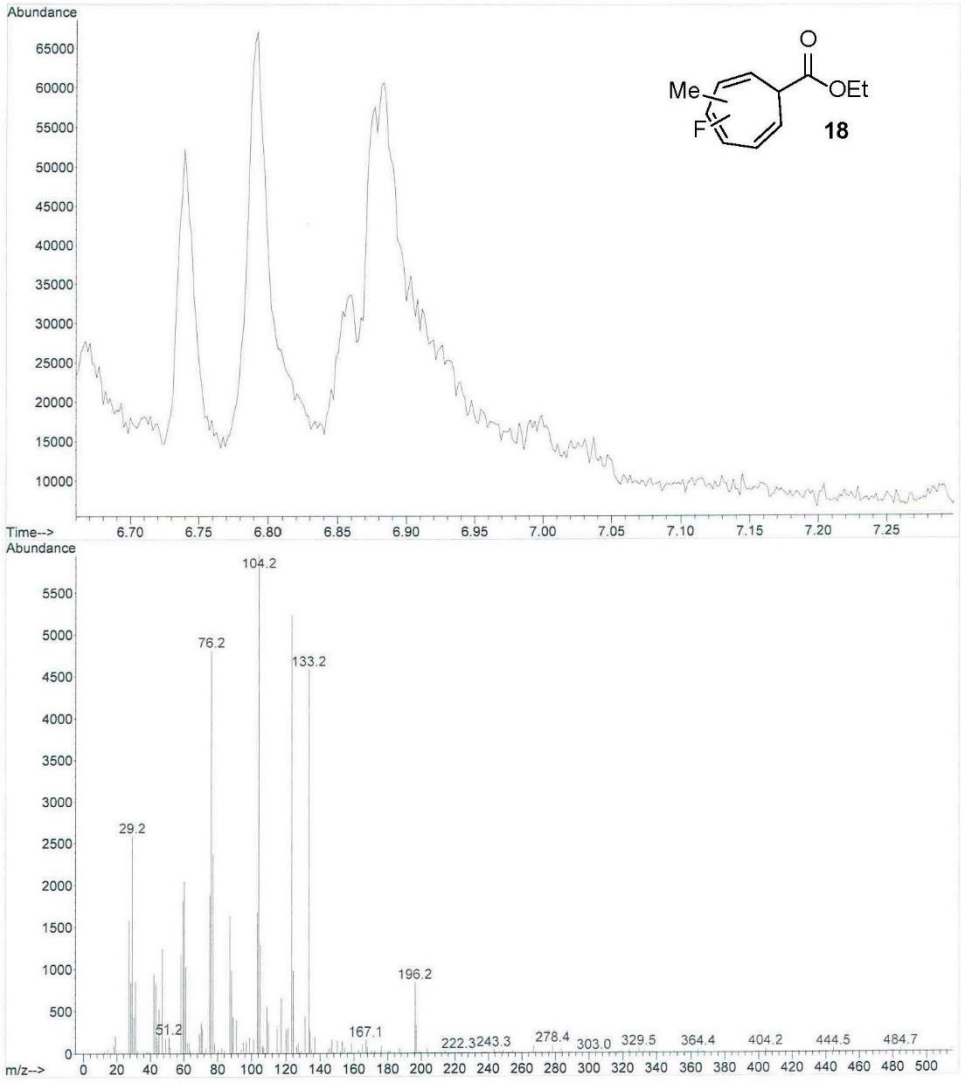
Abundance
65000
60000
55000
50000
45000
40000
35000
30000
25000
20000
15000
10000
Time-->
6.70
6.75
6.80
6.85
6.90
6.95
7.00
7.05
7.10
7.15
7.20
7.25
O
Me
OEt
F
18
Abundance
5500
5000
4500
4000
3500
3000
2500
2000
1500
1000
500
0
m/z-->
104.2
76.2
133.2
29.2
196.2
51.2
167.1
222.3
243.3
278.4
303.0
329.5
364.4
404.2
444.5
484.7
0
20
40
60
80
100
120
140
160
180
200
220
240
260
280
300
320
340
360
380
400
420
440
460
480
500

Corresponding to *Chapter 6*:

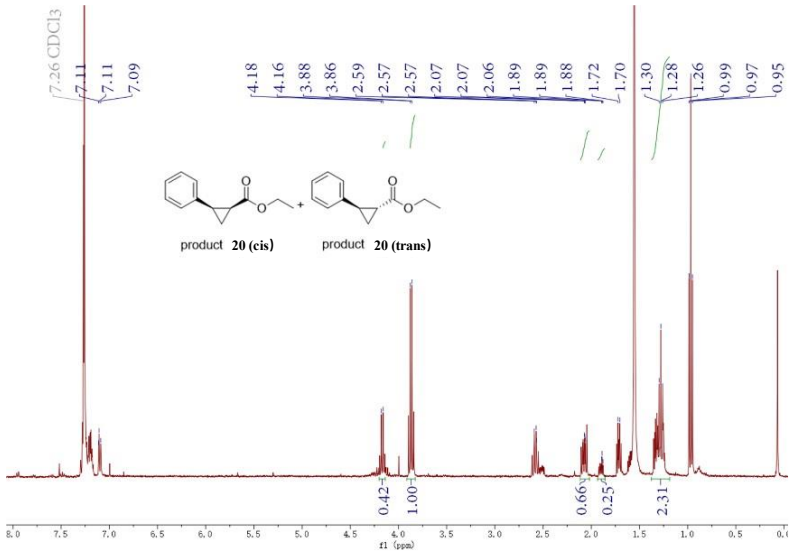

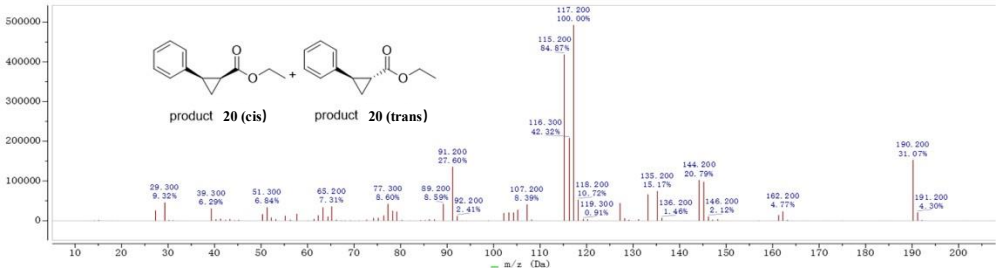

Chapter 4. Carbene insertion reactions by silver-exchanged zeolite Y catalysts

4.1 *Introduction*

Nanomaterials with a dimension of 1-100 nm in at least one direction have been widely applied and attracted much attention in various fields such as environment, energy, biology, and electronics over the past few decades. [240-245] With the advancement of aberration-corrected electron microscopy[246, 247]and X-ray absorption spectroscopy (XAS) on their coordination environment[248], we are now able to observe individual metal atoms and subnanometric metal clusters composed of a few of atoms. In the last decade, single atoms (SACs) supported on solids have become attractive catalysts for organic synthesis. [249-253] Ag is an interesting element, but its catalytic behaviors is hard to study, as it readily aggregates under ambient light, apart from those prepared by atom deposition or electrochemical methods. [254-256]

Silver-supported zeolites have been studied for decades, [257] and found applications in diverse fields such as antimicrobial agents, [258-261] adsorbents of methyl iodide in nuclear power plants, [262, 263] and as catalysts for methane activation, [264-266]1-butene dimerization, [267] and nitrogen oxides and carbon monoxide redox reactions, [266, 268-271] among others[272-276]. However, it is difficult to find in the literature the use of Ag-supported zeolites as catalysts for fine organic synthesis, despite the paramount relevance of Ag as a catalyst in many organic transformations. [277-287] The lack of examples with Ag zeolites is due to the tendency of Ag to aggregate inside the zeolite and block the pores, hampering the diffusion and reactivity of molecules composed of more than 3-4 atoms. [288, 289] The Ag aggregation, and consequently the blocking of pores in the zeolite, limits the diffusion and reactivity of molecules with more than 3-4 atoms, resulting in few examples of Ag zeolites. [288]

Figure 4.1 shows the strategy that we have followed in this chapter to stabilize subnanometer Ag species, using the robust and commercially available zeolite Y as a support. This strategy has consisted of preparing zeolites with different charge-compensating cations by ion exchange, which allows regulating the electron density on the Ag sites. The synthesis of the silver species was carried out by wet exchange with $AgNO_3$ and calcination under air. As will be shown throughout the chapter, once the different silver catalysts were prepared and characterized, their efficiency was evaluated to carry out representative carbene-mediated reactions, such as the Buchner reaction or insertion into C-H or C-O bonds.

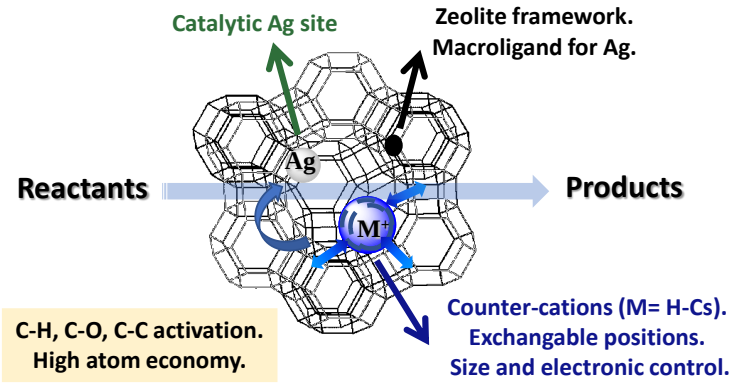

Figure 4.1 Schematic representation of the strategy employed.

4.2 *Synthesis and characterization of Ag-HY zeolite catalysts*

4.2.1 *Synthesis of Ag-HY/ Ag-(Li to Cs)NaY zeolites*

The ion exchanged-calcination method was employed to prepare the different Ag catalysts, **Figure 4.2** illustrates the synthesis procedure. It is noteworthy that the cationic exchange method is favored over the incipient wetness methodology due to its ability to provide a homogeneous distribution of Ag cations on the zeolite surface and a stronger Ag-zeolite interaction. In contrast, the latter method produces a heterogeneous distribution that can promote the aggregation of Ag.

Firstly, commercially available Y zeolite, in H^+-form, was chosen to support Ag in order to minimize their reduction and agglomeration, since this zeolite has the lowest framework electron density among all cation-counterbalanced zeolites Y. For this, the H-USY zeolite (Si/Al = 15) was treated with an aqueous solution of $AgNO_3$ at room temperature for 20 h. Subsequently, the exchanged silver Y zeolite was filtered, washed with deionized water three times, and dry in oven at 100°C overnight. In this way, Ag is homogenously distributed along the zeolite channels and cavities. Finally, the silver-containing zeolites (Ag-HY) were calcined at 450 °C for 10 h.

In the **Figure 4.3** show the synthesis procedure of alkaline silver zeolite catalysts Ag-Na(Li/K/Cs)Y. Commercially available Y zeolite, in Na^+-form (Si/Al = 2.5), were treated with a 1M aqueous solution of Li^+, K^+ or Cs^+ acetate at room temperature, and after repeating this procedure twice, give the corresponding Li^+, K^+ and Cs^+ zeolites (LiNaY, KNaY and CsNaY). The resulting solids were further cationically exchanged with an aqueous solution of $AgNO_3$. In this way, Ag is homogenously distributed along the alkaline zeolite channels and cavities. Finally, zeolites Ag-LiNaY, Ag-NaY and Ag-KNaY were calcined at 450 °C. Sample name “Cal” means after calcination treatment. Calcination was carried out for all zeolites except for Ag-CsNaY, since Ag

is rapidly reduced even after simple drying in an oven at 100 °C (dryness was performed by prolonged vacuum). The spontaneous reduction of Ag within the CsNaY zeolite indicates the propensity of supported Ag cations to accept electrons from the zeolite framework, especially from the CsNaY zeolite.

Changing the counterbalancing cation in zeolites from H^+ to Cs^+ results in an increase in electron density within the framework, since the bigger (softer) the counter cation, the higher the electron density on the framework. [290-293] This change ultimately affects the electronic properties of supported Ag cations, [294] and by manipulating the counterbalancing cation in zeolite Y, [295] we can control the electronics of the catalytic Ag site. If we also account for the size differences among counter cations, the steric hindrance within the supercages also intensifies. The alkaline cation exchange values ranged from 5 to 50 wt%, and the Ag content was approximately 1 wt% in all cases, as shown in detail in the following section. [296]

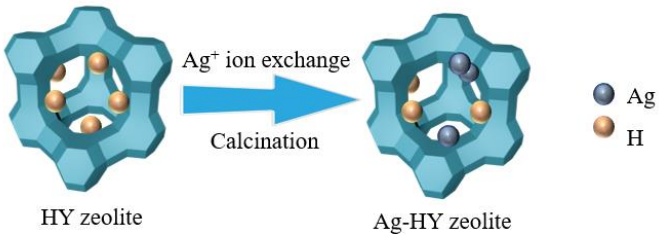

Figure 4.2 Schematic representation of the synthesis procedure of Ag-HY zeolites.

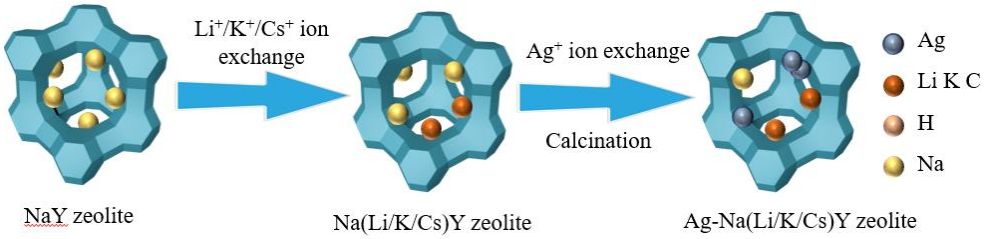

Figure 4.3 Schematic representation of the synthesis procedure of Ag-Na(Li/K/Cs) zeolites.

4.2.2 *Characterization of Ag-HY and Ag-(Li to Cs)NaY zeolite catalysts*

4.2.2.1 *Inductively coupled plasma atomic emission spectroscopy (ICP-AES)*

The amount of metal ions was measured by inductively coupled are plasma atomic emission spectroscopy (ICP-AES). Silver zeolites catalyst be discomposed by hydrofluoric acid before dry to remove all water molecules. The results are shown in **Table 4.1**

Table 4.1 Inductively coupled plasma atomic emission spectroscopy (ICP-AES) results for the different Ag-zeolites.[a]

Entry	Zeolite	Ag%	Na%	Li/K/Cs%
1	Ag-HYCal	1.08(0.99)	-	-
2	Ag-LiNaYCal	0.94(1.00)	5.98(5.89)	1.22(1.17)
3	Ag-NaYCal	0.77	6.30	-
4	Ag-KNaYCal	1.33	2.38	7.13
5	Ag-CsNaY	1.13	2.49	3.81

[a] In parentheses, the results after 10 uses of Ag-HYCal and 5 uses of Ag-LiNaYCal, for the reaction of ethyldiazoacetate (EDA) with toluene at 60 °C for 24 h.

4.2.2.2 *Thermogravimetric analysis (TG)*

The calcination temperature was selected to decompose the nitrate ligands, as confirmed by the absence of N in the elemental analysis (EA) of the calcined sample and by the thermogravimetric analysis. All the calcined samples main same weight after 450°C calcination procedure.

In the **Figure 4.4**, we can observe that with the increase of temperature to 100 °C, the percentage of thermogravimetric analysis gradually decreases. This reduction is due to the loss of water molecules adsorbed on the surface. Beyond 250 °C, the percentage remains constant, indicating that all surface-adsorbed water molecules have been completely removed, along with the decomposition of nitrate ligands.

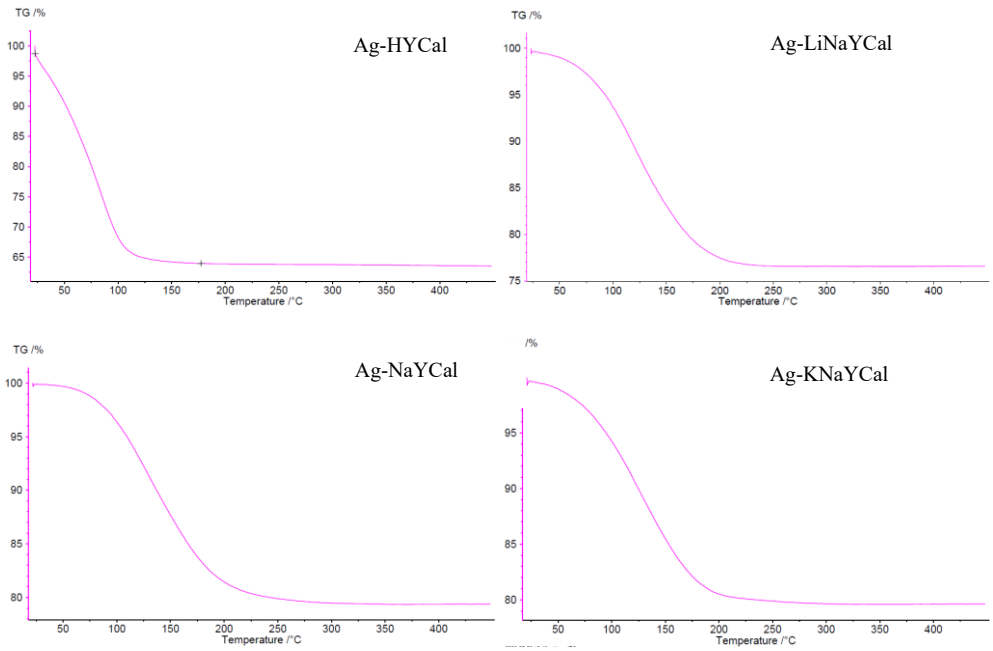

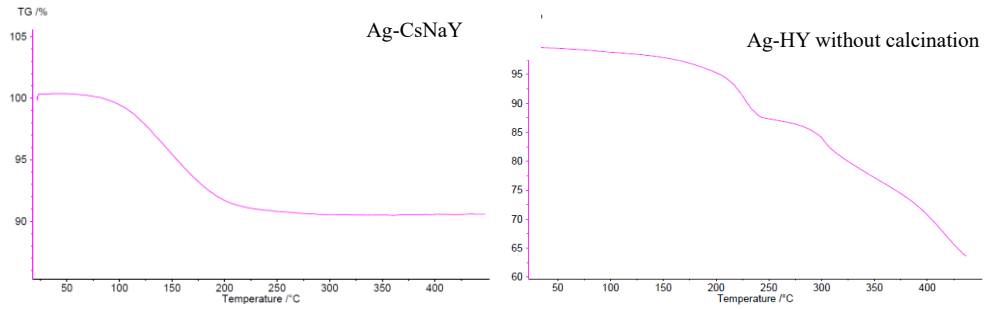

Figure 4.4 Thermogravimetric analysis (TG) of the different cation-exchanged zeolites after calcination (except for CsNaY). The last spectrum corresponds to Ag-HY without calcination.

4.2.2.3 *Powder X-ray diffraction (XRD)*

In certain cases, the non-calcined Ag-HY sample (which was only exchanged, filtered, and dried) was also evaluated for comparison. The XRD analysis of the calcined sample indicates that the starting diffraction peaks of the HY zeolite are retained and that no peak corresponding to Ag nanoparticles (NPs) is detected, as shown in **Figure 4.5**. Compared with Ag-(Li/Na/K/Cs)Y samples, some diffraction peaks reveals the gradual emergence of crystallographic planes (111), (200), (220), and (311) associated with Ag nanoparticles. This trend corresponds to an increasing electron richness in the zeolite framework, transitioning from H^+ to Cs^+.

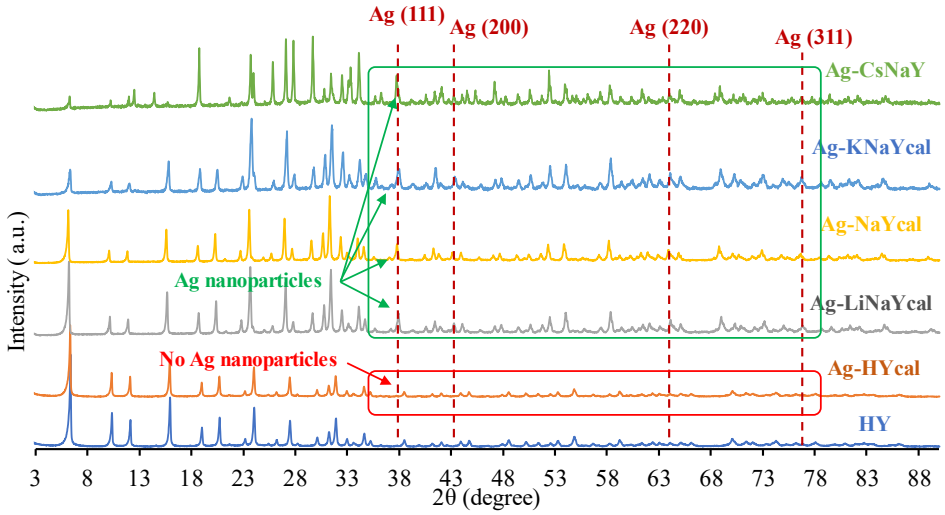

Figure 4.5 Powder X-ray diffractograms (XRD) of the different Ag-zeolites, indicating the formation or not of different crystallite planes of Ag nanoparticles.

4.2.2.4 *Brunauer-Emmett-Teller surface area analysis (BET)*

The Ag-HY and calcined Ag-HY sample were measured. Ag-HYcal zeolite showed a BET surface area of 708.76 m^2/g and t-Plot micropore volume of .312 cm^3/g, while HY zeolite showed a BET surface area of 723.38 m^2/g and -Plot micropore volume of 0.317 cm^3/g. In **Figure 4.6**, it can be seen how BET analysis gives a very similar surface area and microporous volume for both solids, which demonstrates that the incorporation of Ag has not blocked the zeolite channels.

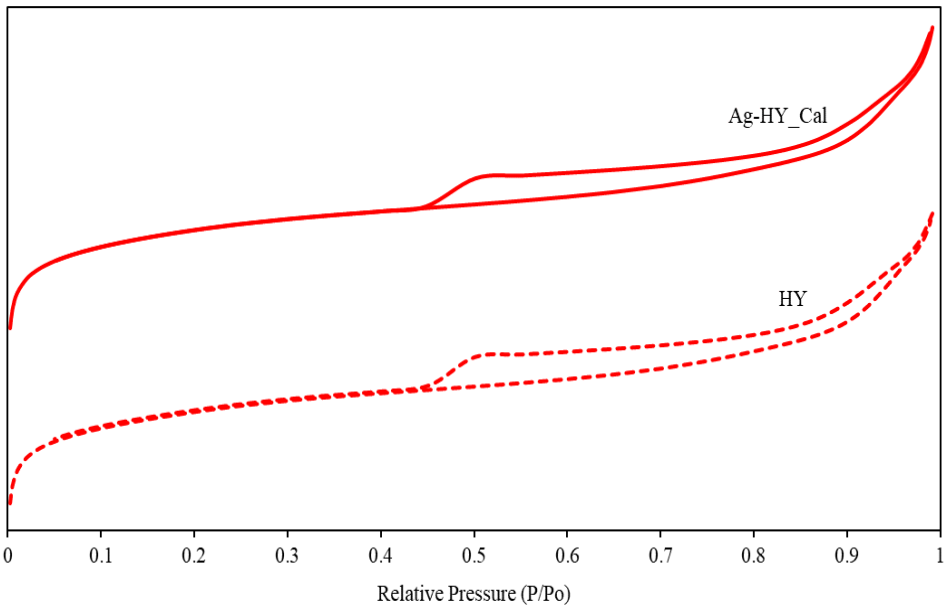

Figure 4.6 Brunauer-Emmett-Teller surface area plots (BET) of HY (top) and Ag-HYcal zeolite (bottom).

4.2.2.5 *Fourier-transformed infrared spectroscopy (FT-IR)*

In the **Figure 4.7**, the FTIR spectrum of the different silver zeolite catalysts is shown. In general, Si-OH or Si-OH-Al and Si-O-Al or Si-O bonds are associated with 3400 cm^{-1} and 1000 cm^{-1}, relatively. Here FT-IR spectrum also confirms the integrity of the aluminosilicate composition after the calcination, so the calcination did not destroy the zeolite structure.

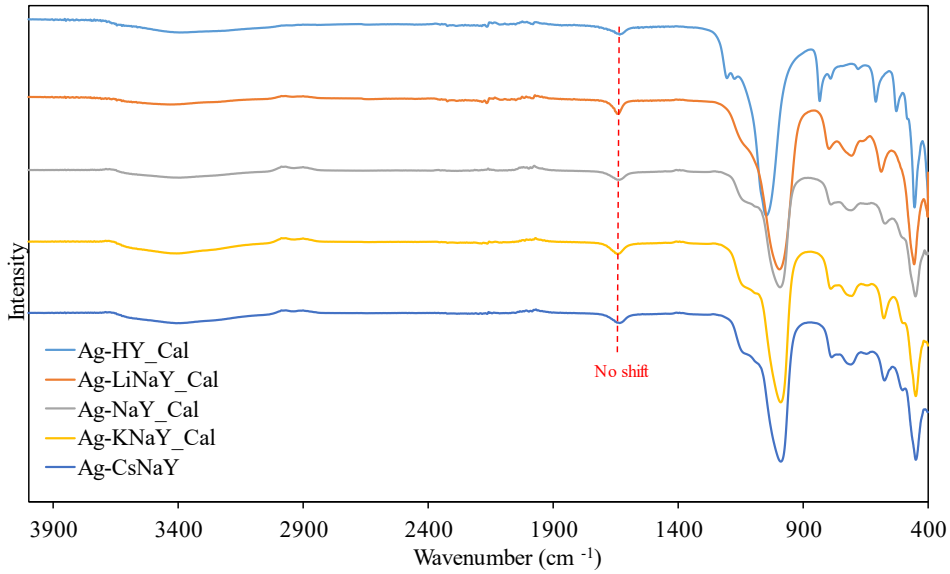

Figure 4.7 Fourier-transformed infrared (FT-IR) spectroscopy of the different Ag-zeolites. The stretching band of adsorbed water, external to the framework, remains unvaried as indicated (~1630 cm^{-1}).

4.2.2.6 *Diffuse reflectance ultraviolet-visible (DR-UV-vis)*

Figure 4.8 shows the DR-UV-vis measurements of Ag-HY, both before and after calcination, revealing bands between 200 nm and 240 nm associated with few-atom Ag^+ species [297, 298]. In addition, the absence of any plasmonic band corresponding to Ag NPs (400 nm - 450 nm) in the Ag-HY sample and only the appearance of a very small band approximately at 360 nm in the Ag-HYcal sample, confirm the exclusive formation of subnanometric Ag entities.

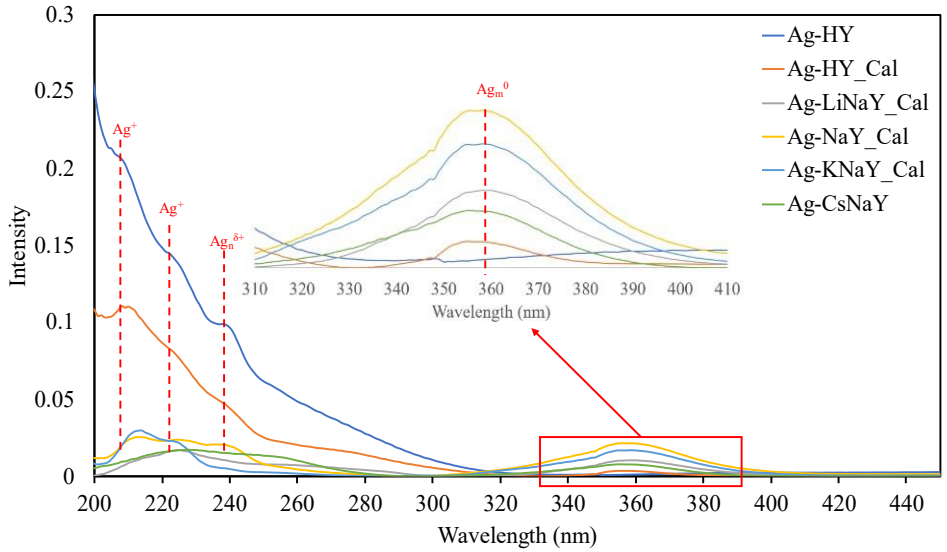

Figure 4.8 Diffuse reflectance UV-vis spectrophotometry (DR-UV-vis) of the different Ag-zeolites. The area around 360 nm is magnified, and the most prominent bands together with their plausible assignations are indicated.

4.2.2.7 *Emission spectrophotometry (fluorescence UV-vis)*

The fluorescence UV-vis spectra obtained at excitation wavelengths ranging from 200 nm to 260 nm, where 2 to 10 Ag atom clusters are expected to emit, [299] reveal distinct fluorescence bands for the Ag-HY solid compared to HY. Specifically, at excitation wavelengths of 200 nm to 210 nm, a Stokes shift of approximately 150 nm is observed in **Figure 4.9**. This shift is attributed to Ag_2 and Ag_3 clusters in the Ag-HY sample. [300]

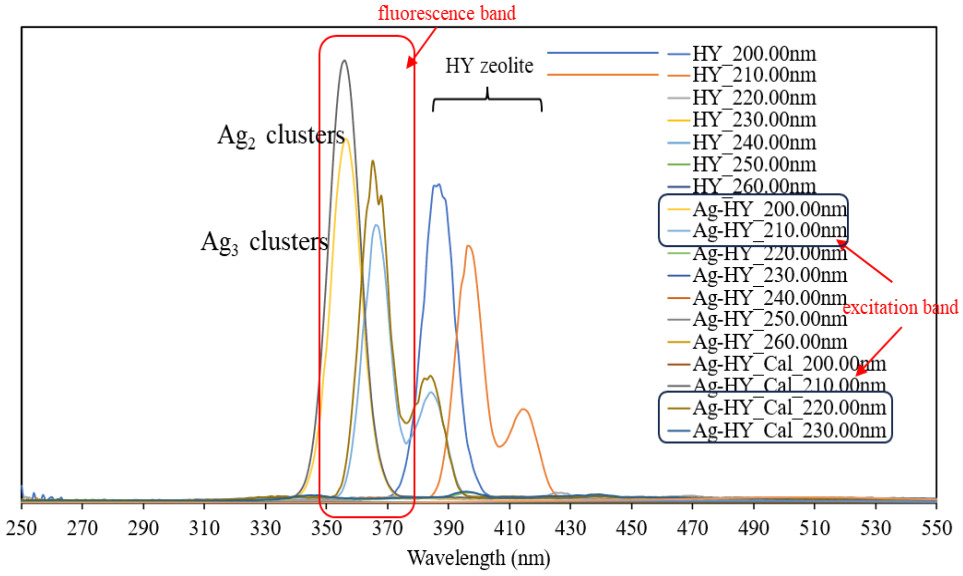

Figure 4.9 UV-vis emission spectrophotometry (fluorescence UV-vis) of HY and Ag-HY zeolites at different excitation wavelengths.

4.2.2.8 *X-ray photoelectron spectroscopy (XPS)*

Figure 4.10 shows the XPS analysis, which suggests the presence of Ag^{+} sites on the HY zeolite, without significant metallic Ag. A subtle shift in the Ag $3d_{5/2}$ peak toward lower values may be due to minor Ag^{0} species. Taking these results into account along with the fact that Ag-HY lacks Ag NP diffraction peaks, plasmonic bands, and fluorescence signals greater than 3 atoms, in addition to its high pore volume, it seems that Ag does not remain or neither reduced nor severely aggregated within the HY zeolite, and all of the supported Ag probably exists in cationic form. [301] On the other hand, the Ag $3d_{5/2}$ XPS signals exhibit a subtle shift toward higher electron-binding values when transitioning HY to CsNaY. This trend is also evident in the corresponding Si 2p, Al 2p (and O 1s XPS signals), [302] as seen in **Figure 4.11**, **Figure 4.12** and **Figure 4.13**, respectively**.** These collective findings strongly indicate the transfer and modification of electron density at the Ag site within the various metal-supported zeolites.

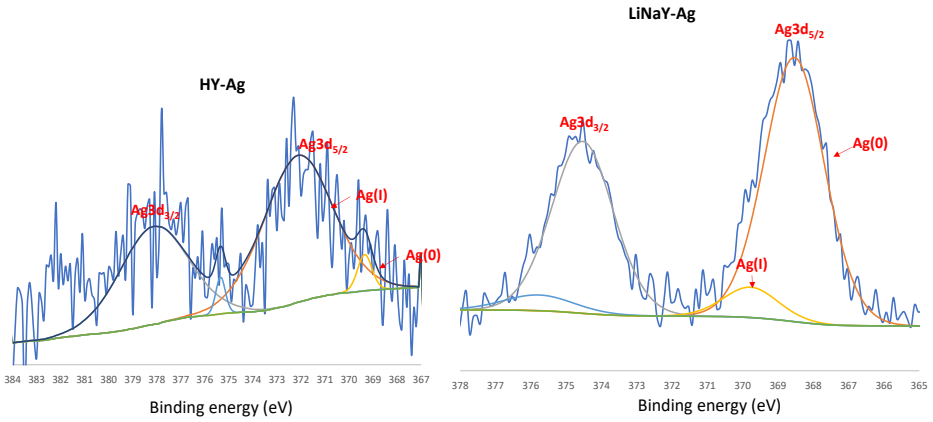

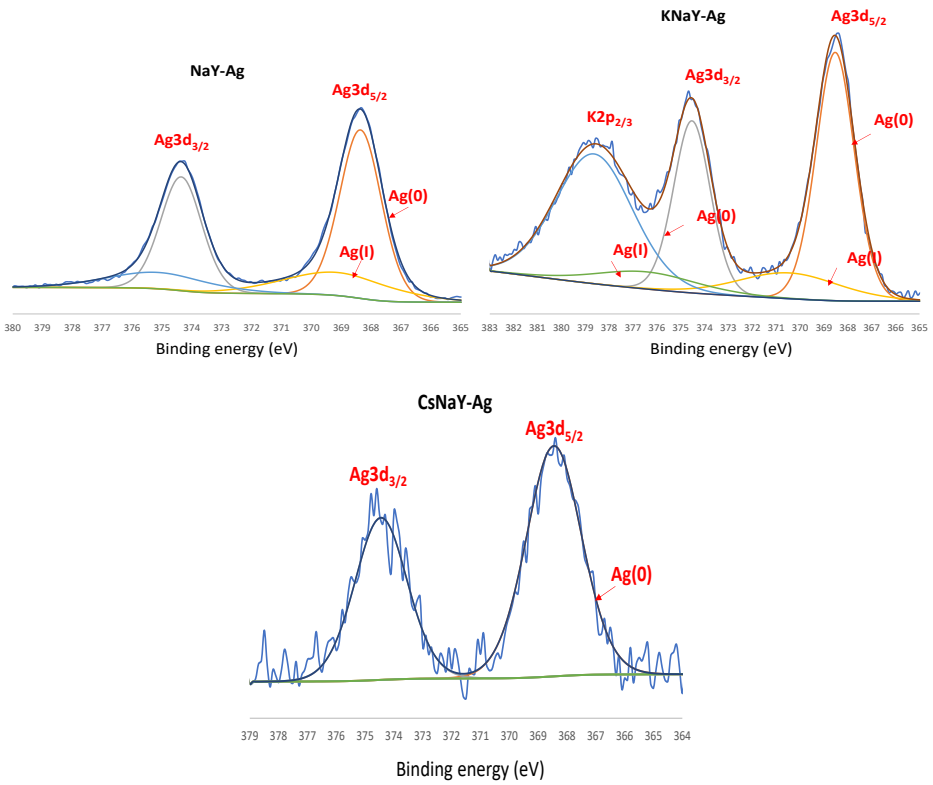

Figure 4.10 Deconvoluted X-ray photoelectron spectra (XPS) for $Ag3d_{5/2}$ for the different cation-exchanged Ag-zeolites, indicating the amount of cationic Ag (Ag^{+}) and reduced Ag (Ag^{0}).

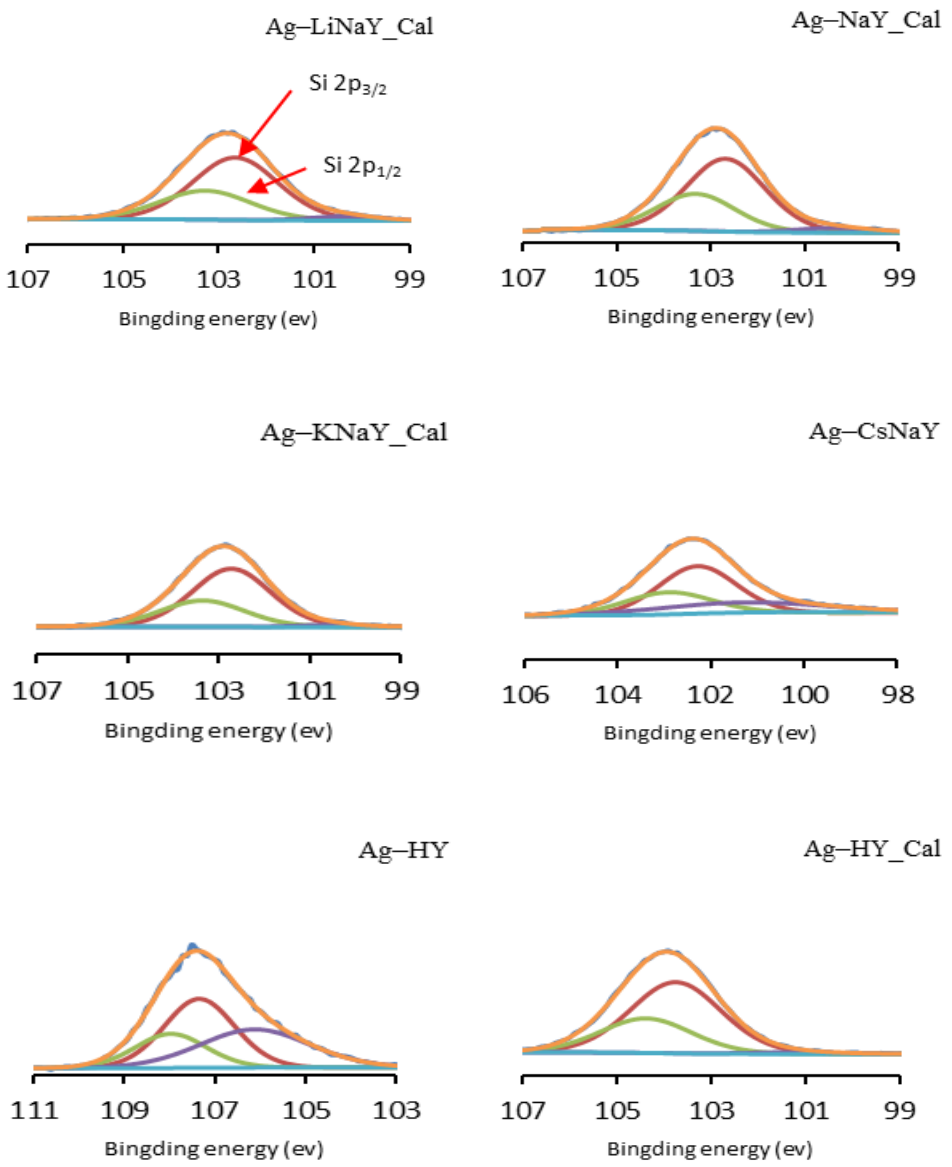

Figure 4.11 Deconvoluted X-ray photoelectron spectra (XPS) for $Si2p_{3/2}$ or $Si2p_{1/2}$ in the different Ag-zeolites.

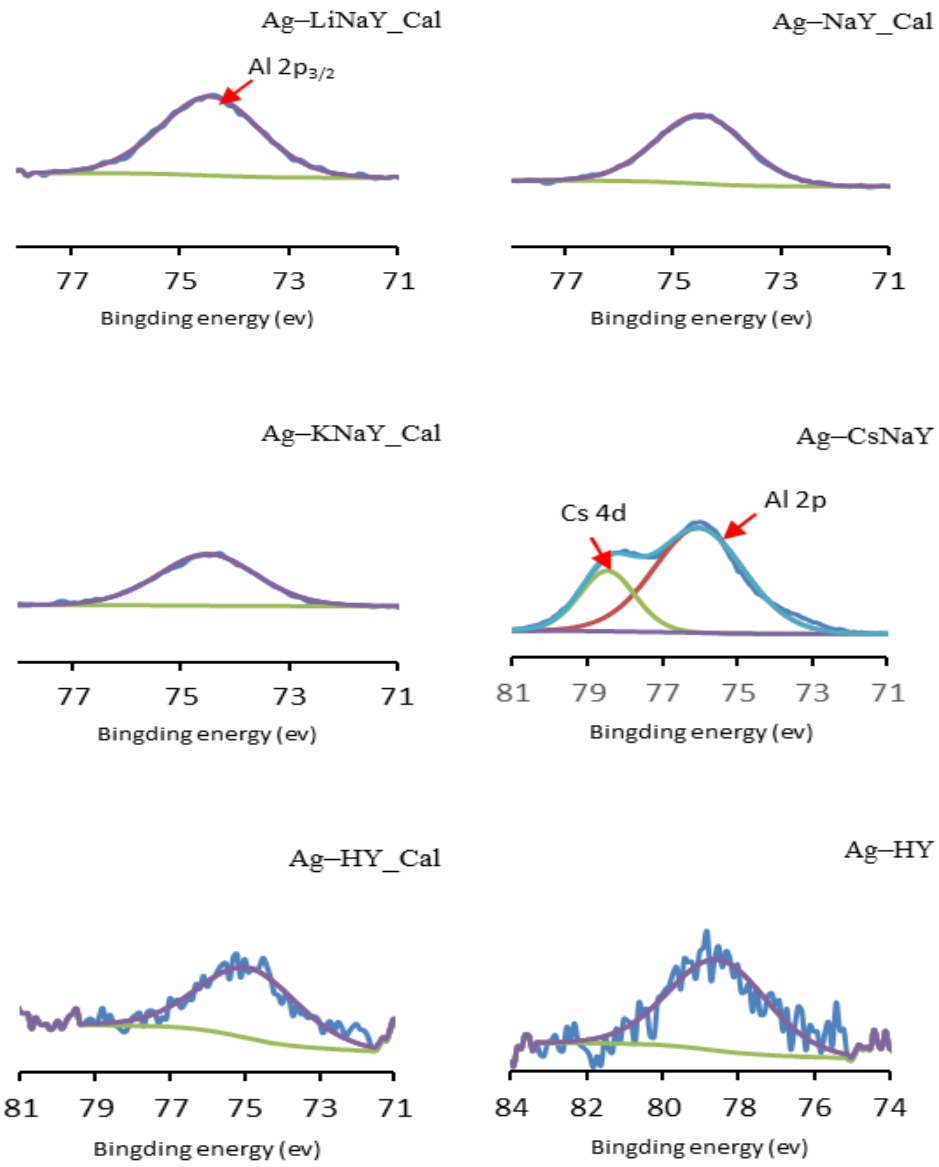

Figure 4.12 X-ray photoelectron spectra (XPS) for $Al2p_{3/2}$ in the different Ag-zeolites.

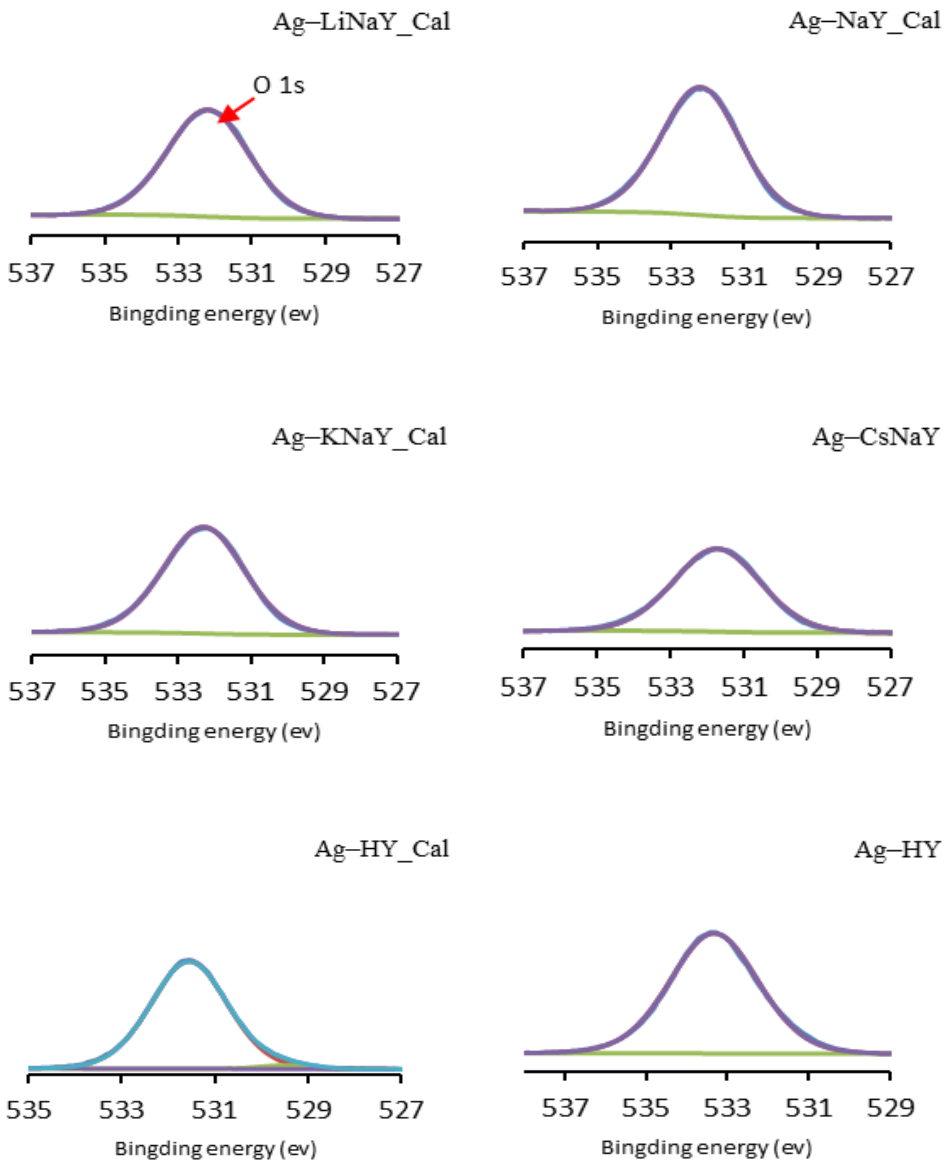

Figure 4.13 X-ray photoelectron spectra (XPS) for O1s in the different Ag-zeolites.

4.2.2.9 *Diffuse reflectance infrared Fourier transform spectroscopy (DRIFTS) with carbon monoxide (CO)*

To further investigate the oxidation and aggregation state of cationic Ag^+ in Ag-HY, the DRIFTS technique with carbon monoxide (CO) as a probe, was employed. At low temperatures, the DRIFTS-CO analysis shown in **Figure 4.14** revealed significant bands at 2180 cm^{-1}, associated with linearly coordinated $Ag^+(CO)$, and bands at 2192 cm^{-1} corresponding to $Ag^+(CO)_2$. [270, 300] Additionally, an expected band at 2158 cm^{-1} emerged due to the interaction between CO and the strong protons of the HY zeolite. [303] Minor bands were also detected at lower wavenumbers (e.g., 2133 cm^{-1}). Overall, the predominant observation was cationic Ag species in the Ag-HY sample. [270, 301, 304]

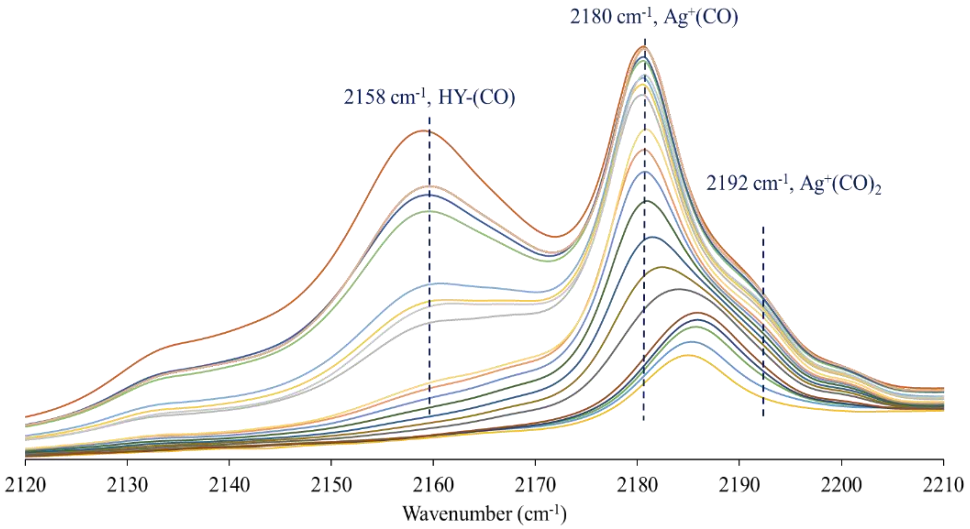

Figure 4.14 Diffuse reflectance infrared Fourier trans-form spectroscopy (DRIFTS) of Ag-HYcal with carbon monoxide as a probe.

4.2.2.10 *Synchrotron Experiments*

X-ray Absorption Spectroscopy (XAS) experiments included two key components: X-ray absorption Near Edge Structure (XANES) provides insight into the oxidation state of Ag, while extended X-ray Absorption Fine Structure (EXAFS) reveals information about coordination and bonding. By analyzing Ag species using XAS, we show valuable data on the electronic structure and chemical environment of Ag^+ in Ag-HY. The XANES and EXAFS spectra, as depicted in **Figure 4.15**, validate that the Ag-HY zeolite predominantly contains cationic Ag. The spectral lines for both calcined and non-calcined zeolites exhibit similarity to Ag_2O rather than to Ag foil. Additionally, the EXAFS spectra provide evidence for the simultaneous presence of individual Ag cations and tiny Ag oxide clusters within Ag-HYcal. The prominent peaks in the material correspond to distances of approximately 1.8 Å (Ag−O bonds) and 2.5 Å (Ag−Ag bonds) [305].

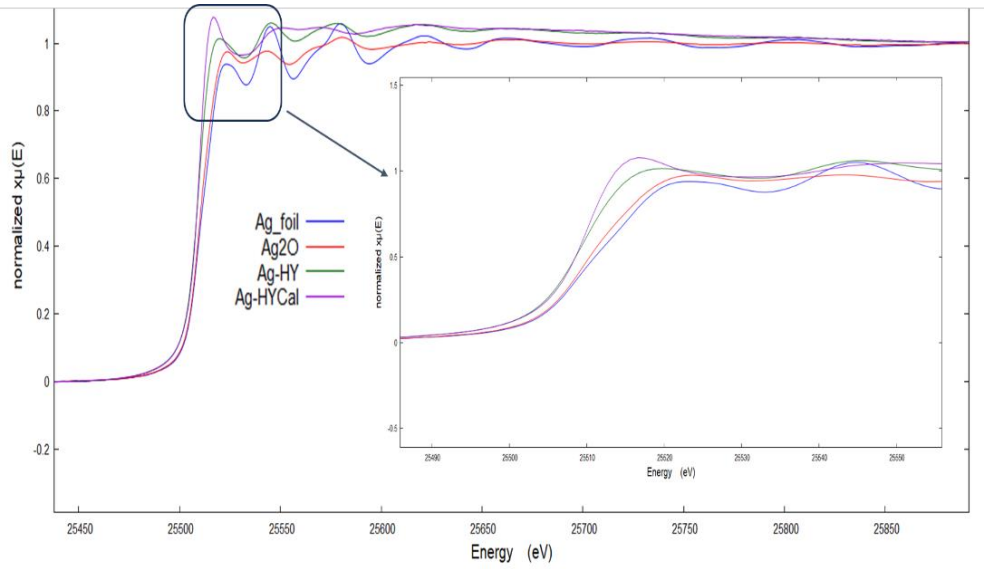

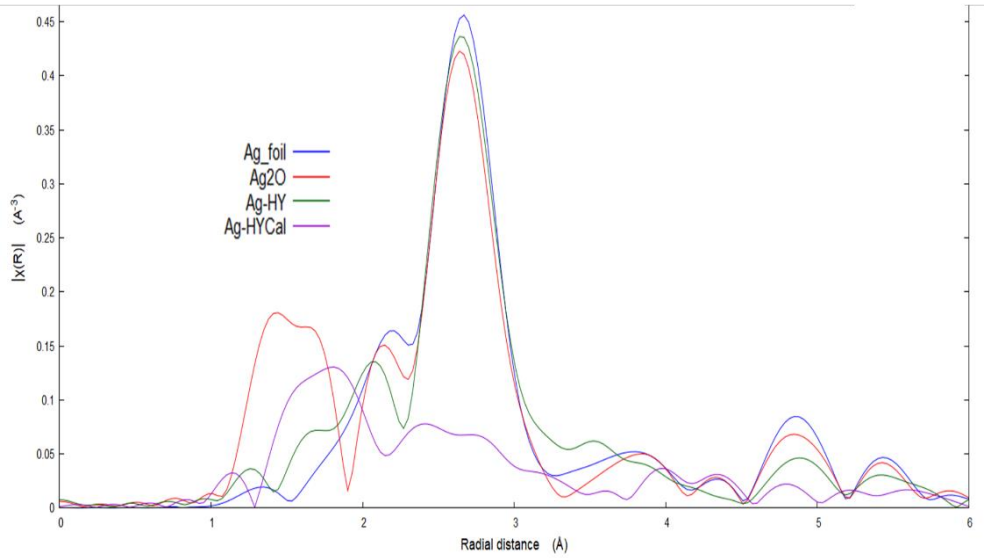

Figure 4.15 X-ray absorption near edge structure (XANES) and extended X-ray absorption fine structure (EXAFS) spectra of Ag-HY (purple line), compared with the uncalcined sample (green line) and Ag foil and Ag_2O as standards (blue and red lines, respectively).

4.2.2.11 *High Resolution Transmission Electron Microscopy (HAADF-STEM)*

We conducted aberration-corrected high-angle annular dark-field scanning transmission electron microscopy (AC HAADF-STEM) measurements on the Ag-LiNaYcal sample. The resulting images, displayed in **Figure 4.16**, reveal valuable insights when mapping the different element. In **Figure 4.17**, there is the energy-dispersive X-ray spectroscopy (EDX) mapping of a zeolite crystallite, confirming the homogeneous distribution of all elements, including silver (Ag), Additionally, it also shows a minor degree of aggregation in the form of nanoparticles (NPs), in agreement with the PXRD analysis presented above (see section **4.2.2.3**). Furthermore, elemental EDX quantification aligns well with the ICP-AES results. These combined techniques

provide a comprehensive understanding of the elemental composition and distribution within the Ag-LiNaYcal sample.

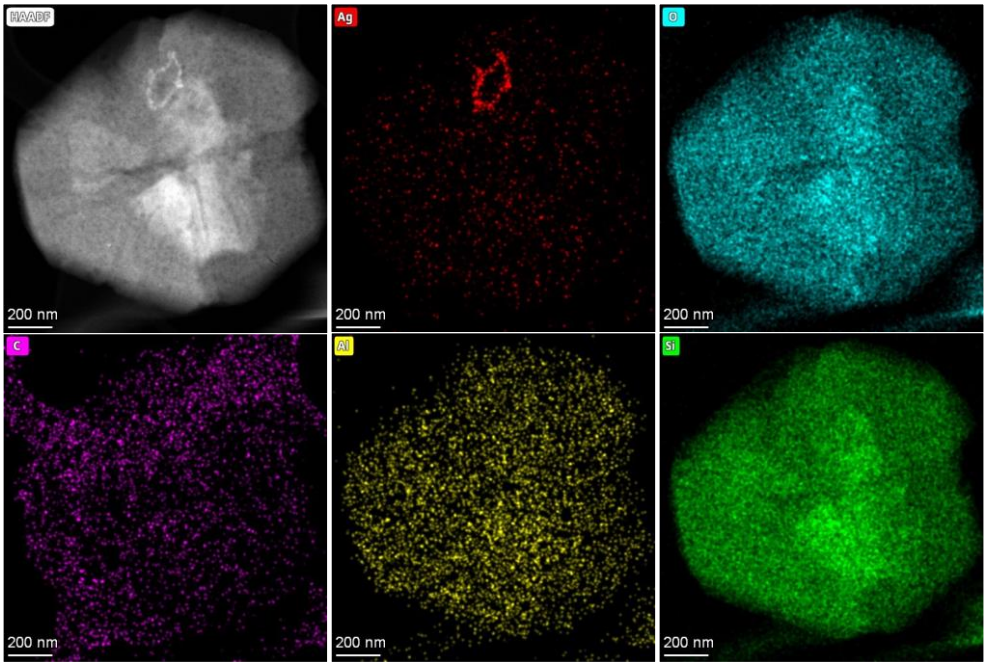

Figure 4.16 Compositional mapping of a representative AC HAADF-STEM image of a Ag-LiNaYcal crystallite, using the EDX spectroscopy to detect the different elements.

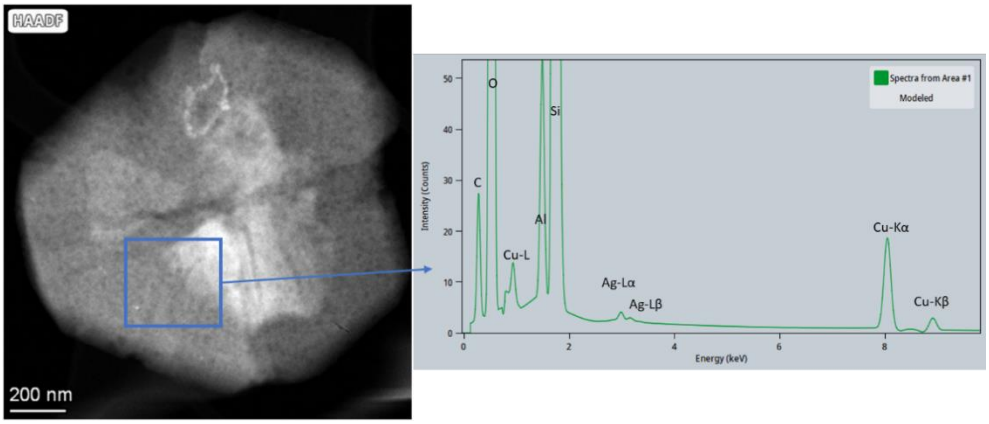

Figure 4.17 High-angle annular dark-field scanning transmission electron microscopy (HAADF-STEM) image of a Ag-LiNaYcal crystallite (left) and the corresponding energy-dispersive X-ray spectroscopy (EDX) elemental analysis from the squared area, including quantification results. Cu signals corresponds to the Cu-carbon grid employed.

Figure 4.18 presents aberration-corrected scanning transmission electron microscopy (AC-STEM) images of the Ag-LiNaYcal sample magnified 2 million times. The integrated differential phase contrast (iDPC) image shows low-Z elements with bright contrast against a dark background. On the other hand, the colored HAADF-STEM image identifies Ag species as the brightest contrasts in these images, because the image is proportional, in good approximation, to the squared atomic number (Z^2).

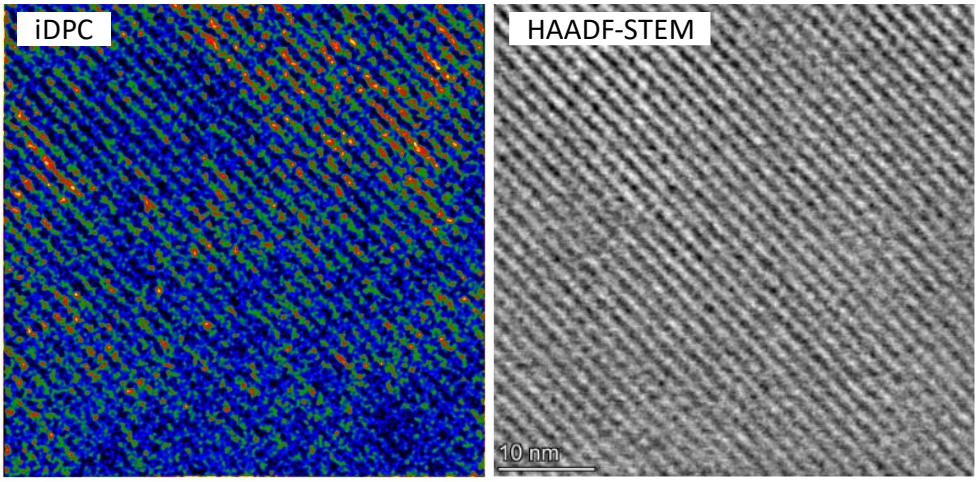

Figure 4.18 High resolution AC HAADF-STEM (left) and iDPC (right) images of an Ag-LiNaYcal sample. The identification of Ag entities is performed on the HAADF image due to the higher contrast and by means of iDPC images, to reveal the atomic structure of the zeolite LiNaYcal (see also **Figure 4.19**). The identification and location of the subnanometric (<1 nm) Ag entities within the zeolite framework is obtained by combining the images obtained in these two modes.

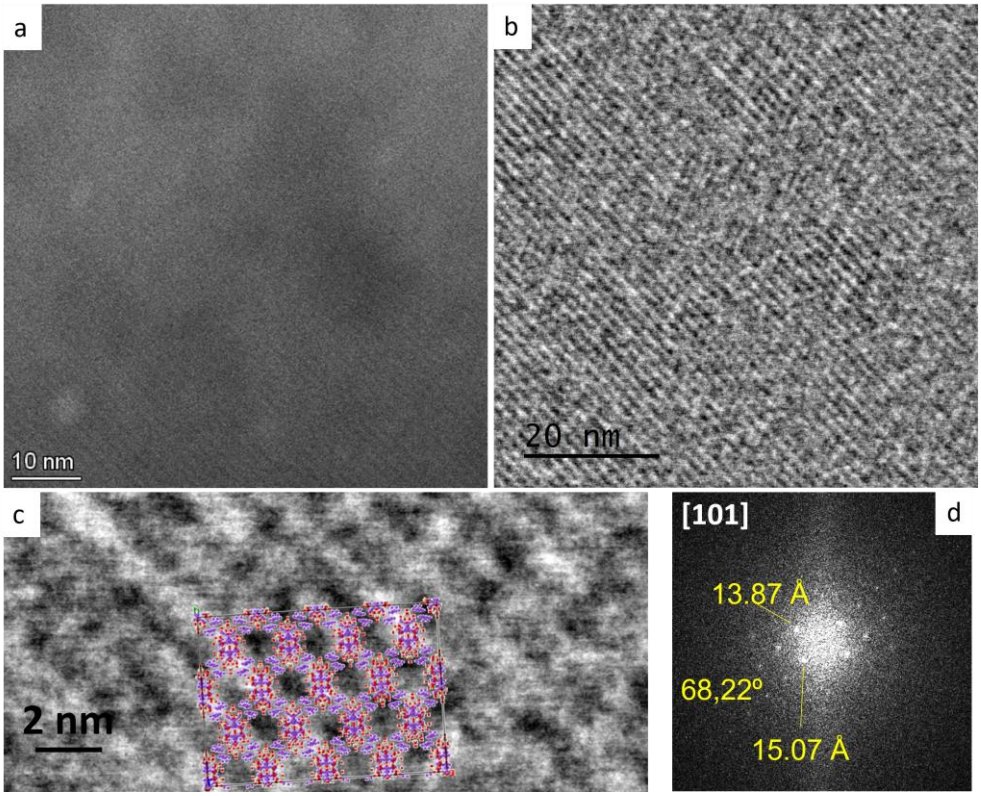

Figure 4.19 (a) Aberration corrected high-angle annular dark-field scanning transmission electron microscopy (AC HAADF-STEM) image of a Ag-LiNaYcal crystallite and (b) the corresponding integrated differential phase contrast (iDPC) image. The visualization of the Ag species is clearly shown by the HAADF mode thanks to contrast, which is roughly proportional to the square atomic number Z^2, whereas for the iDPC mode, the resulting contrast is roughly proportional to the atomic number Z, which drastically improves the detectability of light elements among heavy elements. (c) Detailed visualization of the crystallographic structure of the LiNaYcal zeolite, with modelled crystal structure superimposed, viewed along the [101] zone axis. (d) FFT obtained.

Additionally, as shown in **Figure 4.20**, the visualization of the Ag entities has been enhanced by subjecting raw HAADF images to advanced image processing, which involved denoising and background subtraction. To determine the size of the Ag clusters observed in the experimental images in a fully automated, user-independent, and statistically meaningful manner, a segmentation based on K-means clustering techniques was applied to the HAADF-STEM images. [295, 306] This approach provides valuable insights into the spatial distribution and characteristics of Ag within the sample. **Figure 4.21** shows the application of the K-means clustering method, revealing the predominant presence of Ag single atoms and ultrasmall clusters, with a minor presence of Ag NPs Modeling and image simulations are shown in **Figures 4.22** and **Figures 4.23**, which validate these findings. Collectively, these results provide strong evidence that the majority of Ag species within the zeolite correspond to Ag single atoms and ultrasmall Ag clusters, aligning well with the DR-UV-vis, DRIFTS, and XAS results previously observed for the Ag-HY zeolite.

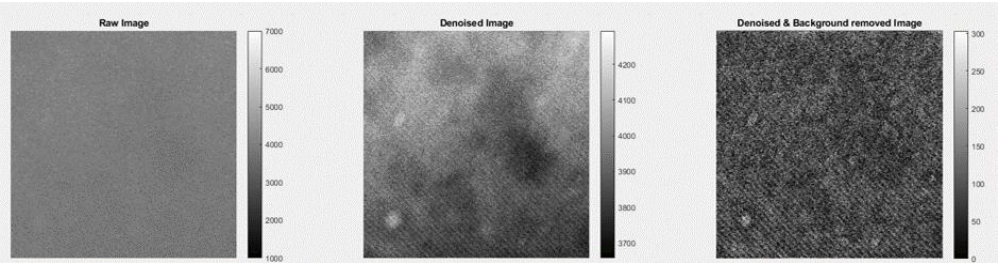

Figure 4.20 AC HAADF-STEM image of the Ag-LiNaYcal sample acquired at 1.4 million magnifications (left) and the corresponding images after de-noising (center) using undecimated wavelet transforms (UWT) and background subtraction (right).

The K-means clustering method has been applied to experimental images, revealing the predominant presence of Ag single atoms and ultrasmall clusters, minor Ag nanoparticles (NPs) (as depicted in **Figure 4.21**). Modeling and image simulations (refer to **Figures 4.22** and **Figures 4.23**) validate these findings. Collectively, these results provide strong evidence that the majority of Ag species within the zeolite correspond to Ag single atoms and ultrasmall Ag clusters.

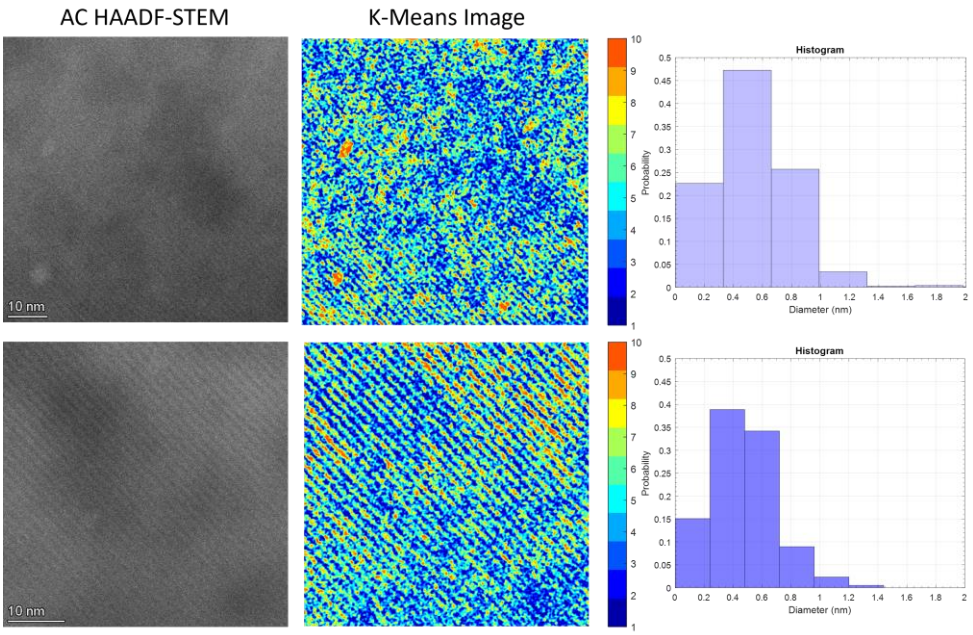

Figure 4.21 (Left row) Experimental AC HAADF-STEM images of Ag-LiNaYcal sample. (Middle row) K-Means clustering analysis of the experimental images after denoising and background subtraction. The K-means clusters analysis of the experimental images, shown that the pixels corresponding to clusters from 8 to 10 atoms can appropriately account for the projected size of the Ag clusters. The segmentation of the clustered images using this threshold allowed to estimate the Ag clusters size as the diameter of the circle whose area equals that of the segmented particle (equivalent circle diameter). Please, note that the word cluster in images refers to the image clustering analysis and not to Ag clusters. (Right row) The size distribution histograms, indicate that the majority of these Ag clusters fall in the size range 0.2-0.6 nm, in good agreement with the expected values for isolated atoms and ultrasmall Ag clusters. The remaining part of the distribution, with size in the range 0.7-2 nm, should correspond either to Ag clusters with a larger number of atoms or, instead, to the superposition of neighboring Ag clusters in the same area.

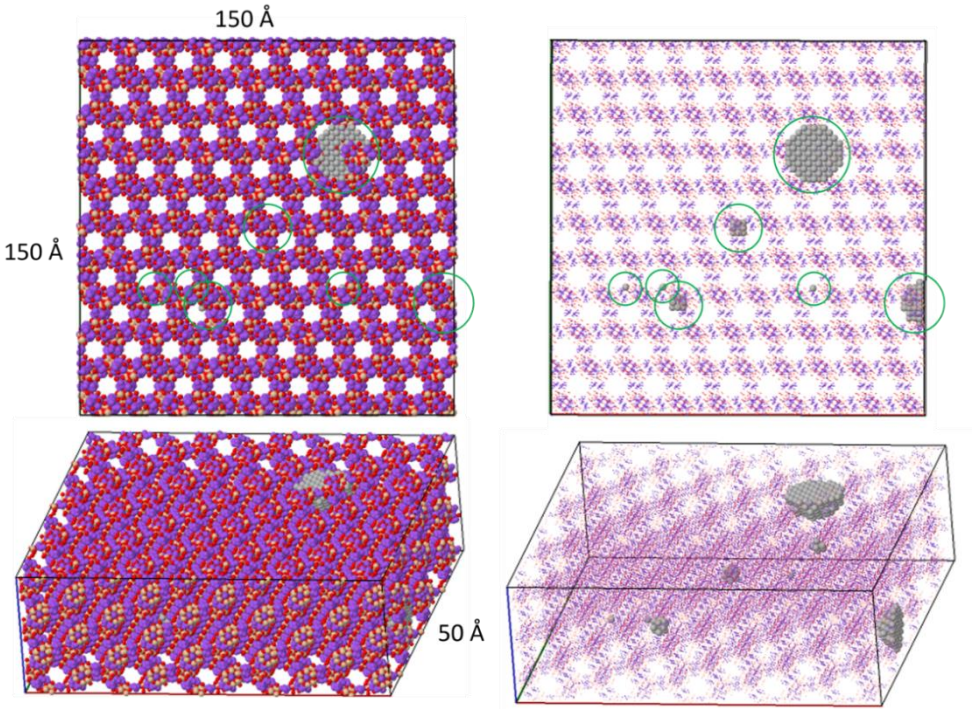

Figure 4.22 150Å × 150Å × 50Å supercell in [101] zone axis including Ag species ranging from single atom to nanometric clusters. By adjusting the orientation of the model, we were able to simulate the images obtained from the experimental studies. Just for a better visualization purpose of the Ag species in this figure, the sizes of the atoms in the right zeolite models were reduced.

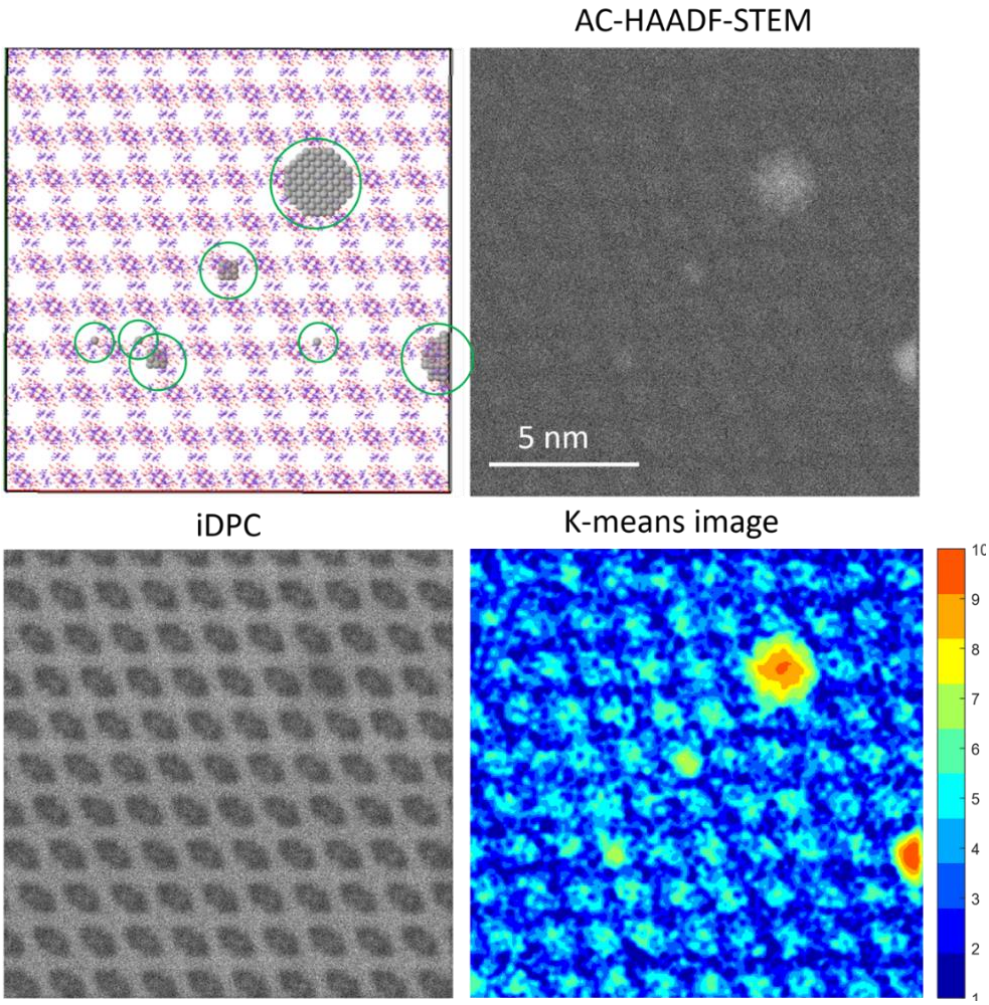

Figure 4.23 Image simulation details of different types of Ag single atom, Ag clusters and Ag nanoparticles in the Ag-HY zeolite along [101] direction. To approach as close as possible to the experimental imaging conditions, a mixture of Poisson and white Gaussian noise was added to the simulated images. Top row: Structural model implementing Ag species and simulated High Resolution HAADF-STEM simulated image after the addition of Poisson and white Gaussian noise. Bottom row: Simulated iDPC image illustrating the only light elements are detected using this technique (i.e. light elements). HR HAADF-STEM image. UWT de-noised image, background subtracted and de-noised image, followed by K-means

clustering analysis. For Ag single atoms, the intensity is very low barely distinguished from the zeolite structure; for Ag small cluster, the intensity is a little bit higher, in some cases even down to the contrast level of the zeolite framework; in the case of Ag nanoparticles, the contrast provided is slightly higher than the zeolite framework, a situation that mimic the situation observed in the experimental images.

4.3 *Carbene insertion reactions into C-C, C-H, and O-H bonds.*

Here, we show that the resulting zeolites catalyze carbene-mediated reactions in organic synthesis, such as the Buchner reaction and C-H insertion in methylene and hydroxyl bonds. [307, 308] The Ag-zeolites enable C-H and C-O bond reactions without pre-functionalized substrates or leaving groups (such as halides, …) and the counter cation of the zeolite determines the catalytic activity and selectivity. These carbene-mediated reactions are uncommonly catalyzed by a solid support, and some of them are here catalyzed by Ag for the first time. [309]

4.3.1 *Catalytic activity of Ag-HY and Ag-(Li to Cs)NaY zeolites.*

Ag-HY and Ag-HYcal zeolites were investigated as catalysts for the Buchner reaction, which is a significant synthetic method for constructing medium-sized ring-containing organic molecules, particularly seven-membered rings. [310, 311] In this reaction, a carbene is directly inserted into the aromatic C−H bond, followed by a C−C bond rearrangement. The product of this transformation is the formation of cycloheptatrienes, which are otherwise challenging to obtain. [312, 313]

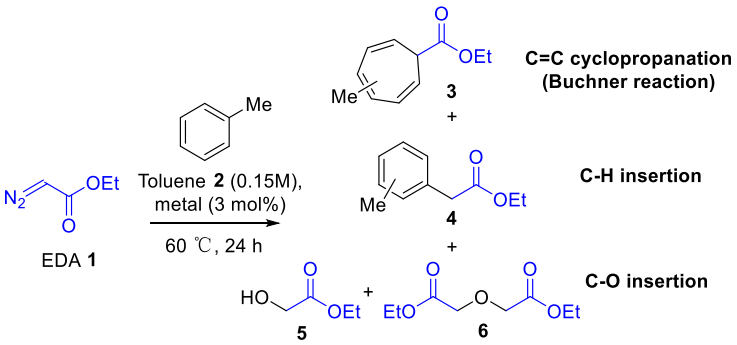

Figure 4.24 Buchner reaction catalyzed by silver supported zeolite catalysts.

Entry	Catalyst	Product yield (%)		
		3	4	5+6
1	-	3	-	-
2	$AgNO_3$	20	60	-
3[a]	$Rh_2(OAc)_4$	42	20	-
4	**Ag-HY**	**5**	**14**	**77+4**
5	Ag-HYcal	5	31	50+12
6	Ag-HYcal and dried	6	31	50+11
7	Ag-HYcal (reused)	25	33	-+42
8	**Ag-HYcal (6th reuse)**	**47**	**38**	**-+14**
9	Ag-Al_2O_3 (5 wt% Ag)	23	16	-
10	Ag-hydrotalcite (5 wt% Ag)	-	5	-
11	Ag-LiNaYcal	30	20	46+-
12	**Ag-LiNaYcal and dried**	**55**	**42**	**-**
13	Ag-NaYcal	14	8	48+-
14	**Ag-NaYcal and dried**	**60**	**37**	**-**
15	Ag-KNaYcal	15	5	50+-
16	Ag-KNaYcal and dried	43	25	-
17	Ag-CsNaY	4	2	43+-

Table 4.2 Results for the reaction of ethyldiazoacetate (EDA) **1** in toluene solvent (0.15M) with different catalysts (3 mol%) under the indicated reaction conditions. [a] A 35% yield for dimers diethyl fumarate and diethyl maleate was obtained.

Table 4.2 presents the catalytic performance of the reaction between ethyl diazoacetate (EDA) **1** and toluene **2** as a solvent at 60 °C. In the case of this aromatic substrate, the carbene can alternatively insert into the methyl C-H bond, resulting in the corresponding benzyl ester. In this table, we can see that without a catalyst the reaction does not proceed (entry 1) and when soluble $AgNO_3$ is used an 80% yield of the products is obtained (entry 2), primarily through C-H insertion. The $Rh_2(OAc)_4$ catalyst, commonly used in the Buchner reaction, yields 42% of the Buchner product **3** and 20% of the C-H insertion product **4**, along with 35% dimers (entry 3). Under the current reaction conditions, $AgNO_3$ appears to be more active and more selective than $Rh_2(OAc)_4$. Considering this, we thought that Ag-HY could also be an active catalyst for the carbene-mediated reaction. It should be noted that products **3** and **4** are formed after the release of N_2 and carbene formation. However, while product **3** is the result of the cyclopropanation reaction between the triplet carbene of compound **1** and the C-C double bonds of **2** (known as the Buchner reaction), product **4** is formed through the insertion of the singlet carbene of compound **1** into the C-H methyl bond of **2**. In other words, these two reactions have different activation mechanisms for compound **1**, which are primarily influenced by the electronic properties (and possibly also the steric factors) of the catalytic metal site.

When using non-calcined Ag-HY zeolite, we observed complete conversion of compound **1**, but the major products obtained were **5** and **6**. These products are likely formed through the insertion of the carbene into the O-H bond of water present in the zeolite, as shown in entry 4 and only a small yield of C-H coupled product (19%) was obtained. However, Ag-HYcal zeolite exhibited a significant increase in the formation of C-C bond-forming coupled products **3** (5%) and **4** (31%), but the main product still originated from water insertion (62%), as observed in entry 5. This suggests that the water molecules are more strongly adsorbed in the Ag-exchanged HY zeolite are participating as reactants during the carbene reaction.

In view of these results, we conducted reactions using 1 or 10 equivalents of externally added water, as shown in **Figure 4.25 and Figure 4.26.** With these tests,

we observed that the reaction proceeded with complete conversion of **1**, but the product selectivity remained largely unchanged, indicating that the external water did not participate in the observed O-H insertion. Moreover, the *in-situ* drying of the zeolite by applying vacuum at 250 °C before the reaction did not result in an improved yield of **3** + **4** (entry 6). Although the Ag-HYcal zeolite had mostly lost the physisorbed water molecules, it still retained strongly chemisorbed water according to the corresponding thermogravimetric analysis, as shown in section **4.2.2.2**. This is why it could be possible that during reuse of the zeolite, most of the O-H insertion products are eliminated due to the previous reaction consuming the chemisorbed water. As a result, any externally added water by the reagents would only have a minimal influence on the reaction. In other words, the reaction of the zeolite with **1** served as a method to thoroughly remove any adsorbed water molecules and dry the zeolite framework.

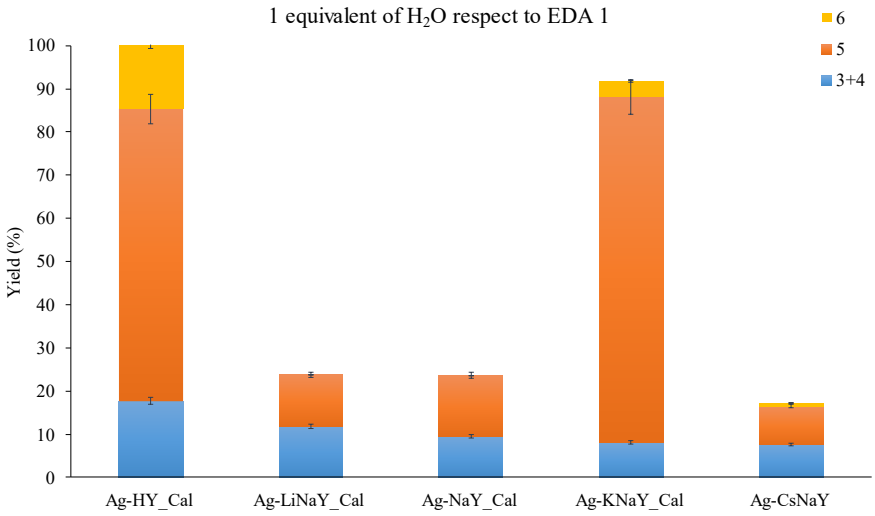

Figure 4.25 Catalytic results for the reaction of ethyldiazoacetate (EDA) **1** in toluene solvent (0.15M) with **1** of added water and different Ag-zeolite catalysts (3 mol% Ag), at 60 ºC for 24 h. Complete conversion of **1**. Error bars account for a 5% uncertainty.

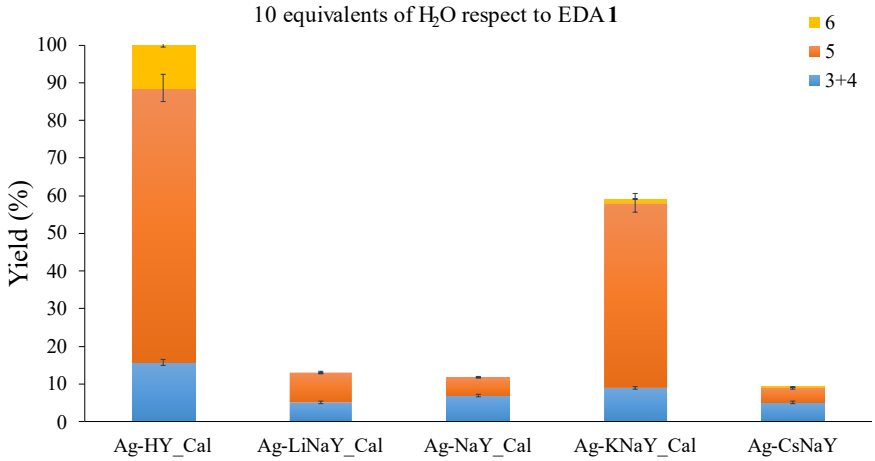

Figure 4.26 Catalytic results for the reaction of ethyldiazoacetate (EDA) **1** in toluene solvent (0.15M) with 10 equivalents of added water and different Ag-zeolite catalysts (3 mol% Ag), at 60 ºC for 24 h. Complete conversion of **1**. Error bars account for a 5% uncertainty.

In order to check the reused catalytic performance of the Ag-zeolite catalysts, Ag-HYcal was reused up to ten times. The data presented in **Figure 4.27** demonstrates that the Ag-HYcal zeolite catalyst maintains its catalytic activity (>90% conversion) Additionally, it exhibits improved selectivity towards the formation of C-C bond products **3** and **4**, with a yield of over 80% in uses 5-7, which is also observed in entries 7 and 8 of **Table 4.1**. The O-H insertion products start to reappear after the eighth use, which could be attributed to the accumulation of water within the zeolite during repeated cycles. Notably, removing chemisorbed water at 400 °C under vacuum overnight caused the zeolite's color to rapidly change to brown and, when used as a catalyst, the conversion rate was significantly lower. The only products detected were those originating from water (products **5** and **6**), suggesting that some residual water remains. In other words, attempts to thermally remove the chemisorbed water from Ag zeolite resulted in severe decomposition of the catalytically active Ag species. It is worth mentioning that the typical dimerization products observed for compound **1**, such as diethyl fumarate and diethyl maleate, were not present. This

absence is likely due to the isolated supported Ag sites preventing the encounter of two carbene fragments, an additional advantage of the supported catalyst compared to the $Rh_2(OAc)_4$ catalyst [314] which produces significant amounts of these dimers (entry 3).

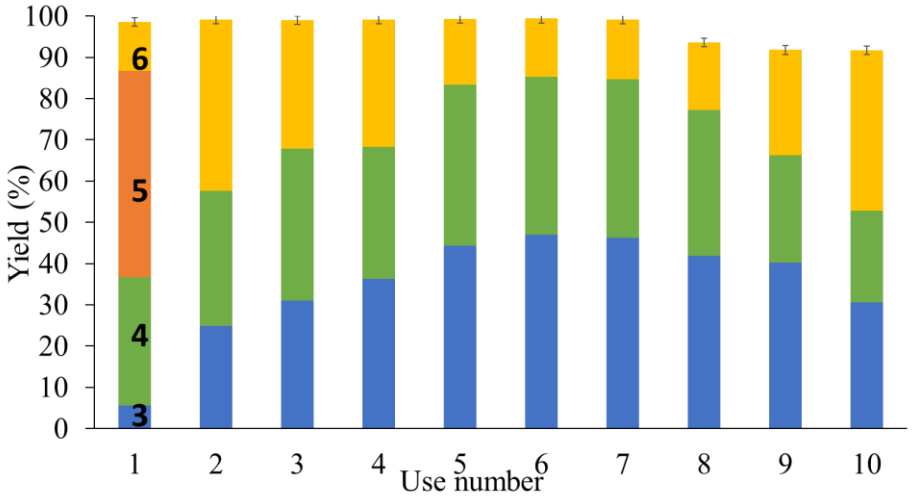

Figure 4.27 Reuses of Ag-HYcal as a catalyst (3 mol% Ag) for the reaction of ethyldiazoacetate (EDA) **1** in toluene solvent (0.15M), at 60 °C for 24 h. Error bars account for a 5% un-certainty.

Supported Ag nanoparticles (NPs) were also tested as catalysts for the reaction. In this study, Ag NPs were prepared on alumina (Al_2O_3) and hydrotalcite (5 wt % Ag), with an average NP size of approximately 2 nm, based on the high-resolution transmission electron microscopy (HR-TEM) images shown in **Figure 4.28**. The entries 9 and 10 of Table 4.2 show that these Ag-supported species, regardless of the support, exhibited minimal activity for the reaction. It is plausible that subnanometric Ag species coexist with the ultrasmall Ag NPs on the Ag-Al_2O_3 and Ag-hydrotalcite solids. However, these subnanometric species do not show catalytic activity, possibly due to their reduced oxidation state (Ag^0) or the absence of confinement effects. Based on this evidence, we can confidently conclude that the ultrasmall cationic Ag species

present in the HY zeolite are responsible for the observed catalytic activity during the reaction.

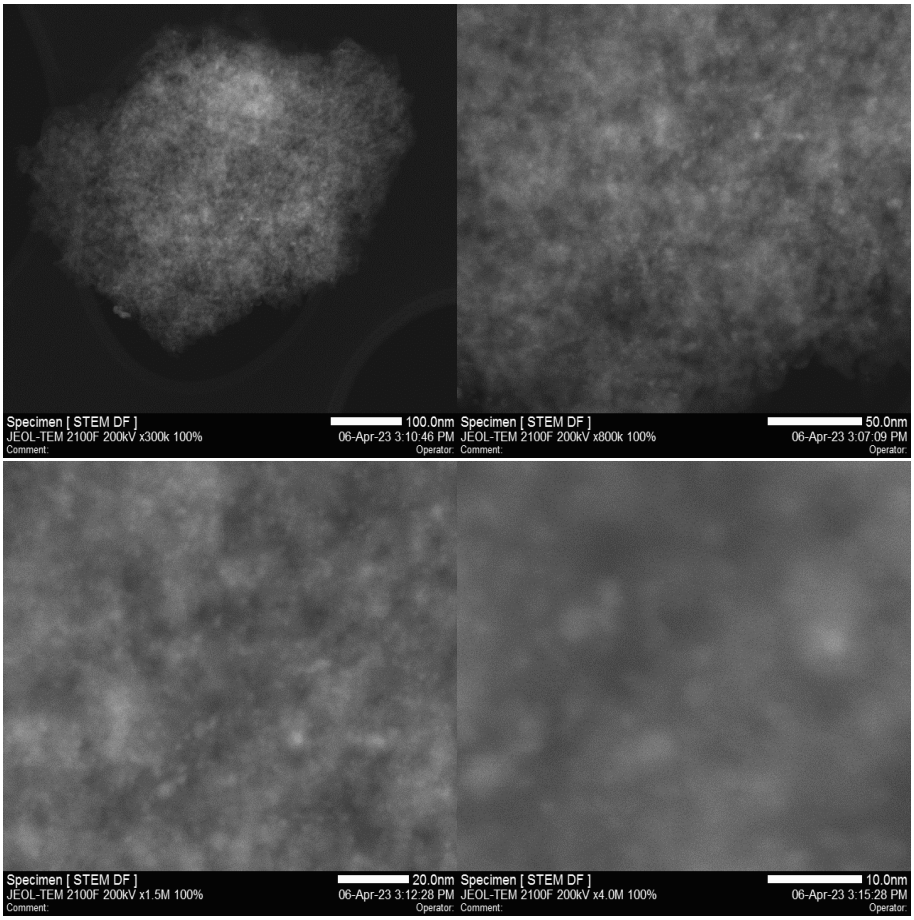

Figure 4.28 High resolution transmission electron microscopy (HR-TEM) images of Ag-Al_2O_3 at increasing magnifications. The average nanoparticle size is ~2 nm

The synthesized Ag-(Li to Cs)NaY zeolites were also tested to carry out the reaction between EDA **1** and toluene **2**. **Table 4.2** reveals that the calcined cation-exchanged zeolite samples exhibit similar behavior to Ag-HYcal, comparing entries 5, 11, 13, and 15. Moreover, the corresponding kinetic results, shown in **Figure 4.29**, confirm that the Ag-HYcal catalyst is the most active among them under these reaction conditions.

However, if the Ag-zeolite catalysts are dried *in-situ* before adding the reactants, the O-H insertion products **5** and **6** disappear, and only the C-C coupling products **3** and **4** are formed, with yields of up to 97% with Ag-LiNaYCal and Ag-NaYCal, as shown in entries 12 and 14, respectively. On the contrary, Ag-CsNaY, which contains the highest amount of Ag^0 species and cannot be dried at temperatures exceeding 100 °C prior to the reaction, yields poor catalytic results as seen in entry 17 of **Table 4.1** as well as in **Figure 4.29**.

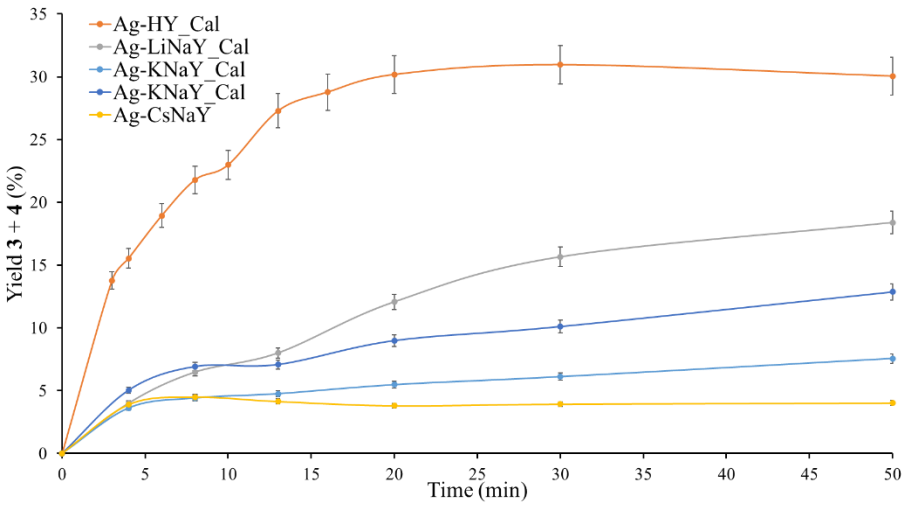

Figure 4.29 Kinetic plot for the first 50 min reaction time of the reaction of ethyldiazoacetate (EDA) **1** in toluene solvent (0.15M) at 60 ºC with different Ag-zeolite catalysts. The formation rate of the O-H insertion products **5** and **6** is omitted for clarity. Error bars account for a 5% uncertainty.

The higher catalytic activity of the alkaline-exchanged zeolites compared to Ag-HY in forming C-C bonds (products **3** and **4**) may be due to a higher intrinsic selectivity of the Ag catalytic site for C-C and C-H bond activation or timely to the absence of water in the zeolite after drying. However, the FT-IR spectra of the calcined solids reveal similar water adsorption across all zeolites, as previously shown in **Figure 4.7**.

4.4 *Carbene insertion studies in O-H and C-H bonds*

To investigate whether Ag-(Li to K)NaYcal zeolites are less catalytically active than Ag-HYcal in the carbene insertion into O-H bonds, we conducted the reaction of EDA **1** in a water/ethanol mixture. Ethanol was added to water to assess the reactivity of an external O-H bond does not present within the zeolite.

The results in **Figure 4.30** show that the Ag-HYcal catalyst yields three times more of the O-H insertion products (**5** + **24**) compared to the alkaline zeolites, with product **24** being the majority. Consequently, we can said that the Ag-(Li to K)NaYcal zeolites exhibit better catalytic activity toward the formation of products **3** and **4** due to their better intrinsic selectivity for the activation of C-C and C-H bonds. In contrast, Ag-HYcal prefers to activate and insert the carbene into O-H bonds. Other alcohols such as 2-chloroethanol (98% yield), phenylethanol (98% yield), allyl alcohol (97% yield), and propargyl alcohol (95% yield) also perform exceptionally well in the Ag-HYcal-catalyzed reaction. This is why we can say that the counter cation and not the water content, influences the activity and selectivity of the carbene insertion reaction. While Ag-HY directs the insertion toward O-H bonds in the presence of O-containing nucleophiles (such as water and alcohols), and equally toward C-C and C-H bonds when water is absent in the reaction media alkaline earth cations divert the insertion towards the C-C and C-H bonds, approximately in a 1:2 ratio. These selectivity results make sense from the fact that O-H bonds are much more polar than C-C or C-H bonds. Therefore, the greater the electron deficiency in the Ag catalytic site (indicating a stronger Lewis acid character), the better the activation of O-H vs C-C or C-H bonds.

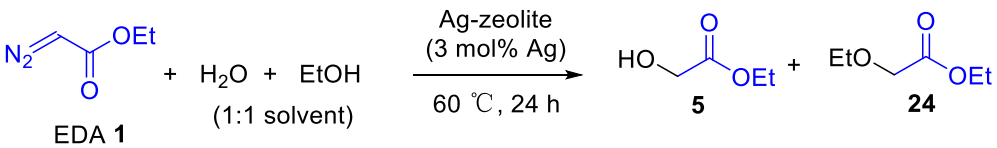

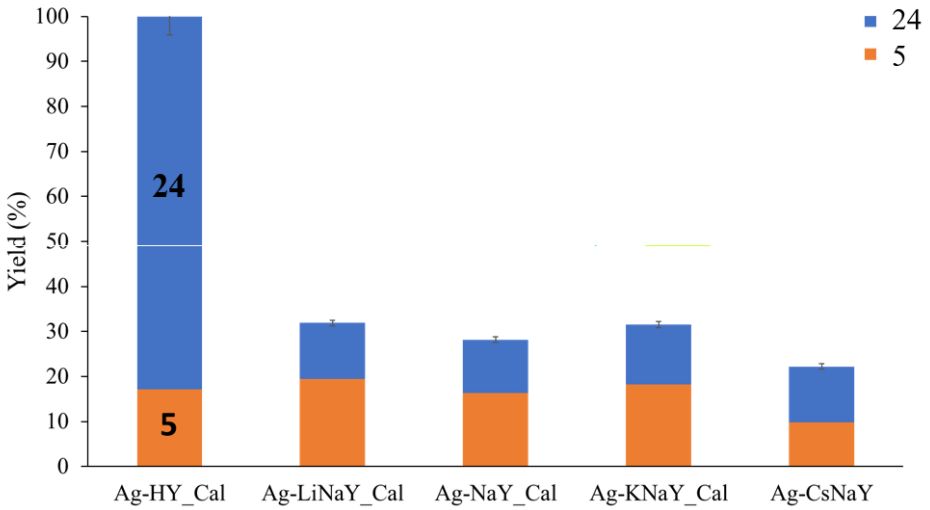

Figure 4.30 Catalytic results for the reaction of ethyldiazoace-tate (EDA) **1** in a 1:1 v:v mixture of water:ethanol (0.15M) with different Ag-zeolites as catalysts (3 mol% Ag), at 60 °C for 24 h. Zeolites were dried at 250 °C under vacuum over-night, except for Ag-CsNaY. Error bars account for a 5% uncertainty.

The catalytic activity of Ag-(Li to Cs)NaYcal zeolites in C-H insertion reactions paves the way for more transformations, including the insertion of EDA **1** into alkanes. **Figure 4.31** reveals that cyclohexane efficiently incorporates the carbene from **1** with a yield exceeding 95%, exhibiting complete selectivity toward product **24** on both the Ag-LiNaYcal and Ag-NaYcal catalysts.

The data shown that the Ag-HYcal promote more O-H insertion catalytic activity compared to the alkaline zeolites. In contrast, Ag-(Li to K)NaYcal zeolites exhibit enhanced catalytic activity in the formation of products **3** and **4** due to their intrinsic selectivity for C-C and C-H bond activation. Ag-HYcal prefers to activate and insert the carbene into O-H bonds.

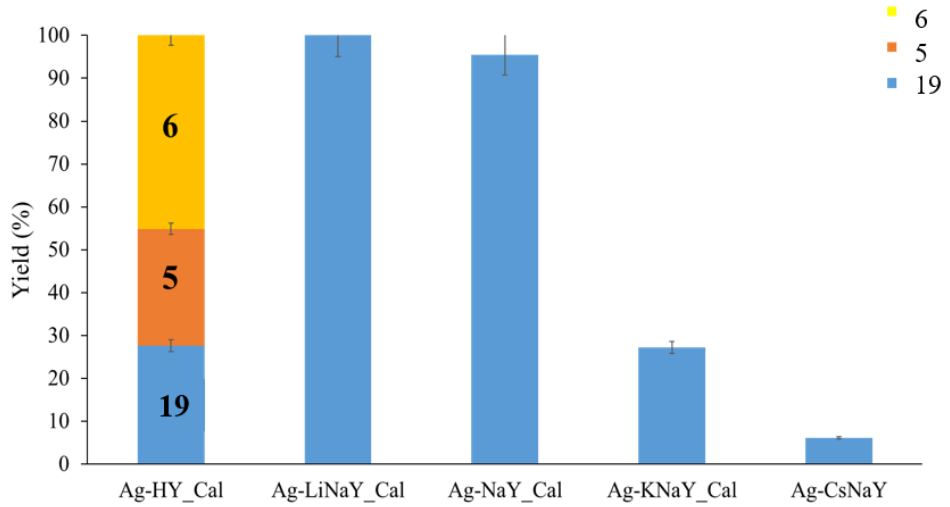

Figure 4.31 Catalytic results for the reaction of ethyl diazoacetate (EDA) **1** in cyclohexane (0.15M) with different Ag-zeolites as catalysts (3 mol% Ag), at 60 °C for 24 h. Zeolites were dried at 250 °C under vacuum overnight, except for Ag-CsNaY. Error bars account for a 5% uncertainty.

4.4.1 *Stability studies of Ag species in the Ag-LiNaY catalyst*

In order to evaluate the stability of the catalyst during the reaction, a hot filtration test was carried out for Ag-LiNaY. **Figure 4.32** reveals the absence of any catalytically active species in solution, confirming the heterogeneous nature of the catalysis and the stability of the zeolite during the reaction. The XRD and FT-IR spectra of the used Ag-LiNaY catalyst closely resemble those of the fresh zeolite sample, as can be seen in **Figure 4.33** and **Figure 4.34**, respectively.

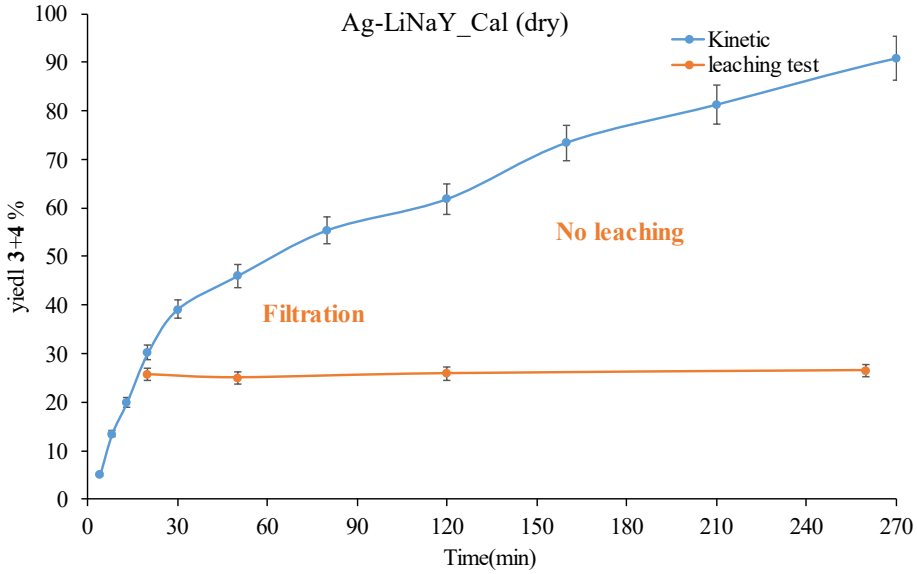

Figure 4.32 Hot filtration test for the Ag-LiNaYcal zeolite catalyst during the reaction of ethyldiazoacetate (EDA) **1** in toluene solvent (0.15M) at 60 ºC. Error bars account for a 5% uncertainty.

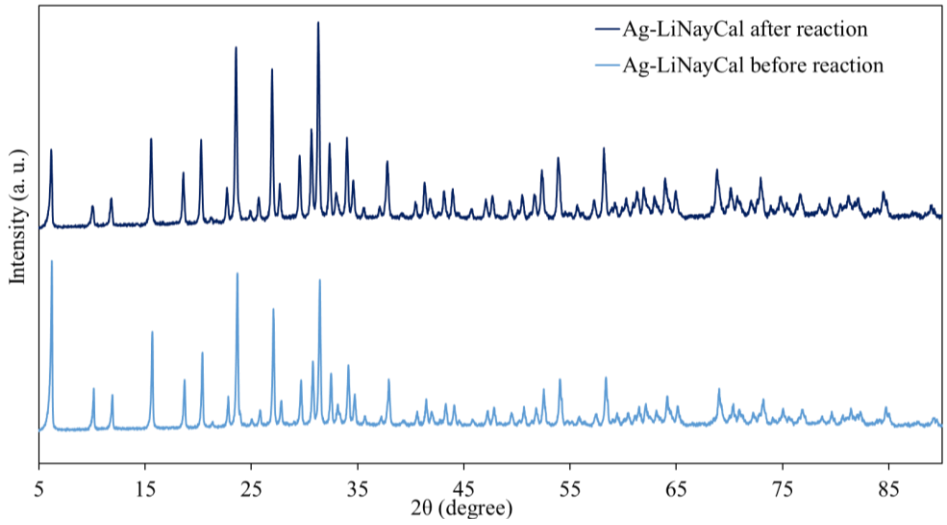

Figure 4.33 Comparison of the X-ray diffractograms (XRD) of the Ag-LiNaYcal zeolite catalyst before and after the reaction of ethyldiazoacetate (EDA) **1** in toluene solvent (0.15M) at 60 ºC for 24 h.

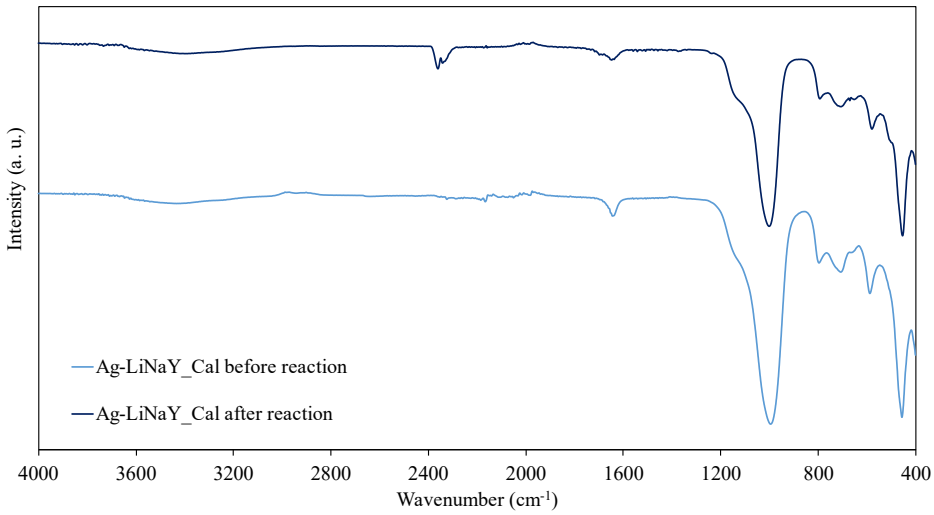

Figure 4.34 Comparison of the Fourier-transformed infrared (FT-IR) spectra of the Ag-LiNaYcal zeolite catalyst before and after the reaction of ethyldiazoacetate (EDA) **1** in toluene solvent (0.15M) at 60 ºC for 24 h. The peak at 2330 cm^{-1} corresponds to residual CO_2 in the FT-IR chamber.

With these results in our hands, we evaluated the reusability of the catalyst. However, the reusability turned out to be lower than that demonstrated by the Ag-HY catalyst, as seen in **Figure 4.35.** We also carried out TEM analysis after the reusability tests, where we can see the formation of Ag NPs (**see Figure 4.36**). Therefore, the stability of Ag species in less acidic zeolites appears to be lower.

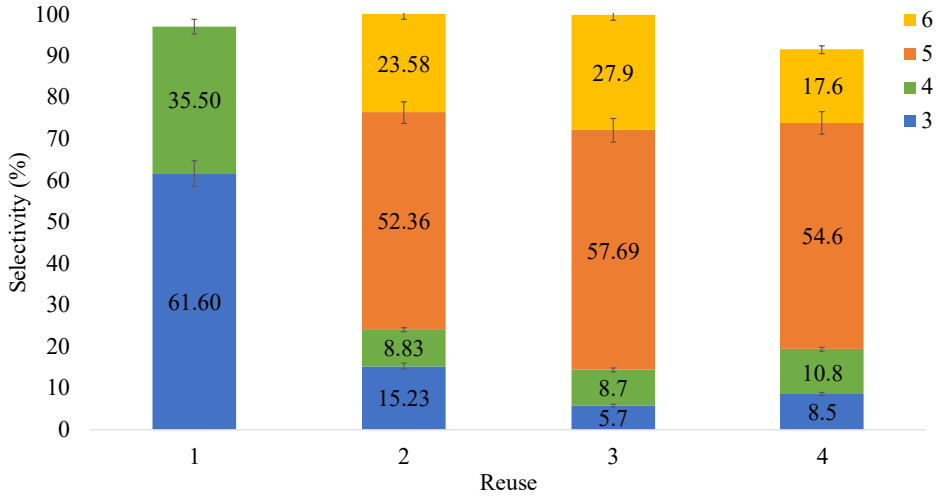

Figure 4.35 Reuses of Ag-LiNaY as a catalyst (3 mol% Ag) for the reaction of ethyldiazoacetate (EDA) **1** in toluene solvent (0.15M), at 60 °C for 24 h. Error bars account for a 5% uncertainty.

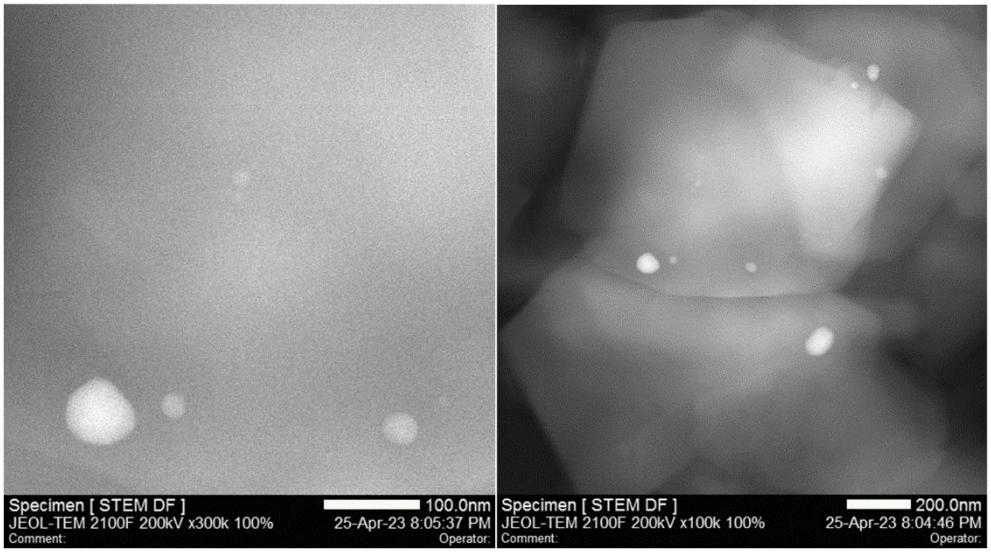

Figure 4.36 High resolution transmission electron microscopy (HR-TEM) images of Ag-LiNaY after reaction.

4.5 *Detection studies of Ag-carbene species*

4.5.1 *Ag-carbene species detection by in-situ ^{13}C cross-polarization magic angle-spinning nuclear magnetic resonance (^{13}C CP/MAS NMR)*

Figure 4.37 displays the ^{13}C cross-polarization magic-angle-spinning nuclear magnetic resonance (^{13}C CP/MAS NMR) spectrum of adsorbed, isotopically labeled EtOOC^{13}CHN$_2$ (^{13}C-**1**) [315] and the resulting spectrum after sealing a vial with EDA **1** and an equimolecular amount of Ag in Ag-LiNaYcal zeolite. The reaction occurred at 60 °C for 3 days. The CP NMR technique allows visualization of carbon atoms containing C-H bonds, which, in this case, highlights the carbene atom in **1**.

In the presence of stoichiometric Ag, the original signal at 45 ppm is replaced by new signals at 11, 28, and 40 ppm. These signals are consistent with a metal carbenoid coordinated through the sp^2 O atom of the carbonyl group to the Ag species. [316, 317] Additionally, signals corresponding to expected products involving water molecules within the zeolite are observed at 64 ppm (product **6**) and 88 ppm (product **5**). Some dimers are produced under these stoichiometric reaction conditions (139 ppm). Notably, the ester signals at approximately 170 ppm are not detected because they do not contain C-H bonds.

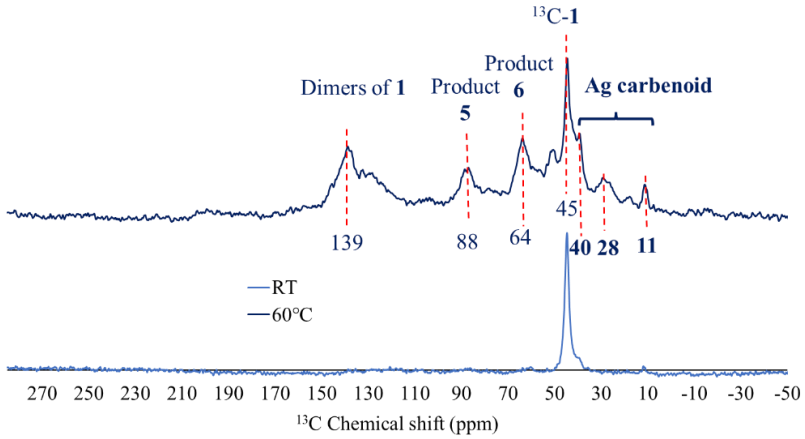

Figure 4.37 ^{13}C cross-polarization magic angle-spinning nuclear magnetic resonance (^{13}C CP/MAS NMR) spectra of (**1**-^{13}C) [254] and after reaction of EDA **1** within the Ag-LiNaYcal zeolite.

4.5.2 *Ag-carbene species detection by in-situ Raman spectroscopy*

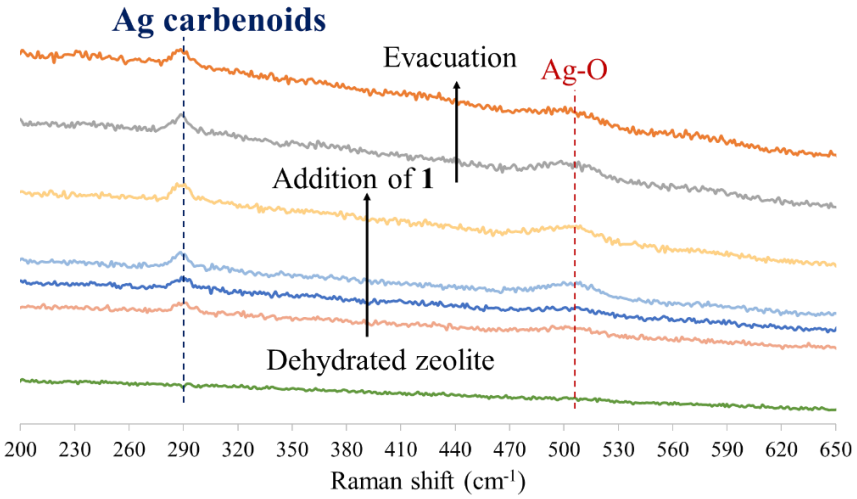

Figure 4.38 Raman spectroscopy of the Ag-LiNaY zeolite after dosing EDA **1** (four shots) and evacuating under vacuum (twice).

On the other hand, **Figure 4.38** displays the time-resolved Raman spectra of the Ag-LiNaY zeolite following the addition of EDA **1**. Notably, new bands emerge at approximately 290 cm^{-1} and 510 cm^{-1}. These bands correspond to reported metal carbene complexes[316] and Ag-O bonds [300], respectively, both involving sp^2 ester O atom coordination. Remarkably, these bands remain stable even after the vacuum evacuation of the sample.

^{13}C CP/MAS NMR, and Raman analyses converge to provide robust evidence that Ag_n-carbene complexes form within the zeolite, where n = 1−3. The selectivity toward specific products depends on the electronic properties of Ag, which are deftly modulated by the zeolite. Electron-poor zeolites like HY stabilize highly cationic Ag species, enabling them to catalyze the insertion of the carbene into O-H bonds. Conversely, Li- to K-exchanged zeolites stabilize less cationic Ag species, facilitating the carbene's insertion into C-H bonds.

4.5.3 *Reaction mechanism for the carbene formation and water insertion on the Ag-zeolite catalyst*

The Raman and ^{13}C CP/MAS NMR spectra provide insights into the possible configuration of the Ag carbene intermediate. In order to deeper insights into the reaction pathway and understand the molecular-level reaction mode, we conducted kinetic analysis by varying the amounts of different reagents, under semistationary state conditions. This allowed us to determine the reaction order for each reagent and derive the corresponding rate equation.

Figure 4.40 shows the experimental results revealing a reaction order of one for the Ag-HYcal zeolite catalyst, one for EDA, and zero for water. The same result is observed for EDA **1** with the Ag-LiNaYcal zeolite catalyst. Consequently, the rate equation can be expressed as $v_0 = k_{exp}$[Ag-zeolite][EDA **1**] (v_0 is initial reaction rate

and, k_{exp} is an experimental constant), signifying that the rate-determining step (rds) of the reaction involves the formation of the Ag-carbene complex. That is why the carbene intermediate is only briefly observed, since once formed it rapidly reacts with water to produce products **5** and **6**.

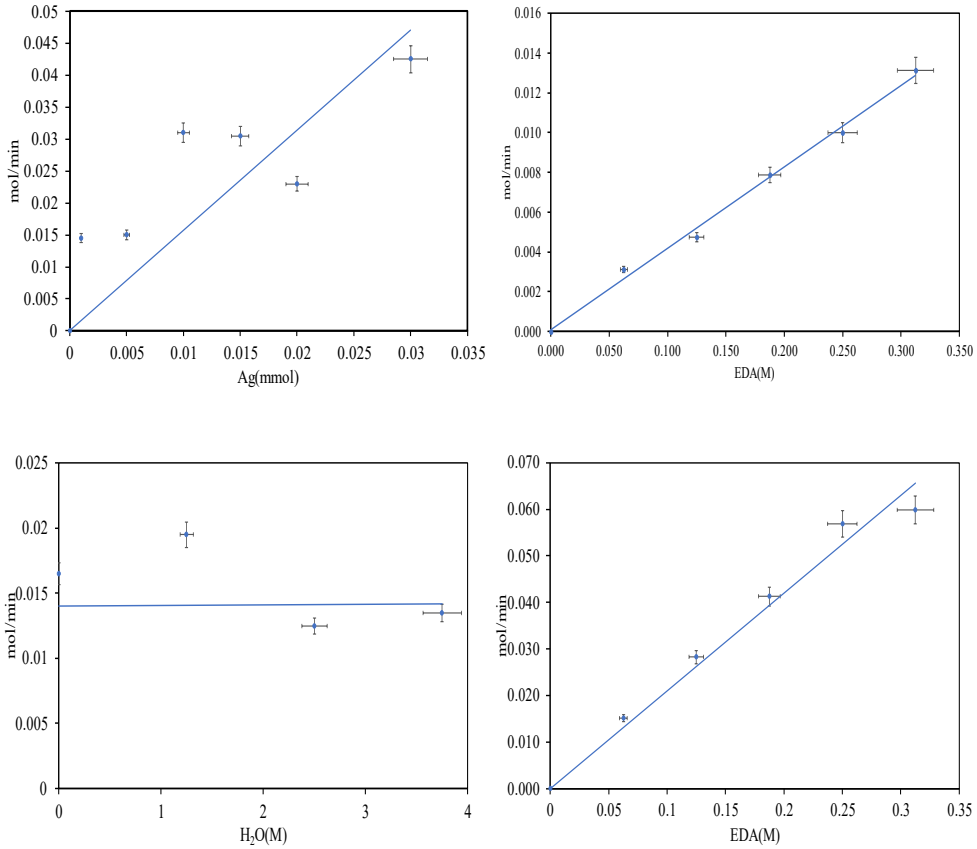

Figure 4.40 From top left to bottom right: Initial rates vs reagent concentration plots for the Ag-HYcal zeolite catalyst, EDA **1** and water, during the carbene insertion reaction, and the relationship with EDA **1** concentration for Ag- LiNaYcal zeolite catalyst. Error bars account for a 5% uncertainty.

The **Figure 4.41** show the proposed reaction mechanism for the reaction with water, including the formation of carbene. The initial step involves the creation of the

Ag carbene, which is the rds of the reaction. The configuration of this carbene intermediate reveals that the carbonyl ester group coordinates to the metal site. This insight is supported by both Raman and ^{13}C CP/MAS NMR spectra. [316, 317] This carbene is then inserted into the O-H water bond to give the final product 5 and regenerate the initial Ag-zeolite catalyst.

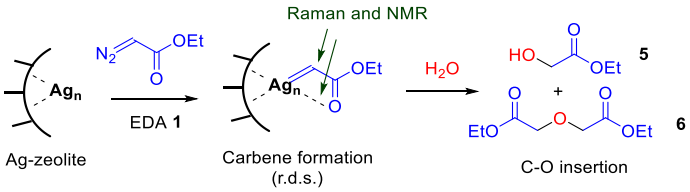

Figure 4.41 Proposed reaction mechanism for the carbene formation and water insertion on the Ag-zeolite catalyst (rds: rate-determining step), also showing the possible configuration of the Ag carbene intermediate according to the Raman and ^{13}C CP/MAS NMR spectra.

During the reaction order studies, we realized that the amount of Ag-zeolite can be decreased very significantly, to $\leqslant$ 0.1 mol % in Ag, obtaining significant conversion after only 30 minutes of reaction. Thus, much better selectivity for C-C and C-H insertion products is obtained since the amount of water contributed by the zeolite is minimized. **Figure 4.42** shows this new result, which indicates that the catalytic activity of Ag in zeolite is remarkable.

EDA **1** → Toluene **2** (0.15M), Ag-HYcal (**x mol%**), 60 °C, 30 min

	x mol%	**3**[a]	**0.1**	**0.01**	**0.001**
3 C-C insertion		5	15	16	15
4 C-H insertion		28	11	5	5
5+6 C-O insertion		59+9	35+8	-	-

Figure 4.42 Reaction results for decreasing amounts of Ag-HYcal zeolite catalyst after 30 min of reaction time. [a] Results for 24 h of reaction time.

4.6 *Conclusions*

The synthesis of ultrasmall Ag species within zeolite Y has been successfully achieved through a straightforward exchange-calcination procedure. This process yields cationic single- and few-atom silver clusters. These supported Ag zeolites exhibit high catalytic activity in carbene-mediated organic reactions, resulting in good yields and selectivity, depend on the zeolite's counterbalancing cation, as it dictates the electronics of the Ag active site. The amount of catalyst required can be as low as ≤0.1 mol % Ag. These findings underscore the effectiveness of Ag in organic synthesis, particularly when obtained in subnanometric form. [318-321] Furthermore, zeolites serve as easily tunable macroligands, allowing the generation and stabilization of these ultrasmall supported metal species. [322, 323] As an intriguing aside, we have also discovered a method to thoroughly dry the HY zeolite by leveraging the strong adsorption of water and its reaction with the *in-situ* formed carbenes.

These findings significantly broaden the spectrum of economically viable silver species that can be harnessed for catalytic applications within the realm of organic synthesis, thereby paving the way for the design and implementation of carbene-mediated organic transformations utilizing commercially available and reusable catalytic solids.

Chapter 5. MOF-supported silver clusters as catalysts for carbene reactions

5.1 *Introduction*

Ag subnanometer metal clusters find applications in various fields like photovoltaic cells, biological sensors, and gas sensors. However, the formulation, stabilization, and characterization of subnanometer metal clusters (SNMCs) has posed a significant challenge for chemists in recent years. [174, 324-329] Indeed, the synthesis of such ultrasmall entities is exceedingly complex and often necessitates, for instance, the utilization of stabilizing blocking ligands that inhibit their aggregation into larger metal nanoparticles (MNPs) [330] but, conversely, may diminish their catalytic properties. Furthermore, the analysis of such tiny SNMCs is undeniably a challenging task and necessitates the utilization of high-resolution microscopy techniques, such as HAADF− STEM[331] However, despite these complications, the remarkable medical, optical, and/or catalytic properties exhibited by SNMCs make the endeavor highly worthwhile, as we have shown in the previous chapter. [332, 333]

The use of ligands to stabilize SNMCs dramatically reduces their catalytic activity, since they prevent an adequate contact with reactants and trigger their decomposition under reaction conditions. Therefore, to offer better catalytic activity, all metal atoms should be exposed, that is, it would be to have “naked” SNMCs. [334, 335] In this context, a promising approach for obtaining ligand-free subnanometer metal clusters involves supporting these metal species within porous solids. One of these solids are zeolites, which we have shown in the previous chapter to be suitable supports for stabilizing subnanometer Ag species. [336] Another porous solids that can be used as supports are Metal-Organic Frameworks (MOFs). They consist of single metal ions or polynuclear metal clusters linked with a wide variety of organic ligands, through coordination bonds, forming a three-dimensional network. MOFs not only

serve as hosts for SNMCs but also act as chemical reactors for *in-situ* synthesis of these ultrasmall metal species. [337, 338]

MOFs are ordered porous materials that have garnered considerable interest over the last two decades due to the diverse array of applications in which they can be employed. [339] Furthermore, with the purpose of encapsulating/synthesizing single-nucleus metal catalysts or even catalysts consisting of individual atoms, [314, 340-343] MOFs present distinct advantages when compared to zeolites, such as precise regulation of the functionalities adorning the channels. This enables to retain and position metals in specific locations and controlled stoichiometries. Additionally, MOFs offer the possibility of utilizing single-crystal X-ray crystallography to disclose the crystal structure of the extremely small metal entities. [344-346]

In this scenario, our research group has extensive experience, and in collaboration with a specialized group in MOF from the University of Valencia, MOFs have been used as a chemical reactor to synthesize various subnanometer metal species. In this chapter we have used a highly robust anionic three-dimensional MOF, [314] with the chemical formula $Ni^{II}_2 \cdot 54H_2O[Me_3mpba_4$=N,N′-2,4,6-trimethyl-1,3-phenylenebis(oxamate)], for the MOF-driven synthesis of ligand-free Ag_2^0 nanoclusters. As will be shown throughout the chapter, once this novel silver catalyst was prepared and characterized, their efficiency was evaluated to carry out the Buchner ring expansion reaction shown in **Figure 5.1**.

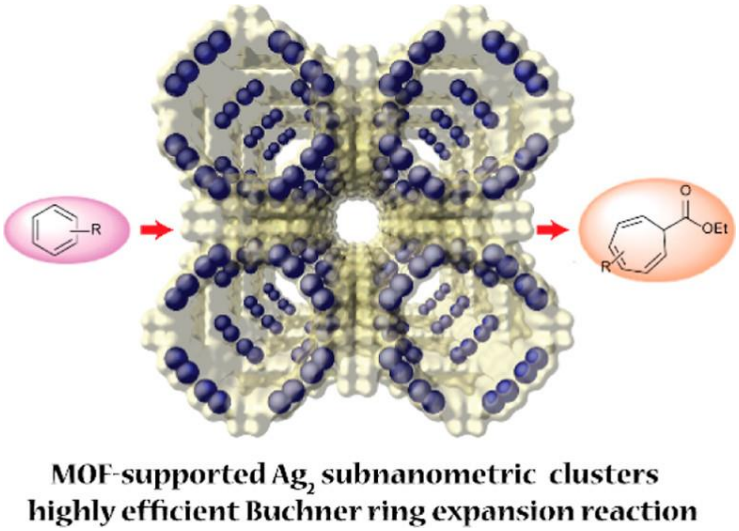

Figure 5.1. Catalytic Buchner reaction by MOF-supported silver subnanomertic clusters.

5.2 *Synthesis and characterization of small subnanometer Ag_2^0 clusters in the channels of an anionic MOF*

5.2.1 *Synthesis of small subnanometer Ag_2^0 clusters on MOF and description of the resulting material*

In this section, we will be discussed on the preparation of the novel Ag_2^0@MOF material. In this context, we carried out a straightforward process involving the exchange of silver ions and their subsequent reduction to create Ag_2^0@MOF material, containing subnanometer silver clusters accommodated in its channels. As a host matrix, the previously documented MOF $Ni^{II}_2\{Ni^{II}_4[Cu^{II}_2(Me_3mpba)_2]_3\}\cdot 54H_2O$ (**Figure 5.2a, 21**) was used. This material is an anionic MOF that presents Ni^{2+} cations in the channels, counterbalancing the charge of the network, as shown in **Figure 5.2**.

To prepare the Ag species, initially, the nickel (II) cations, situated within the pores of **21**, are replaced by Ag^+ cations, resulting in the creation of the novel compound $Ag^{I}_4\{Ni^{II}_4[Cu^{II}_2(Me_3mpba)_2]_3\}\cdot 54H_2O$ (**Figure 5.2b, 22**). Subsequently, upon the introduction of $NaBH_4$, the reduction process takes place to yield the final material $[Ag_2^0]$@$Ag^{I}_2Na^{I}_2\{Ni^{II}_4[Cu^{II}_2(Me_3mpba)_2]_3\}\cdot 48H_2O$ (**Figure 5.2c, 23**). The entire procedure can be monitored through single-crystal X-ray diffraction (SCXRD), revealing specific details regarding the formation of the nanoclusters, which represents one of the few instances of MOF-hosted silver subnanometer clusters, [347] after cationic exchange.

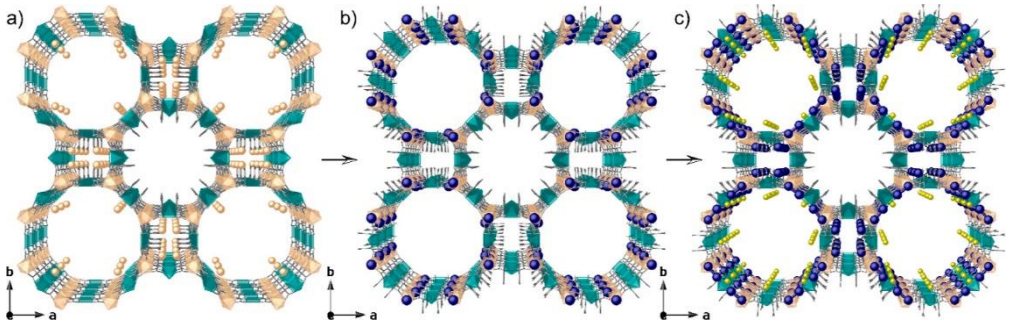

Figure 5.2. Design approach showing the crystal structures of **21** (a), **22** (b), and **23** (c) showing the two-step post-synthetic process consisting of the exchange of the Ni^{II} cations in the pores of 1 by Ag^{I} ones to yield **22** and the reduction process to form the Ag_2^0 clusters in **23**. Virtual diameters of larger octagonal pores are 2.0 nm for MOFs **21**−**23**, respectively. Copper and nickel atoms from the network are represented by cyan and orange polyhedra, respectively, whereas organic ligands are depicted as gray sticks. Orange, yellow, and blue spheres represent Ni, Na, and Ag atoms, respectively.

In the **Figure 5.2** both materials **22** and **23**, which are anionic $Ni^{II}_4Cu^{II}_6$ materials, exhibit isoreticular structure and crystallize in the *P4/mmm* space group of the tetragonal system. In material **22**, Ag^+ cations are located within hydrophilic octagonal pores, with a virtual diameter of 2.0 nm, and Ag^+ cations are stabilized by noncovalent interactions involving oxamate oxygen atom, the $[Ag^+\cdots O_{oxamate}]$ distance ranges from 2.72(1) Å to 2.79(1) Å, indicating a complete exchange of the previously present Ni^{2+} cations. Additionally, the Ag^+ ion surroundings suggest interactions with oxygen atoms from nitrate anions or solvent water molecules. The $Ag^+\cdots O$ distance ranges from 2.38(3) Å to 2.56(3) Å, with an $Ag^+\cdots Ag^+$ separation of 2.74(2) Å, shorter than the van der Waals contact distance. These interactions may serve as precursors to the Ag_2^0 dimers observed in **23**. The structure of this material is described in more detail in **Figure 5.3** to **Figure 5.5**.

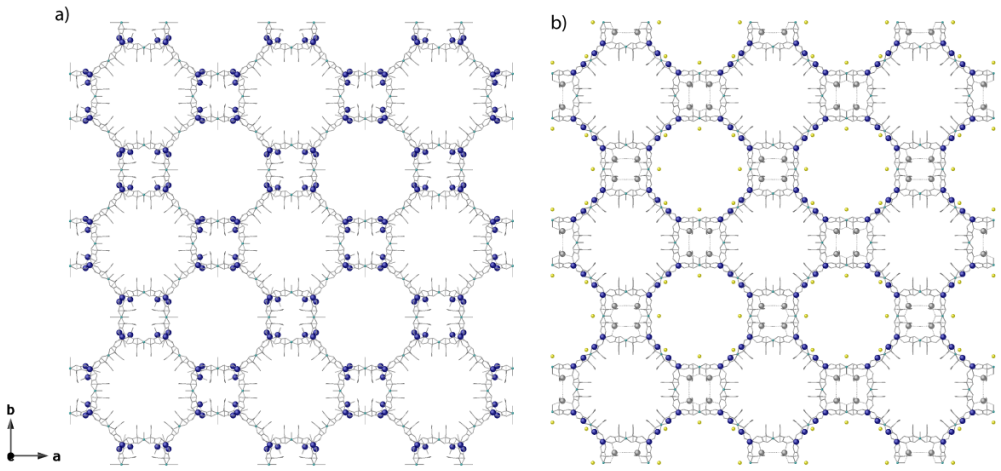

Figure 5.3 Perspective view along c crystallographic axis of crystal structures of **22** (a) and **23** (b) presenting channels filled by Ag^{+} complexes (**22**) or Ag_0^2 NCs and Ag+ ions (confined in square pores) (**23**). Lattice water molecules and hydrogen atoms have been omitted for clarity. Color scheme: Silver, blue sphere (octagonal pores of **22** and **23**) and grey spheres (Ag^{+} ions not reduced in square pores in **23**); sodium, yellow spheres, ligands atoms and metal ions of the whole net have been depicted as grey sticks.

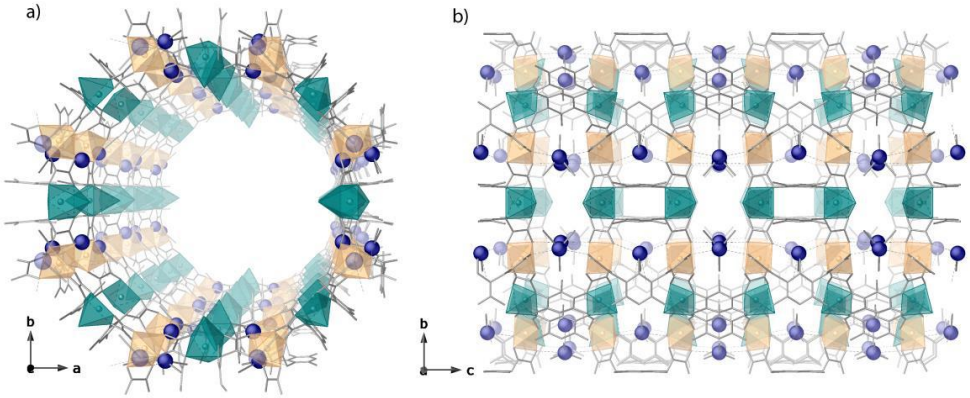

Figure 5.4 Details along c (a) and a (b) crystallographic axis of a single octagonal pore in **22**. Color scheme: silver, blue sphere; copper and nickel, cyan and orange polyhedral, respectively; ligands atoms of the whole net have been depicted as grey sticks.

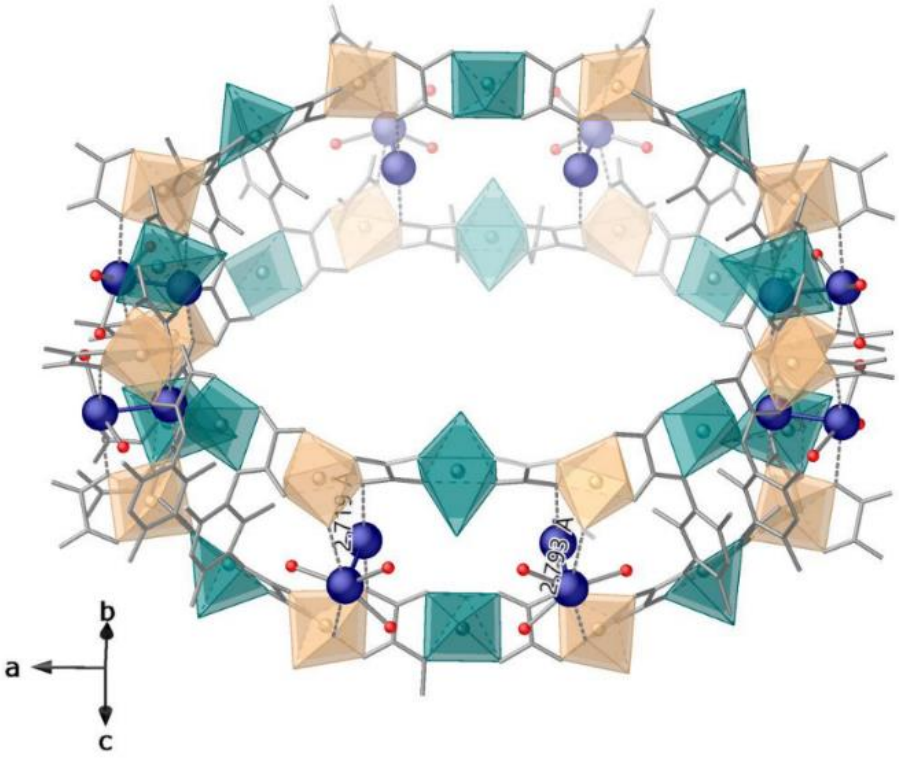

Figure 5.5 One single channel of **22** showing supramolecular interactions involving oxamate ligands of the network stabilizing Ag^{+} dimers. Color scheme: silver, blue sphere; copper and nickel, cyan and orange polyhedral, respectively; ligands atoms of the whole net have been depicted as grey sticks. Modelled oxygen atoms (likely belonging to NO_3^- anions) surrounding Ag^{+} ions are depicted as red spheres.

In the case of material **23**, the nano-confined space of the MOF stabilizes the as-synthesized Ag_2^0 dimers within the walls of the hydrophilic octagonal channels, as shown in **Figure 5.6** and **Figure 5.7**. The smaller square pores of the MOF also contain unreduced $Ag^{+}\cdots Ag^{+}$ dimers. Hydrated charge-counterbalancing alkali Na^{+} cations are retained in the preferential cationic sites, which stabilizes the material, giving it exceptional robustness. The limited accessibility of solvated $NaBH_4$ to the small square pores likely explains the presence of still unreduced $Ag^{+}\cdots Ag^{+}$ dimers. These dimers are blocked by $Ag^{+}\cdots O_{oxamate}$ interactions at a distance of 2.84(1) Å.

Figure 5.8 demonstrates that the Ag_2^0 dimers, with an intradimer Ag···Ag distance of 3.19(1) Å, are firmly fixed and stabilized within the walls of the largest pores of the network. Ultimately, this stability is achieved through supramolecular interactions involving oxamate ligands and weak connections with solvent molecules.

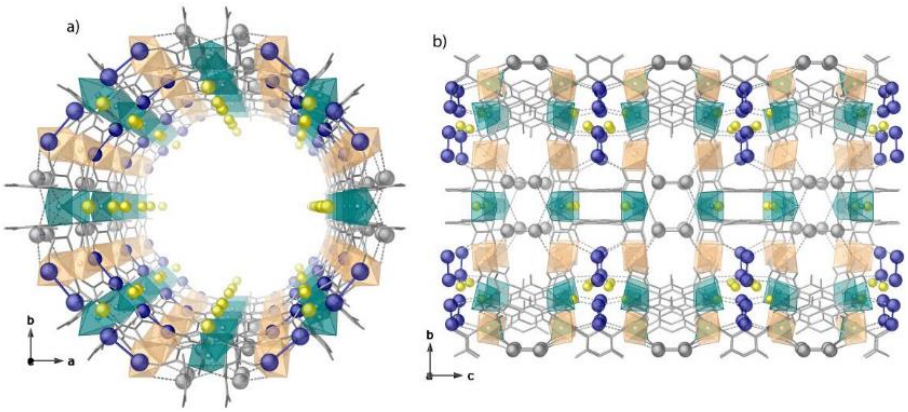

Figure 5.6 Details along c (a) and a (b) crystallographic axis of a single octagonal pore in **23**. Color scheme: silver, blue sphere; sodium, yellow spheres; copper and nickel, cyan and orange polyhedral, respectively; ligands atoms of the whole net have been depicted as grey sticks.

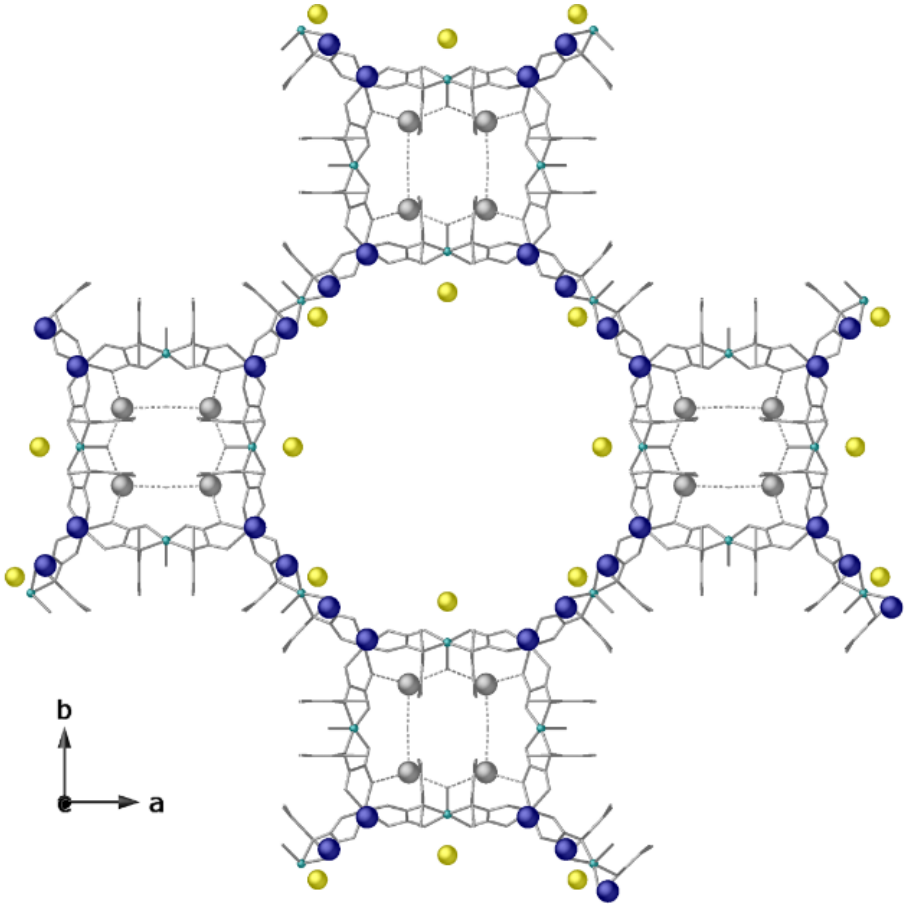

Figure 5.7 Details along c crystallographic axis of a portion of crystal structure of **23** showing disposition of Ag^+ ions (grey spheres) residing in poorer accessible small square pores. Color scheme: silver, blue and grey spheres (Ag^+ ions not reduced in square pores); sodium, yellow spheres.; copper and nickel, cyan and orange polyhedral, respectively; ligands atoms of the whole net have been depicted as grey sticks.

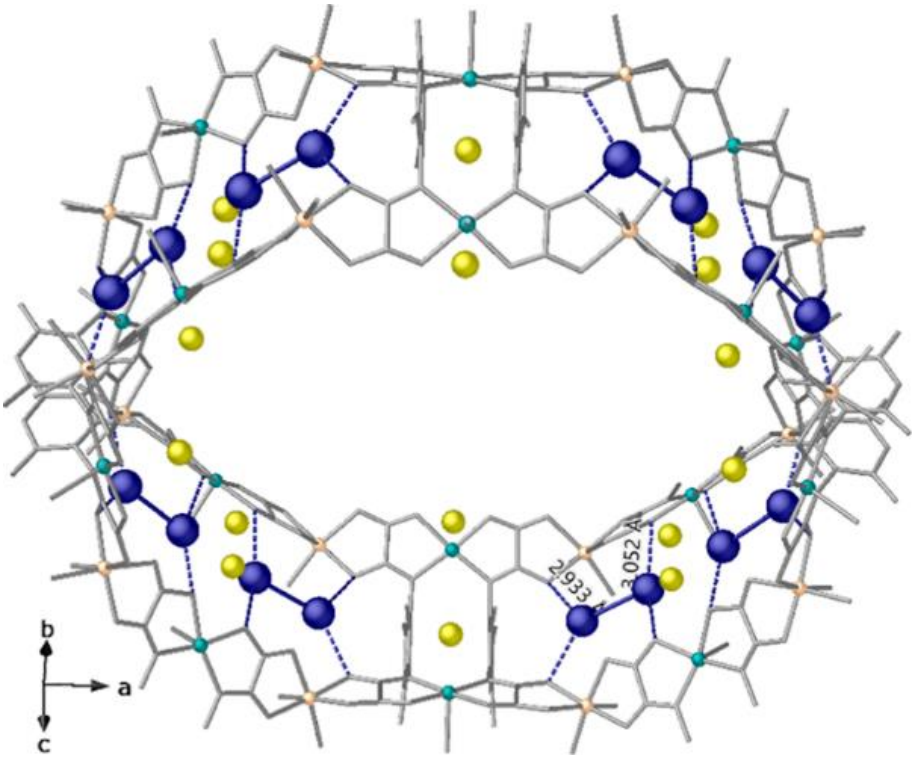

Figure 5.8 One single channel of **23**, showing supramolecular interactions involving oxamate ligands of the network (distances are reported in angstroms).

5.2.2 *Characterization of small subnanometer Ag_2^0 clusters on MOFs*

In this section, we discuss the further characterization of the synthesized silver clusters on the MOF. To better understand this final hybrid material, denoted as **3**, consists of Ag_2 clusters species, together with unreduced Ag^+ ions, a combination of diverse characterization techniques has been used, which include ICP-MS, PXRD, TGA, XPS and SEM. Additionally, N_2 adsorption isotherms at 77 K have verified the enduring porosity of materials **22** and **23**.

5.2.2.1 *Scanning Electron Microscopy (SEM) and Energy-Dispersive X-ray Spectrometry (EDX)*

SEM coupled with EDX were used to observe the morphology and distribution of elements on the surface of the material. **Figure 5.9** and **Figure 5.10** show the images of the measurements carried out. The EDX elemental mappings of Cu, Ni, Ag, and Na elements reveal a heterogeneous spatial distribution of Ag atoms, consistently found adjacent to Cu and Ni atoms. Furthermore, no obvious Ag NPs were observed, which is consistent with what was observed by SCXRD.

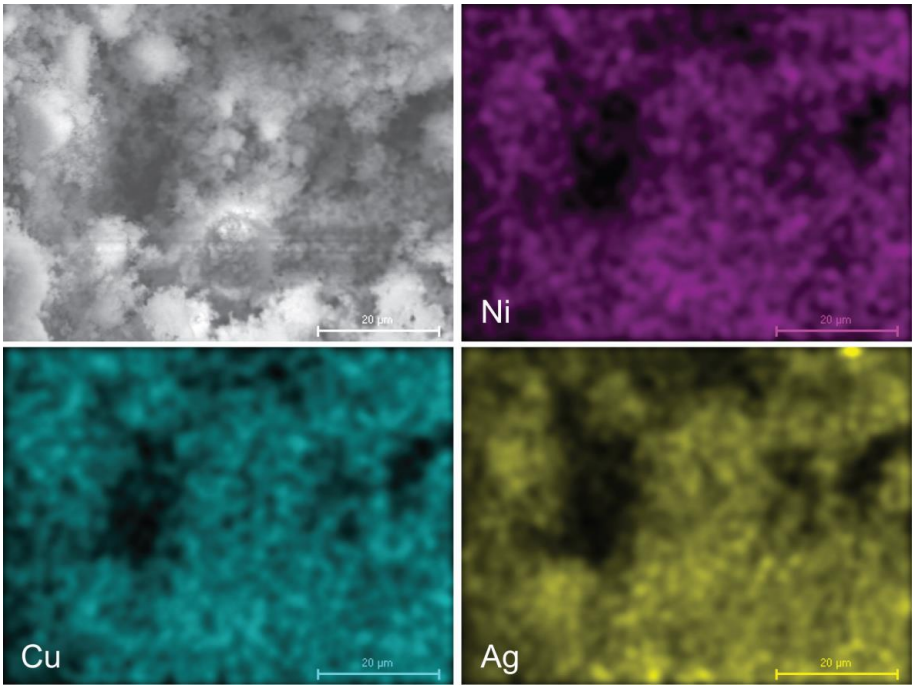

Figure 5.9 Backscattered SEM image of **22** and the corresponding EDX elemental mapping for Cu (cyan), Ni (magenta) and Ag (yellow) elements. The backscattering detector highlights the MOF particles as brighter areas due to crystalline MOF structure and to the presence of heavier atoms in the MOF than in the polymer matrix.

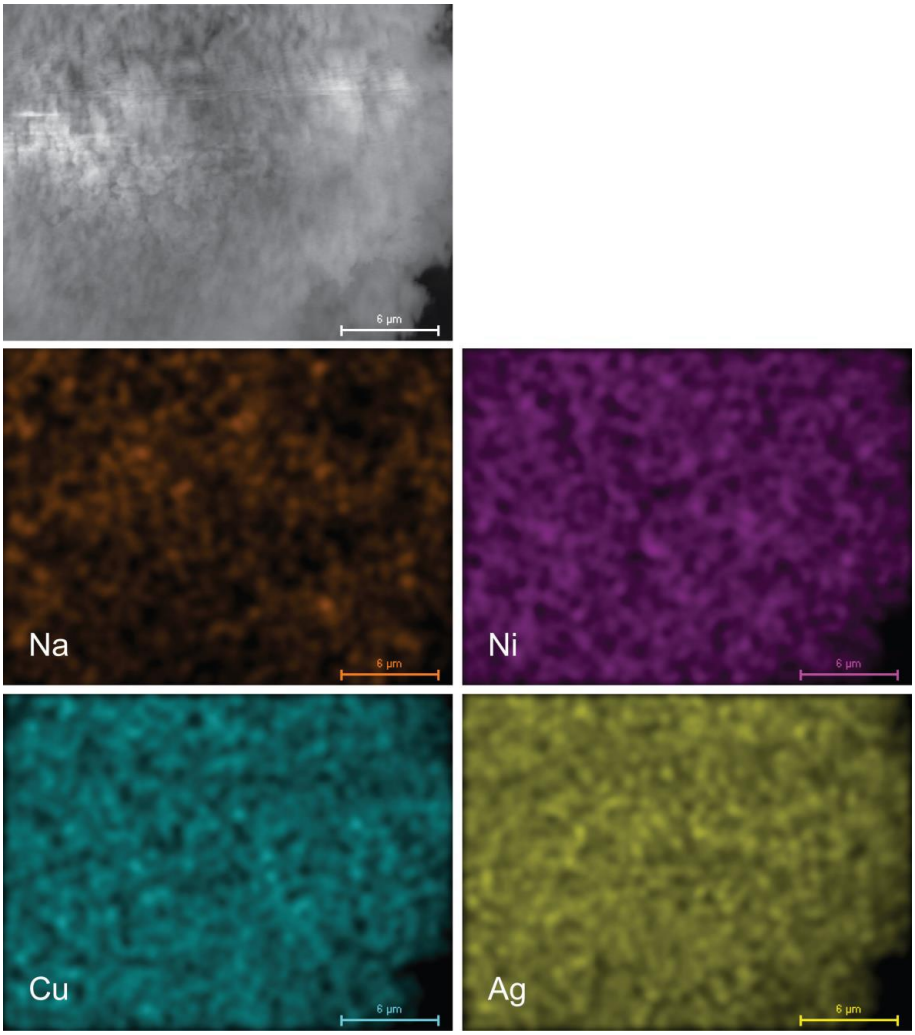

Figure 5.10 Backscattered SEM image of **23** and the corresponding EDX elemental mapping for Cu (cyan), Na (orange), Ni (magenta) and Ag (yellow) elements. The backscattering detector highlights the MOF particles as brighter areas due to crystalline MOF structure and to the presence of heavier atoms in the MOF than in the polymer matrix.

5.2.2.2 *High-Angle Annular Dark-Field Scanning Transmission Electron Microscopy (HAADF-STEM)*

In order to verify the existence of Ag_2 dimer, we applied HAADF-STEM technology to characterize MOF **23**. In the **Figure 5.11** presents aberration-corrected HAADF-STEM images, which provide a direct visualization of both Ag_2 dimers and Ag_1 species, which are likely to be silver atoms residing in smaller square channels.

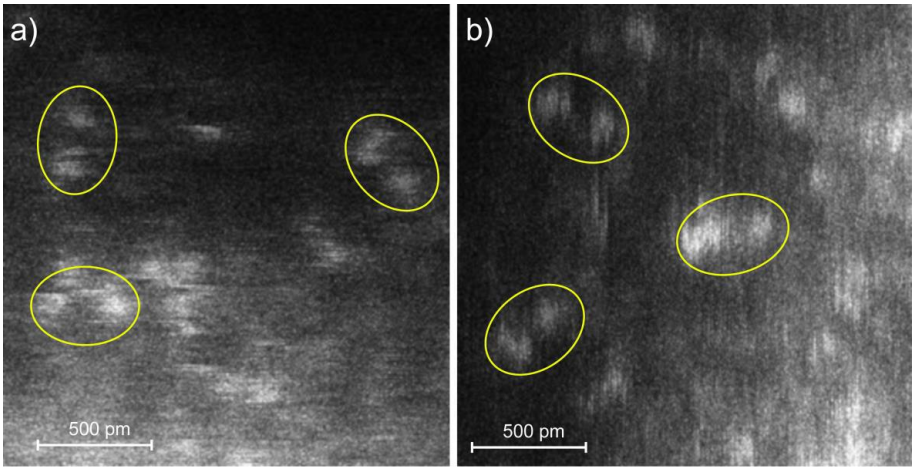

Figure 5.11 AC-HAADF-STEM images of MOF **23** showing the presence of both Ag single atoms and Ag_2 dimers (yellow circles).

5.2.2.3 *Thermo-Gravimetric Analyses (TGA)*

In the **Figure 5.12** shown the thermogravimetric analysis on the MOF materials **22** and **23**, from which the solvent content is known. When the temperature rose to 80 °C, the thermogravimetric ratio of the material decreases to ~80%, due to the loss of solvent in the material, such as methanol. Then the temperature increased to 100 °C and water molecules adsorbed in the MOF channels begin to be lost. Finally, at temperatures close to 300 °C, the MOF material begins to decompose.

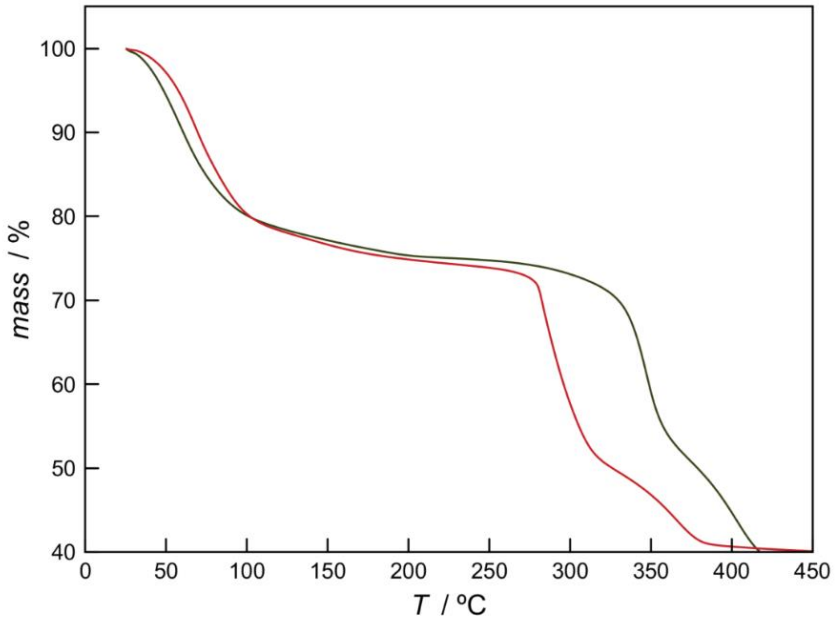

Figure 5.12 Thermo-Gravimetric Analyses (TGA) of **22** (red) and **23** (green) under a dry N_2 atmosphere.

5.2.2.4 *Powder X-Ray Diffraction (PXRD)*

In the PXRD patterns of both materials **22** and **23** indicate that the bulk samples are pure and crystalline, with no observable peaks of Ag^0 nanoparticles, as shown in **Figure 5.13**. This is consistent with the previous EDX and HAADF-STEM characterization results. In fact, the experimental diffraction patterns of **22** and **23** closely resemble the theoretical patterns derived from the SCXRD data.

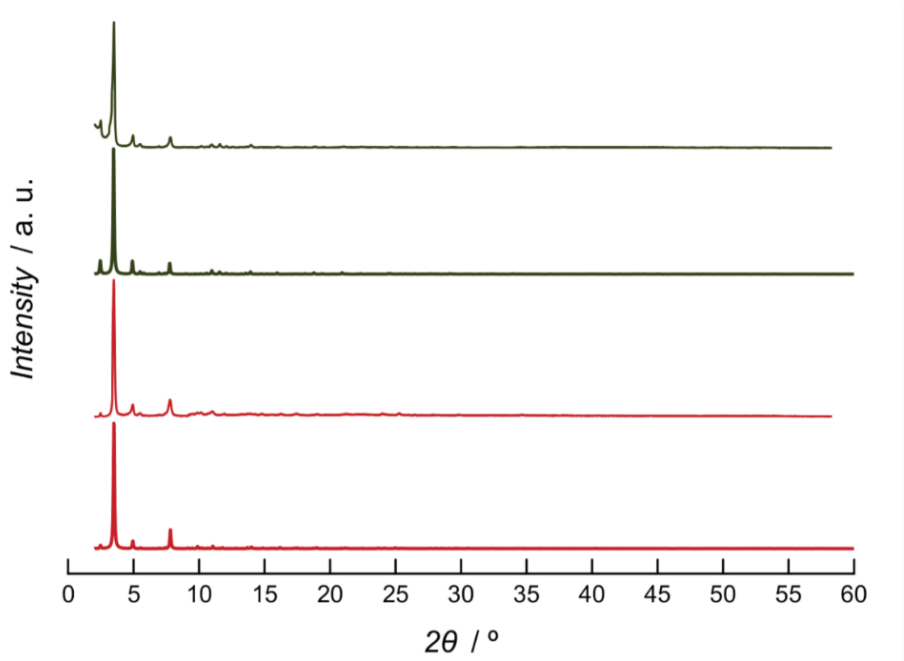

Figure 5.13 Theoretical (bold lines) and experimental (solid lines) PXRD pattern profiles of **22** (red) and **23** (green) in the 2θ range 2-60°.

5.2.2.5 *X-ray Photoelectron Spectroscopy (XPS)*

The XPS spectra of compounds **22** and **23** are shown in **Figure 5.14**. For MOF **22**, which only contains Ag^{+} cations, two bands at 367.6 and 373.6 eV corresponding to Ag $3d_{5/2}$ and Ag $3d_{3/2}$ binding energies, [348] respectively, are observed (**Figure 5.14a**). On the other hand, for MOF **23**, where both Ag^{+} cations and Ag_2^{0} nanoclusters are present according to SCXRD and elemental analyses, in addition to the Ag^{+} bands at 367.6 and 373.6 eV, two additional peaks at 368.4 and 374.4 eV can be seen, which are attributed to reduced Ag^{0} atoms (**Figure 5.14b**).

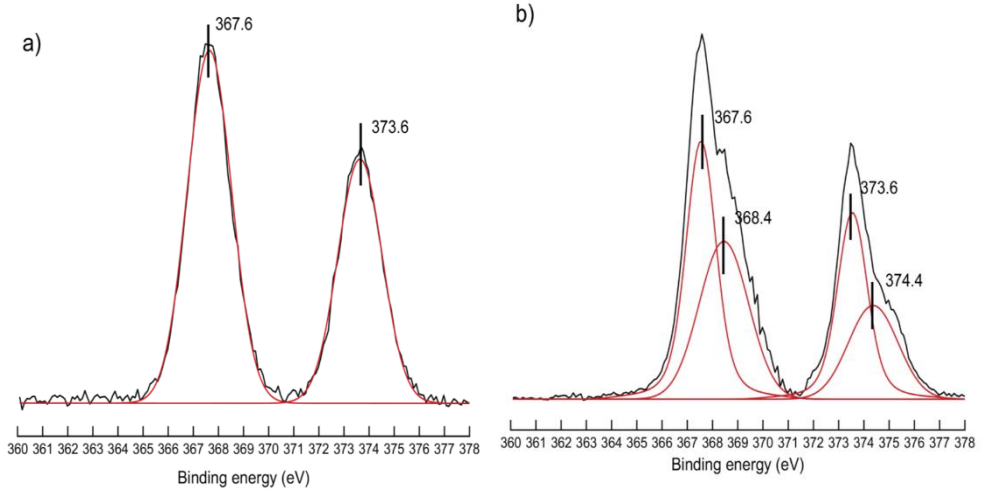

Figure 5.14 X-ray photoelectron spectroscopy (XPS) of **22** (a) and **23** (b).

5.2.2.6 *Diffuse Reflectance Infrared Fourier Transform Spectroscopy (DRIFTS) with CO*

On the other hand, the **Figure 5.15** shows CO-probe diffuse reflectance infrared Fourier transformed spectroscopy (DRIFTS) performed on MOF **23** at 77 K, to avoid any *in-situ* reduction of Ag^{+} and to observe potential Ag^{0}-CO species. The results show three main peaks, one at 1938 cm^{-1}, indicating CO bridged-bonded to Ag^{0} atoms, [304] a second at 2059 cm^{-1}, attributable to $Ag(CO)^{+}$ species, [349] and a last peak at 2043 cm^{-1}, corresponding to free CO after saturation. It is known that the adsorption of CO on Ag^{0} is lower than Ag^{+}, [350] hence the lower intensity of the former, which could correspond to a 1:1 ratio between Ag oxidation states. These findings strongly suggest that 50% of the Ag^{+} present in **22** are reduced by $NaBH_4$ to form Ag_2^{0} nanoclusters, while the remaining 50% of Ag^{+} cations occupy sheltered interstitial positions that are inaccessible to the reducing agent.

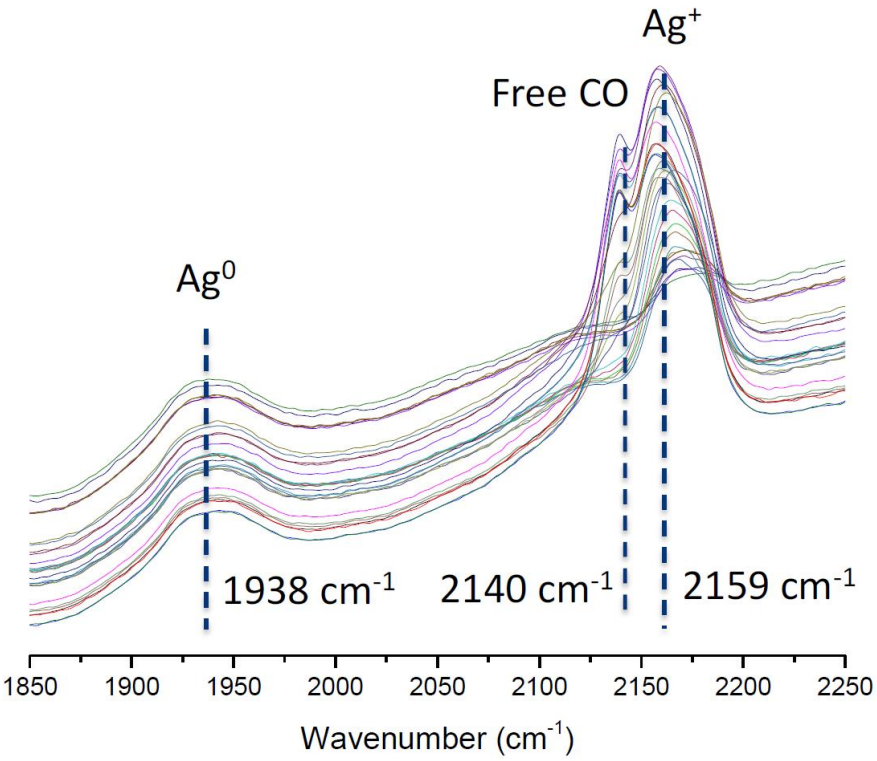

Figure 5.15 CO-probe diffuse reflectance infrared Fourier transform spectroscopy (DRIFTS) of MOF **23**, run at 77 K with different CO doses at later desorption.

5.2.2.7 *N_2/CO_2 Adsorption Isotherms*

The N_2 and CO_2 adsorption isotherms for compounds **21-23** confirm their permanent porosity, as can be seen in **Figures 5.16** and **5.17**. The N_2 adsorption isotherms for **21-23**, with calculated BET[351] surface areas of 974, 1013, and 625 m^2/g, respectively, indicate a very similar permanent porosity for **21** and **23**, consistent with their identical estimated virtual diameters of 2.0 nm. However, MOF **22** exhibits lower N_2 adsorption despite having the same virtual diameter, which could be attributed to a partial collapse of the structure during solvent evacuation treatment. Interestingly, the CO_2 adsorption isotherms show a 66% increase in uptake for **23**, suggesting quadrupole interactions between CO_2 molecules and Na^+ cations.

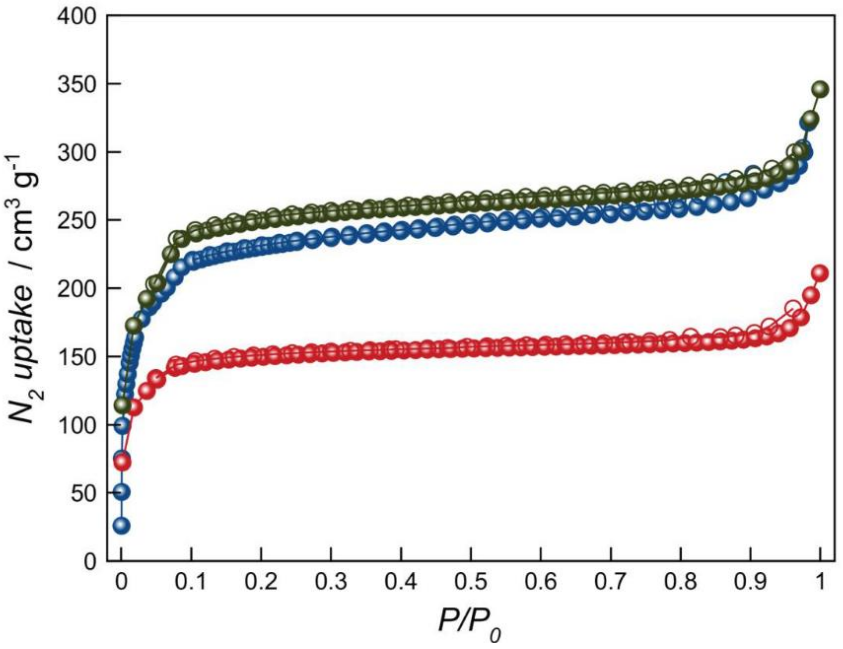

Figure 5.16 N_2 sorption (filled circles) and desorption (empty circles) isotherms for the activated compounds **21** (blue), **22** (red) and **23** (green) at 77 K.

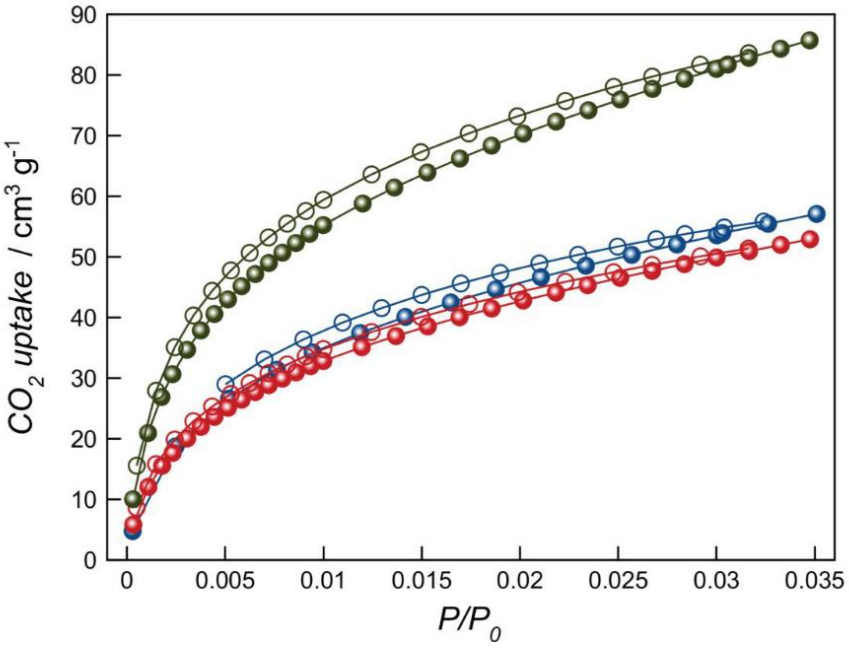

Figure 5.17 CO_2 sorption (filled circles) and desorption (empty circles) isotherms for the activated compounds **21** (blue), **22** (red) and **23** (green) at 273 K.

5.3 *Buchner ring expansion reaction catalyzed by the Ag_2^0@MOF catalyst.*

The Buchner ring expansion reaction was attempted with catalytic amounts of **23**. The results show that the reaction between toluene (**2**) and ethyl diazoacetate, EDA (**5**) proceeds rapidly (30 min) in a very high yield, under standard reaction conditions, as shown in **Figure 5.18**. [314, 352] Blank experiments without any catalyst gave a 8% conversion, and the use of MOFs **21** and **22** as catalysts showed the lower catalytic activity of these MOFs **23**, with a 3 times lower initial rate for the former (**Figure 5.19**). Commercial Ag NPs on alumina only gave a 16% conversion, and remarkably, the state-of-the art catalyst for this reaction, that is, $Rh_2(OAc)_4$, gave a lower result than MOF **23**, under this reaction conditions, that is 63% after the addition of **1** at once (see the *Chapter 4*). An optimum >95% yield of product **3** was obtained after maintaining a low concentration of **1** during the reaction, which was achieved by adding a solution of **1** (in dichloromethane) into the reaction mixture using a syringe pump, instead of adding it at once. Otherwise, the unwanted dimerization reaction of **1** occurs. It is worth noting here that product **3** corresponds to the typical mixture of cycloheptatriene isomers, in accordance with previous results.

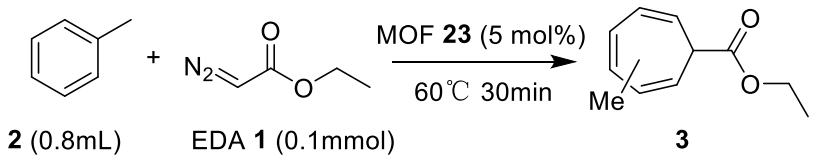

Figure 5.18 The Buchner ring expansion reaction.

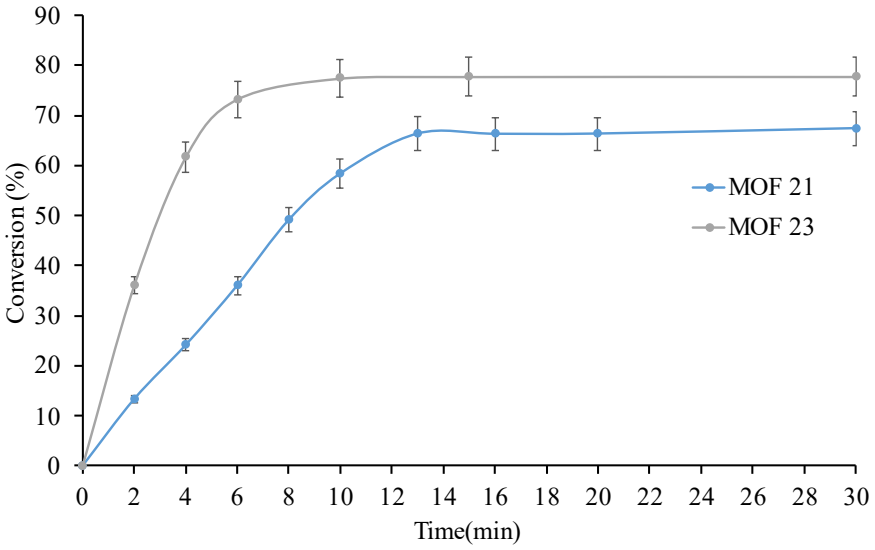

Figure 5.19 Kinetics for the Buchner ring expansion reaction between toluene **2** and ethyl diazoacetate **1** catalyzed by MOFs **21** and **23**. Error bars account for a 5% uncertainty. **1** is added at once.

In the **Figure 5.20,** a hot filtration test, wherein the solid MOF catalyst **23** is removed from the reaction mixture at the reaction temperature (60 °C) at an initial conversion (~30%), is shown. The reaction conversion of the filtered sample is ~30%, over time it seems that there is only leaching effect of 10.3%, so this result shows that the catalytic active species are not present in solution, corroborating the relative stability of the solid catalyst.

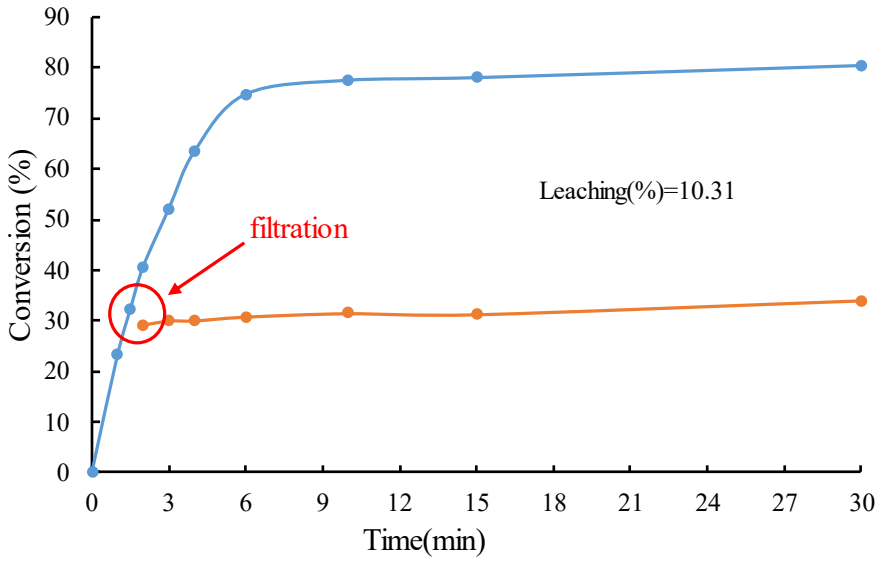

Figure 5.20 Hot filtration test after adding **1** at once, error bars account for 5% uncertainty.

To test the reusability of MOF materials (**Figure 5.21**), up to 6 reactions were carried out with the same catalyst. **Figure 2.21** shows that MOF **23** can be recovered at the end of the reaction via centrifugation, washed, and reused six times, maintaining a good catalytic activity. Nonetheless, the catalytic efficiency of MOF **23** diminished to 30% after six uses, which could be attributed to the gradual (minor) leaching of active species during the reaction.

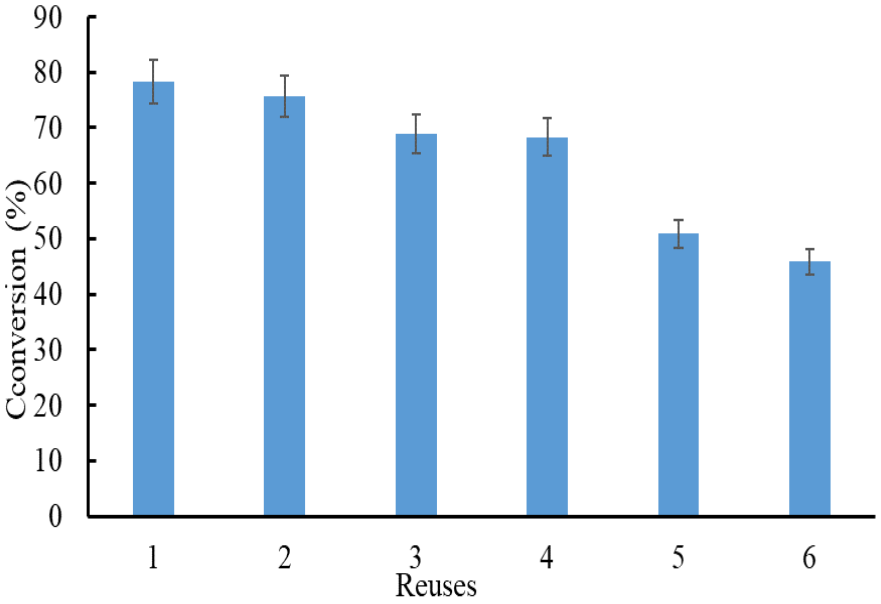

Figure 5.21 Catalytic reuses for the Buchner ring expansion reaction between toluene **2** and ethyl diazoacetate **1** catalyzed by MOF **23** under the reaction conditions indicated in the main text. Error bars account for a 5% uncertainty.

Herein, to assess the scope of the MOF **23** catalyst for the Buchner ring expansion reaction, other aromatic substrates were tested, as can be seen in **Table 5.1**. The reaction with halogenated, cyano, methoxy, and ortho-disubstituted aromatic compounds (products **13, 14, 17, 15, 16,** and **18,** respectively) yielded good to excellent results with short reaction times (<2 h). These findings are noteworthy due to the difficulty in finding the results in the existing literature on Ag-catalyzed Buchner ring expansion reactions.[352-355] The slightly lower yields obtained with larger substrates **11** and **12** can be attributed to the size selectivity of MOF **23**'s microporous structure. This theory was supported by the absence of product **20** when 1,3,5-triisopropylbenzene **19** was used as a substrate, as shown in **Figure 5.21**. However, when the $Rh_2(OAc)_4$ salt was used as a catalyst (5 mol %) with this substrate **19**, the yield was 69%. Additionally, **Figure 5.22** shows diffusion tests conducted with different stirring speeds, confirming that the initial reaction rate is influenced by the

stirring, providing further evidence that the reaction takes place within the channels of the MOF, where diffusion is limited.

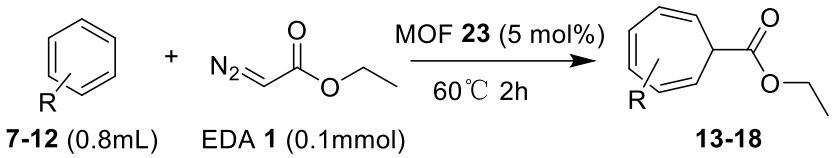

entry	aryl substrate	substituent(s)	product	yield (%)[a]
1	7	Cl	13	66.5
2	8	Br	14	64.9
3	9	CN	15	92.8
4	10	OMe	16	82.6
5	11	CH_2Br	17	50.2
6	12	Me-*ortho*-F	18	72.7

[a]:GC yields after syringe pump addition of **1**.

Table 5.1 Results for the Buchner ring expansion reaction between different aromatics **7**−**12** and **1**, Catalyzed by MOF **23**

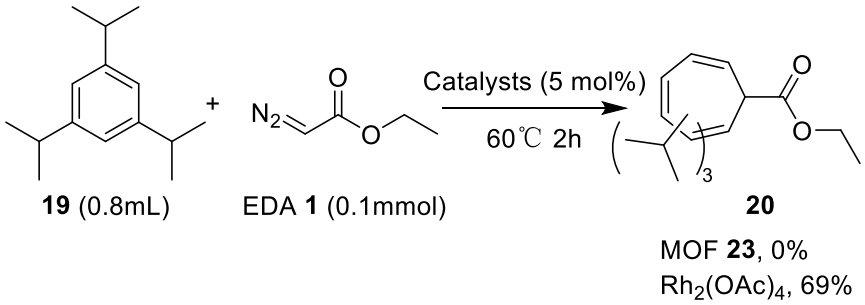

Figure 5.21 1,3,5-Triisopropylbenzene as a substrate for the Buchner ring expansion reaction with ethyl diazoacetate **1** catalyzed by MOF **23** and $Rh_2(OAc)_4$.

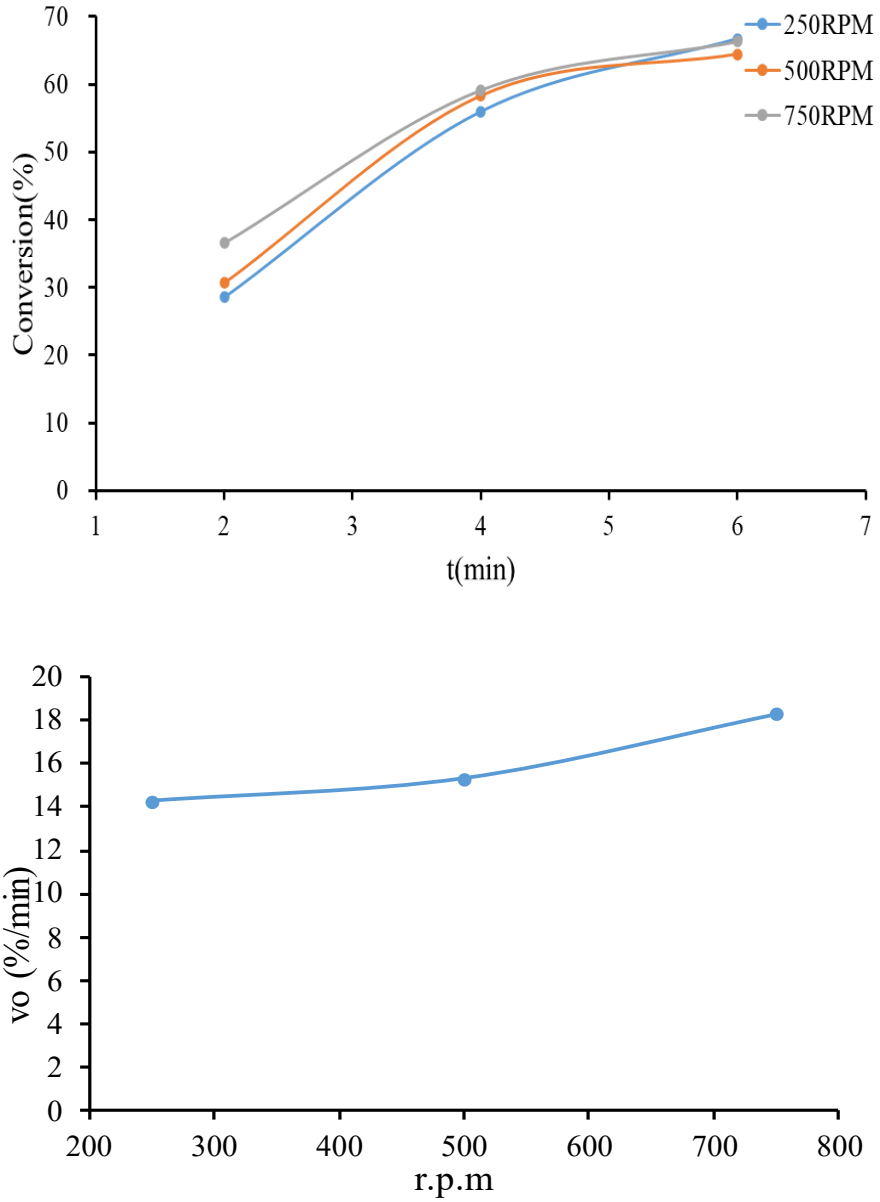

Figure 5.22 Top: Kinetics for the Buchner ring expansion reaction between toluene **2** and ethyl diazoacetate **1** catalyzed by MOF **23** under increasing stirring speeds. Bottom: The corresponding initial rate-stirring rate correlation.

Finally, the stability of the catalyst after the reaction was evaluated. **Figure 5.23** and **Figure 5.24** show, respectively, the PXRD and XPS measurements of the used MOF catalysts, which confirm the integrity of MOF **23** after reaction.

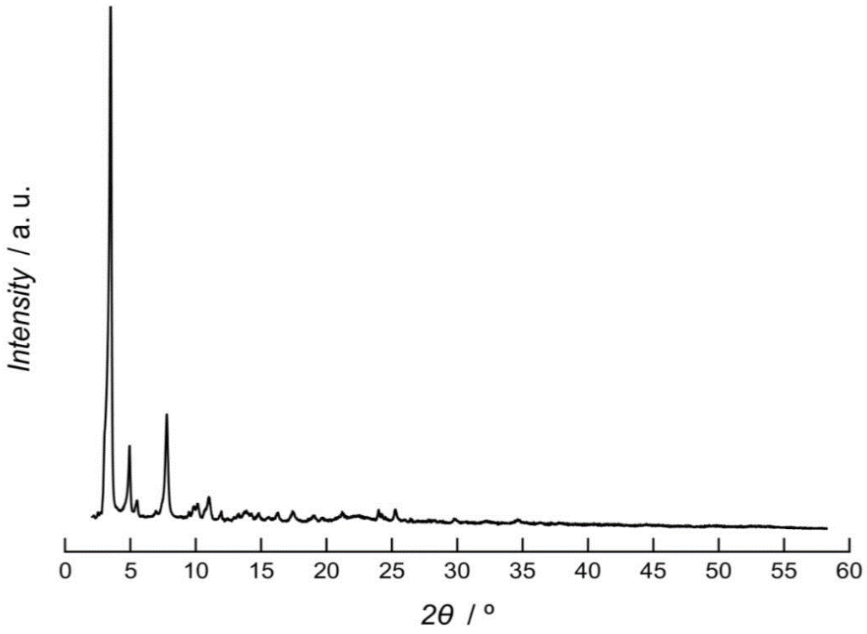

Figure 5.23 Experimental PXRD pattern profile of **23**, in the 2θ range 2-60°, after catalytic experiments.

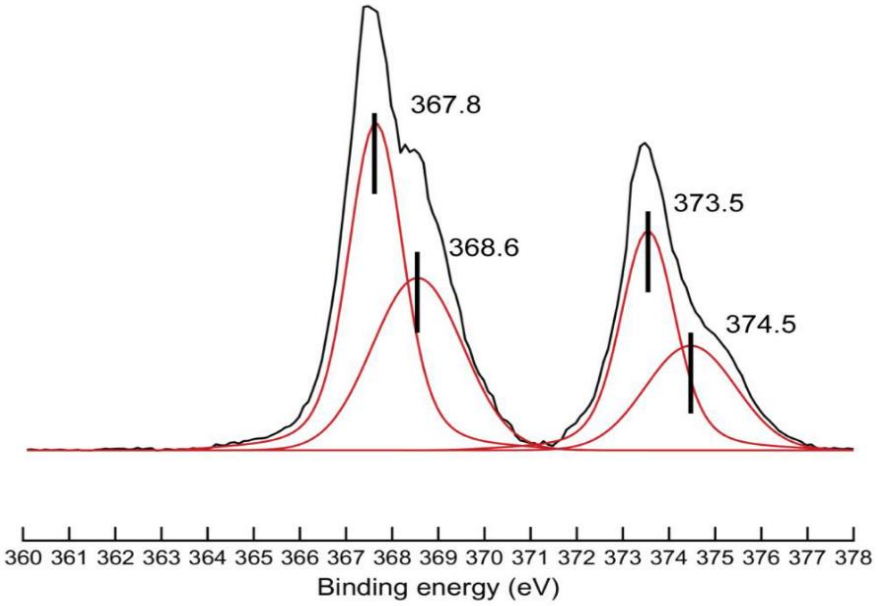

Figure 5.24 X-ray photoelectron spectroscopy (XPS) of **23** after catalytic experiments.

5.4 *Conclusions*

In conclusion, using a previously reported MOF as a chemical reactor, the synthesis, stabilization, and characterization of ligand-free Ag_2^0 clusters has been successfully achieved. The use of this support has not only allowed the catalytic use of Ag in a complex organic synthesis reaction, such as the Buchner ring expansion reaction, but also its recovery and reuse. After being reused six times, the catalyst still maintains high activity.

Chapter 6. Carbene insertion reactions by dealuminated zeolites

6.1 *Introduction*

As we have already mentioned throughout this thesis, carbene-mediated reactions systematically require the use of soluble and unrecoverable metal complexes, often expensive, which renders the processes unaffordable for high-scale synthesis. The use of metals is necessary in order to control not only the generation of carbenes, but also the selective insertion reaction into the desired bond. [356] Without proper control, this sequential process can be plagued by unwanted side reactions, including carbene decomposition, oligomerization, unproductive water insertion, and others.

Figure 6.1 illustrates that metal complexes are the predominant catalysts employed for the insertion reaction of carbenes. [352] Copper (Cu), silver (Ag), and rhodium (Rh) are commonly used as the metal atom site, although other metals such as gold (Au), [357] palladium (Pd), [358] iron (Fe), [359] and ruthenium (Ru) [360] also exhibit catalytic activity with the appropriate coordination environment. The precise coordination environment required for these reactions is similar to that found in enzymes, which is why metal-catalyzed carbene-mediated reactions have been incorporated into the Nobel Prize-winning directed evolution of enzymes methodology. This need for a precise catalytic structure to selectively perform carbene insertion reactions has hindered the development of solid metal catalysts, with only a few reported examples in the literature, [145, 314, 359-366] among which are the solid catalysts described in *Chapters 4* and *5*.

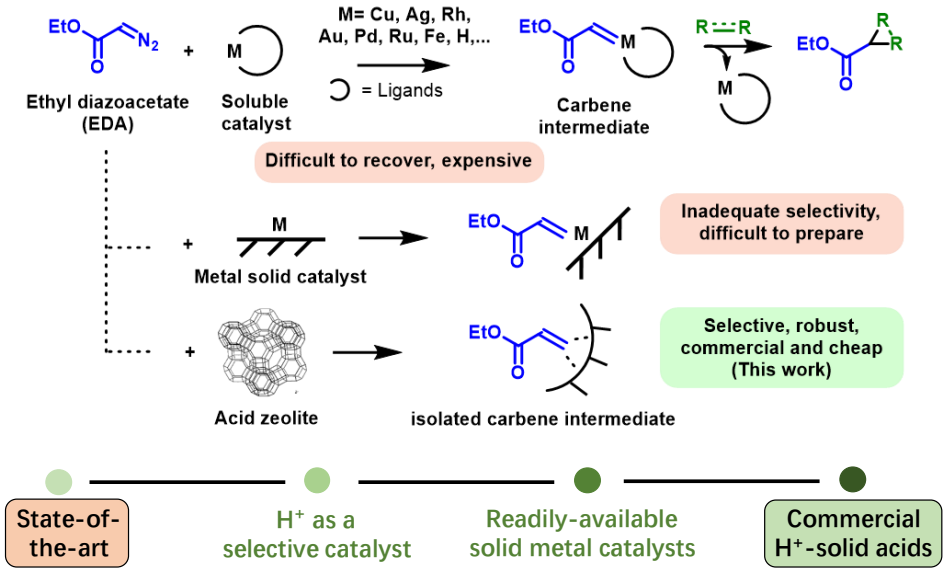

Figure 6.1 State-of-the-art of carbene insertion reactions and desired evolution for wider implementation of the reactions: from soluble metal (Lewis) complex and Brønsted acid catalysts, to supported metals and commercially available solid acids (zeolites, this work).

In addition to metals, simple protons are capable of generating and catalyzing carbene insertion reactions. [367] However, like metals, protons also require a specific structural site to control the carbene generation and subsequent reactivity, even more precisely than in metals. This could explain why there are significantly fewer reported Brønsted-catalyzed carbene insertion reactions compared to metal catalysts. [368] In some cases, a combination of metals and protons are used. [369] Interestingly, the historical origins of catalytic carbene insertion reactions can be traced back to simple protons. [370, 371] In 1928, Robinson and Bradley reported the insertion of a diazoketone in acetic acid, [370] and just three years later, in 1931, Brønsted and Bell studied the insertion reaction of ethyl diazoacetate (EDA) in H_2O or alcohols catalyzed by various acids, to further support the acid theory. [371] However, the limited scope of the reaction and the lack of selectivity in more complex substrates have traditionally relegated Brønsted catalysts for carbene insertion reactions to a secondary role.

Zeolites are commercially available in both acid and base forms, [372] and exhibit a high inner surface area. For example, in the 1990s, Kupfer[142] utilized diazirine undergo decomposition into nitrogen and corresponding zeolite−carbene complexes within several alkali/alkaline earth cation-exchanged X-type/Y-type Faujasite zeolite. In the year of 2006, Moya-Barrios[147] presented the first spectroscopic evidence for the formation of halo-phenylcarbene within alkaline cation-exchanged Y zeolites. Unlike soluble acids, the acid or base sites in zeolites are located within the cavities of the material, isolated from each other. [373] The discovery of the carbene insertion reaction of diazocarbonyl compounds has demonstrated that this reaction is facilitated by acid catalysis. Furthermore, the level of selectivity in this reaction is directly proportional to the degree of definition and isolation of the catalytic site. Therefore, acid zeolites have the potential to catalyze the carbene insertion reaction in a highly selective manner. A notable example is the zeolite H-ZSM5, which was shown to catalyze the polymerization of CH_2 units by decomposing EDA. [374] Although the EDA carbene did not insert into other molecules in this case, it suggests that a specific acid zeolite from the commercially available options could catalyze the generation and carbene insertion reaction of diazocarbonyl compounds with good selectivity towards useful organic compounds. The key to achieving this selectivity lies in finding an acid zeolite with the appropriate strength and steric environment to minimize potential by-reactions such as polymerization. **Figure 6.1** also illustrates how this approach represents a significant advancement in the design of carbene insertion organic reactions, by utilizing a metal-free catalyst [375] that is both solid and easily recoverable and commercially available. This strategy is the one that has been followed in this *Chapter*, in which we will show how simple and commercially available microporous solid Brønsted acids catalyze the carbene generation and insertion reaction of common diazoacetates, after dealuminating zeolites.

6.2 *Synthesis and characterization of HY dealuminated zeolite catalysts*

6.2.1 *Synthesis of HY dealuminated zeolite catalysts*

Commercially available CBV720 HY, CBV760 HY, CBV780 HY, Hβ and ZSM-5 zeolite (3g), were treated with a 0.085M (3g, 200mL H_2O) aqueous solution of ammonium fluorosilicate for 20h at room temperature, to give the corresponding dealuminated zeolites. The resulting solids were filtered and dried on the oven at 100℃. Subsequently, dealuminated HY zeolites were dried under vacuum at 250 ℃ overnight

6.2.2 *Inductively coupled plasma atomic emission spectroscopy (ICP-AES)*

In order to assess the possible existence of trace metals in the zeolites, the analyses of residual metals in the commercial zeolites HY and the corresponding dealuminates zeolites are shown in **Tables 6.1** and **6.2**. It can be seen that the main metal impurities in the zeolites that could catalyze any carbene formation correspond to Ni, Cu, Fe and Pt. Therefore, we prepared samples with intentionally metal added quantities, and the corresponding analyses are shown in **Tables 6.3** and **6.4**. All these zeolites will be tested to catalyze the carbene-mediated reactions.

Table 6.1 Inductively coupled plasma-atomic emission spectroscopy (ICP-AES) results for the CBV 720 HY zeolite (Si/Al= 15).

CBV 720 HY analyte	Concentration average (ppm)
Pt	10.44
Cr	1.19
Ni	3.17
Co	-1.17
Ru	-3.61
Au	9.47
Mn	0.64
Fe	146.25
Cu	11.65
Ag	0.95
Pd	-15.64
Rh	-46.64
Al	30874.97

Table 6.2 Inductively coupled plasma-atomic emission spectroscopy (ICP-AES) results for the dealuminated CBV 720 HY zeolite (Si/Al= 15).

dealuminated CBV 720 HY analyte	Concentration average (ppm)
Pt	11.76
Cr	0.36
Ni	6.84
Co	-0.16
Ru	-4.98
Au	4.07
Mn	1.19
Fe	143.76
Cu	8.63
Ag	-0.72
Pd	-10.724
Rh	-30.66
Al	10030.426

Table 6.3 Inductively coupled plasma-atomic emission spectroscopy (ICP-AES) results for Ni-NaY.

Ni-NaY analyte	Concentration average (ppm)
Pt	-5.14
Cr	-10.37
Ni	45126.77
Co	26.03
Ru	8.21
Au	5.15
Mn	2.47
Fe	161.07
Cu	18.36
Ag	-1.25
Pd	-24.95
Rh	-72.57
Al	120355.12

Table 6.4 Inductively coupled plasma-atomic emission spectroscopy (ICP-AES) results for CuFePt-dealuminated HY.

CuFePt-dealuminated HY analyte	Concentration average (ppm)
Pt	24.77
Fe	279.69
Cu	131.99

6.2.3 *Brunauer-Emmett-Teller surface area analysis (BET)*

Compared with fresh HY zeolites (**Figure 6.2**), the different dealuminated HY zeolites (**Figure 6.3**) have similar micropore and mesopore volume, the Brunauer, Emmett and Teller (BET) surface area is ca. 730 $m^2 \cdot g^{-1}$, mesopore volume is around 0.18-0.2 cm^3/g, and all the BET values are shown in **Table 6.5**.

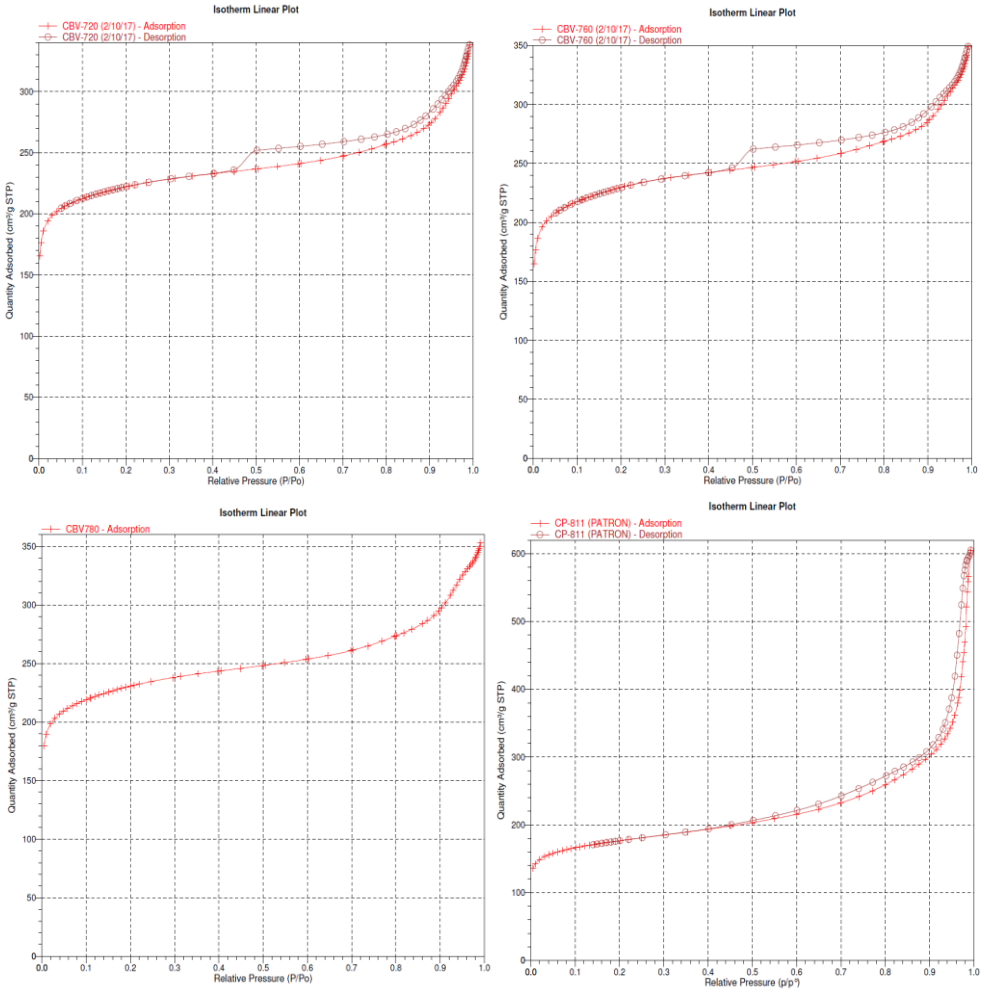

Figure 6.2 Isotherm plots for HY /dealuminated zeolite HY (from commercial CBV 720) and H-Beta zeolite with Si/Al ratio of 15 (top), 30 (middle) and 40 (bottom).

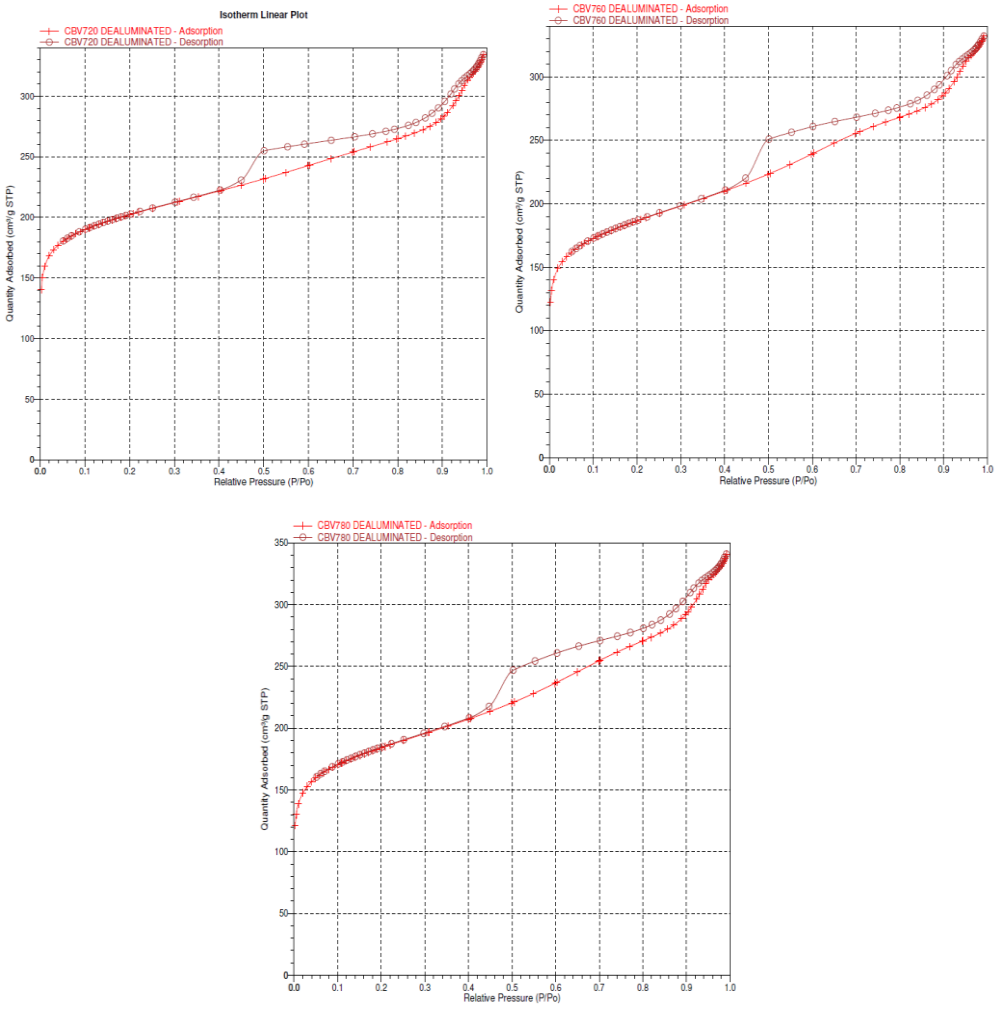

Figure 6.3 Isotherm plots for dealuminated zeolites HY (from commercial CBV 720, 760 and 780).

Table 6.5 Physicochemical properties of the active acid zeolites employed in this work.

Solid Acid	Si/Al molar	BET surface area ($m^2 \cdot g^{-1}$)[a]	Total pore volume ($cm^3 \cdot g^{-1}$)[a]	Particle or crystal size (μm)	Micropore volume ($cm^3 \cdot g^{-1}$)[a]	Mesopore volume ($cm^3 \cdot g^{-1}$)[a]
HY (720)	15	723	0.44	0.70-1.00	0.32	0.13
HY (760)	30	753	0.52	0.70-1.00	0.33	0.14
HY (780)	40	756	0.55	0.70-1.00	0.32	0.16
HY (dealuminated)	N.D.	667	0.51	0.70-1.00	0.24	0.20
H-Beta	12.5	566	0.89	0.6	0.19	0.30

[a] Brunauer, Emmett and Teller (BET) surface area and total pore volume values were determined by nitrogen adsorption-desorption experiments. N.D.: Non-determined.

6.2.4 *Field emission scanning electron microscopy (FESEM)*

Figure 6.4 shows that the crystallites in the H-Y zeolite (CBV720 Si/Al = 15) are homogenous in size and composition, between 0.7 and 1.0 μm, according to FESEM. The Beta-H zeolite also shows relatively similar characteristics, shown in **Figure 6.5.**

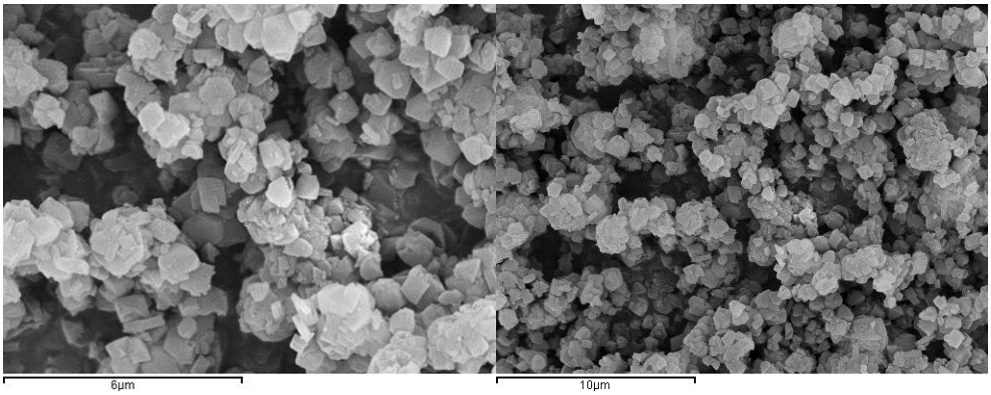

Figure 6.4 Representative field emission scanning electron microscope (FESEM) images of H-Y zeolite with CBV 720 Si/Al ratio of 15.

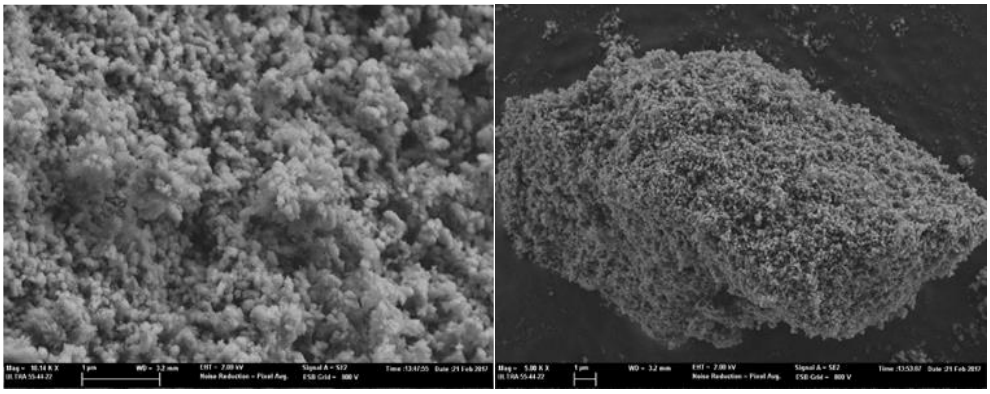

Figure 6.5 Representative field emission scanning electron microscope (FESEM) images of H-Beta zeolite

6.2.5 *High-resolution transmission electron microscopy (HR-TEM) and electron diffraction x-ray detector (EDX)*

Here, the HR-TEM and EDX measurements carried out on the H-Y zeolite (Si/Al = 15, CBV720) both fresh and dealuminated, and H-Beta are shown, which corresponds to **Figure 6.6, Figure 6.7** and **Figure 6.8**, respectively. Comparing the EDX of **Figure 6.6** and **Figure 6.7**, we can see that all elements are homogeneously distributed on the catalyst surface. At the same time, the dealuminated sample shows that the aluminum content is significantly reduced, which is consistent with ICP results.

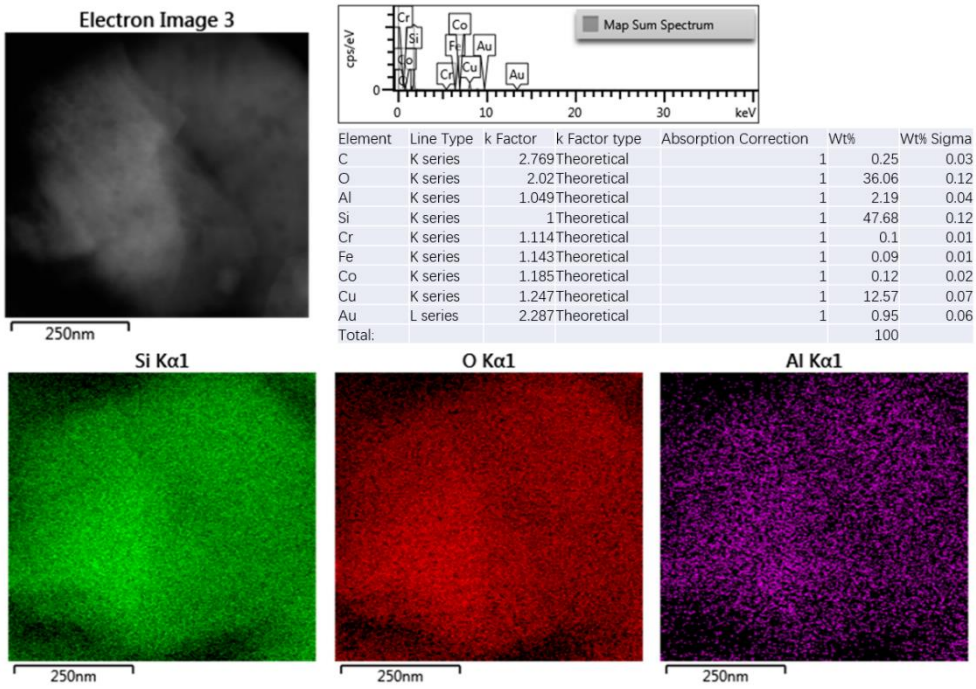

Element	Line Type	k Factor	k Factor type	Absorption Correction	Wt%	Wt% Sigma
C	K series	2.769	Theoretical	1	0.25	0.03
O	K series	2.02	Theoretical	1	36.06	0.12
Al	K series	1.049	Theoretical	1	2.19	0.04
Si	K series	1	Theoretical	1	47.68	0.12
Cr	K series	1.114	Theoretical	1	0.1	0.01
Fe	K series	1.143	Theoretical	1	0.09	0.01
Co	K series	1.185	Theoretical	1	0.12	0.02
Cu	K series	1.247	Theoretical	1	12.57	0.07
Au	L series	2.287	Theoretical	1	0.95	0.06
Total:					100	

Figure 6.6 Representative high-resolution transmission electron microscopy (HR-TEM) images of HY zeolite with Si/Al ratio of 15 (top) and the corresponding electron diffraction X-ray (EDX) analysis and mapping.

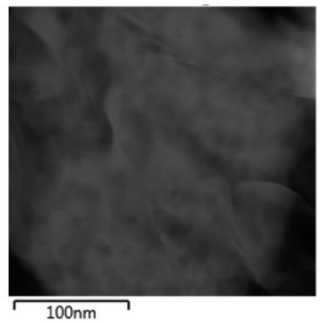

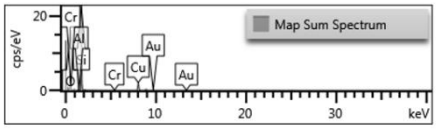

Element	Line Type	k Factor	k Factor type	Absorption Correction	Wt%	Wt% Sigma
C	K series	2.769	Theoretical	1	2.81	0.09
O	K series	2.02	Theoretical	1	43.4	0.17
Al	K series	1.049	Theoretical	1	0.37	0.03
Si	K series	1	Theoretical	1	43.14	0.16
Cr	K series	1.114	Theoretical	1	0.06	0.02
Cu	K series	1.247	Theoretical	1	9.77	0.09
Au	L series	2.287	Theoretical	1	0.46	0.06
Total:					100	

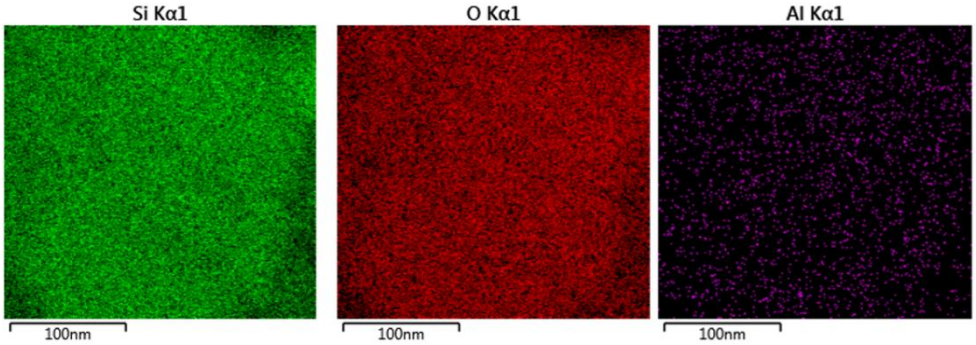

Figure 6.7 High-resolution transmission electron microscopy (HR-TEM) image, and corresponding EDX analysis and mapping of dealuminated zeolite HY (from commercial CBV 720).

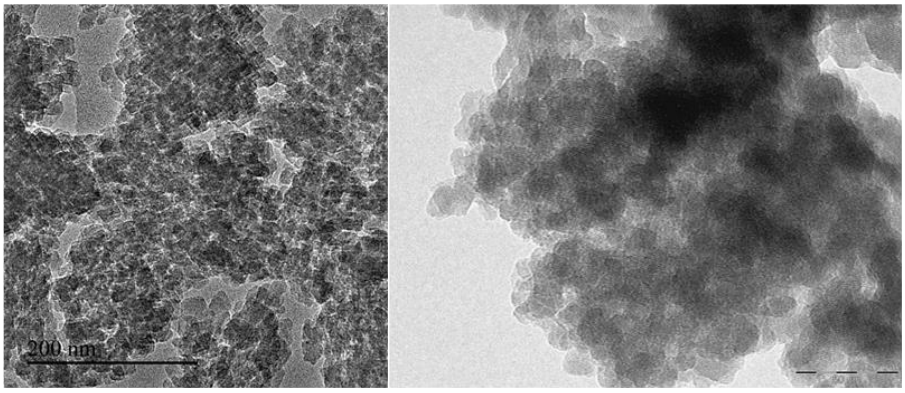

Figure 6.8 High-resolution transmission electron microscopy (HR-TEM, bottom) images of the H-Beta zeolite

6.2.6 *^{27}Al solid-state nuclear magnetic resonance (^{27}Al ssNMR)*

Figures 6.9 to **6.12** show the ^{27}Al ssNM spectra of the different zeolites, where the aluminum in the framework and extra framework can be evaluated. From the Figures, we can see that the integrated areas of the solid NMR peaks, corresponding to silicon-to-aluminum ratios, are different. Comparing **Figures 6.9** with **Figure 6.12**, the latter being that of the dealuminated zeolite, the peak area of aluminum at the -0.5 ppm position has been significantly reduced, demonstrating the disappearance of extra-framework aluminum.

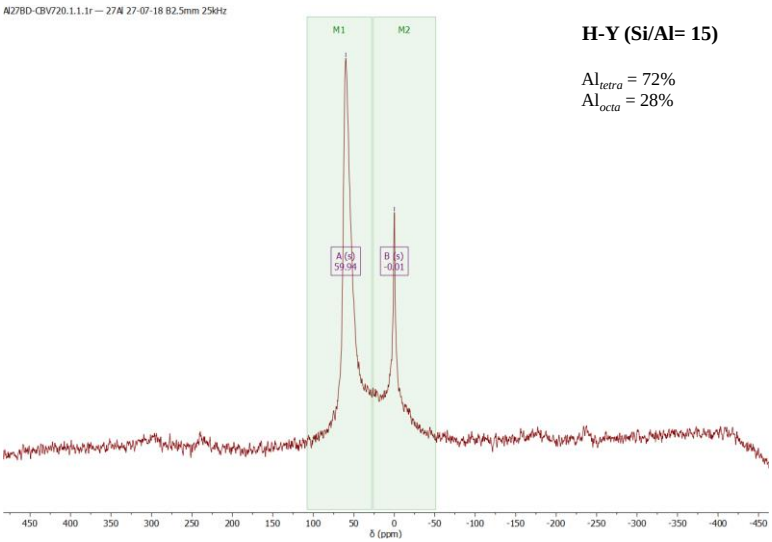

Figure 6.9 ^{27}Al solid-state nuclear magnetic resonance (ssNMR) of HY zeolite (Si/Al= 15).

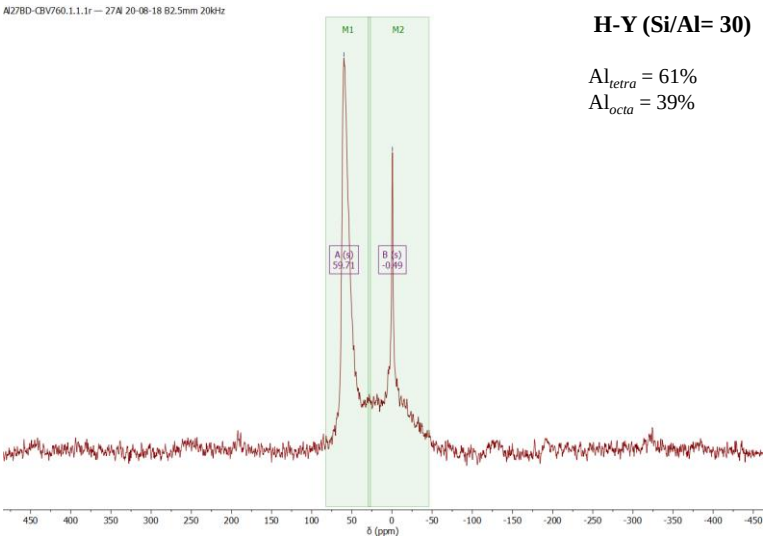

Figure 6.10 ^{27}Al solid-state nuclear magnetic resonance (ssNMR) of HY zeolite (Si/Al= 30).

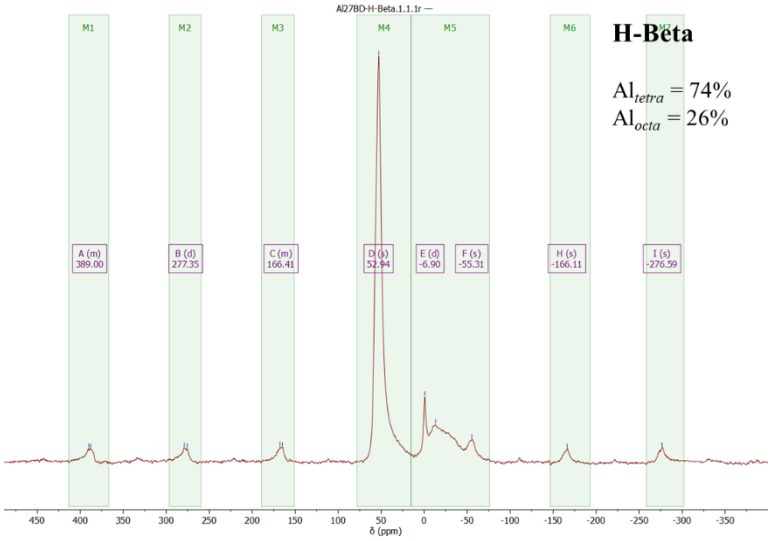

Figure 6.11 ^{27}Al solid-state nuclear magnetic resonance (ssNMR) of H-Beta zeolite (Si/Al= 12.5).

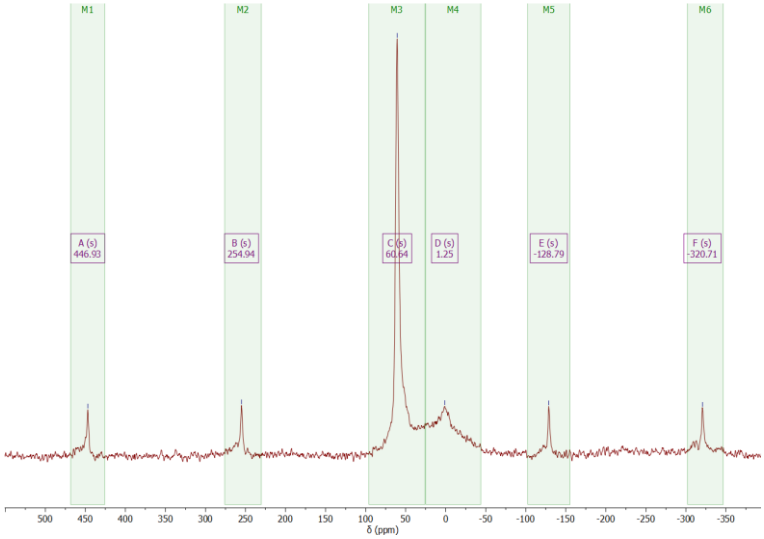

Figure 6.12 ^{27}Al solid-state nuclear magnetic resonance (^{27}Al ssNM) of dealuminated HY zeolite (Si/Al= 15).

6.2.7 *Fourier transformed infrared spectroscopy (FT-IR)*

In **Figure 6.13**, the FTIR spectrum of various silver zeolite catalysts is depicted. The FT-IR spectrum presented here also validates the preservation of the aluminosilicate composition following the dealuminated process, indicating that the zeolite structure remained unaffected by the calcination.

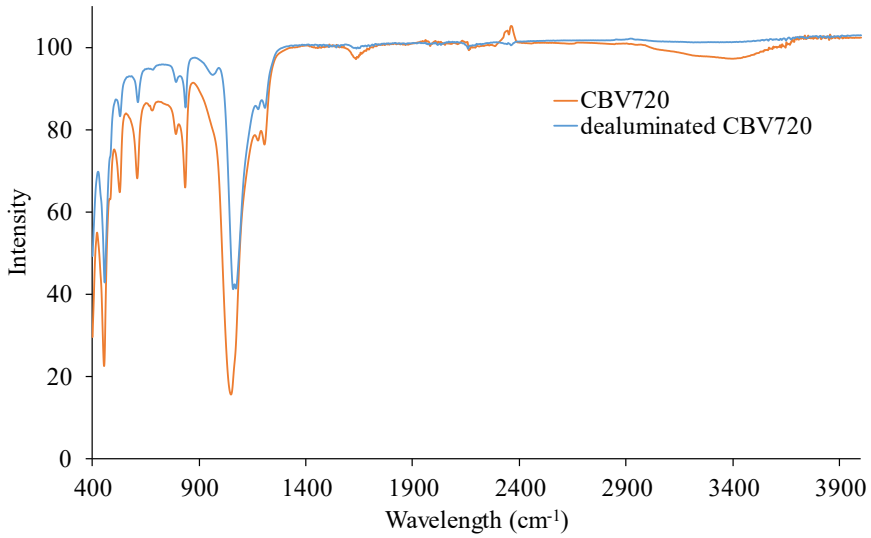

Figure 6.13 Fourier transformed infrared spectroscopy (FT-IR) of the dealuminated HY zeolite compared to the starting HY zeolite (Si/Al = 15).

6.2.8 *Powder X-ray diffraction (XRD)*

From **Figure 6.14** to **Figure 6.16** shown are fresh HY zeolite XRD, dealuminated HY XRD, and dealuminated zeolite after 5 cycles. In certain cases, the dealuminated HY sample was also evaluated for comparison. The XRD analysis of the 5 cycles dealuminated HY sample indicates that the diffraction peaks of the zeolite are retained after 5 catalyst cycles (see ahead), as shown in **Figure 6.14**.

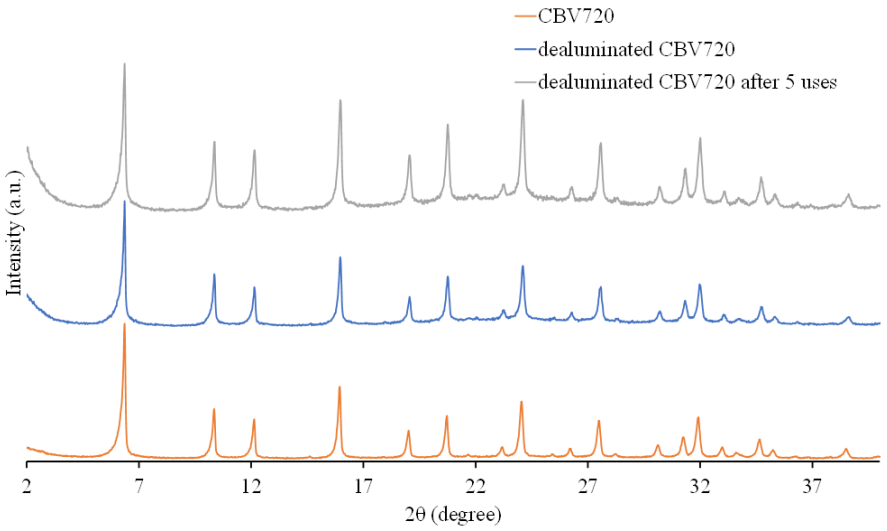

Figure 6.14 Powder X-ray diffractions (PRXD) of the HY zeolite (Si/Al= 15, CBV 720), after dealumination and after 5 catalytic uses.

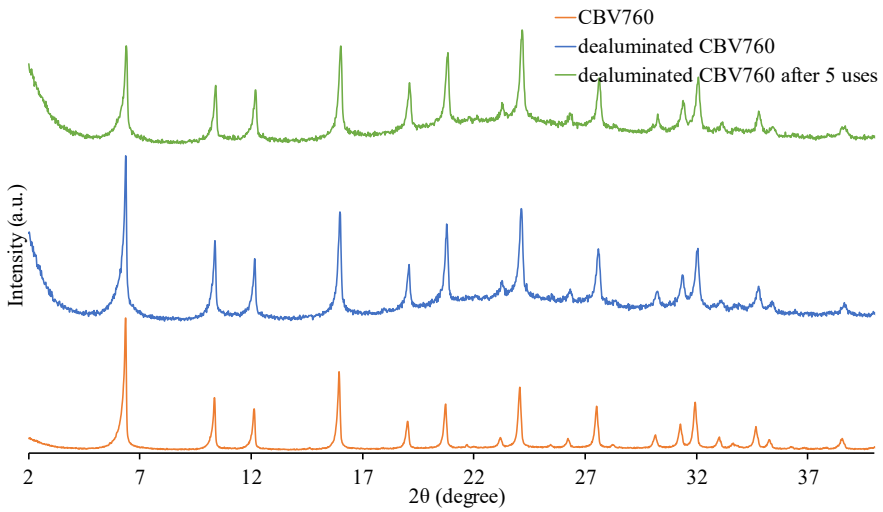

Figure 6.15 Powder X-ray diffractions (PRXD) of the HY zeolite (Si/Al= 30, CBV 760), after dealumination and after 5 catalytic uses.

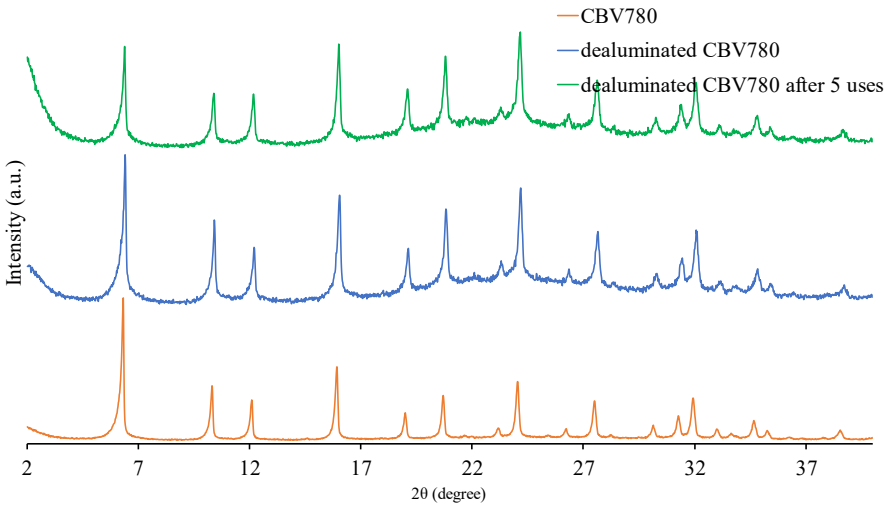

Figure 6.16 Powder X-ray diffractions (PRXD) of the HY zeolite (Si/Al= 40, CBV 780), after dealumination and after 5 catalytic uses.

6.3 *Dealuminated zeolite as a catalyst for carbene reaction of EDA*

In this section, the catalytic activity of different solid acids was investigated by studying the reaction between ethyl diazoacetate (EDA **1)** and toluene **2,** the Buncher ring expanding reaction, and the results are shown in **Table 6.6**. In order to activate the inorganic solids (zeolites and oxides) for the reaction, they were dried at 250 ºC under vacuum for more than 20 h. In the case of the organic Amberlyst solids, they were dried at a lower temperature (150 ºC) to prevent any decomposition. [376] It is important to note that although this drying procedure does not remove all the water from the solids, a significant portion is eliminated, which is sufficient to activate the acid sites on the solids. The reaction model allows for the identification of various products, including product **3,** that is formed through the insertion reaction into an aromatic C=C bond (the Buchner reaction), product **4,** that is formed through the insertion reaction into the C-H bond of the methyl group, and product **5,** that is formed through the expected O-H insertion of the remaining water in the solids. Additionally, ether **6** can be formed through the condensation of product **5** or through the more challenging activation of O_2. To investigate this possibility, the reactions were conducted under dry air. Interestingly, it was observed that the dimers of **1** (diethyl fumarate and maleate) were not detected under these specific reaction conditions.

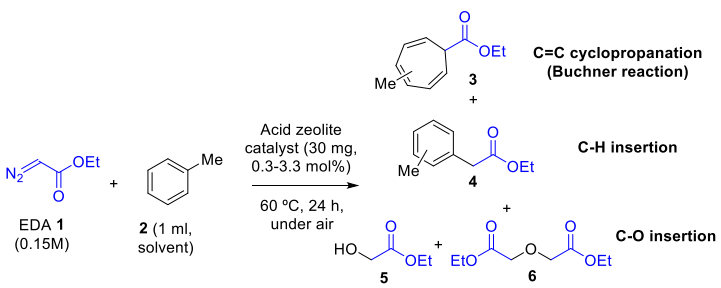

Figure 6.17 Catalytic Buncher ring expanding reaction by dealuminated acid zeolite catalysts.

Table 6.6 Catalytic results for the reaction of ethyl diazoacetate (EDA) **1** in toluene solvent **2** (0.15M) in the presence of different acid solids (30 mg, typically 0.3 to 3.3 H^+ mol%) under the indicated reaction conditions.

Entry	Commercial solid	Si/Al[a]	$H^{+,b}$	Conv. of 1(%)[c]	Selectivity (%)[c]			
					3	4	5	6
1	H-Beta	12	3.3	4.9	3.2	1.7	-	-
2	H-USY (CBV720)	15	3.0	>99.0	-	23.2	62.2	14.6
3	H-USY (CBV760)	30	1.5	>99.0	-	34.9	18.9	46.2
4	H-USY (CBV780)	40	1.2	>99.0	-	18.4	4.2	77.4
5	Na-Y	2.5	-	-	-	-	-	-
6	Al_2O_3	-	<0.5	-	-	-	-	-
7	SiO_2 -Al_2O_3	7	<1.0	34.8	-	0.3	27.9	6.5
8	Amberlyst A15	-	3.0	33.8	-	8.4	16.7	8.7
9	Amberlyst A16	-	3.0	3.2	-	-	-	3.2
	Further dealuminated solid acids							
10[d]	HY dealuminated (from Si/Al 15)	>100	0.3	>99.0 (>99.0)	29.3 (47.0)	26.2 (30.0)	3.0 (6.7)	41.2 (16.2)
11	(from Si/Al 30)	>100	<0.5	>99.0	35.0	25.3	2.1	37.7
12[d]	(from Si/Al 40)	>100	<0.5	>99.0 (87.4)	38.5 (51.8)	21.7 (30.4)	1.9 (3.7)	37.8 (1.5)
13	H-Beta dealuminated	>100	<0.5	4.9	3.1	1.8	-	-
14	H-ZSM5 dealuminated	>100	<0.5	19.6	5.3	1.0	13.3	-

[a] Provided by the commercial houses and checked by inductively coupled plasma-atomic emission spectroscopy.

[b] Total number of Brønsted acid sites determined by pyridine titrations, followed by Fourier-transformed infrared spectroscopy (FT-IR) after in-situ adsorption/desorption cycles at different temperatures.

[c] Measured by gas-chromatography coupled to mass spectrometry (GC-MS) and checked by ^1H, ^{13}C and distortionless enhancement by polarization transfer (DEPT) nuclear magnetic resonance (NMR).

[d] Results between parentheses correspond to reactions performed under N_2 atmosphere.

The Si/Al ratio did not assume the acidity of the different zeolites; rather, it was measured through pyridine titrations using in-situ Fourier-transformed infrared spectroscopy (FT-IR) instrumentation. The measurements were carried out with adsorption/desorption cycles at different temperatures, as indicated in **Table 6.7** for values and **Figures 6.18** and **6.19** for representative spectra. Pyridine was chosen as the base probe due to its similarity in size to the reactants and products **1**-**6** in the studied reaction, making it more suitable than NH_3. NH_3 would have measured unproductive acid sites. However, the validity of the pyridine titration values at different reaction temperatures was confirmed through temperature-programmed ammonia desorption (TPD) analysis of the HY and H-Beta zeolites, which showed linear results (**Figure 6.20**). The detailed analysis of the FT-IR pyridine titration results revealed that the number of total Brønsted acid sites in the HY zeolites decreases linearly with the Si/Al ratio, with approximately 0.01, 0.05, and 0.025 mmol $H^+ \cdot g^{-1}$ for Si/Al ratios of 15, 30, and 40, respectively. Similarly, the H-Beta zeolite (Si/Al= 12.5) exhibited a loading of ~0.01 mmol $H^+ \cdot g^{-1}$. It is worth noting that the number of Lewis sites also correlated well with the Si/Al ratio for the Faujasite zeolites, as shown in **Table 6.7.**

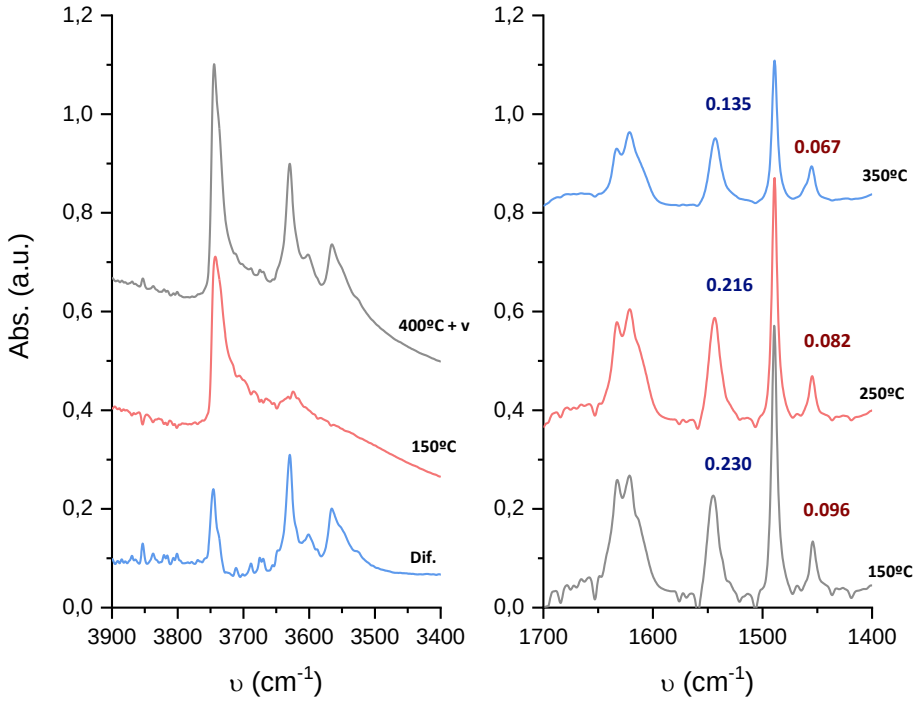

Figure 6.18 Pyridine titrations of the HY zeolite (Si/Al = 15), followed by *in-situ* FT-IR after desorption under vacuum at different temperatures. Left: FT-IR spectra of HY zeolite at 150, 400 ºC and the difference between them. Right: FT-IR spectra of pyridine adsorbed HY zeolite at 150, 250 and 350 ºC. The three bands observed in the OH stretching region at 3746, 3630 and 3566 cm^{-1} are attributed to silanol groups, acidic OH groups in supercages (β cages) and acidic OH groups in sodalite cages (α cages), respectively. The band attributed to pyridine molecules coordinated to Lewis's acid sites and that to pyridinium ions formed by protonation of pyridine on Brønsted acid sites are observed at 1455 and 1544 cm^{-1}, respectively.

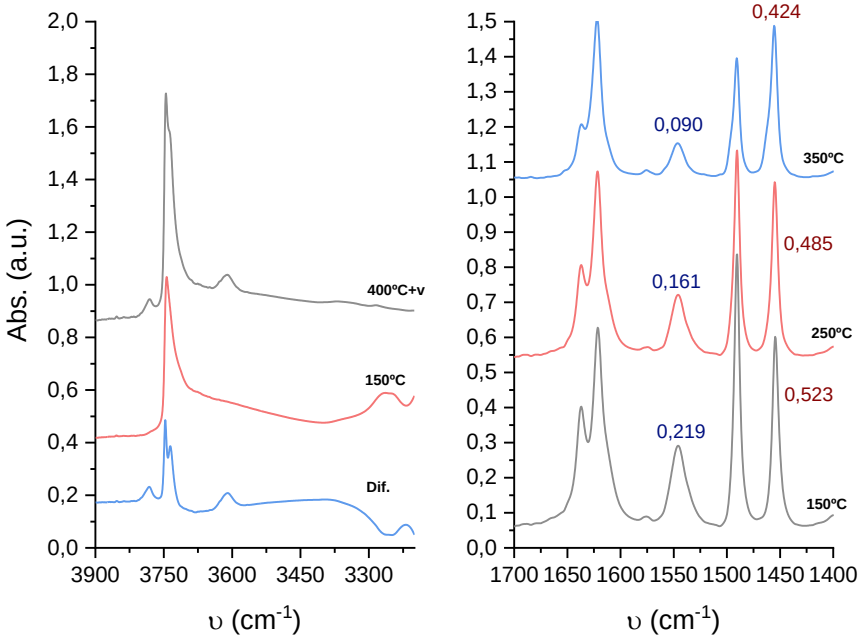

Figure 6.19 Pyridine titrations of the H-Beta zeolite, followed by *in-situ* FT-IR after desorption under vacuum at different temperatures. Left: FT-IR spectra of H-Beta zeolite at 150, 400 ºC and the difference between them. Right: FT-IR spectra of pyridine adsorbed HY zeolite at 150, 250 and 350 ºC.

Table 6.7 Acidic properties of the zeolites employed in this work, determined from the corresponding FT-IR spectra after pyridine desorption.

		Brønsted acidity (umol pyridine · g^{-1} catalyst)[a]				Lewis acidity (umol pyridine · g^{-1} catalyst)[a]			
Solid	Si/Al molar	150 ºC	250 ºC	350 ºC	400 ºC	150 ºC	250 ºC	350 ºC	400 ºC
HY (720)	15	289.56	327.66	172.72	154.1	58.71	80.94	58.14	16.67
HY (760)	30	185.42	172.72	87.63	-	45.6	41.61	19.38	-
HY (780)	40	100.33	82.55	59.69	-	16.53	15.39	11.97	-
HY (deAl)	<1	41.61	8.55	8.55	-	-	-	-	-
H-Beta	12.5	374.65	278.13	154.94	-	393.3	372.21	324.90	-

[a] Measured by Fourier-transformed infrared spectroscopy (FT-IR) with adsorption and desorption of pyridine at different temperatures. Values of (mmol pyridine · g^{-1} of catalyst) were calculated using the extinction molar coefficients given by Emeis.

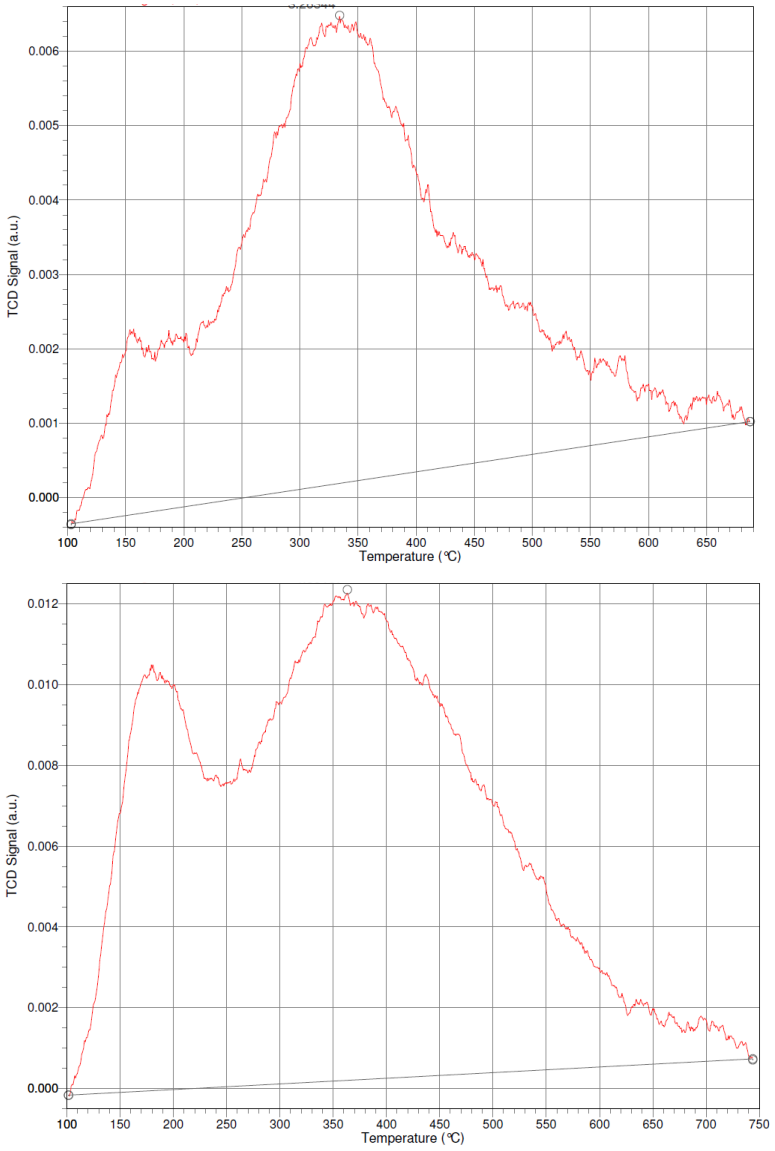

Figure 6.20 Temperature-programmed ammonia desorption (TPD) analysis of the HY zeolite (top, Si/Al = 15) and H-Beta zeolite (bottom, Si/Al = 12.5).

The catalytic results presented in **Table 6.6** demonstrate that the H-Beta zeolite only exhibited minimal activity in the activation of EDA **1**, with small amounts of the insertion reaction products (<5%, entry **1**). In contrast, the different H-Y zeolites

displayed complete conversion of **1** and clear amounts of the carbene insertion products **4**-**6**. These results were confirmed through gas-chromatography coupled to mass spectrometry (GC-MS) and ^{1}H, ^{13}C, and distortionless enhancement by polarization transfer (DEPT) nuclear magnetic resonance (NMR) measurements of the reaction mixture, after zeolite filtration (entries **2**-**4**). Exhaustive Soxhlet extractions of the used zeolites with dichloromethane (CH_2Cl_2), after the reaction, confirmed that over 90% of the products diffused out to the solution, and the relative composition inside the zeolite was similar to that measured in the solution. The products obtained consisted of the C-H (product **4**), C-O (product **5**, resulting from H_2O insertion), and either condensation reaction of **5** or the O=O insertion reaction (product **6**, as explained later). However, the C=C insertion product **3** was not detected in solution, which is reasonable considering that it is arguably the most difficult insertion reaction to achieve without a metal catalyst. It is important to highlight that the HY zeolites with higher Si/Al ratios catalyzed the insertion reactions equally well, but with lower H^+ mol% amounts. Kinetic experiments using the same H^+ mol% amount but varying the wt% amount of the HY zeolite, confirmed the enhanced catalytic activity of the higher Si/Al ratio solids, at least for the commercial CBV760 HY zeolite (Si/Al = 30, **Figure 6.21**).

The Y zeolite lacking any Brønsted acidity (NaY), exhibited no catalytic activity (entry **5**), just like Al_2O_3 (entry **6**). The reaction was somewhat catalyzed by SiO_2-Al_2O_3, resulting in a 35% conversion of **1** (entry **7**), as well as by the organic solid acid Amberlyst A15, with a similar conversion (entry **8**), but barely by Amberlyst A16. These findings confirm that partially dealuminated H-Y zeolites are superior catalysts for the reaction.

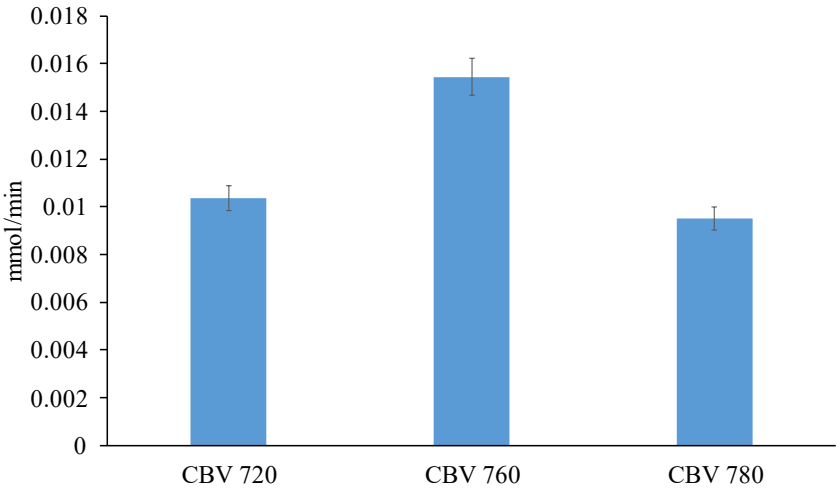

Figure 6.21 Initial conversion rates for the reaction of ethyl diazoacetate (EDA) **1** in toluene solvent **2** (0.15M), in the presence of different HY acid solids (5, 15 and 20 mg for Si/Al ratios of 15, 30 and 40, respectively) under the reaction conditions indicated in **Table 6.6**. GC results. Error bars account for a 5% uncertainty.

Based on these results, we further dealuminated the H-Y zeolite (Si/Al= 15) using a standard protocol (see section 6.2). **Figure 6.14, Figure 6.15** and **Figure 6.16** illustrates that the new dealuminated zeolite maintains the crystallinity and some Brønsted acidity of the parent zeolite but loses most of the Lewis acidity and Al extra-framework, as indicated by powder X-ray diffraction (PRXD), pyridine adsorption FT-IR spectroscopy, and ^{27}Al ssNMR measurements. The new dealuminated HY zeolite also preserves the crystal size of the starting HY zeolite (Si/Al= 15), but the mesoporosity increases by over 50% (**Table 6.5**), while the total Brønsted acidity decreases nearly tenfold.

The increased mesoporosity can be advantageous for the carbene insertion reaction due to enhanced diffusion. However, the significantly lower Brønsted acidity of the new dealuminated HY material raises doubts about its catalytic activity. Surprisingly, the dealuminated HY zeolite catalyzes the carbene insertion reactions of **1** with over 90% conversion and, more importantly, exhibits a 36% selectivity towards

the challenging C=C insertion product **3**, with only 0.3 mol% of acid sites. A hot filtration test demonstrates that there are no catalytically active species in solution (**Figure 6.22**), and accordingly, the zeolite can be reused at least five times with reasonable stability in the reaction yields for each insertion product (**Figure 6.23**) and without any erosion in the crystallinity of the material (see 5.2.8, **Figure 6.14**). Therefore, further dealumination treatment of HY not only enhances the catalytic activity through acid sites but also promotes the formation of product **3** as the primary product of the reaction, suggesting that the Brønsted acid sites are responsible for the catalysis.

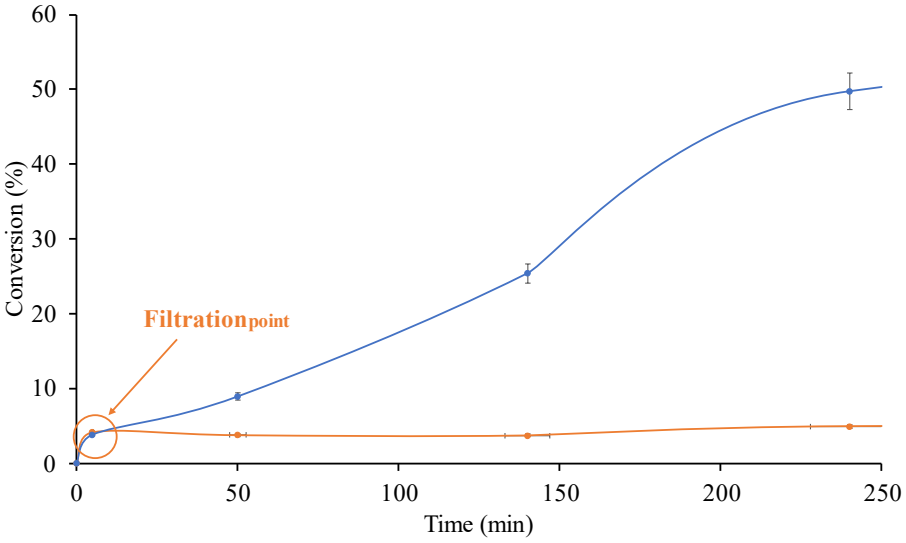

Figure 6.22 Hot filtration test for the reaction of ethyl diazoacetate (EDA) **1** in toluene solvent **2** (0.15M) at 60 ºC, 24 h and air atmosphere, catalyzed by dealuminated HY zeolite (from Si/Al= 15). GC results. Error bars account for a 5% uncertainty.

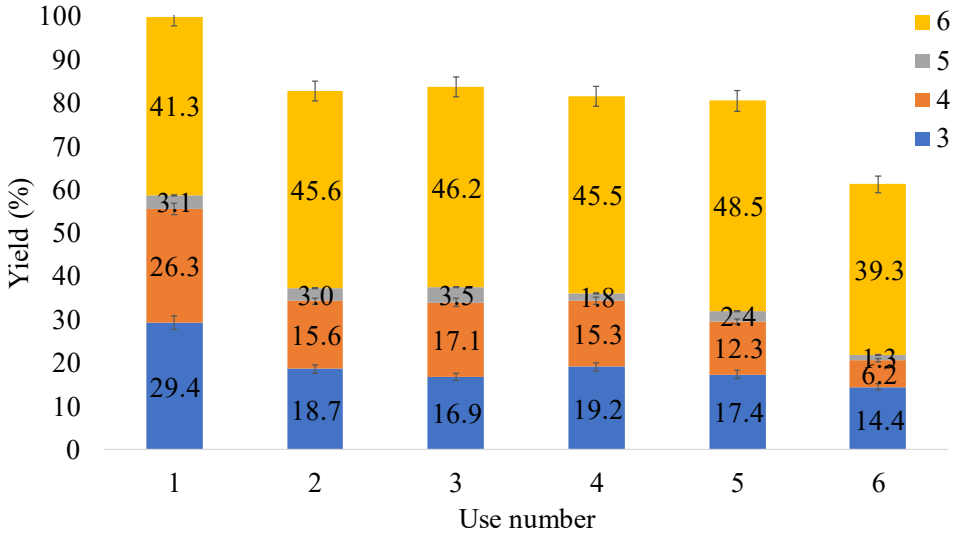

Figure 6.23 Reuses of the dealuminated HY zeolite (from Si/Al= 15) catalyst for the reaction of ethyl diazoacetate (EDA) **1** in toluene solvent **2** (0.15M) at 60 ºC, 24 h and air atmosphere. GC results. Error bars account for a 5% uncertainty.

For the sake of comparison, the other H-Y, H-Beta and, also, the H-ZSM5 zeolite, were submitted to the dealuminization treatment and tested in the model catalytic reaction. The results in **Table 6.6** show that both dealuminated HY zeolites (from Si/Al= 30 and 40) gave very high conversions of **1** and ~50% selectivity to product **3** (entries 11 and 12). In contrast, the dealuminated H-Beta and H-ZSM5 zeolites gave very low conversion of **1** (entries 13 and 14). The two dealuminated zeolites are reusable for at least for 5 times without any apparent erosion of the crystallinity (**Figures 6.14 to 6.16**). These results confirm the extraordinary catalytic activity of high Si/Al HY zeolites compared to any other solid acid tested here for the insertion reaction of the carbene of **1** into toluene **2**.

Product **6** was still obtained in significant amounts, thus decreasing the overall insertion reaction yield of **1** in toluene **2**. The amount of **6** could be significantly diminished when the reaction was run under an inert atmosphere (N_2), to achieve >80% combined yield for C=C and C-H insertion products **3** + **4** (entries 10 and 12, results

between parentheses). The decrease in the formation of **6** when air is not present in the reaction mixture suggests that the product could come from O_2 and not from the condensation reaction of **5**. To check this hypothesis, alcohol **5** was used as a reactant under the same reaction conditions, with or without **1** present in the reaction medium, and the results show any conversion of **5.** The reaction was also carried out using cyclohexane as a solvent in the presence of EDA **1**, to avoid the reaction with toluene **2**, but as shown in **Figure 6.24**, no conversion was observed either. The **Figure 6.25** show the kinetic plot of the reaction where it is seen that all products **6** are primary, thus they do not interconvert between each other.

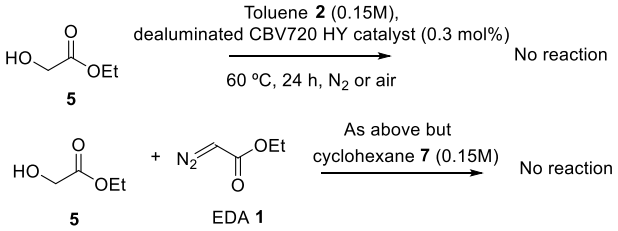

Figure 6.24 Reactivity tests with alcohol **5** to study the formation of product **6**.

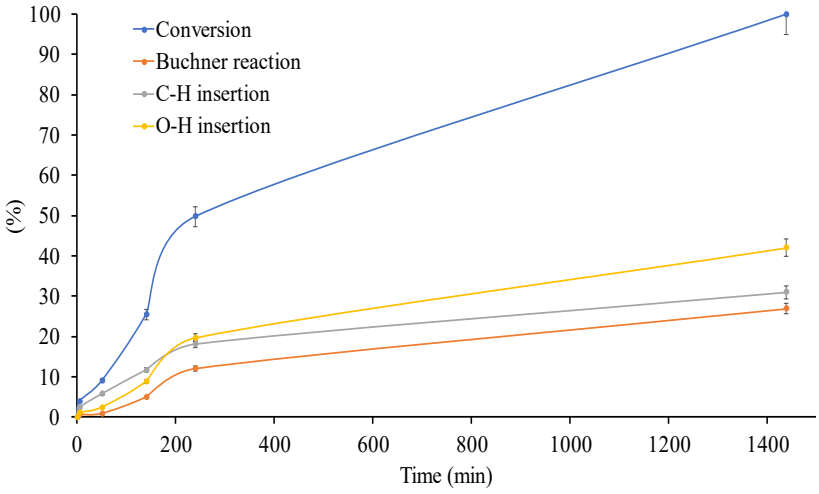

Figure 6.25 Kinetics for the reaction of ethyl diazoacetate (EDA) **1** in toluene solvent **2** (0.15M) catalyzed by dealuminated HY zeolite (0.3 mol%), at 60 ºC, for 24 h and under air atmosphere. GC results. Error bars account for a 5% uncertainty.

The potential catalytic activity of metal impurities in both the commercial HY (Si/Al= 15) and its corresponding dealuminated HY zeolite was then examined. Initially, a comprehensive analysis of the solids was conducted using inductively coupled plasma-atomic emission spectroscopy (ICP-AES, **Tables 6.1 to 6.4**) to determine the presence of metal impurities that could potentially be catalytically relevant. The results revealed that Ni, Cu, Fe, and Pt were the predominant metal impurities in both materials. However, their concentrations were all below 150 ppm. To assess whether these metal impurities were actually participating in the reaction, two new materials were prepared, the dealuminated H-Y zeolite impregnated with the acetate salts of Cu^{2+}, Fe^{2+}, and Pt^{2+} (**Tables 6.4**). In these cases, the amount of incorporated metal was significantly higher than that in the catalytic HY zeolites, thus any metal-catalyzed reaction should have been detected. Furthermore, the plot of initial rate versus the amount of dealuminated CuFePt-HY zeolite (**Figure 6.26**) revealed that the y-intercept value was only 0.0002 mmol·min^{-1}, more than 50 times lower than that of the H-Y zeolite (see **Figures 6.21** and **6.25**) which confirms that any catalysis by trace metals is negligible.

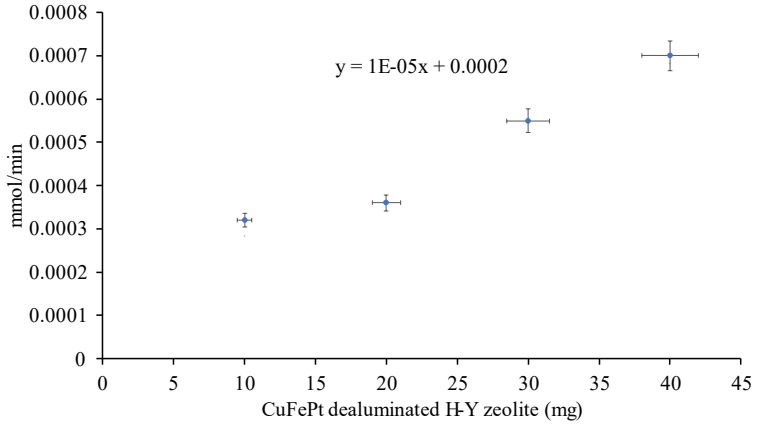

Figure 6.26 Initial rate vs amount of dealuminated CuFePt-HY zeolite catalyst plot for the reaction of ethyl diazoacetate (EDA) **1** in toluene solvent **2** (0.15M) at 60 ºC, for 24 h and under air atmosphere. GC results. Error bars account for a 5% uncertainty.

6.4 *Substrate Scopes*

Figure 6.27 and Figure 6.28 shows that the dealuminated H – Y zeolite catalyzes the insertion of ethyl diazoacetates not only in toluene 2, H2O or O2, but also in different alkanes (2a – c), alkenes (2d – f), alcohols (2g – o), other aromatics (2p – v), amines (2w – v) and silanes (2y) (for starting substrate structures, see Figure S27).The results revealed excellent yields, >99% in some cases, according to GC – MS, for most alcohols 3g – o, and notable yields of 56 – 80% for the aromatics 3p, 3s, 3t and 3u, and also for amine 3x. For alkanes and alkenes, the yields were low to moderate, approximately 15 to 39%, however, these results must be remarked taken in account the simplicity of the catalytic system. In addition, substrates that have different functional groups such as alcohol – alkene (2l, 2m), aromatic – alcohol (2n, 2o) were also tested, observing that in all cases the insertion in the O – H bonds prevails.

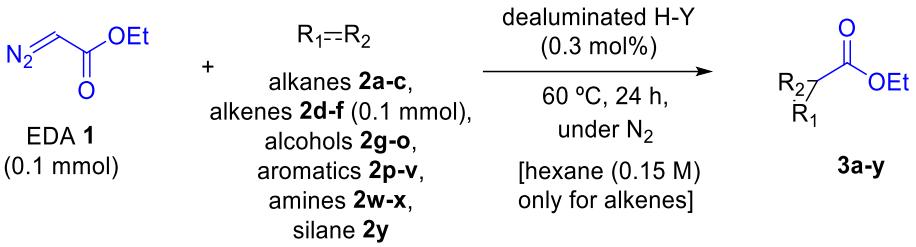

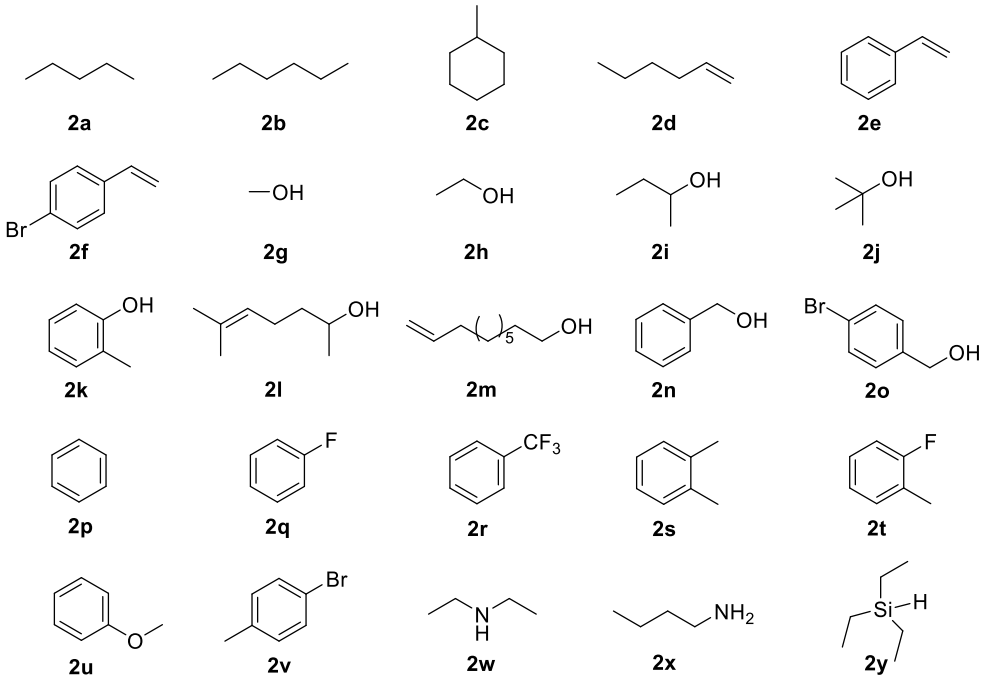

Figure 6.27 Structures of the different starting materials employed in the scope.

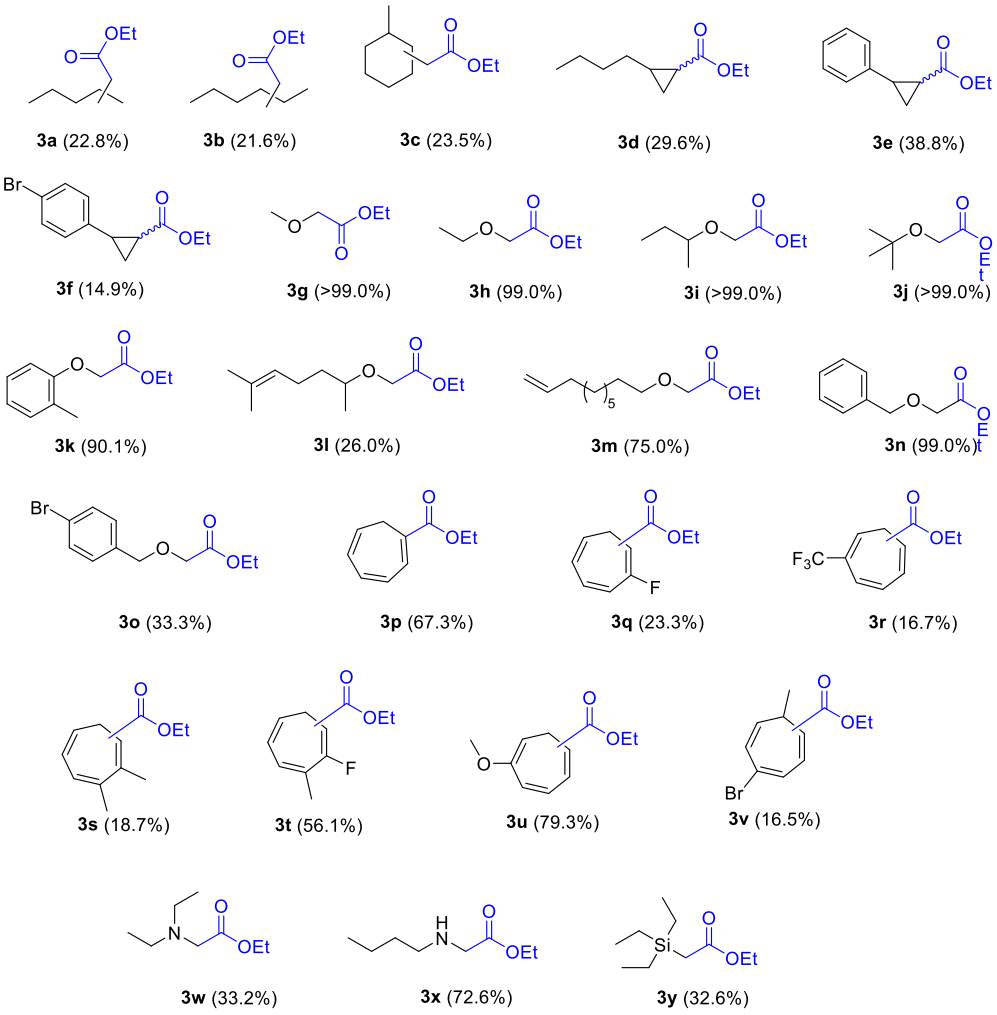

Figure 6.28 Scope of insertion reactions with dealuminated H－Y zeolite (from H－Y Si/Al= 15) as a catalyst, at 60 °C, for 24 h and under N_2 atmosphere.

6.5 *Experimental mechanistic insights*

Kinetic experiments under pseudo-stationary reaction conditions, i.e. varying the amount of one reagent while keeping the rest of them constant, show that the initial insertion reaction rate linearly increases with the amount of dealuminated H-Y zeolite and EDA **1** (**Figure 6.29**), but remains constant with the amount of either H_2O, toluene, cyclohexane or air. The adsorption of D_2O in the zeolite to replace H_2O was carried out, as assessed by ^1H NMR (**Figures 6.30**) and FT-IR experiments (**Figure 6.31**), and the corresponding kinetic experiments do not show any change in the reaction rate (**Figure 6.32, Figure 6.33**), with a measured kinetic isotopic effect (KIE) of ~1.0. The same KIE is also found when toluene **2-d^8** is employed as the reactant (**Figure 6.32**). These results indicate that a common rate equation $v_0=k_{exp}$[zeolite][**1**] (v_0 is initial reaction rate and, k_{exp} is an experimental constant) operates for all the reactions tested, which strongly suggests that the r.d.s. for the insertion reaction could be the activation of EDA **1** in the zeolite.

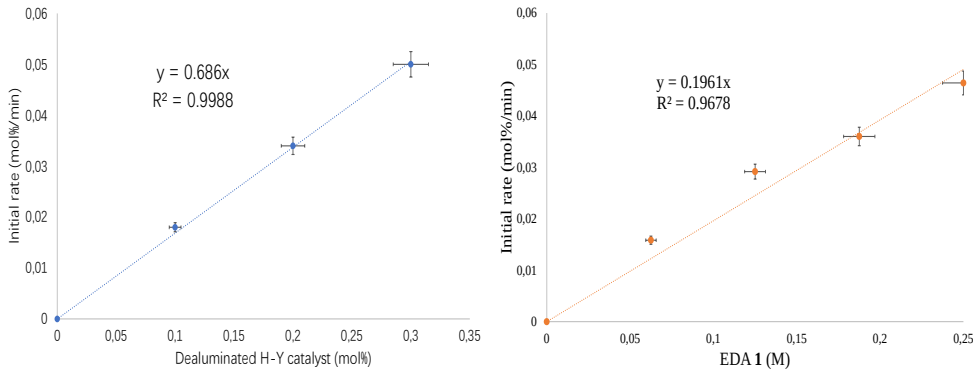

Figure 6.29 Initial reaction rates vs different amounts of dealuminated H-Y zeolite (from Si/Al= 15) catalyst (left) or EDA **1** (right) plots, at 60 ºC. The variation in the amount of either H_2O, toluene, cyclohexane or air did not produce noticeable changes in the reaction rates. GC results. Error bars account for a 5% uncertainty.

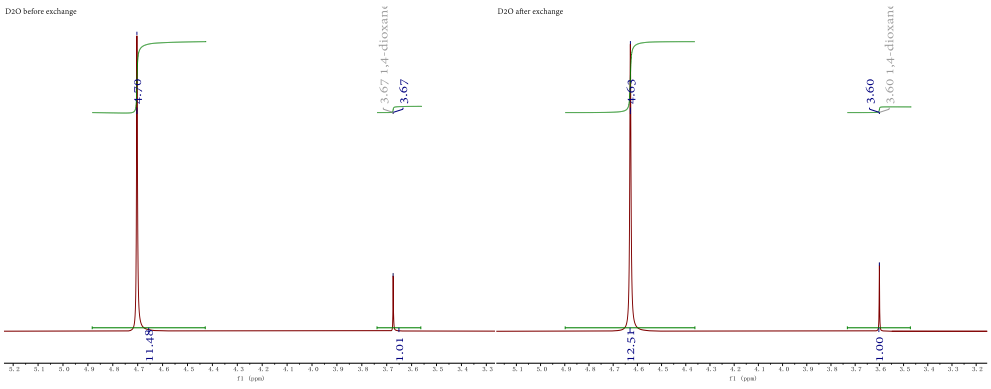

Figure 6.30 ^{1}H nuclear magnetic resonance (^{1}H NMR) of the D_2O solution before (top) and after treating the dealuminated H-Y zeolite (from Si/Al= 15, bottom). The increase in the HDO signal respect to 1,4-dioxane as an external standard indicates the D_2O / H_2O exchange in the zeolite.

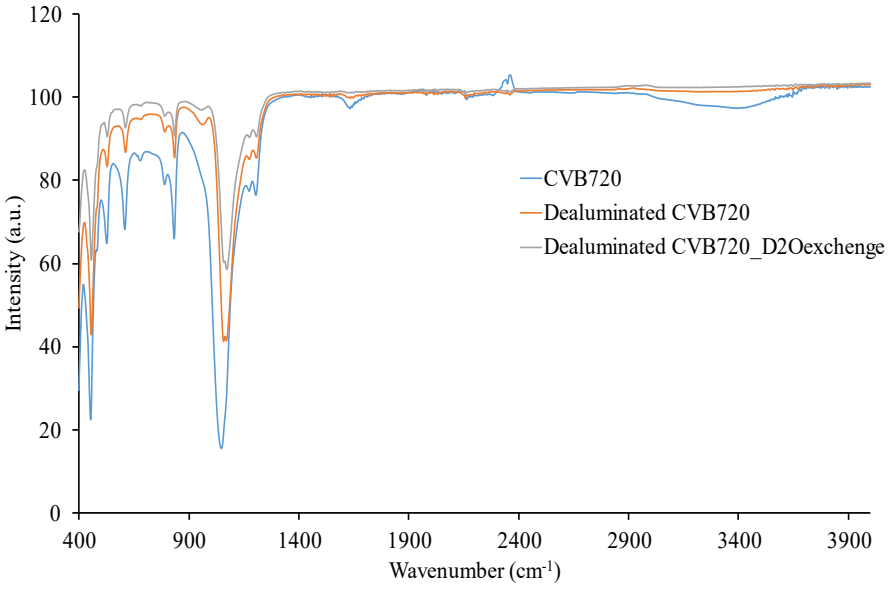

Figure 6.31 Fourier transform infrared spectroscopy (FT-IR) of the dealuminated H-Y zeolite before and after the treatment with D_2O.

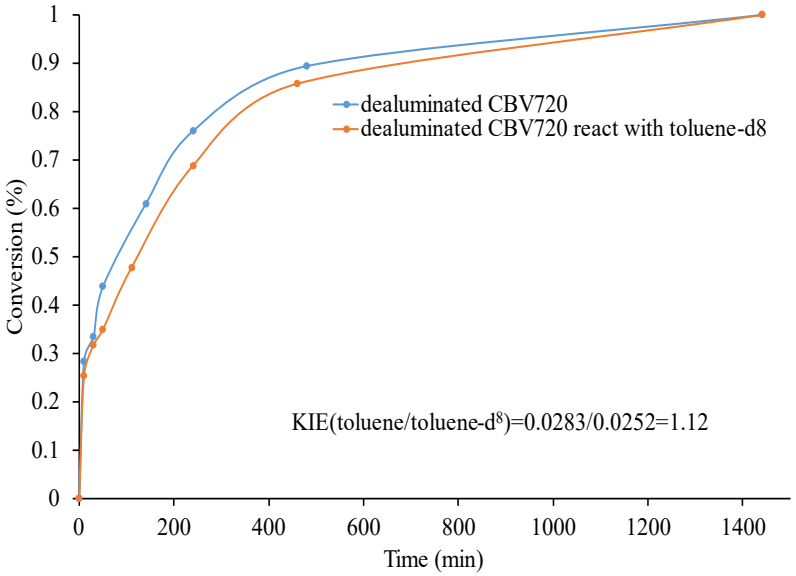

Figure 6.32 Kinetics for the reaction of ethyl diazoacetate (EDA) **1** in either toluene solvent **2** (blue line) or octadeuterated toluene solvent **2-d^8** (orange line, 0.15M), catalyzed by dealuminated HY zeolite (0.3 mol%), at 60 ºC, for 24 h and under air atmosphere. GC results. Error bars account for a 5% uncertainty.

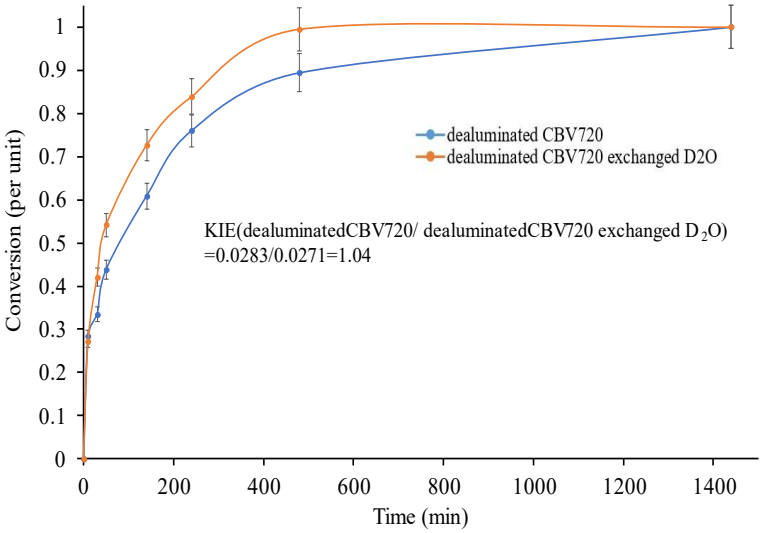

Figure 6.33 Kinetics for the reaction of ethyl diazoacetate (EDA) **1** in either H_2O **2** (blue line) or exchanged D_2O solvent (orange line, 0.15M), catalyzed by dealuminated HY zeolite (0.3 mol%), at 60 ºC, for 24 h and under air atmosphere. GC results. Error bars account for a 5% uncertainty.

If this is so, the intermediate carbene could be observed. **Figure 6.36** shows the diagnostic area of the in-situ FT-IR spectra of the dealuminated H-Y zeolite after adsorption of EDA **1** into the zeolite at 25 ºC and heating up to 60 ºC in the FT-IR chamber. The results clearly show the rapid disappearance of the signals at 2115 cm^{-1}, corresponding to the diazo group, and at 1670 and 1604 cm^{-1}, corresponding to the ester bonds of **1**, together with the appearance of a new signal at 1720 cm^{-1}, which nicely fits with the typical value of a classical, electron-poor carbene.[377] Remarkably, any signal below 1600 cm^{-1} could not be found, thus discarding the formation of electron-rich carbenes such as those formed with catalytic metals for insertion reactions.[364]

An Arrhenius plot, calculated by kinetic experiments between 40 and 90 ºC reaction temperature (**Figure 6.34**), gives that the enthalpy and entropy values of the transition state are $\Delta H^{\ddagger}$=+24.59 ($KJ \cdot K^{-1} \cdot mol^{-1}$) and $\Delta S^{\ddagger}$=-368.8 ($KJ \cdot K^{-1} \cdot mol^{-1}$),

respectively. This enthalpy value of ~6 Kcal per mol is within the expected energy range for a reaction that occurs at 30-60 ºC, but the entropy value is much more informative, since it is very exothermic, in line with the expected loss of N_2 gas in the r.d.s. of the reaction. [378] These results, together, indicate that a carbene with electron-poor nature is formed and stabilized on the zeolite surface, without receiving any significant back-donated electron density, in good agreement with the fact that acid zeolites catalyze the reaction.

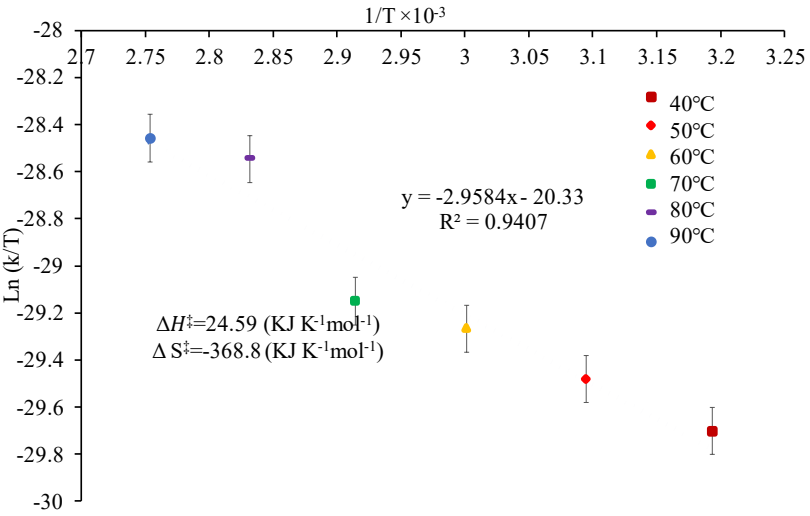

Figure 6.34 Arrhenius plot for the reaction of ethyl diazoacetate (EDA) **1** in toluene solvent **2** (0.15M) catalyzed by dealuminated H-Y zeolite (0.3 mol%), at 40-90 ºC, for 24 h and under air atmosphere. GC results. Error bars account for a 5% uncertainty.

Figure 6.35 presents the ^{13}C solid-state nuclear magnetic resonance (^{13}C ssNMR, bottom) spectra of the dealuminated HY zeolite after adsorption of isotopically labelled ^{13}C EDA **1**. Due to the inability of the ssNMR instrument's chamber to heat the sample, the reaction mixture was analyzed at room temperature over a period of 3 days. The results indicate a gradual disappearance of the initial ^{13}C-**1** signal at 45 ppm, accompanied by the emergence of new signals at 11 and 40 ppm, which can be attributed to the corresponding carbene. [366] These signals between 55 and 70 ppm

correspond to the carbon bonds of the newly formed C-O product, and only a very minor signal of the **1** dimers, at 130 ppm, can be observed, which is consistent with the catalytic results. These findings support the formation and stabilization of the carbene on the zeolite surface, as well as its reactivity with water.

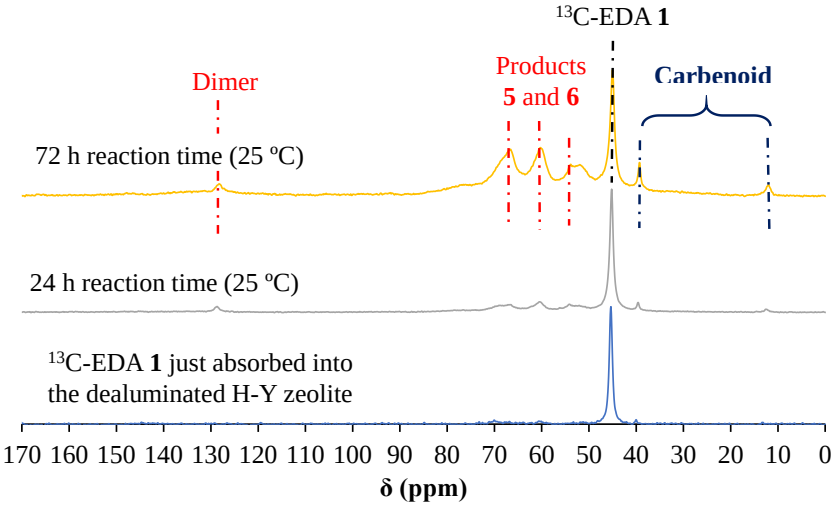

Figure 6.35 ^{13}C solid-state nuclear magnetic resonance (^{13}C ssNMR) of the dealuminated HY zeolite (from Si/Al= 15) after adsorption of ^{13}C-EDA **1** and reacting at 25 ºC (^{13}C ssNMR).

Figure 6.36 shows the in-situ FT-IR analysis and reveals a broadening of the band at 1720 cm^{-1} with reaction time, reaching up to 1740 cm^{-1}, indicating the presence of the O-H and O=O insertion products. [364] This further confirms the formation of products **5** and **6** over time. Notably, only the signals corresponding to the electron-poor carbene are observed in the ^{13}C ssNMR, while the signals of an electron-rich carbene (28 and 9 ppm) are absent. [366] Therefore, the results obtained from in-situ FT-IR and ^{13}C ssNMR are in agreement. Although attempts were made to employ Raman spectroscopy to track the in-situ reaction, as we did in the Ag-basic zeolites, the high fluorescence of the HY zeolite hindered any informative measurements.

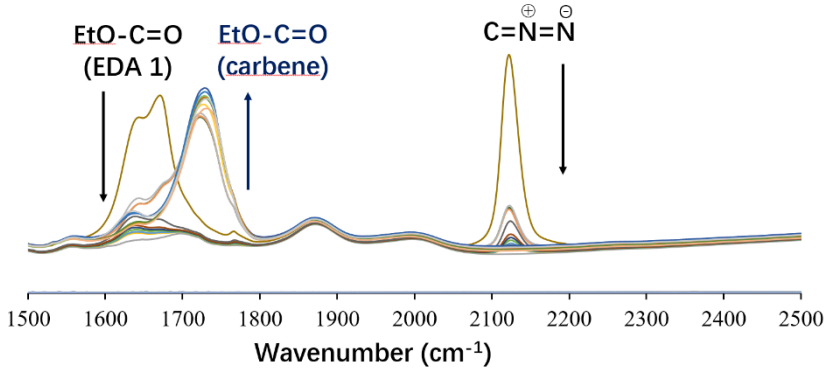

Figure 6.36 In-situ Fourier-transformed infrared spectroscopy (FT-IR) of the dealuminated H-Y zeolite (from Si/Al= 15) after adsorption of either EDA **1** and heating from 25 to 60 ºC (FT-IR).

In order to acquire information regarding the nature of the active H species within the zeolite, varying quantities of Na^+ were introduced into the zeolite via cation exchange utilizing an aqueous solution of NaOAc. The Na^+ content progressively increased from approximately 300 to 7000 ppm, representing a more than 50-fold increase, across independently synthesized samples (**Table 6.8**). Confirmation of the crystallinity of the novel materials is provided through PXRD measurements (**Figure 6.37**). **Figure 6.38** illustrates that the initial conversion rate of EDA **1** experiences a rapid decline as the quantity of incorporated Na^+ increases, in accordance with the kinetic results (**Figure 6.39**). Given that the exchange of H^+ with Na^+ initially takes place at the more acidic positions of the zeolite, [379, 380] these findings strongly indicate that the formation, stabilization, and insertion reaction of the carbene occur at the Brønsted acid sites.

Table 6.8 Na content of the cation exchanged H-Y dealuminated zeolite (from Si/Al 15) with NaOAc in water.

Na^+-exchanged dealuminated H-Y	ppm Na (ICP-AES)	Na (%)
Sample 1	322.829	0.032283
Sample 2	408.53	0.040853
Sample 3	425.08	0.042508
Sample 4	1,230.27	0.123027
Sample 5	1,544.43	0.154443
Sample 6	2,666.17	0.266617
Sample 7	3,137.14	0.313714
Sample 8	3,568.76	0.356876
Sample 9	3,864.54	0.386454
Sample 10	5,422.12	0.542212

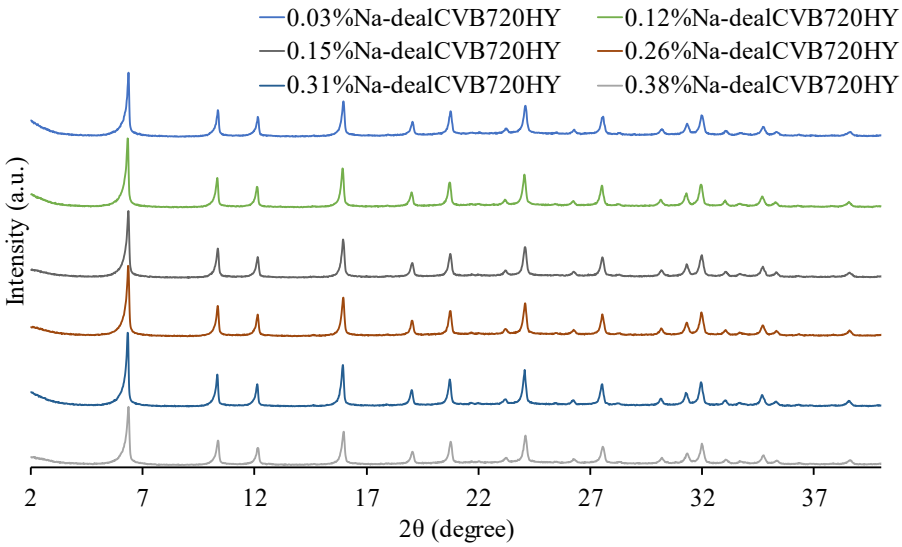

Figure 6.37 Powder X-ray diffractions (PRXD) of the dealuminated H-Y zeolite (from Si/Al= 15) after exchange with different NaOAc aqueous solutions.

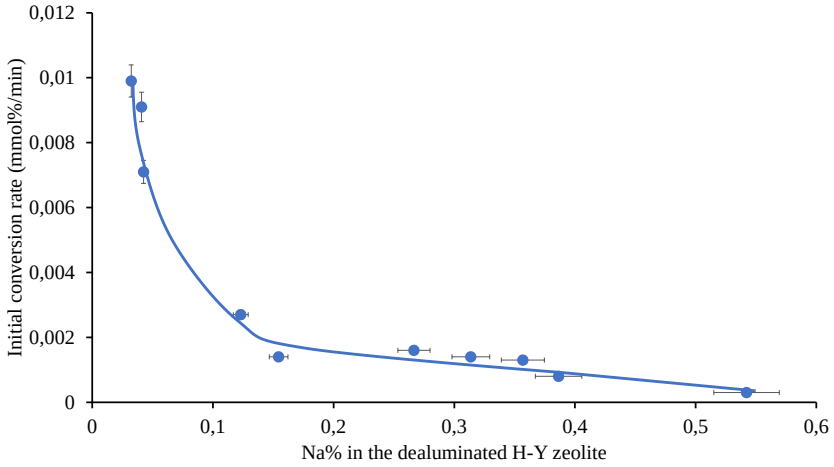

Figure 6.38 Initial conversion rates vs different amounts of Na^+ exchanged in the dealuminated HY zeolite (from Si/Al= 15) catalyst, for the reaction of ethyl diazoacetate (EDA) **1** in toluene solvent **2** (0.15M) at 60 ºC, for 24 h and under air atmosphere. GC results. Error bars account for a 5% uncertainty.

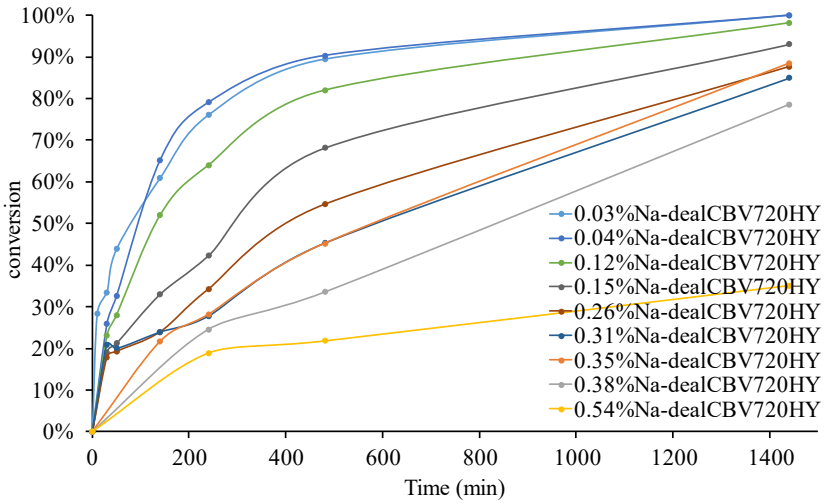

Figure 6.39 Kinetics for the reaction of ethyl diazoacetate (EDA) **1** in toluene solvent **2** (0.15M) catalyzed by different Na^+-exchanged dealuminated H-Y zeolites (0.3 mol%), at 60 ºC, for 24 h and under air atmosphere. GC results. Error bars account for a 5% uncertainty.

6.6 *Proposed reaction mechanism*

Figure 6.40 illustrates the proposed reaction pathway, which is established through the integration of experimental data discussed earlier. The interaction of the diazocarbonyl compound takes place exclusively at the isolated Brønsted acid sites within the zeolite framework, leading to the formation of the respective carbene species. This carbene, characterized by its electron-deficient nature and residing in a triplet configuration, remains stable when supported by the solid matrix, as observed in the case of EDA **1**, exhibiting resistance to dimerization. Subsequently, the carbene interacts with a diverse array of soft nucleophiles, encompassing aromatic structures, alkenes, alcohols, alkanes, and potentially O_2, resulting in the formation of insertion products while concurrently restoring the zeolite catalyst for subsequent catalytic turnovers.

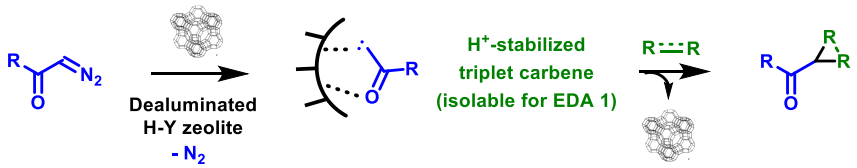

Figure 6.40 Proposed mechanism for the generation, stabilization and insertion of carbenes from diazocarbonyl compounds in catalytic dealuminated HY zeolites.

6.7 *Conclusions*

Dealuminated zeolites are able to generate and stabilize carbenes from EDA **1**, to catalyze the insertion reaction of this carbene into different bonds, including C-H, C=C, O-H and O=O bonds. Silanols are involved in the catalytic process, and the solids can be reused. Confinement effects in the zeolite play a role. These results open the study of simple acid solids as catalysts for carbene reactions, without the involvement of expensive / toxic metals or ligands.

Chapter 7. General Conclusions

In this *thesis*, silver single atom, silver dimers, silver clusters, and metal-free dealuminated zeolites were effectively synthesized, stabilized, and characterized on microporous solid substrates, such as zeolites and MOF materials. These materials were employed in the Buchner ring expansion reaction for C-H insertion, exhibiting high yields and selectivity in the transformation of toluene. Furthermore, when these catalysts were applied in cyclohexane for C-H insertion, it was observed that the choice of counterbalancing cation significantly influenced the selectivity of the reaction towards either C-H or O-H insertion. Additionally, silver carbenes were identified through *in-situ* Raman spectroscopy and *in-situ* ^{13}C CP/MAS NMR. These results enhance the range of economically accessible silver species for use in heterogeneous catalysis within organic synthesis. Protonation, an innovative approach, was also found to serve as a catalyst for the catalysis of the Buchner reaction. The catalytic activity in the insertion of carbene reactions of diazocarbonyl compounds into C=C, C-H, C-O, and O=O bonds is facilitated by the Brønsted acid sites present in dealuminated HY zeolites. A triplet carbene, characterized by electron deficiency and stabilized by H^+, has been detected within the zeolite structure via experimental techniques. Therefore, it has been established that the pivotal phase in the reaction involves the formation and stabilization of the electron-poor carbene at specific acid sites, thereby enabling a variety of insertion reactions. These discoveries introduce innovative avenues for the generation and maintenance of carbenes, as well as the execution of insertion reactions, utilizing simple, robust, and transition metal-free materials that obviate the necessity for expensive and non-recoverable soluble metal catalysts.

Chapter 8. Publications

8.1 *Publications related to the thesis*

(1) **Zheng, Y.**; Vidal-Moya, A.; Hernández-Garrido, J. C.; Mon, M.; Leyva-Pérez, A. Silver-Exchanged Zeolite Y Catalyzes a Selective Insertion of Carbenes into C-H and O-H Bonds. *Journal of the American Chemical Society* **2023**, *145 (45)*, 24736-24745.

(2) Tiburcio, E. [#]; **Zheng, Y.** [#]; Mon, M.; Martin, N.; Ferrando Soria, J.; Armentano, D.; Leyva Perez, A.; Pardo, E. Highly Efficient MOF-Driven Silver Subnanometer Clusters for the Catalytic Buchner Ring Expansion Reaction. *Inorganic Chemistry* **2022**, *61 (30)*, 11796-11802.

(3) **Zheng, Y.**; Espinosa, M.; Mon, M.; Leyva-Pérez, A. Catalytic dealuminated H-Y zeolites generate, stabilize and insert carbenes from diazocarbonyl compounds. **2024,** submitted.

8.2 *Other publications*

(4) Tiburcio, E.[#]; **Zheng, Y.** [#]; Bilanin, C.; Hernandez-Garrido, J. C.; Vidal-Moya, A.; Oliver-Meseguer, J.; Martin, N.; Mon, M.; Ferrando-Soria, J.; Armentano, D.; et al. MOF-Triggered Synthesis of Subnanometer Ag_0^2 Clusters and Fe^{3+} Single Atoms: Heterogenization Led to Efficient and Synergetic One-Pot Catalytic Reactions. *Journal of the American Chemical Society* **2023**, *145 (18)*, 10342-10354.

(5) **Zheng, Y.**; Martín, N.; Boronat, M.; Ferrando-Soria, J.; Mon, M.; Armentano, D.; Pardo, E.; Leyva-Pérez, A. $Ag_2(0)$ dimers within a thioether-functionalized MOF catalyze the CO_2 to CH_4 hydrogenation reaction. *Scientific Reports* **2023**, *13 (1)*, 10376.

(6) Bilanin, C.[#]; **Zheng, Y.[#]**; Vidal-Moya, A.; Pardo, E.; Mon, M.; Leyva-Pérez, A. Single-atom Cu catalysts for the oxidative coupling of styrenes with aryl sulfones: from salts and zeolites to MOFs. *Molecular Catalysis* **2024**, *553*, 113786.

(7) Fernández-Conde, C.; **Zheng, Y.**; Mon, M.; Ribera, A.; Leyva-Pérez, A.; Martí-Gastaldo, C. Time-resolved control of nanoparticle integration in titanium-organic frameworks for enhanced catalytic performance. *Chemical Science* **2024**, *15 (7)*, 2351-2358.

(8) Bačić, M.; Tejeda-Serrano, M.; **Zheng, Y.**; Oliver-Meseguer, J.; Leyva-Pérez, A. HY zeolite catalyzes the ortho-methylation of 1-naphthol. *Applied Surface Science Advances* **2024**, 21, 100598.

[#]: equal contribution

References

(1) Buchner, E.; Curtius, T. Ueber die Einwirkung von Diazoessigäther auf aromatische Kohlenwasserstoffe. *Berichte der deutschen chemischen Gesellschaft* **1885**, *18* (2), 2377-2379.

(2) Staudinger, H.; Kupfer, O. Über reaktionen des methylens. III. Diazomethan. *Berichte der deutschen chemischen Gesellschaft* **1912**, *45* (1), 501-509.

(3) Tschugajeff, L.; Skanawy-Grigorjewa, M.; Posnjak, A.; Skanawy-Grigorjewa, M. Über Die Hydrazin-Carbylamin-Komplexe des Platins. *Zeitschrift fur Anorganische und Allgemeine Chemie* **1925**, *148* (1), 37-42.

(4) Breslow, R. On the Mechanism of Thiamine Action. IV.1 Evidence from Studies on Model Systems. *Journal of the American Chemical Society* **1958**, *80* (14), 3719-3726.

(5) von E. Doering, W.; Hoffmann, A. K. The addition of dichlorocarbene to olefins. *Journal of the American Chemical Society* **1954**, *76* (23), 6162-6165.

(6) Fischer, E.; Maasböl, A. On the existence of a tungsten carbonyl carbene complex. *Angewandte Chemie International Edition* **1964**, *3* (8), 580-581.

(7) Wanzlick, H. W. Aspects of Nucleophilic Carbene Chemistry. *Angewandte Chemie International Edition* **1962**, *1* (2), 75-80.

(8) Skell, P. S.; Garner, A. Y. Reactions of Bivalent Carbon Compounds. Reactivities in Olefin-Dibromocarbene Reactions. *Journal of the American Chemical Society* **1956**, *78* (20), 5430-5433.

(9) Arduengo, A. J., III; Harlow, R. L.; Kline, M. A stable crystalline carbene. *Journal of the American Chemical Society* **1991**, *113* (1), 361-363.

(10) Nguyen, S. T.; Johnson, L. K.; Grubbs, R. H.; Ziller, J. W. Ring-opening

metathesis polymerization (ROMP) of norbornene by a Group VIII carbene complex in protic media. *Journal of the American Chemical Society* **1992**, *114* (10), 3974-3975.

(11) Hermann, M. Ueber die bei der technischen Gewinnung des Broms beobachtete flüchtige Bromverbindung. *Justus Liebigs Annalen der Chemie* **1855**, *95* (2), 211-225.

(12) Goumri-Magnet, S.; Kato, T.; Gornitzka, H.; Baceiredo, A.; Bertrand, G. Stereoselectivity and Stereospecificity of Cyclopropanation Reactions with Stable (Phosphanyl)(silyl)carbenes. *Journal of the American Chemical Society* **2000**, *122* (18), 4464-4470.

(13) Gao, X.; Ohtsuka, Y.; Ishimura, K.; Nagase, S. Mechanism and Dynamic Correlation Effects in Cycloaddition Reactions of Singlet Difluorocarbene to Alkenes and Disilene. *The Journal of Physical Chemistry A* **2009**, *113* (36), 9852-9860.

(14) Xu, L.; Doubleday, C. E.; Houk, K. N. Dynamics of Carbene Cycloadditions. *Journal of the American Chemical Society* **2011**, *133* (44), 17848-17854.

(15) Bernardi, F.; Bottoni, A.; Canepa, C.; Olivucci, M.; Robb, M. A.; Tonachini, G. MCSCF/MP2 Study of the Cheletropic Addition of Singlet and Triplet CF_2 and $C(OH)_2$ to the Ethene Double Bond. *The Journal of Organic Chemistry* **1997**, *62* (7), 2018-2025.

(16) Arduengo, A. J.; Bertrand, G. Carbenes Introduction. *Chemical Reviews* **2009**, *109* (8), 3209-3210.

(17) Jones, M., Jr.; Ando, W.; Hendrick, M. E.; Kulczycki, A., Jr.; Howley, P. M.; Hummel, K. F.; Malament, D. S. Irradiation of methyl diazomalonate in solution. Reactions of singlet and triplet carbenes with carbon-carbon double bonds. *Journal of the American Chemical Society* **1972**, *94* (21), 7469-7479.

(18) Su, M.-D. Role of Spin−Orbit Coupling and Symmetry in Triplet Carbenic Addition Chemistry. *The Journal of Physical Chemistry* **1996**, *100* (11), 4339-4349.

(19) Skell, P. S. The beginnings of modern carbene chemistry triplets and singlets. *Tetrahedron* **1985**, *41* (8), 1427-1428.

(20) de Frémont, P.; Marion, N.; Nolan, S. P. Carbenes: Synthesis, properties, and organometallic chemistry. *Coordination Chemistry Reviews* **2009**, *253* (7), 862-892.

(21) Tomioka, H.; Iwamoto, E.; Itakura, H.; Hirai, K. Generation and characterization of a fairly stable triplet carbene. *Nature* **2001**, *412* (6847), 626-628.

(22) Tomioka, H. Triplet carbenes: From fleeting existence to attractive molecular units. *Pure and Applied Chemistry* **2003**, *75* (8), 1041-1047.

(23) Forrester, A. R.; Sadd, J. S. Indirect detection of carbenes by electron spin resonance: triplet trapping. *Journal of the Chemical Society* **1982**, (10), 1273-1278.

(24) Forrester, A. R.; Sadd, J. S. Detection of carbenes by electron spin resonance spectroscopy: 'triplet trapping'. *Journal of the Chemical Society, Chemical Communications* **1976**, (16), 631-632.

(25) Singh, M. S. *Reactive Intermediates in Organic Chemistry: Structure, Mechanism, and Reactions*; Wiley, **2014**.

(26) Bourissou, D.; Guerret, O.; Gabbaï, F. P.; Bertrand, G. Stable Carbenes. *Chemical Reviews* **2000**, *100* (1), 39-92.

(27) Deng, Y.; Jing, C.; Arman, H.; Doyle, M. P. Reactivity and Selectivity in Catalytic Reactions of Enoldiazoacetamides. Assessment of Metal Carbenes as Intermediates. *Organometallics* **2016**, *35* (19), 3413-3420.

(28) Chu, G. M.; Fernández, I.; Sierra, M. A. Control over the E/Z Selectivity of the Catalytic Dimerization of Group 6 (Fischer) Metal Carbene Complexes. *The Journal of Organic Chemistry* **2013**, *78* (3), 865-871.

(29) Lotz, S.; Crause, C.; Olivier, A. J.; Liles, D. C.; Görls, H.; Landman, M.; Bezuidenhout, D. I. Synthesis and reactivity of metal carbene complexes with

heterobiaryl spacer substituents. *Dalton Transactions* **2009**, (4), 697-710.

(30) de Brito Sá, E.; Rimola, A.; Rodríguez-Santiago, L.; Sodupe, M.; Solans-Monfort, X. Reactivity of Metal Carbenes with Olefins: Theoretical Insights on the Carbene Electronic Structure and Cyclopropanation Reaction Mechanism. *The Journal of Physical Chemistry A* **2018**, *122* (6), 1702-1712.

(31) Fischer, E. O.; Schubert, U.; Fischer, H. Selectivity and specificity in chemical reactions of carbene and carbyne metal complexes. *Pure and Applied Chemistry* **1978**, *50* (9-10), 857-870.

(32) Anusha, C.; De, S.; Parameswaran, P. Effect of Transition Metal Fragments on the Reverse Fritsch-Buttenberg-Wiechell Type Ring Contraction Reaction of Metallabenzynes to Metal-Carbene Complexes. *The Journal of Physical Chemistry A* **2018**, *122* (8), 2160-2167.

(33) Montgomery, C. D. Fischer and Schrock Carbene Complexes: A Molecular Modeling Exercise. *Journal of Chemical Education* **2015**, *92* (10), 1653-1660.

(34) Dötz, K. H.; Stendel, J., Jr. Fischer Carbene Complexes in Organic Synthesis: Metal-Assisted and Metal-Templated Reactions. *Chemical Reviews* **2009**, *109* (8), 3227-3274.

(35) Taylor, T. E.; Hall, M. B. Theoretical comparison between nucleophilic and electrophilic transition metal carbenes using generalized molecular orbital and configuration interaction methods. *Journal of the American Chemical Society* **1984**, *106* (6), 1576-1584.

(36) Zhou, G.; Guo, Z.; Shen, X. Electron-Rich Oxycarbenes: New Synthetic and Catalytic Applications beyond Group 6 Fischer Carbene Complexes. *Angewandte Chemie International Edition* **2023**, *62* (13).

(37) Hoskovcová, I.; Ludvík, J. Electrochemical approach to Fischer carbene complexes. *Current Opinion in Electrochemistry* **2019**, *15*, 165-174.

(38) Härterich, M.; Matler, A.; Dewhurst, R. D.; Sachs, A.; Oppel, K.; Stoy, A.; Braunschweig, H. A step-for-step main-group replica of the Fischer carbene synthesis at a borylene carbonyl. *Nature Communications* **2023**, *14* (1), 2764.

(39) Feliciano, A.; Vázquez, J. L.; Benítez-Puebla, L. J.; Velazco-Cabral, I.; Cruz Cruz, D.; Delgado, F.; Vázquez, M. A. Fischer Carbene Complexes: A Glance at Two Decades of Research on Higher-Order Cycloaddition Reactions. *Chemistry - A European Journal* **2021**, *27* (32), 8233-8251.

(40) Veit, P.; Seibert, S.; Förster, C.; Heinze, K. Unexpected C-C Bond Formation with a Ferrocenyl Fischer Carbene Complex. *Zeitschrift fur Anorganische und Allgemeine Chemie* **2020**, *646* (13), 940-947.

(41) Belof, J. L.; Cioce, C. R.; Xu, X.; Zhang, X. P.; Space, B.; Woodcock, H. L. Characterization of Tunable Radical Metal-Carbenes: Key Intermediates in Catalytic Cyclopropanation. *Organometallics* **2011**, *30* (10), 2739-2746.

(42) Dzik, W. I.; Xu, X.; Zhang, X. P.; Reek, J. N. H.; de Bruin, B. 'Carbene Radicals' in Co^{II}(por)-Catalyzed Olefin Cyclopropanation. *Journal of the American Chemical Society* **2010**, *132* (31), 10891-10902.

(43) Russell, S. K.; Hoyt, J. M.; Bart, S. C.; Milsmann, C.; Stieber, S. C. E.; Semproni, S. P.; DeBeer, S.; Chirik, P. J. Synthesis, electronic structure and reactivity of bis(imino)pyridine iron carbene complexes: evidence for a carbene radical. *Chemical Science* **2014**, *5* (3), 1168-1174.

(44) Dzik, W. I.; Zhang, X. P.; de Bruin, B. Redox Noninnocence of Carbene Ligands: Carbene Radicals in (Catalytic) C−C Bond Formation. *Inorganic Chemistry* **2011**, *50* (20), 9896-9903.

(45) Das, B. G.; Chirila, A.; Tromp, M.; Reek, J. N. H.; de Bruin, B. Co^{III}-Carbene Radical Approach to Substituted 1*H*-Indenes. *Journal of the American Chemical Society* **2016**, *138* (28), 8968-8975.

(46) Doyle, M. P. Catalytic methods for metal carbene transformations. *Chemical Reviews* **1986**, *86* (5), 919-939.

(47) Cheng, Q. Q.; Doyle, M. P. Chapter One - The Selection of Catalysts for Metal Carbene Transformations. In *Advances in Organometallic Chemistry*, Pérez, P. J. Ed.; Vol. 66; Academic Press, **2016;** 1-31.

(48) Yates, P. The copper-catalyzed decomposition of diazoketones1. *Journal of the American Chemical Society* **1952**, *74* (21), 5376-5381.

(49) Bredt, J.; Holz, W. Über das β-Pericyclocamphanon ein Beitrag zur Aufklärung der Konstitution des Camphenons Angelis (Schiffscher Dehydrocampher). *Journal für Praktische Chemie* **1917**, *95* (1), 133-159.

(50) Burke, S. D.; Grieco, P. A. Intramolecular Reactions of Diazocarbonyl Compounds. In *Organic Reactions*, 361-475.

(51) Ford, A.; Miel, H.; Ring, A.; Slattery, C. N.; Maguire, A. R.; McKervey, M. A. Modern Organic Synthesis with α-Diazocarbonyl Compounds. *Chemical Reviews* **2015**, *115* (18), 9981-10080.

(52) Xu, X.; Doyle, M. P. The [3 + 3]-Cycloaddition Alternative for Heterocycle Syntheses: Catalytically Generated Metalloenolcarbenes as Dipolar Adducts. *Accounts of Chemical Research* **2014**, *47* (4), 1396-1405.

(53) Mckervey, M. A.; Doyle, M. P.; Ye, T. Modern Catalytic Methods for Organic Synthesis with Diazo Compounds: From Cyclopropanes to Ylides. **1998**.

(54) Ye, T.; McKervey, M. A. Organic Synthesis with .alpha.-Diazo Carbonyl Compounds. *Chemical Reviews* **1994**, *94* (4), 1091-1160.

(55) Soldi, C.; Lamb, K. N.; Squitieri, R. A.; González-López, M.; Di Maso, M. J.; Shaw, J. T. Enantioselective Intramolecular C-H Insertion Reactions of Donor-Donor Metal Carbenoids. *Journal of the American Chemical Society* **2014**, *136* (43), 15142-15145.

(56) Cui, X.; Xu, X.; Jin, L.-M.; Wojtas, L.; Zhang, X. P. Stereoselective radical C-H alkylation with acceptor/acceptor-substituted diazo reagents via Co(ii)-based metalloradical catalysis. *Chemical Science* **2015**, *6* (2), 1219-1224.

(57) Gessner, V. H. Stability and reactivity control of carbenoids: recent advances and perspectives. *Chemical Communications* **2016**, *52* (81), 12011-12023.

(58) Davies, H. M. L.; Antoulinakis, E. G. Recent progress in asymmetric intermolecular C-H activation by rhodium carbenoid intermediates. *Journal of Organometallic Chemistry* **2001**, *617-618*, 47-55.

(59) Davies, H. M. L. Catalytic asymmetric C-H activation of sp^3 hybridized C-H bonds by means of carbenoid C-H insertions: applications in organic synthesis. *Journal of Molecular Catalysis A: Chemical* **2002**, *189* (1), 125-135.

(60) Davies, H. M. L.; Denton, J. R. Application of donor/acceptor-carbenoids to the synthesis of natural products. *Chemical Society Reviews* **2009**, *38* (11), 3061-3071.

(61) Davies, H. M. L.; Nikolai, J. Catalytic and enantioselective allylic C-H activation with donor-acceptor-substituted carbenoids. *Organic & Biomolecular Chemistry* **2005**, *3* (23), 4176-4187.

(62) Doyle, M. P.; Duffy, R.; Ratnikov, M.; Zhou, L. Catalytic Carbene Insertion into C−H Bonds. *Chemical Reviews* **2010**, *110* (2), 704-724.

(63) Lebel, H.; Marcoux, J.-F.; Molinaro, C.; Charette, A. B. Stereoselective Cyclopropanation Reactions. *Chemical Reviews* **2003**, *103* (4), 977-1050.

(64) Zhu, S.-F.; Zhou, Q.-L. Transition-Metal-Catalyzed Enantioselective Heteroatom-Hydrogen Bond Insertion Reactions. *Accounts of Chemical Research* **2012**, *45* (8), 1365-1377.

(65) Guo, X.; Hu, W. Novel Multicomponent Reactions via Trapping of Protic Onium Ylides with Electrophiles. *Accounts of Chemical Research* **2013**, *46* (11), 2427-2440.

(66) P. Doyle, M.; Liu, Y.; Ratnikov, M. Catalytic, Asymmetric, Intramolecular Carbon-Hydrogen Insertion. In *Organic Reactions*, 1-132.

(67) Liu, C.-X.; Yin, S.-Y.; Zhao, F.; Yang, H.; Feng, Z.; Gu, Q.; You, S.-L. Rhodium-Catalyzed Asymmetric C-H Functionalization Reactions. *Chemical Reviews* **2023**, *123* (16), 10079-10134.

(68) Álvarez, M.; Caballero, A.; Pérez, P. J. Alkane Functionalization by Metal-Catalyzed Carbene Insertion from Diazo Reagents. In *Transition Metal-Catalyzed Carbene Transformations*, **2022;** 1-24.

(69) Samanta, R.; Bera, S.; Jana, S. Recent Progress on Copper-Catalyzed C-C Bond Formation via C(sp^2)-H Insertions Using Diazo and Related Compounds. *Synthesis* **2023**, *56* (01), 29-46.

(70) Faisca Phillips, A. M.; Pombeiro, A. J. L. Alkane Carbonylation and Carbene Insertion Reactions. In *Alkane Functionalization*, **2019;** 371-426.

(71) Davies, H. M. L.; Beckwith, R. E. J. Catalytic Enantioselective C-H Activation by Means of Metal-Carbenoid-Induced C-H Insertion. *Chemical Reviews* **2003**, *103* (8), 2861-2904.

(72) Cheng, S.; Li, Q.; Cheng, X.; Lin, Y.-M.; Gong, L. Recent Advances in Asymmetric Transformations of Unactivated Alkanes and Cycloalkanes through Direct C-H Functionalization. *Chinese Journal of Chemistry* **2022**, *40* (23), 2825-2837.

(73) He, Y.; Huang, Z.; Wu, K.; Ma, J.; Zhou, Y.-G.; Yu, Z. Recent advances in transition-metal-catalyzed carbene insertion to C-H bonds. *Chemical Society Reviews* **2022**, *51* (7), 2759-2852.

(74) Álvarez, M.; Molina, F.; Pérez, P. J. Carbene-Controlled Regioselective Functionalization of Linear Alkanes under Silver Catalysis. *Journal of the American Chemical Society* **2022**, *144* (51), 23275-23279.

(75) Honma, M.; Takeda, H.; Takano, M.; Nakada, M. Development of catalytic asymmetric intramolecular cyclopropanation of α-diazo-β-keto sulfones and applications to natural product synthesis. *Synlett* **2009**, *2009* (11), 1695-1712.

(76) Giedyk, M.; Goliszewska, K.; ó Proinsias, K.; Gryko, D. Cobalt(i)-catalysed CH-alkylation of terminal olefins, and beyond. *Chemical Communications* **2016**, *52* (7), 1389-1392.

(77) de Meijere, A.; Kozhushkov, S. I.; Schill, H. Three-Membered-Ring-Based Molecular Architectures. *Chemical Reviews* **2006**, *106* (12), 4926-4996.

(78) Davies, I. W.; Gerena, L.; Castonguay, L.; Senanayake, C. H.; Larsen, R. D.; Verhoeven, T. R.; Reider, P. J. The influence of ligand bite angle on the enantioselectivity of copper(II)-catalysed Diels-Alder reactions. *Chemical Communications* **1996**, (15), 1753-1754.

(79) Talele, T. T. The "Cyclopropyl Fragment" is a Versatile Player that Frequently Appears in Preclinical/Clinical Drug Molecules. *Journal of Medicinal Chemistry* **2016**, *59* (19), 8712-8756.

(80) Caballero, A.; Díaz-Requejo, M. M.; Fructos, M. R.; Olmos, A.; Urbano, J.; Pérez, P. J. Catalytic functionalization of low reactive C(sp^3)-H and C(sp^2)-H bonds of alkanes and arenes by carbene transfer from diazo compounds. *Dalton Transactions* **2015**, *44* (47), 20295-20307.

(81) Liu, Z.; Liu, B.; Zhao, X.-F.; Wu, Y.-B.; Bi, X. Silver-Catalyzed Cross-Olefination of Donor and Acceptor Diazo Compounds: Use of N-Nosylhydrazones as Diazo Surrogate. *European Journal of Organic Chemistry* **2017**, *2017* (4), 928-932.

(82) Aggarwal, V. K.; de Vicente, J.; Bonnert, R. V. Catalytic Cyclopropanation of Alkenes Using Diazo Compounds Generated in Situ. A Novel Route to 2-Arylcyclopropylamines. *Organic Letters* **2001**, *3* (17), 2785-2788.

(83) Jiang, H.; Fu, W.; Chen, H. Palladium-Catalyzed Cross-Coupling Reactions

of Electron-Deficient Alkenes with N-Tosylhydrazones: Functional-Group-Controlled C-C Bond Construction. *Chemistry - A European Journal* **2012**, *18* (38), 11884-11888.

(84) Liang, R.; Ma, T.; Zhu, S. Silver-Catalyzed Reaction of Enynals with Alkenes: A Tandem 1,3-Dipolar Cycloaddition/Cyclopropanation. *Organic Letters* **2014**, *16* (17), 4412-4415.

(85) Cui, X.-Y.; Ye, Z.-T.; Wu, H.-H.; Ji, C.-G.; Zhou, F.; Zhou, J. Au(I)-Catalyzed Formal Intermolecular Carbene Insertion into Vinylic C(sp^2)-H Bonds and Allylic C(sp^3)-H Bonds. *ACS Catalysis* **2023**, *13* (3), 1554-1561.

(86) Zhu, S.; Perman, J. A.; Zhang, X. P. Acceptor/Acceptor-Substituted Diazo Reagents for Carbene Transfers: Cobalt-Catalyzed Asymmetric Z-Cyclopropanation of Alkenes with α-Nitrodiazoacetates. *Angewandte Chemie International Edition* **2008**, *47* (44), 8460-8463.

(87) Lindsay, V. N. G.; Nicolas, C.; Charette, A. B. Asymmetric Rh(II)-Catalyzed Cyclopropanation of Alkenes with Diacceptor Diazo Compounds: p-Methoxyphenyl Ketone as a General Stereoselectivity Controlling Group. *Journal of the American Chemical Society* **2011**, *133* (23), 8972-8981.

(88) Basato, M.; Tubaro, C.; Biffis, A.; Bonato, M.; Buscemi, G.; Lighezzolo, F.; Lunardi, P.; Vianini, C.; Benetollo, F.; Del Zotto, A. Reactions of Diazo Compounds with Alkenes Catalysed by [RuCl(cod)(Cp)]: Effect of the Substituents in the Formation of Cyclopropanation or Metathesis Products. *Chemistry - A European Journal* **2009**, *15* (6), 1516-1526.

(89) Che, C.-M.; Huang, J.-S. Ruthenium and osmium porphyrin carbene complexes: synthesis, structure, and connection to the metal-mediated cyclopropanation of alkenes. *Coordination Chemistry Reviews* **2002**, *231* (1), 151-164.

(90) Wu, Y.; Cao, S.; Douair, I.; Maron, L.; Bi, X. Computational Insights into Different Mechanisms for Ag-, Cu-, and Pd-Catalyzed Cyclopropanation of Alkenes and Sulfonyl Hydrazones. *Chemistry - A European Journal* **2021**, *27* (19), 5999-6006.

(91) Shishkov, I. V.; Rominger, F.; Hofmann, P. Remarkably Stable Copper(I) α-Carbonyl Carbenes: Synthesis, Structure, and Mechanistic Studies of Alkene Cyclopropanation Reactions. *Organometallics* **2009**, *28* (4), 1049-1059.

(92) Cronstedt, A. F. *Rön och beskrifning om en obekant bärg art, som kallas Zeolites*; **1756**.

(93) Pérez-Botella, E.; Valencia, S.; Rey, F. Zeolites in Adsorption Processes: State of the Art and Future Prospects. *Chemical Reviews* **2022**, *122* (24), 17647-17695.

(94) Colella, C.; Gualtieri, A. F. Cronstedt's zeolite. *Microporous and Mesoporous Materials* **2007**, *105* (3), 213-221.

(95) Martínez, C.; Corma, A. 5.05 - Zeolites. In *Comprehensive Inorganic Chemistry II (Second Edition)*, Reedijk, J., Poeppelmeier, K. Eds.; Elsevier, **2013;** 103-131.

(96) Peng, M.; Deng, Q.; Zhao, Y.; Xu, H.; Guan, Y.; Jiang, J.; Han, L.; Wu, P. ECNU-13: A High-Silica Zeolite with Three-Dimensional and High-Connectivity Multi-Pore Structures for Selective Alkene Cracking. *Angewandte Chemie International Edition* **2023**, *62* (15).

(97) Yu, J.; Zhao, D. Preface to special topic on new era of zeolite science. *National Science Review* **2022**, *9* (9).

(98) Jarrin, T.; de Bruin, T.; Chizallet, C. Stability and Acidity of Sites at the External Surface and at Point Defects of Faujasite. *ChemCatChem* **2023**, *15* (3).

(99) Boer, D. G.; Asgar Pour, Z.; Langerak, J.; Bakker, B.; Pescarmona, P. P. Binderless Faujasite Beads with Hierarchical Porosity for Selective CO_2 Adsorption for Biogas Upgrading. *Molecules* **2023**, *28* (5), 2198.

(100) Derbe, T.; Temesgen, S.; Bitew, M. A Short Review on Synthesis, Characterization, and Applications of Zeolites. *Advances in Materials Science and Engineering* **2021**, *2021*, 6637898.

(101) Nandini, D.; Jugal Kishore, D. Zeolites: An Emerging Material for Gas Storage and Separation Applications. In *Zeolites*, Karmen, M., Anamarija, F. Eds.; IntechOpen, **2020;** Ch. 6.

(102) Cundy, C. S.; Cox, P. A. The hydrothermal synthesis of zeolites: Precursors, intermediates and reaction mechanism. *Microporous and Mesoporous Materials* **2005**, *82* (1), 1-78.

(103) Byrappa, K.; Keerthiraj, N.; Byrappa, S. M. 14 - Hydrothermal Growth of Crystals—Design and Processing. In *Handbook of Crystal Growth (Second Edition)*, Rudolph, P. Ed.; Elsevier, **2015;** 535-575.

(104) Demazeau, G. Review. Solvothermal Processes: Definition, Key Factors Governing the Involved Chemical Reactions and New Trends. *Zeitschrift für Naturforschung B* **2010**, *65* (8), 999-1006.

(105) Yu, J. Chapter 3 - Synthesis of Zeolites. In *Studies in Surface Science and Catalysis*, Čejka, J., van Bekkum, H., Corma, A., Schüth, F. Eds.; Vol. 168; Elsevier, **2007;** 39-103.

(106) Moliner, M.; Rey, F.; Corma, A. Towards the Rational Design of Efficient Organic Structure-Directing Agents for Zeolite Synthesis. *Angewandte Chemie International Edition* **2013**, *52* (52), 13880-13889.

(107) Davis, M. E. Zeolites: Can they be synthesized by design. *CHEMTECH; (United States)* **1994**, *24:9*, Medium: X; Size: Pages: 22-26 2009-2012-2017.

(108) Gálvez-Llompart, M.; Gálvez, J.; Rey, F.; Sastre, G. Identification of New Templates for the Synthesis of BEA, BEC, and ISV Zeolites Using Molecular Topology and Monte Carlo Techniques. *Journal of Chemical Information and*

Modeling **2020**, *60* (6), 2819-2829.

(109) Lee, H.; Zones, S. I.; Davis, M. E. Zeolite Synthesis Using Degradable Structure-Directing Agents and Pore-Filling Agents. *The Journal of Physical Chemistry B* **2005**, *109* (6), 2187-2191.

(110) Daeyaert, F.; Deem, M. W. Design of Organic Structure-Directing Agents for the Controlled Synthesis of Zeolites for Use in Carbon Dioxide/Methane Membrane Separations. *ChemPlusChem* **2020**, *85* (2), 277-284.

(111) Li, J.; Corma, A.; Yu, J. Synthesis of new zeolite structures. *Chemical Society Reviews* **2015**, *44* (20), 7112-7127.

(112) Qi, X.; Balankura, T.; Zhou, Y.; Fichthorn, K. A. How Structure-Directing Agents Control Nanocrystal Shape: Polyvinylpyrrolidone-Mediated Growth of Ag Nanocubes. *Nano Letters* **2015**, *15* (11), 7711-7717.

(113) Grünewald-Lüke, A.; Marler, B.; Hochgräfe, M.; Gies, H. Quinuclidine derivatives as structure directing agents for the synthesis of boron containing zeolites. *Journal of Materials Chemistry* **1999**, *9* (10), 2529-2536.

(114) A, C.; Giménez, I.; Leiva, S.; Rey, F.; Sabater, M. J.; Sastre, G.; Valencia, S. An study of cyclohexylpyrrolidine-derived quaternary organic cations as structure directing agents for synthesis of zeolites. In *Studies in Surface Science and Catalysis*, van Steen, E., Claeys, I. M., Callanan, L. H. Eds.; Vol. 154; Elsevier, **2004;** 265-274.

(115) Daeyaert, F.; Deem, M. W. Design of organic structure directing agents to control the synthesis of zeolites for carbon capture and storage. *RSC Advances* **2019**, *9* (71), 41934-41942.

(116) Sastre, G. A computational chemistry insight in the role of structure directing agents in the synthesis of zeolites. *Physical Chemistry Chemical Physics* **2007**, *9* (9), 1052-1058.

(117) Millini, R.; Perego, C.; Frigerio, F.; Carluccio, L. C.; Bellussi, G. Azonia-

spiro compounds as structure directing agents: A computational study. In *Studies in Surface Science and Catalysis*, van Steen, E., Claeys, I. M., Callanan, L. H. Eds.; Vol. 154; Elsevier, **2004;** 275-282.

(118) Pophale, R.; Daeyaert, F.; Deem, M. W. Computational prediction of chemically synthesizable organic structure directing agents for zeolites. *Journal of Materials Chemistry A* **2013**, *1* (23), 6750-6760.

(119) Li, J.; Yu, J.; Xu, R. Progress in heteroatom-containing aluminophosphate molecular sieves. *Proceedings of the Royal Society A: Mathematical, Physical and Engineering Sciences* **2012**, *468* (2143), 1955-1967.

(120) Roth, W. J.; Nachtigall, P.; Morris, R. E.; Čejka, J. Two-Dimensional Zeolites: Current Status and Perspectives. *Chemical Reviews* **2014**, *114* (9), 4807-4837.

(121) Díaz, U.; Corma, A. Layered zeolitic materials: an approach to designing versatile functional solids. *Dalton Transactions* **2014**, *43* (27), 10292-10316.

(122) Li, A.; Wang, X.; Wang, T.; Liu, H.; Gao, T.; Fan, M.; Huo, Q.; Qiao, Z.-A. A Topotactic Synthetic Methodology for the Synthesis of Nanosized MFI Zeolites with Hierarchical Structures. *Chemistry - A European Journal* **2018**, *24* (48), 12600-12606.

(123) Schmidt, J. E.; Xie, D.; Davis, M. E. High-silica, heulandite-type zeolites prepared by direct synthesis and topotactic condensation. *Journal of Materials Chemistry A* **2015**, *3* (24), 12890-12897.

(124) Mazur, M.; Arévalo-López, Angel M.; Wheatley, P. S.; Bignami, G. P. M.; Ashbrook, S. E.; Morales-García, Á.; Nachtigall, P.; Attfield, J. P.; Čejka, J.; Morris, R. E. Pressure-induced chemistry for the 2D to 3D transformation of zeolites. *Journal of Materials Chemistry A* **2018**, *6* (13), 5255-5259.

(125) Souza, I. M. S.; García-Villén, F.; Viseras, C.; Pergher, S. B. C. Zeolites as Ingredients of Medicinal Products. *Pharmaceutics* **2023**, *15* (5), 1352.

(126) Liu, X.; Wang, C.; Zhou, J.; Liu, C.; Liu, Z.; Shi, J.; Wang, Y.; Teng, J.; Xie, Z. Molecular transport in zeolite catalysts: depicting an integrated picture from macroscopic to microscopic scales. *Chemical Society Reviews* **2022**, *51* (19), 8174-8200.

(127) Wang, X.; Ma, Y.; Wu, Q.; Wen, Y.; Xiao, F.-S. Zeolite nanosheets for catalysis. *Chemical Society Reviews* **2022**, *51* (7), 2431-2443.

(128) Sun, Q.; Wang, N.; Yu, J. Advances in Catalytic Applications of Zeolite-Supported Metal Catalysts. *Advanced Materials* **2021**, *33* (51), 2104442.

(129) Velty, A.; Corma, A. Advanced zeolite and ordered mesoporous silica-based catalysts for the conversion of CO_2 to chemicals and fuels. *Chemical Society Reviews* **2023**, *52* (5), 1773-1946.

(130) Yan, P.; Wang, H.; Liao, Y.; Wang, C. Zeolite catalysts for the valorization of biomass into platform compounds and biochemicals/biofuels: A review. *Renewable and Sustainable Energy Reviews* **2023**, *178*, 113219.

(131) Zhang, Q.; Yu, J.; Corma, A. Applications of Zeolites to C_1 Chemistry: Recent Advances, Challenges, and Opportunities. *Advanced Materials* **2020**, *32* (44), 2002927.

(132) Azhari, N. J.; Nurdini, N.; Mardiana, S.; Ilmi, T.; Fajar, A. T. N.; Makertihartha, I. G. B. N.; Subagjo; Kadja, G. T. M. Zeolite-based catalyst for direct conversion of CO_2 to C_{2+} hydrocarbon: A review. *Journal of CO_2 Utilization* **2022**, *59*, 101969.

(133) Wang, Y.; Wang, C.; Wang, L.; Wang, L.; Xiao, F.-S. Zeolite Fixed Metal Nanoparticles: New Perspective in Catalysis. *Accounts of Chemical Research* **2021**, *54* (11), 2579-2590.

(134) Wang, H.; Wang, L.; Xiao, F.-S. Metal@Zeolite Hybrid Materials for Catalysis. *ACS Central Science* **2020**, *6* (10), 1685-1697.

(135) Rakanović, M.; Vukojević, A.; Savanović, M. M.; Armaković, S.; Pelemiš, S.; Živić, F.; Sladojević, S.; Armaković, S. J. Zeolites as Adsorbents and Photocatalysts for Removal of Dyes from the Aqueous Environment. *Molecules* **2022**, *27* (19), 6582.

(136) Ibrahim, A. H.; Lyu, X.; ElDeeb, A. B. Synthesized Zeolite Based on Egyptian Boiler Ash Residue and Kaolin for the Effective Removal of Heavy Metal Ions from Industrial Wastewater. *Nanomaterials* **2023**, *13* (6), 1091.

(137) Wang, T.; Chu, Y.; Li, X.; Liu, Y.; Luo, H.; Zhou, D.; Deng, F.; Song, X.; Lu, G.; Yu, J. Zeolites as a Class of Semiconductors for High-Performance Electrically Transduced Sensing. *Journal of the American Chemical Society* **2023**, *145* (9), 5342-5352.

(138) Igau, A.; Grutzmacher, H.; Baceiredo, A.; Bertrand, G. Analogous .alpha.,.alpha.'-bis-carbenoid, triply bonded species: synthesis of a stable .lambda.3-phosphino carbene-.lambda.5-phosphaacetylene. *Journal of the American Chemical Society* **1988**, *110* (19), 6463-6466.

(139) Brinker, U. H.; Mieusset, J.-L.; Rosenberg, M. G. Supramolecular Carbene Chemistry. In *Contemporary Carbene Chemistry*, **2013;** 274-323.

(140) Rosenberg, M. G.; Brinker, U. H. Constrained Carbenes. *European Journal of Organic Chemistry* **2006**, *2006* (24), 5423-5440.

(141) Gupta, S.; Choudhury, R.; Krois, D.; Wagner, G.; Brinker, U. H.; Ramamurthy, V. Photochemical Generation and Reactivity of Carbenes within an Organic Cavitand and Capsule: Photochemistry of Adamantanediazirines. *Organic Letters* **2011**, *13* (22), 6074-6077.

(142) Kupfer, R.; Poliks, M. D.; Brinker, U. H. Carbene rearrangements. 43. Carbenes in Constrained Systems. 2. First Carbene Reactions within Zeolites: Solid-State Photolysis of Adamantane-2-spiro-3'-diazirine. *Journal of the American*

Chemical Society **1994**, *116* (16), 7393-7398.

(143) Gong, X.; Caglayan, M.; Ye, Y.; Liu, K.; Gascon, J.; Dutta Chowdhury, A. First-Generation Organic Reaction Intermediates in Zeolite Chemistry and Catalysis. *Chemical Reviews* **2022**, *122* (18), 14275-14345.

(144) Moya-Barrios, R.; Cozens, F. L. Generation and Reactivity of Simple Chloro(aryl)carbenes within the Cavities of Nonacidic Zeolites. *Journal of the American Chemical Society* **2006**, *128* (46), 14836-14844.

(145) Zheng, Y.; Vidal-Moya, A.; Hernández-Garrido, J. C.; Mon, M.; Leyva-Pérez, A. Silver-Exchanged Zeolite Y Catalyzes a Selective Insertion of Carbenes into C-H and O-H Bonds. *Journal of the American Chemical Society* **2023**, *145* (45), 24736-24745.

(146) Kupfer, R.; Brinker, U. H. Carbenes in constrained systems, 3. Solid-State photolysis of cycloheptane- and cyclooctanespirodiazirine within cyclodextrins and zeolites. *Liebigs Annalen* **1995**, *1995* (10), 1721-1725.

(147) Moya-Barrios, R.; Cozens, F. L. First Direct Observation of Reactive Carbenes in the Cavities of Cation-Exchanged Y Zeolites. *Organic Letters* **2004**, *6* (6), 881-884.

(148) Hashimoto, S.; Saitoh, M.; Taira, N.; Schmidt, W.; Hirai, K.; Tomioka, H. Emission Spectroscopic Investigation of Triplet Diarylcarbene Generated in Molecular Sieve VPI-5. *The Journal of Physical Chemistry B* **2005**, *109* (43), 20407-20414.

(149) Koy, M.; Bellotti, P.; Das, M.; Glorius, F. N-Heterocyclic carbenes as tunable ligands for catalytic metal surfaces. *Nature Catalysis* **2021**, *4* (5), 352-363.

(150) Zhukhovitskiy, A. V.; MacLeod, M. J.; Johnson, J. A. Carbene Ligands in Surface Chemistry: From Stabilization of Discrete Elemental Allotropes to Modification of Nanoscale and Bulk Substrates. *Chemical Reviews* **2015**, *115* (20),

11503-11532.

(151) Böhm, V. P. W.; Gstöttmayr, C. W. K.; Weskamp, T.; Herrmann, W. A. N-Heterocyclic carbenes: Part 26. N-Heterocyclic carbene complexes of palladium(0): synthesis and application in the Suzuki cross-coupling reaction. *Journal of Organometallic Chemistry* **2000**, *595* (2), 186-190.

(152) del Pozo, C.; Corma, A.; Iglesias, M.; Sánchez, F. Immobilization of (NHC)NN-Pincer Complexes on Mesoporous MCM-41 Support. *Organometallics* **2010**, *29* (20), 4491-4498.

(153) del Pozo, C.; Iglesias, M.; Sánchez, F. Pincer-type Pyridine-Based N-Heterocyclic Carbene Amine Ru(II) Complexes as Efficient Catalysts for Hydrogen Transfer Reactions. *Organometallics* **2011**, *30* (8), 2180-2188.

(154) Jin, L.; Weinberger, D. S.; Melaimi, M.; Moore, C. E.; Rheingold, A. L.; Bertrand, G. Trinuclear Gold Clusters Supported by Cyclic (alkyl)(amino)carbene Ligands: Mimics for Gold Heterogeneous Catalysts. *Angewandte Chemie International Edition* **2014**, *53* (34), 9059-9063.

(155) Jiang, Y.; Yu, Y.; Zhang, X.; Weinert, M.; Song, X.; Ai, J.; Han, L.; Fei, H. N-Heterocyclic Carbene-Stabilized Ultrasmall Gold Nanoclusters in a Metal-Organic Framework for Photocatalytic CO_2 Reduction. *Angewandte Chemie International Edition* **2021**, *60* (32), 17388-17393.

(156) Ye, R.; Zhukhovitskiy, A. V.; Kazantsev, R. V.; Fakra, S. C.; Wickemeyer, B. B.; Toste, F. D.; Somorjai, G. A. Supported Au Nanoparticles with N-Heterocyclic Carbene Ligands as Active and Stable Heterogeneous Catalysts for Lactonization. *Journal of the American Chemical Society* **2018**, *140* (11), 4144-4149.

(157) Gou, X.-X.; Liu, T.; Wang, Y.-Y.; Han, Y.-F. Ultrastable and Highly Catalytically Active N-Heterocyclic-Carbene-Stabilized Gold Nanoparticles in Confined Spaces. *Angewandte Chemie International Edition* **2020**, *59* (38), 16683-

16689.

(158) Ernst, J. B.; Muratsugu, S.; Wang, F.; Tada, M.; Glorius, F. Tunable Heterogeneous Catalysis: N-Heterocyclic Carbenes as Ligands for Supported Heterogeneous Ru/K-Al_2O_3 Catalysts To Tune Reactivity and Selectivity. *Journal of the American Chemical Society* **2016**, *138* (34), 10718-10721.

(159) Gianotti, E.; Miletto, I.; Ivaldi, C.; Paul, G.; Marchese, L.; Meazza, M.; Rios, R.; Raja, R. Hybrid catalysts based on N-heterocyclic carbene anchored on hierarchical zeolites. *RSC Advances* **2019**, *9* (61), 35336-35344.

(160) Wu, Y.; Sun, X.; Dai, S.; Li, M.; Zheng, L.; Wen, Q.; Tang, B.; Yun, D.-Q.; Xiao, L. Broad-Band-Enhanced Plasmonic Perovskite Solar Cells with Irregular Silver Nanomaterials. *ACS Applied Materials & Interfaces* **2022**, *14* (14), 16269-16278.

(161) García-Olivares, A. Substituting silver in solar photovoltaics is feasible and allows for decentralization in smart regional grids. *Environmental Innovation and Societal Transitions* **2015**, *17*, 15-21.

(162) Wei, Y.; Zhang, Q.-l.; Wan, H.-j.; Zhang, Y.-n.; Zheng, S.-w.; Zhang, Y. A facile synthesis of segmented silver nanowires and enhancement of the performance of polymer solar cells. *Physical Chemistry Chemical Physics* **2018**, *20* (27), 18837-18843.

(163) Shen, W.; Tang, J.; Wang, Y.; Liu, J.; Huang, L.; Chen, W.; Yang, L.; Wang, W.; Wang, Y.; Yang, R.; et al. Strong Enhancement of Photoelectric Conversion Efficiency of Co-hybridized Polymer Solar Cell by Silver Nanoplates and Core-Shell Nanoparticles. *ACS Applied Materials & Interfaces* **2017**, *9* (6), 5358-5365.

(164) Nguyen, T. H.; Kawaguchi, T.; Chantana, J.; Minemoto, T.; Harada, T.; Nakanishi, S.; Ikeda, S. Structural and Solar Cell Properties of a Ag-Containing Cu_2ZnSnS_4 Thin Film Derived from Spray Pyrolysis. *ACS Applied Materials &*

Interfaces **2018**, *10* (6), 5455-5463.

(165) Xiao, X.; Pu, Y.; Zhang, W.; Ye, H.; Wang, L.; Jia, Y.; Ge, X.; Wang, Y.; Ong, A.; Zhang, D.; et al. Hierarchical Bamboo/Silver Nanoparticle Composites for Sustainable Water Purification. *Langmuir* **2023**, *39* (22), 7766-7774.

(166) Qi, Z.; Miyazaki, Y.; Sugasawa, M.; Yang, Y.; Negishi, N. Antibacterial silver-loaded TiO_2 ceramic photocatalyst for water purification. *Journal of Water Process Engineering* **2022**, *50*, 103225.

(167) Amjad, M. U.; Ahmed, B. A.; Ahmed, F.; Saeed, H. A. Development and Characterization of Silver-Doped Multi-Walled Carbon Nanotube Membranes for Water Purification Applications. *Membranes* **2022**, *12* (2), 179.

(168) Raheem, S. A.; Alfatlawi, A. H. Surface-water purification using cellulose paper impregnated with silver nanoparticles. *Drinking Water Engineering and Science* **2021**, *14* (1), 95-102.

(169) Zhu, D.; Wu, M. Highly Conductive Nano-Silver Circuits by Inkjet Printing. *Journal of Electronic Materials* **2018**, *47* (9), 5133-5147.

(170) Pagliaro, M.; Della Pina, C.; Mauriello, F.; Ciriminna, R. Catalysis with Silver: From Complexes and Nanoparticles to MORALs and Single-Atom Catalysts. *Catalysts* **2020**, *10* (11), 1343.

(171) Bi, X.; Li, C.-J. Editorial: Special Collection of Silver Catalysis in Organic Synthesis. *ChemCatChem* **2021**, *13* (14), 3200-3201.

(172) Wu, Y.; Frank, N.; Song, Q.; Liu, M.; Anderson, E. A.; Bi, X. Chapter Two - Silver catalysis in organic synthesis: A computational view. In *Advances in Organometallic Chemistry*, Pérez, P. J. Ed.; Vol. 80; Academic Press, **2023;** 39-75.

(173) Mkrtchyan, K. V.; Zezin, A. A.; Zezina, E. A.; Abramchuk, S. S.; Baranova, I. A. Formation of metal nanostructures under X-ray radiation in films of interpolyelectrolyte complexes with different silver ion content. *Russian Chemical*

Bulletin **2020**, *69* (9), 1731-1739.

(174) Liu, L.; Corma, A. Metal Catalysts for Heterogeneous Catalysis: From Single Atoms to Nanoclusters and Nanoparticles. *Chemical Reviews* **2018**, *118* (10), 4981-5079.

(175) Putta, S.; Sharma, R. K.; Khandelwal, P. Metal Nanoparticles: Synthesis, Characterization, and Biomedical Applications. In *Nanomaterials: Advances and Applications*, Singh, D. K., Singh, S., Singh, P. Eds.; Springer Nature Singapore, **2023;** 85-102.

(176) Nicolae-Maranciuc, A.; Chicea, D.; Chicea, L. M. Ag Nanoparticles for Biomedical Applications—Synthesis and Characterization—A Review. *International Journal of Molecular Sciences* **2022**, *23* (10), 5778.

(177) Nene, A.; Galluzzi, M.; Hongrong, L.; Somani, P.; Ramakrishna, S.; Yu, X.-F. Synthetic preparations and atomic scale engineering of silver nanoparticles for biomedical applications. *Nanoscale* **2021**, *13* (33), 13923-13942.

(178) Hasan, L. I.; Jabbar, H. S. Silver Nanoparticles Application as a Colorimetric Probe for the Spectrophotometric Determination of Hyoscine Butylbromide in Pharmaceutical Formulations. *Journal of AOAC International* **2023**, *106* (2), 285-295.

(179) Sandulovici, R. C.; Carmen-Marinela, M.; Grigoroiu, A.; Moldovan, C. A.; Savin, M.; Ordeanu, V.; Voicu, S. N.; Cord, D.; Costache, G. M.; Galatanu, M. L.; et al. The Physicochemical and Antimicrobial Properties of Silver/Gold Nanoparticles Obtained by "Green Synthesis" from Willow Bark and Their Formulations as Potential Innovative Pharmaceutical Substances. *Pharmaceuticals* **2023**, *16* (1), 48.

(180) Ramana, E. V.; Naseem. Development, Characterization and Antibacterial Properties of Silver Nanoparticles Loaded Sodium Alginate/Xanthan Gum Microbeads For Drug Delivery Applications. *International Journal of Applied Pharmaceutics* **2023**, *15* (3), 278-284.

(181) Malaikozhundan, B.; Vinodhini, J.; Manivannan, N.; Boopathi, T.; Vijayakumar, S. 11 - Bioapplications of nanoparticles. In *Nano-Bioremediation : Fundamentals and Applications*, Iqbal, H. M. N., Bilal, M., Nguyen, T. A. Eds.; Elsevier, **2022;** 213-239.

(182) Mehta, T.; Mishra, R.; Pansara, C.; Dhal, C.; Dhas, N.; Hariharan, K.; Patel, J. K. Manufacturing Techniques for Carbon Nanotubes, Gold Nanoparticles, and Silver Nanoparticles. In *Emerging Technologies for Nanoparticle Manufacturing*, Patel, J. K., Pathak, Y. V. Eds.; Springer International Publishing, **2021;** 397-420.

(183) Nath, I.; Chakraborty, J.; Kumari, N.; Verpoort, F.; Roy, S. An ODE to Nanoparticles in Catalysis. *Journal of Molecular and Engineering Materials* **2023**, *11*.

(184) Lara, P.; Martínez-Prieto, L. M. Metal Nanoparticle Catalysis. *Catalysts* **2021**, *11* (10), 1210.

(185) Zhong, C.-J.; Maye, M. M.; Luo, J.; Han, L.; Kariuki, N. Nanoparticles in Catalysis. In *Nanoparticles: Building Blocks for Nanotechnology*, Rotello, V. Ed.; Springer US, **2004;** 113-143.

(186) González-Béjar, M. Silver Nanoparticles in Heterogeneous Plasmon Mediated Catalysis. In *Silver Nanoparticle Applications: In the Fabrication and Design of Medical and Biosensing Devices*, Alarcon, E. I., Griffith, M., Udekwu, K. I. Eds.; Springer International Publishing, **2015;** 71-92.

(187) Remziye, G.; Gülbahar, E. Synthesis of Silver Nanoparticles. In *Silver Nanoparticles*, Khan, M. Ed.; IntechOpen, **2018;** Ch. 1.

(188) Zhu, M.; Du, Y. Chapter 8 - Practical applications of metal nanoclusters. In *Metal Nanocluster Chemistry*, Zhu, M. Ed.; Elsevier, **2023;** 289-372.

(189) Jašík, J.; Fortunelli, A.; Vajda, Š. Exploring the materials space in the smallest particle size range: from heterogeneous catalysis to electrocatalysis and photocatalysis. *Physical Chemistry Chemical Physics* **2022**, *24* (20), 12083-12115.

(190) Zhang, B.; Chen, Y.; Wang, J.; Pan, H.; Sun, W. Supported Sub-Nanometer Clusters for Electrocatalysis Applications. *Advanced Functional Materials* **2022**, *32* (24), 2202227.

(191) Abdel-Karim, R. 21 - Metal nanoclusters for catalytic applications: synthesis and characterization. In *Luminescent Metal Nanoclusters*, Thomas, S., Joseph, K., Appukuttan, S., Mathew, M. S. Eds.; Woodhead Publishing, **2022;** 589-623.

(192) Fan, Q.-Y.; Wang, Y.; Cheng, J. Size-Sensitive Dynamic Catalysis of Subnanometer Cu Clusters in CO_2 Dissociation. *The journal of physical chemistry letters* **2021**, *12* (16), 3891-3897.

(193) Moomtaheen, F.; Killeen, M.; Oswald, J.; Gonzàlez-Rosell, A.; Mastracco, P.; Gorovits, A.; Copp, S. M.; Bogdanov, P. DNA-Stabilized Silver Nanocluster Design via Regularized Variational Autoencoders. In Proceedings of the 28th ACM SIGKDD Conference on Knowledge Discovery and Data Mining, Washington DC, USA; **2022**.

(194) Ritchie, C. M.; Johnsen, K. R.; Kiser, J. R.; Antoku, Y.; Dickson, R. M.; Petty, J. T. Ag Nanocluster Formation Using a Cytosine Oligonucleotide Template. *The Journal of Physical Chemistry C* **2007**, *111* (1), 175-181.

(195) Korotcenkov, G.; Cho, B. K.; Gulina, L. B.; Tolstoy, V. P. Gas sensor application of Ag nanoclusters synthesized by SILD method. *Sensors and Actuators B: Chemical* **2012**, *166-167*, 402-410.

(196) Piskaeva, A.; Sidorin, Y. Y.; Dyshlyuk, L.; Zhumaev, Y. V.; Prosekov, A. Y. Research on the influence of silver clusters on decomposer microorganisms and e. coli bacteria. *Foods and Raw materials* **2014**, *2* (1), 62.

(197) Primitivo, L.; De Angelis, M.; Necci, A.; Di Pietro, F.; Ricelli, A.; Caschera, D.; Pilloni, L.; Suber, L.; Righi, G. Silver thiolate nanoclusters as support for chiral ligands: application in heterogeneous phase asymmetric catalysis. *Nanoscale*

Advances **2023**, *5* (3), 627-632.

(198) Sun, G.; Sautet, P. 6.09 - Nanocluster heterogeneous catalysts: Insights from theory. In *Comprehensive Inorganic Chemistry III (Third Edition)*, Reedijk, J., Poeppelmeier, K. R. Eds.; Elsevier, **2023;** 201-221.

(199) Oyem, H. H. Fluorescent copper nanoclusters. *Journal of Chemical Society of Nigeria* **2023**, *48* (2).

(200) Yuan, X.; Zhu, M. Recent advances in atomically precise metal nanoclusters for electrocatalytic applications. *Inorganic Chemistry Frontiers* **2023**, *10* (14), 3995-4007.

(201) Zhong, Y.-J.; Liao, J.-H.; Chiu, T.-H.; Wen, Y.-S.; Liu, C. W. A New Synthetic Methodology in the Preparation of Bimetallic Chalcogenide Clusters via Cluster-to-Cluster Transformations. *Molecules* **2021**, *26* (17), 5391.

(202) Wleklinski, M.; Sarkar, D.; Hollerbach, A.; Pradeep, T.; Cooks, R. G. Ambient preparation and reactions of gas phase silver cluster cations and anions. *Physical Chemistry Chemical Physics* **2015**, *17* (28), 18364-18373.

(203) Shellie, R. A.; Heng, W. S. Gas Chromatography. In *Encyclopedia of Forensic Sciences, Third Edition (Third Edition)*, Houck, M. M. Ed.; Elsevier, **2023;** 1-9.

(204) Hopfer, H. Gas Chromatography. In *Encyclopedia of Dairy Sciences (Third Edition)*, McSweeney, P. L. H., McNamara, J. P. Eds.; Academic Press, **2022;** 382-390.

(205) Wongsa, P.; Rattanapanone, N. Chapter six - Gas chromatography and multivariate analysis for wheat flours. In *Food Quality Analysis*, Shukla, A. K. Ed.; Academic Press, **2023;** 149-169.

(206) Hubbard, A. T. *The Handbook of surface imaging and visualization*; CRC press, **2022**.

(207) Boiani, M.; Pacheco, C. Nuclear Magnetic Resonance. In *Encyclopedia of Dairy Sciences (Third Edition)*, McSweeney, P. L. H., McNamara, J. P. Eds.; Academic Press, **2022;** 490-496.

(208) Tatman, B. P.; Franks, W. T.; Brown, S. P.; Lewandowski, J. R. Nuclear spin diffusion under fast magic-angle spinning in solid-state NMR. *The Journal of Chemical Physics* **2023**, *158* (18).

(209) Nishiyama, Y.; Hou, G.; Agarwal, V.; Su, Y.; Ramamoorthy, A. Ultrafast Magic Angle Spinning Solid-State NMR Spectroscopy: Advances in Methodology and Applications. *Chemical Reviews* **2023**, *123* (3), 918-988.

(210) Reif, B.; Ashbrook, S. E.; Emsley, L.; Hong, M. Solid-state NMR spectroscopy. *Nature Reviews Methods Primers* **2021**, *1* (1), 2.

(211) Singh, M. K.; Singh, A. Chapter 18 - Inductively coupled plasma-atomic emission spectrometry. In *Characterization of Polymers and Fibres*, Singh, M. K., Singh, A. Eds.; Woodhead Publishing, **2022;** 421-434.

(212) Vogt, C.; Wondergem, C. S.; Weckhuysen, B. M. Ultraviolet-Visible (UV-Vis) Spectroscopy. In *Springer Handbook of Advanced Catalyst Characterization*, Wachs, I. E., Bañares, M. A. Eds.; Springer International Publishing, **2023;** 237-264.

(213) Zhao, K.; Zhang, J.; Luo, W.; Li, M.; Moioli, E.; Spodaryk, M.; Züttel, A. A combined diffuse reflectance infrared Fourier transform spectroscopy-mass spectroscopy-gas chromatography for the operando study of the heterogeneously catalyzed CO_2 hydrogenation over transition metal-based catalysts. *Review of Scientific Instruments* **2020**, *91* (7).

(214) Zhao, Y.; Liu, H.; Jiang, Y.; Song, S.; Zhao, Y.; Zhang, C.; Xin, J.; Yang, B.; Lin, Q. Detection of Various Biomarkers and Enzymes via a Nanocluster-Based Fluorescence Turn-on Sensing Platform. *Analytical Chemistry* **2018**, *90* (24), 14578-14585.

(215) Chen, W.-T.; Hsu, Y.-J.; Kamat, P. V. Realizing Visible Photoactivity of Metal Nanoparticles: Excited-State Behavior and Electron-Transfer Properties of Silver (Ag_8) Clusters. *The journal of physical chemistry letters* **2012**, *3* (17), 2493-2499.

(216) Chapter 5. Infrared spectroscopy. In *Analytical Methods in Chemical Analysis*, Shikha, K., Banty, K. Eds.; De Gruyter, **2023;** 81-116.

(217) Nabeel, O. IR Spectroscopy in Qualitative and Quantitative Analysis. In *Infrared Spectroscopy*, Marwa, E.-A., Khalid, A.-S., Ahmed, S. E.-S. Eds.; IntechOpen, **2022;** Ch. 4.

(218) Infrared Spectroscopy. In *Practical Guide to Materials Characterization*, **2022;** 183-197.

(219) Timmer, P.; Weber, T.; Glatthaar, L.; Over, H. Operando CO Infrared Spectroscopy and On-Line Mass Spectrometry for Studying the Active Phase of IrO_2 in the Catalytic CO Oxidation Reaction. *Inorganics* **2023**, *11* (3), 102.

(220) Tereshchenko, A.; Guda, A.; Polyakov, V.; Rusalev, Y.; Butova, V.; Soldatov, A. Pd nanoparticle growth monitored by DRIFT spectroscopy of adsorbed CO. *Analyst* **2020**, *145* (23), 7534-7540.

(221) Moon, J.; Li, M.; Ramirez-Cuesta, A. J.; Wu, Z. Raman Spectroscopy. In *Springer Handbook of Advanced Catalyst Characterization*, Wachs, I. E., Bañares, M. A. Eds.; Springer International Publishing, **2023;** 75-110.

(222) Velvarská, R.; Tišler, Z.; Raichlová, V.; Hidalgo-Herrador, J. M. Raman Spectroscopy as Molybdenum and Tungsten Content Analysis Tool for Mesoporous Silica and Beta Zeolite Catalysts. *Molecules* **2020**, *25* (21), 4918.

(223) Nefedov, V. I. *X-ray photoelectron spectroscopy of solid surfaces*; CRC Press, **2023**.

(224) Mathur, A.; Kaushik, R.; Halder, A. Application of X-Ray Photoelectron

Spectroscopy in Materials for Energy Conversion and Environmental Remediation. In *Modern Techniques of Spectroscopy: Basics, Instrumentation, and Applications*, Singh, D. K., Pradhan, M., Materny, A. Eds.; Springer Singapore, **2021;** 411-430.

(225) Weckhuysen, B. M.; Wondergem, C. S.; Vogt, C. Time-Resolved X-Ray Absorption Spectroscopy (XAS). In *Springer Handbook of Advanced Catalyst Characterization*, Wachs, I. E., Bañares, M. A. Eds.; Springer International Publishing, **2023;** 601-623.

(226) Bartlett, S. A. 10.13 - X-ray transient absorption spectroscopies in the study of excited state structures. In *Comprehensive Inorganic Chemistry III (Third Edition)*, Reedijk, J., Poeppelmeier, K. R. Eds.; Elsevier, **2023;** 344-383.

(227) Li, J.; Huang, P.; Guo, F.; Huang, J.; Xiang, S.; Yang, K.; Deskins, N. A.; Batista, V. S.; Li, G.; Frenkel, A. I. X-ray Absorption Spectroscopy Studies of a Molecular CO_2-Reduction Catalyst Deposited on Graphitic Carbon Nitride. *The Journal of Physical Chemistry C* **2023**, *127* (7), 3626-3633.

(228) Le Pevelen, D. D. Anomalous Scattering Single Crystal X-ray Diffraction☆. In *Reference Module in Chemistry, Molecular Sciences and Chemical Engineering*, Elsevier, **2023**.

(229) X-ray Diffraction. In *Practical Guide to Materials Characterization*, **2022;** 15-42.

(230) Shimizu, S.; Matubayasi, N. Surface Area Estimation: Replacing the Brunauer-Emmett-Teller Model with the Statistical Thermodynamic Fluctuation Theory. *Langmuir* **2022**, *38* (26), 7989-8002.

(231) Aquino, C. B.; Silva, J. M. R.; Oliveira, M. H. R.; Coriolano, A. C. F.; Delgado, R. C. O. B.; Fernandes, V. J.; Araujo, A. S. Thermogravimetry applied for catalytic degradation of atmospheric residue of petroleum on mesoporous catalyst. *Journal of Thermal Analysis and Calorimetry* **2019**, *136* (5), 2139-2144.

(232) Pennycook, S. J. Microscopy: Transmission electron microscopy. In *Encyclopedia of Condensed Matter Physics (Second Edition)*, Chakraborty, T. Ed.; Academic Press, **2024;** 63-70.

(233) Hubbard, A. T. *The Handbook of surface imaging and visualization*; CRC press, **1995**.

(234) Joy, D. C. Scanning Electron Microscopy: Theory, History and Development of the Field Emission Scanning Electron Microscope. In *Biological Field Emission Scanning Electron Microscopy*, **2019;** 1-6.

(235) Singh, M. K.; Singh, A. Chapter 17 - Scanning electron microscope. In *Characterization of Polymers and Fibres*, Singh, M. K., Singh, A. Eds.; Woodhead Publishing, **2022;** 387-419.

(236) Dombrowski, P.-M.; Kachel, S. R.; Neuhaus, L.; Gottfried, J. M.; Witte, G. Temperature-programmed desorption of large molecules: influence of thin film structure and origin of intermolecular repulsion. *Nanoscale* **2021**, *13* (32), 13816-13826.

(237) Wang, K.-T.; Nachimuthu, S.; Jiang, J.-C. Temperature-programmed desorption studies of NH_3 and H_2O on the RuO_2(110) surface: effects of adsorbate diffusion. *Physical Chemistry Chemical Physics* **2018**, *20* (37), 24201-24209.

(238) Arena, F.; Chio, R. D.; Trunfio, G. An experimental assessment of the ammonia temperature programmed desorption method for probing the surface acidic properties of heterogeneous catalysts. *Applied Catalysis A: General* **2015**, *503*, 227-236.

(239) Barrie, P. J. Analysis of temperature programmed desorption (TPD) data for the characterisation of catalysts containing a distribution of adsorption sites. *Physical Chemistry Chemical Physics* **2008**, *10* (12), 1688-1696.

(240) Sun, Q.; Wang, N.; Xu, Q.; Yu, J. Nanopore-supported metal nanocatalysts

for efficient hydrogen generation from liquid-phase chemical hydrogen storage materials. *Advanced Materials* **2020**, *32* (44), 2001818.

(241) Xu, M.; Lai, C.; Liu, X.; Li, B.; Zhang, M.; Xu, F.; Liu, S.; Li, L.; Qin, L.; Yi, H. COF-confined catalysts: from nanoparticles and nanoclusters to single atoms. *Journal of Materials Chemistry A* **2021**, *9* (43), 24148-24174.

(242) Tanaka, S.-I.; Miyazaki, J.; Tiwari, D. K.; Jin, T.; Inouye, Y. Fluorescent Platinum Nanoclusters: Synthesis, Purification, Characterization, and Application to Bioimaging. *Angewandte Chemie International Edition* **2011**, *50* (2), 431-435.

(243) Du, M.; Li, X.; Pang, H.; Xu, Q. Alloy electrocatalysts. *EnergyChem* **2023**, *5* (2), 100083.

(244) Quílez-Bermejo, J.; García-Dalí, S.; Daouli, A.; Zitolo, A.; Canevesi, R. L.; Emo, M.; Izquierdo, M. T.; Badawi, M.; Celzard, A.; Fierro, V. Advanced Design of Metal Nanoclusters and Single Atoms Embedded in C_1N_1-Derived Carbon Materials for ORR, HER, and OER. *Advanced Functional Materials* **2023**, 2300405.

(245) Casteleiro, B.; Martinho, J. M. G.; Farinha, J. P. S. Encapsulation of gold nanoclusters: stabilization and more. *Nanoscale* **2021**, *13* (41), 17199-17217.

(246) Thomas, J. M.; Midgley, P. A. The Merits of Static and Dynamic High-Resolution Electron Microscopy (HREM) for the Study of Solid Catalysts. *ChemCatChem* **2010**, *2* (7), 783-798.

(247) Yang, J. C.; Small, M. W.; Grieshaber, R. V.; Nuzzo, R. G. Recent developments and applications of electron microscopy to heterogeneous catalysis. *Chemical Society Reviews* **2012**, *41* (24), 8179-8194.

(248) Cuenya, B. R.; Behafarid, F. Nanocatalysis: size-and shape-dependent chemisorption and catalytic reactivity. *Surface Science Reports* **2015**, *70* (2), 135-187.

(249) Zhang, L.; Ren, Y.; Liu, W.; Wang, A.; Zhang, T. Single-atom catalyst: a rising star for green synthesis of fine chemicals. *National Science Review* **2018**, *5* (5),

653-672.

(250) Yan, H.; Su, C.; He, J.; Chen, W. Single-atom catalysts and their applications in organic chemistry. *Journal of Materials Chemistry A* **2018**, *6* (19), 8793-8814.

(251) Hu, Y.; Li, H.; Li, Z.; Li, B.; Wang, S.; Yao, Y.; Yu, C. Progress in batch preparation of single-atom catalysts and application in sustainable synthesis of fine chemicals. *Green Chemistry* **2021**, *23* (22), 8754-8794.

(252) Li, W.-H.; Yang, J.; Wang, D.; Li, Y. Striding the threshold of an atom era of organic synthesis by single-atom catalysis. *Chem* **2021**.

(253) Greco, R.; Mon, M.; Leyva-Pérez, A. Supported Metal Single Atom Thermocatalysts forC C, C Si, andC BBond-Forming (Coupling) Reactions and Biomedical Applications. In *Supported Metal Single Atom Catalysis*, **2022;** 473-502.

(254) Lei, Y.; Mehmood, F.; Lee, S.; Greeley, J.; Lee, B.; Seifert, S.; Winans, R. E.; Elam, J. W.; Meyer, R. J.; Redfern, P. C.; et al. Increased silver activity for direct propylene epoxidation via subnanometer size effects. *Science* **2010**, *328* (5975), 224-228.

(255) Vajda, S.; White, M. G. Catalysis applications of size-selected cluster deposition. *ACS Catalysis* **2015**, *5* (12), 7152-7176.

(256) Buceta, D.; Busto, N.; Barone, G.; Leal, J. M.; Dominguez, F.; Giovanetti, L. J.; Requejo, F. G.; Garcia, B.; Lopez-Quintela, M. A. Ag_2 and Ag_3 clusters: synthesis, characterization, and interaction with DNA. *Angewandte Chemie International Edition* **2015**, *54* (26), 7612-7616.

(257) Sun, T.; Seff, K. Silver clusters and chemistry in zeolites. *Chemical Reviews* **1994**, *94* (4), 857-870.

(258) Boschetto, D. L.; Lerin, L.; Cansian, R.; Pergher, S. B. C.; Di Luccio, M. Preparation and antimicrobial activity of polyethylene composite films with silver exchanged zeolite-Y. *Chemical Engineering Journal* **2012**, *204*, 210-216.

(259) Singh, V. V.; Jurado-Sánchez, B.; Sattayasamitsathit, S.; Orozco, J.; Li, J.; Galarnyk, M.; Fedorak, Y.; Wang, J. Multifunctional silver-exchanged zeolite micromotors for catalytic detoxification of chemical and biological threats. *Advanced Functional Materials* **2015**, *25* (14), 2147-2155.

(260) Cerrillo, J. L.; Palomares, A. E.; Rey, F.; Valencia, S.; Palou, L.; Pérez-Gago, M. B. Ag-zeolites as fungicidal material: Control of citrus green mold caused by Penicillium digitatum. *Microporous and Mesoporous Materials* **2017**, *254*, 69-76.

(261) Cerrillo, J.; Palomares, A.; Rey, F. Silver exchanged zeolites as bactericidal additives in polymeric materials. *Microporous and Mesoporous Materials* **2020**, *305*, 110367.

(262) Chebbi, M.; Azambre, B.; Cantrel, L.; Huvé, M.; Albiol, T. Influence of structural, textural and chemical parameters of silver zeolites on the retention of methyl iodide. *Microporous and Mesoporous Materials* **2017**, *244*, 137-150.

(263) Azambre, B.; Chebbi, M. Evaluation of silver zeolites sorbents toward their ability to promote stable CH_3I storage as AgI precipitates. *ACS Applied Materials & Interfaces* **2017**, *9* (30), 25194-25203.

(264) Baba, T. Conversion of methane over Ag^+-exchanged zeolite in the presence of ethene. *Catalysis surveys from Asia* **2005**, *9*, 147-154.

(265) Baba, T.; Iwase, Y.; Inazu, K.; Masih, D.; Matsumoto, A. Catalytic properties of silver-exchanged zeolites for propene production by conversion of methane in the presence of ethene. *Microporous and Mesoporous Materials* **2007**, *101* (1-2), 142-147.

(266) Shi, C.; Cheng, M.; Qu, Z.; Bao, X. Investigation on the catalytic roles of silver species in the selective catalytic reduction of NO_x with methane. *Applied Catalysis B: Environmental* **2004**, *51* (3), 171-181.

(267) Sugihara, H.; Chen, L. Y.; Yasumori, I. The Catalytic Activity of AgX-type Zeolite for the Isomerization of 1-Butene. *Bulletin of the Chemical Society of Japan*

1974, *47* (9), 2089-2093.

(268) Teng, J. W.; Cai, T. X.; Bao, X. H. Ag-ZSM-5 catalyst for the catalytic decomposition of NO. *Chinese Chemical Letters* **1999**, *10* (1), 83-86.

(269) Lagunov, O.; Chakarova, K.; Hadjiivanov, K. Silver-catalyzed low-temperature CO isotopic scrambling reaction: 12 C 16 O+ 13 C 18 O→ 12 C 18 O+ 13 C 16 O. *Physical Chemistry Chemical Physics* **2012**, *14* (7), 2178-2182.

(270) Tarach, K.; Góra-Marek, K.; Chrzan, M.; Walas, S. Quantification of silver sites in zeolites: Carbon monoxide sorption monitored by IR spectroscopy. *Journal of Physical Chemistry C* **2014**, *118* (41), 23751-23760.

(271) Martinez-Ortigosa, J.; Lopes, C. W.; Agostini, G.; Palomares, A. E.; Blasco, T.; Rey, F. AgY zeolite as catalyst for the selective catalytic oxidation of NH_3. *Microporous and Mesoporous Materials* **2021**, *323*, 111230.

(272) Beer, R.; Binder, F.; Calzaferri, G. Photochemical oxidation of water on a 1 μ Ag^+ zeolite layer. *Journal of Photochemistry and Photobiology A: Chemistry* **1992**, *69* (1), 67-72.

(273) Kennes, K.; Coutino-Gonzalez, E.; Martin, C.; Baekelant, W.; Roeffaers, M. B.; Van der Auweraer, M. Silver Zeolite Composites-Based LEDs: A Novel Solid-State Lighting Approach. *Advanced Functional Materials* **2017**, *27* (14), 1606411.

(274) Baekelant, W.; Aghakhani, S.; Coutino-Gonzalez, E.; Kennes, K.; D'Acapito, F.; Grandjean, D.; Van der Auweraer, M.; Lievens, P.; Roeffaers, M. B. J.; Hofkens, J.; et al. Shaping the Optical Properties of Silver Clusters Inside Zeolite A via Guest-Host-Guest Interactions. *Journal of physical chemistry letters* **2018**, *9* (18), 5344-5350.

(275) Lopes, C. W.; Martinez-Ortigosa, J.; Góra-Marek, K.; Tarach, K.; Vidal-Moya, J. A.; Palomares, A. E.; Agostini, G.; Blasco, T.; Rey, F. Zeolite-driven Ag species during redox treatments and catalytic implications for SCO of NH_3. *Journal of Materials Chemistry A* **2021**, *9* (48), 27448-27458.

(276) Li, N.; Huang, B.; Dong, X.; Luo, J.; Wang, Y.; Wang, H.; Miao, D.; Pan, Y.; Jiao, F.; Xiao, J. Bifunctional zeolites-silver catalyst enabled tandem oxidation of formaldehyde at low temperatures. *Nature Communications* **2022**, *13* (1), 2209.

(277) Li, M.; Wu, W.; Jiang, H. Recent Advances in Silver-Catalyzed Transformations of Electronically Unbiased Alkenes and Alkynes. *ChemCatChem* **2020**, *12* (20), 5034-5050.

(278) Sekine, K.; Yamada, T. Silver-catalyzed carboxylation. *Chemical Society Reviews* **2016**, *45* (16), 4524-4532.

(279) Fang, G.; Bi, X. Silver-catalysed reactions of alkynes: recent advances. *Chemical Society Reviews* **2015**, *44* (22), 8124-8173.

(280) Naodovic, M.; Yamamoto, H. Asymmetric silver-catalyzed reactions. *Chemical Reviews* **2008**, *108* (8), 3132-3148.

(281) Thompson, J. L.; Davies, H. M. Enhancement of cyclopropanation chemistry in the silver-catalyzed reactions of aryldiazoacetates. *Journal of the American Chemical Society* **2007**, *129* (19), 6090-6091.

(282) Hashmi, A. S. K. A Critical Comparison: Copper, Silver, and Gold. In *Silver in Organic Chemistry*, **2010;** 357-379.

(283) Fructos, M. R.; Belderrain, T. R.; de Fremont, P.; Scott, N. M.; Nolan, S. P.; Diaz-Requejo, M. M.; Perez, P. J. A gold catalyst for carbene-transfer reactions from ethyl diazoacetate. *Angewandte Chemie International Edition* **2005**, *44* (33), 5284-5288.

(284) Caballero, A.; Despagnet-Ayoub, E.; Diaz-Requejo, M. M.; Diaz-Rodriguez, A.; Gonzalez-Nunez, M. E.; Mello, R.; Munoz, B. K.; Ojo, W. S.; Asensio, G.; Etienne, M.; et al. Silver-catalyzed C-C bond formation between methane and ethyl diazoacetate in supercritical CO_2. *Science* **2011**, *332* (6031), 835-838.

(285) Sanchez-Sanchez, C.; Orozco, N.; Holgado, J. P.; Beaumont, S. K.; Kyriakou,

G.; Watson, D. J.; Gonzalez-Elipe, A. R.; Feria, L.; Fernandez Sanz, J.; Lambert, R. M. Sonogashira cross-coupling and homocoupling on a silver surface: chlorobenzene and phenylacetylene on Ag(100). *Journal of the American Chemical Society* **2015**, *137* (2), 940-947.

(286) Clarke, A. K.; James, M. J.; O'Brien, P.; Taylor, R. J.; Unsworth, W. P. Silica-Supported Silver Nitrate as a Highly Active Dearomatizing Spirocyclization Catalyst: Synergistic Alkyne Activation by Silver Nanoparticles and Silica. *Angewandte Chemie International Edition* **2016**, *55* (44), 13798-13802.

(287) Gui, Q.; Han, K.; Liu, Z.; Su, Z.; He, X.; Jiang, H.; Tian, B.; Li, Y. E-Selective synthesis of vinyl sulfones via silver-catalyzed sulfonylation of styrenes. *Organic & Biomolecular Chemistry* **2018**, *16* (32), 5748-5751.

(288) Baldansuren, A.; Dilger, H.; Eichel, R. d.-A.; van Bokhoven, J. A.; Roduner, E. Interaction and reaction of ethylene and oxygen on six-atom silver clusters supported on LTA zeolite. *Journal of Physical Chemistry C* **2009**, *113* (45), 19623-19632.

(289) Ono, Y.; Baba, T. Unique properties of silver cations in solid-acid catalysis by zeolites and heteropolyacids. *Physical Chemistry Chemical Physics* **2015**, *17* (24), 15637-15654.

(290) Dempsey, E. Calculation of Madelung potentials for faujasite-type zeolites. I. *Journal of Physical Chemistry* **1969**, *73* (11), 3660-3668.

(291) Ferenczy, G. G.; Ángyán, J. G. Calculations on electrostatic properties of HY zeolite. *Journal of the Chemical Society, Faraday Transactions* **1990**, *86* (20), 3461-3466.

(292) Areán, C. O.; Palomino, G. T.; Zecchina, A.; Spoto, G.; Bordiga, S.; Roy, P. Cation-carbon stretching vibration of adducts formed upon CO adsorption on alkaline zeolites. *Physical Chemistry Chemical Physics* **1999**, *1* (17), 4139-4140.

(293) Concepcion-Heydorn, P.; Jia, C.; Herein, D.; Pfänder, N.; Karge, H. G.; Jentoft, F. C. Structural and catalytic properties of sodium and cesium exchanged X and Y zeolites, and germanium-substituted X zeolite. *Journal of Molecular Catalysis A: Chemical* **2000**, *162* (1-2), 227-246.

(294) Corma, A.; García, H.; Leyva, A. Controlling the softness-hardness of Pd by strong metal-zeolite interaction: cyclisation of diallylmalonate as a test reaction. *Journal of Catalysis* **2004**, *225* (2), 350-358.

(295) Garnes-Portolés, F.; Greco, R.; Oliver-Meseguer, J.; Castellanos-Soriano, J.; Consuelo Jiménez, M.; López-Haro, M.; Hernández-Garrido, J. C.; Boronat, M.; Pérez-Ruiz, R.; Leyva-Pérez, A. Regioirregular and catalytic Mizoroki-Heck reactions. *Nature Catalysis* **2021**, *4* (4), 293-303.

(296) Oudenhuijzen, M. K.; van Bokhoven, J. A.; Miller, J. T.; Ramaker, D. E.; Koningsberger, D. C. Three-site model for hydrogen adsorption on supported platinum particles: influence of support ionicity and particle size on the hydrogen coverage. *Journal of the American Chemical Society* **2005**, *127* (5), 1530-1540.

(297) Bartolomeu, R.; Bertolo, R.; Casale, S.; Fernandes, A.; Henriques, C.; da Costa, P.; Ribeiro, F. Particular characteristics of silver species on Ag-exchanged LTL zeolite in K and H form. *Microporous and Mesoporous Materials* **2013**, *169*, 137-147.

(298) Chebbi, M.; Azambre, B.; Cantrel, L.; Koch, A. A combined drifts and DR-UV-Vis spectroscopic in situ study on the trapping of CH_3I by silver-exchanged faujasite zeolite. *Journal of Physical Chemistry C* **2016**, *120* (33), 18694-18706.

(299) Santillan, J. M. J.; Muneton Arboleda, D.; Muraca, D.; Schinca, D. C.; Scaffardi, L. B. Highly fluorescent few atoms silver nanoclusters with strong photocatalytic activity synthesized by ultrashort light pulses. *Scientific Reports* **2020**, *10* (1), 8217.

(300) Bartolomeu, R.; Azambre, B.; Westermann, A.; Fernandes, A.; Bertolo, R.;

Hamoud, H. I.; Henriques, C.; Da Costa, P.; Ribeiro, F. Investigation of the nature of silver species on different Ag-containing NO_x reduction catalysts: On the effect of the support. *Applied Catalysis B: Environmental* **2014**, *150*, 204-217.

(301) Sandoval, A.; Delannoy, L.; Methivier, C.; Louis, C.; Zanella, R. Synergetic effect in bimetallic Au-Ag/TiO_2 catalysts for CO oxidation: New insights from in situ characterization. *Applied Catalysis A: General* **2015**, *504*, 287-294.

(302) Huang, M.; Adnot, A.; Kaliaguine, S. Characterization of basicity in alkaline cation faujasite zeolites—An XPS study using pyrrole as a probe molecule. *Journal of Catalysis* **1992**, *137* (2), 322-332.

(303) Hadjiivanov, K. Identification and Characterization of Surface Hydroxyl Groups by Infrared Spectroscopy. In *Advances in Catalysis*, Jentoft, F. C. Ed.; Advances in Catalysis, Vol. 57; Academic Press, **2014;** 99-318.

(304) Müslehiddinoğlu, J.; Vannice, M. A. CO adsorption on supported and promoted Ag epoxidation catalysts. *Journal of Catalysis* **2003**, *213* (2), 305-320.

(305) Tiburcio, E.; Zheng, Y.; Bilanin, C.; Hernandez-Garrido, J. C.; Vidal-Moya, A.; Oliver-Meseguer, J.; Martin, N.; Mon, M.; Ferrando-Soria, J.; Armentano, D.; et al. MOF-Triggered Synthesis of Subnanometer Ag^0_2 Clusters and Fe^{3+} Single Atoms: Heterogenization Led to Efficient and Synergetic One-Pot Catalytic Reactions. *Journal of the American Chemical Society* **2023**, *145* (18), 10342-10354.

(306) Porto, V.; Buceta, D.; Domínguez, B.; Carneiro, C.; Borrajo, E.; Fraile, M.; Davila-Ferreira, N.; Arias, I. R.; Blanco, J. M.; Blanco, M. C. Silver clusters of five atoms as highly selective antitumoral agents through irreversible oxidation of thiols. *Advanced Functional Materials* **2022**, *32* (29), 2113028.

(307) Díaz-Requejo, M. M.; Pérez, P. J. Copper, silver and gold-based catalysts for carbene addition or insertion reactions. *Journal of Organometallic Chemistry* **2005**, *690* (24-25), 5441-5450.

(308) Bergstrom, B. D.; Nickerson, L. A.; Shaw, J. T.; Souza, L. W. Transition Metal Catalyzed Insertion Reactions with Donor/Donor Carbenes. *Angewandte Chemie International Edition* **2021**, *60* (13), 6864-6878.

(309) Oliver-Meseguer, J.; Boronat, M.; Vidal-Moya, A.; Concepcion, P.; Rivero-Crespo, M. A.; Leyva-Perez, A.; Corma, A. Generation and Reactivity of Electron-Rich Carbenes on the Surface of Catalytic Gold Nanoparticles. *Journal of the American Chemical Society* **2018**, *140* (9), 3215-3218.

(310) Ma, G.; Wei, K.-F.; Song, M.; Dang, Y.-L.; Yue, Y.; Han, B.; Su, H.; Shen, W.-B. Recent advances in transition-metal-catalyzed Büchner reaction of alkynes. *Organic & Biomolecular Chemistry* **2023**, *21* (25), 5150-5157.

(311) Zhu, D.; Cao, T.; Chen, K.; Zhu, S. Rh_2(ii)-catalyzed enantioselective intramolecular Büchner reaction and aromatic substitution of donor-donor carbenes. *Chemical Science* **2022**, *13* (7), 1992-2000.

(312) Komine, N.; Flores, J. A.; Pal, K.; Caulton, K. G.; Mindiola, D. J. Büchner Reactions Catalyzed by a Silver (I) Pyridylpyrrolide: Understanding Arene C=C Insertion Selectivity. *Organometallics* **2013**, *32* (11), 3185-3191.

(313) Fortea-Perez, F. R.; Mon, M.; Ferrando-Soria, J.; Boronat, M.; Leyva-Perez, A.; Corma, A.; Herrera, J. M.; Osadchii, D.; Gascon, J.; Armentano, D.; et al. The MOF-driven synthesis of supported palladium clusters with catalytic activity for carbene-mediated chemistry. *Nature Materials* **2017**, *16* (7), 760-766.

(314) Fortea-Pérez, F. R.; Mon, M.; Ferrando-Soria, J.; Boronat, M.; Leyva-Pérez, A.; Corma, A.; Herrera, J. M.; Osadchii, D.; Gascon, J.; Armentano, D.; et al. The MOF-driven synthesis of supported palladium clusters with catalytic activity for carbene-mediated chemistry. *Nature Materials* **2017**, *16* (7), 760-766.

(315) Ranocchiari, M.; Mezzetti, A. Ru/PNNP-catalyzed asymmetric imine aziridination by diazo ester activation. *Organometallics* **2009**, *28* (13), 3611-3613.

(316) Oliver-Meseguer, J.; Boronat, M.; Vidal-Moya, A.; Concepcion, P.; Rivero-Crespo, M. A.; Leyva-Perez, A.; Corma, A. Generation and Reactivity of Electron-Rich Carbenes on the Surface of Catalytic Gold Nanoparticles. *Journal of the American Chemical Society* **2018**, *140* (9), 3215-3218.

(317) Pujol, A.; Lafage, M.; Rekhroukh, F.; Saffon-Merceron, N.; Amgoune, A.; Bourissou, D.; Nebra, N.; Fustier-Boutignon, M.; Mezailles, N. A Nucleophilic Gold(III) Carbene Complex. *Angewandte Chemie International Edition* **2017**, *56* (40), 12264-12267.

(318) Tyo, E. C.; Vajda, S. Catalysis by clusters with precise numbers of atoms. *Nat Nanotechnol* **2015**, *10* (7), 577-588.

(319) Malola, S.; Hakkinen, H. Prospects and challenges for computer simulations of monolayer-protected metal clusters. *Nature Communications* **2021**, *12* (1), 2197.

(320) Zaker, Y.; Ashenfelter, B. A.; Bhattarai, B.; Diemler, N. A.; Brewer, T. R.; Bigioni, T. P. Sequential growth as a mechanism of silver-glutathione monolayer-protected cluster formation. *Small* **2021**, *17* (27), 2002238.

(321) Dong, C.; Gao, Z.; Li, Y.; Peng, M.; Wang, M.; Xu, Y.; Li, C.; Xu, M.; Deng, Y.; Qin, X. Fully exposed palladium cluster catalysts enable hydrogen production from nitrogen heterocycles. *Nature Catalysis* **2022**, *5* (6), 485-493.

(322) Liu, L.; Corma, A. Confining isolated atoms and clusters in crystalline porous materials for catalysis. *Nature Reviews Materials* **2021**, *6* (3), 244-263.

(323) Liu, L.; Lopez-Haro, M.; Perez-Omil, J. A.; Boronat, M.; Calvino, J. J.; Corma, A. Direct assessment of confinement effect in zeolite-encapsulated subnanometric metal species. *Nature Communications* **2022**, *13* (1), 821.

(324) Li, Z.; Ji, S.; Liu, Y.; Cao, X.; Tian, S.; Chen, Y.; Niu, Z.; Li, Y. Well-Defined Materials for Heterogeneous Catalysis: From Nanoparticles to Isolated Single-Atom Sites. *Chemical Reviews* **2020**, *120* (2), 623-682.

(325) Mitchell, S.; Qin, R.; Zheng, N.; Pérez-Ramírez, J. Nanoscale engineering of catalytic materials for sustainable technologies. *Nature nanotechnology* **2021**, *16* (2), 129-139.

(326) Wang, N.; Sun, Q.; Yu, J. Ultrasmall Metal Nanoparticles Confined within Crystalline Nanoporous Materials: A Fascinating Class of Nanocatalysts. *Advanced Materials* **2019**, *31* (1), 1803966.

(327) Xu, L.; Ma, W.; Wang, L.; Xu, C.; Kuang, H.; Kotov, N. A. Nanoparticle assemblies: dimensional transformation of nanomaterials and scalability. *Chemical Society Reviews* **2013**, *42* (7), 3114-3126.

(328) Grzelczak, M.; Pérez-Juste, J.; Mulvaney, P.; Liz-Marzán, L. M. Shape control in gold nanoparticle synthesis. *Chemical Society Reviews* **2008**, *37* (9), 1783-1791.

(329) Pérez-Juste, J.; Pastoriza-Santos, I.; Liz-Marzán, L. M.; Mulvaney, P. Gold nanorods: Synthesis, characterization and applications. *Coordination Chemistry Reviews* **2005**, *249* (17), 1870-1901.

(330) Kang, X.; Wang, S.; Song, Y.; Jin, S.; Sun, G.; Yu, H.; Zhu, M. Bimetallic Au_2Cu_6 Nanoclusters: Strong Luminescence Induced by the Aggregation of Copper(I) Complexes with Gold(0) Species. *Angewandte Chemie International Edition* **2016**, *55* (11), 3611-3614.

(331) Egerton, R. F.; Li, P.; Malac, M. Radiation damage in the TEM and SEM. *Micron* **2004**, *35* (6), 399-409.

(332) Ni, B.; Wang, X. Chemistry and properties at a sub-nanometer scale. *Chemical Science* **2016**, *7* (7), 3978-3991.

(333) Shang, L.; Dong, S.; Nienhaus, G. U. Ultra-small fluorescent metal nanoclusters: Synthesis and biological applications. *Nano Today* **2011**, *6* (4), 401-418.

(334) Boronat, M.; Leyva-Pérez, A.; Corma, A. Theoretical and Experimental Insights into the Origin of the Catalytic Activity of Subnanometric Gold Clusters: Attempts to Predict Reactivity with Clusters and Nanoparticles of Gold. *Accounts of Chemical Research* **2014**, *47* (3), 834-844.

(335) Jash, M.; Pradeep, T. Chapter 17 - Naked clusters and ion chemistry of clusters. In *Atomically Precise Metal Nanoclusters*, Pradeep, T. Ed.; Elsevier, **2023;** 427-460.

(336) Liu, L.; Lopez-Haro, M.; Lopes, C. W.; Li, C.; Concepcion, P.; Simonelli, L.; Calvino, J. J.; Corma, A. Regioselective generation and reactivity control of subnanometric platinum clusters in zeolites for high-temperature catalysis. *Nature Materials* **2019**, *18* (8), 866-873.

(337) Viciano-Chumillas, M.; Mon, M.; Ferrando-Soria, J.; Corma, A.; Leyva-Pérez, A.; Armentano, D.; Pardo, E. Metal-Organic Frameworks as Chemical Nanoreactors: Synthesis and Stabilization of Catalytically Active Metal Species in Confined Spaces. *Accounts of Chemical Research* **2020**, *53* (2), 520-531.

(338) Young, R. J.; Huxley, M. T.; Pardo, E.; Champness, N. R.; Sumby, C. J.; Doonan, C. J. Isolating reactive metal-based species in Metal-Organic Frameworks - viable strategies and opportunities. *Chemical Science* **2020**, *11* (16), 4031-4050.

(339) Freund, R.; Zaremba, O.; Arnauts, G.; Ameloot, R.; Skorupskii, G.; Dincă, M.; Bavykina, A.; Gascon, J.; Ejsmont, A.; Goscianska, J.; et al. The Current Status of MOF and COF Applications. *Angewandte Chemie International Edition* **2021**, *60* (45), 23975-24001.

(340) Bilanin, C.; Tiburcio, E.; Ferrando-Soria, J.; Armentano, D.; Leyva-Pérez, A.; Pardo, E. Crystallographic Visualization of a Double Water Molecule Addition on a Pt_1-MOF during the Low-temperature Water-Gas Shift Reaction. *ChemCatChem* **2021**, *13* (4), 1195-1200.

(341) Tiburcio, E.; Greco, R.; Mon, M.; Ballesteros-Soberanas, J.; Ferrando-Soria, J.; López-Haro, M.; Hernández-Garrido, J. C.; Oliver-Meseguer, J.; Marini, C.; Boronat, M.; et al. Soluble/MOF-Supported Palladium Single Atoms Catalyze the Ligand-, Additive-, and Solvent-Free Aerobic Oxidation of Benzyl Alcohols to Benzoic Acids. *Journal of the American Chemical Society* **2021**, *143* (6), 2581-2592.

(342) Rivero-Crespo, M. A.; Mon, M.; Ferrando-Soria, J.; Lopes, C. W.; Boronat, M.; Leyva-Pérez, A.; Corma, A.; Hernández-Garrido, J. C.; López-Haro, M.; Calvino, J. J.; et al. Confined Pt_1^{1+} Water Clusters in a MOF Catalyze the Low-Temperature Water-Gas Shift Reaction with both CO_2 Oxygen Atoms Coming from Water. *Angewandte Chemie International Edition* **2018**, *57* (52), 17094-17099.

(343) Mon, M.; Rivero-Crespo, M. A.; Ferrando-Soria, J.; Vidal-Moya, A.; Boronat, M.; Leyva-Pérez, A.; Corma, A.; Hernández-Garrido, J. C.; López-Haro, M.; Calvino, J. J.; et al. Synthesis of Densely Packaged, Ultrasmall Pt^0_2 Clusters within a Thioether-Functionalized MOF: Catalytic Activity in Industrial Reactions at Low Temperature. *Angewandte Chemie International Edition* **2018**, *57* (21), 6186-6191.

(344) Burgun, A.; Coghlan, C. J.; Huang, D. M.; Chen, W.; Horike, S.; Kitagawa, S.; Alvino, J. F.; Metha, G. F.; Sumby, C. J.; Doonan, C. J. Mapping-Out Catalytic Processes in a Metal-Organic Framework with Single-Crystal X-ray Crystallography. *Angewandte Chemie International Edition* **2017**, *56* (29), 8412-8416.

(345) Inokuma, Y.; Yoshioka, S.; Ariyoshi, J.; Arai, T.; Hitora, Y.; Takada, K.; Matsunaga, S.; Rissanen, K.; Fujita, M. X-ray analysis on the nanogram to microgram scale using porous complexes. *Nature* **2013**, *495* (7442), 461-466.

(346) Mon, M.; Bruno, R.; Ferrando-Soria, J.; Bartella, L.; Di Donna, L.; Talia, M.; Lappano, R.; Maggiolini, M.; Armentano, D.; Pardo, E. Crystallographic snapshots of host-guest interactions in drugs@metal-organic frameworks: towards mimicking molecular recognition processes. *Materials Horizons* **2018**, *5* (4), 683-690.

(347) Zhuang, P.; Zhang, P.; Li, K.; Kumari, B.; Li, D.; Mei, X. Silver Nanoclusters

Encapsulated into Metal-Organic Frameworks for Rapid Removal of Heavy Metal Ions from Water. *Molecules* **2019**, *24* (13), 2442.

(348) Ferraria, A. M.; Carapeto, A. P.; Botelho do Rego, A. M. X-ray photoelectron spectroscopy: Silver salts revisited. *Vacuum* **2012**, *86* (12), 1988-1991.

(349) Tarach, K.; Góra-Marek, K.; Chrzan, M.; Walas, S. Quantification of Silver Sites in Zeolites: Carbon Monoxide Sorption Monitored by IR Spectroscopy. *The Journal of Physical Chemistry C* **2014**, *118* (41), 23751-23760.

(350) Bartolomeu, R.; Azambre, B.; Westermann, A.; Fernandes, A.; Bértolo, R.; Hamoud, H. I.; Henriques, C.; Da Costa, P.; Ribeiro, F. Investigation of the nature of silver species on different Ag-containing NO_x reduction catalysts: On the effect of the support. *Applied Catalysis B: Environmental* **2014**, *150-151*, 204-217.

(351) De Lange, M. F.; Vlugt, T. J. H.; Gascon, J.; Kapteijn, F. Adsorptive characterization of porous solids: Error analysis guides the way. *Microporous and Mesoporous Materials* **2014**, *200*, 199-215.

(352) Díaz-Requejo, M. M.; Pérez, P. J. Copper, silver and gold-based catalysts for carbene addition or insertion reactions. *Journal of Organometallic Chemistry* **2005**, *690* (24), 5441-5450.

(353) Lovely, C. J.; Browning, R. G.; Badarinarayana, V.; Dias, H. V. R. A silver-catalyzed Büchner reaction. *Tetrahedron Letters* **2005**, *46* (14), 2453-2455.

(354) Deng, Y.; Jing, C.; Zavalij, P. Y.; Doyle, M. P. $Hg(OTf)_2$ Catalyzed Intramolecular 1,4-Addition of Donor-Acceptor Cyclopropenes to Arenes. *Organic Letters* **2015**, *17* (17), 4312-4315.

(355) Radhika, S.; Abdulla, C. M. A.; Aneeja, T.; Anilkumar, G. Silver-catalysed C-H bond activation: a recent review. *New Journal of Chemistry* **2021**, *45* (35), 15718-15738.

(356) Peña-López, M.; Beller, M. Functionalization of Unactivated $C(sp^3)$–H

Bonds Using Metal-Carbene Insertion Reactions. *Angewandte Chemie International Edition* **2017**, *56* (1), 46-48.

(357) Fructos, M. R.; Belderrain, T. R.; de Frémont, P.; Scott, N. M.; Nolan, S. P.; Díaz-Requejo, M. M.; Pérez, P. J. A Gold Catalyst for Carbene-Transfer Reactions from Ethyl Diazoacetate. *Angewandte Chemie International Edition* **2005**, *44* (33), 5284-5288.

(358) Arredondo, V.; Hiew, S. C.; Gutman, E. S.; Premachandra, I. D. U. A.; Van Vranken, D. L. Enantioselective Palladium-Catalyzed Carbene Insertion into the N-H Bonds of Aromatic Heterocycles. *Angewandte Chemie International Edition* **2017**, *56* (15), 4156-4159.

(359) Yoo, J.; Park, N.; Park, J. H.; Park, J. H.; Kang, S.; Lee, S. M.; Kim, H. J.; Jo, H.; Park, J.-G.; Son, S. U. Magnetically Separable Microporous Fe-Porphyrin Networks for Catalytic Carbene Insertion into N-H Bonds. *ACS Catalysis* **2015**, *5* (1), 350-355.

(360) Wolf, M. W.; Vargas, D. A.; Lehnert, N. Engineering of RuMb: Toward a Green Catalyst for Carbene Insertion Reactions. *Inorganic Chemistry* **2017**, *56* (10), 5623-5635.

(361) Fraile, J. M.; Mayoral, J. A.; Ravasio, N.; Roldán, M.; Sordelli, L.; Zaccheria, F. Heterogeneous catalysts for carbene insertion reactions. *Journal of Catalysis* **2011**, *281* (2), 273-278.

(362) Zhou, M.; Zhang, H.; Xiong, L.; He, Z.; Wang, T.; Xu, Y.; Huang, K. Fe-Porphyrin functionalized microporous organic nanotube networks and their application for the catalytic olefination of aldehydes and carbene insertion into N-H bonds. *Polymer Chemistry* **2017**, *8* (24), 3721-3730.

(363) Chen, L.; Cui, H.; Wang, Y.; Liang, X.; Zhang, L.; Su, C.-Y. Carbene insertion into N-H bonds with size-selectivity induced by a microporous ruthenium-

porphyrin metal-organic framework. *Dalton Transactions* **2018**, *47* (11), 3940-3946.

(364) Oliver-Meseguer, J.; Boronat, M.; Vidal-Moya, A.; Concepción, P.; Rivero-Crespo, M. Á.; Leyva-Pérez, A.; Corma, A. Generation and Reactivity of Electron-Rich Carbenes on the Surface of Catalytic Gold Nanoparticles. *Journal of the American Chemical Society* **2018**, *140* (9), 3215-3218.

(365) Zhang, Z.; Yu, Y.; Huang, F.; Yi, X.; Xu, Y.; He, Y.; Baell, J. B.; Huang, H. Catalytic O-H bond insertion reactions using surface modified sewage sludge as a catalyst. *Green Chemistry* **2020**, *22* (5), 1594-1604.

(366) Tiburcio, E.; Zheng, Y.; Mon, M.; Martin, N.; Ferrando Soria, J.; Armentano, D.; Leyva Perez, A.; Pardo, E. Highly Efficient MOF-Driven Silver Subnanometer Clusters for the Catalytic Buchner Ring Expansion Reaction. *Inorganic Chemistry* **2022**, *61* (30), 11796-11802.

(367) Ren, Y.-Y.; Zhu, S.-F.; Zhou, Q.-L. Chiral proton-transfer shuttle catalysts for carbene insertion reactions. *Organic & Biomolecular Chemistry* **2018**, *16* (17), 3087-3094.

(368) Moody, C. J. Enantioselective Insertion of Metal Carbenes into N-H Bonds: A Potentially Versatile Route to Chiral Amine Derivatives. *Angewandte Chemie International Edition* **2007**, *46* (48), 9148-9150.

(369) Sharland, J. C.; Dunstan, D.; Majumdar, D.; Gao, J.; Tan, K.; Malik, H. A.; Davies, H. M. L. Hexafluoroisopropanol for the Selective Deactivation of Poisonous Nucleophiles Enabling Catalytic Asymmetric Cyclopropanation of Complex Molecules. *ACS Catalysis* **2022**, *12* (20), 12530-12542.

(370) Bradley, W.; Robinson, R. CLXXIV.—The interaction of benzoyl chloride and diazomethane together with a discussion of the reactions of the diazenes. *Journal of the Chemical Society* **1928**, (0), 1310-1318.

(371) Bronsted, J.; Bell, R. A Kinetic Study of Some Reactions of Diazoacetic

Ester in Benzene Solution. *Journal of the American Chemical Society* **1931**, *53* (7), 2478-2498.

(372) Cabrero-Antonino, J. R.; Leyva-Pérez, A.; Corma, A. Beyond Acid Strength in Zeolites: Soft Framework Counteranions for Stabilization of Carbocations on Zeolites and Its Implication in Organic Synthesis. *Angewandte Chemie International Edition* **2015**, *54* (19), 5658-5661.

(373) Kobe, J.; Gluszak, T.; Dumesic, J.; Root, T. Deuterium NMR Characterization of Broested Acid Sites and Silanol Species in Zeolites. *Journal of Physical Chemistry* **1995**, *99* (15), 5485-5491.

(374) Hunter, R.; Hutchings, G. J. Reaction of ethyl diazoacetate with the zeolite catalyst H-ZSM-5: a model study of carbon-carbon bond formation. *Journal of the Chemical Society, Chemical Communications* **1986**, (13), 1006-1008.

(375) Zhang, H.; Wang, Z.; Wang, Z.; Chu, Y.; Wang, S.; Hui, X.-P. Visible-Light-Mediated Formal Carbene Insertion Reaction: Enantioselective Synthesis of 1,4-Dicarbonyl Compounds Containing All-Carbon Quaternary Stereocenter. *ACS Catalysis* **2022**, *12* (9), 5510-5516.

(376) Martínez-Castelló, A.; Tejeda-Serrano, M.; Nowacka, A. E.; Oliver-Meseguer, J.; Leyva-Pérez, A. Solid-catalyzed esterification reaction of long-chain acids and alcohols in fixed-bed reactors at pilot plant scale. *Chemical Engineering and Processing: Process Intensification* **2022**, *178*, 109038.

(377) Penoni, A.; Wanke, R.; Tollari, S.; Gallo, E.; Musella, D.; Ragaini, F.; Demartin, F.; Cenini, S. Cyclopropanation of Olefins with Diazoalkanes, Catalyzed by Co^{II}(porphyrin) Complexes − A Synthetic and Mechanistic Investigation and the Molecular Structure of Co^{III}(TPP)(CH_2CO_2Et) (TPP = Dianion of meso-Tetraphenylporphyrin). *European Journal of Inorganic Chemistry* **2003**, *2003* (7), 1452-1460.

(378) Gallego, E. M.; Paris, C.; Cantín, Á.; Moliner, M.; Corma, A. Conceptual similarities between zeolites and artificial enzymes. *Chemical Science* **2019**, *10* (34), 8009-8015.

(379) Caldarelli, S.; Buchholz, A.; Hunger, M. Investigation of Sodium Cations in Dehydrated Zeolites LSX, X, and Y by ^{23}Na Off-Resonance RIACT Triple-Quantum and High-Speed MAS NMR Spectroscopy. *Journal of the American Chemical Society* **2001**, *123* (29), 7118-7123.

(380) Su, H.; Kim, H. S.; Seo, S. M.; Ko, S. O.; Suh, J. M.; Kim, G. H.; Lim, W. T. Location of Na^+ ions in fully dehydrated Na^+-saturated zeolite Y (FAU, Si/Al= 1.56). *Bulletin of the Korean Chemical Society* **2012**, *33* (8), 2785.